RePLASMA Final Report

by

Group 20

Student Name	Student Number
Walid Brachmi	4554337
Prajwal Deval	4811526
Guido Insinger	4846419
Gopal Kandiyoor	4797795
Aytek Korkmaz	4850459
Jakub Łabor	4876563
Mayank Prashar	4643526
Aleksandar Shokolarov	4836839
Mark van Spronsen	4866959
Emmanouil 'Manos' Vretoudakis	4799216

Version	**Date**
1.0	22/06/2021
2.0 (current)	29/06/2021

Principal Tutor: Dr. Matteo Pini
Coaches: Dr. Dries Allaerts
Ir. Marie Bieber
Institution: Delft University of Technology
Place: Faculty of Aerospace Engineering, Delft

Project Duration: April-July, 2021

Cover Image : RePLASMA

TU Delft

Contents

Executive summary

The culmination of the bachelor program of Aerospace Engineering at the Delft University of Technology is marked by the Design Synthesis Exercise. The aim of this report is to provide the reader an overview of the project and the design process undertaken over the course of the project.

Climate change poses a severe threat to the Earth as we know it, and is often regarded as the main challenge faced by mankind in the 21st century. In order to counteract the effects thereof, it is critical that scientists have access to atmospheric samples, capable of reflecting the presence of and characteristics of the relevant chemical species. This is the mission profile defined for the RePLASMA mission. As a result of this, the project objective statement is defined as follows:

> *"To provide a novel remotely controlled aircraft for in-situ and remote sensing atmospheric measurements at high altitudes designed for researching and monitoring climate change."*

In addition the mission need statement is:

> *"To design a cost-effective unmanned subsonic aircraft for atmospheric measurements at altitudes exceeding 25 km using sustainable fuels by 10 students in 10 weeks".*

These two statements allow for the project to guide itself towards successful completion of the goals stated.

After the project planning was set up, requirements were identified, both from stakeholders and from a market analysis. From these, key requirements were then established that would play a major role in later design choices. These are shown in the table below, and were identified as the most important requirements.

REQ-ID	Requirement
PLS-U-OPS-1	Mission shall facilitate sampling at an altitude above 25 km
PLS-U-PERF-4	Mission shall operate in an airspeed range of 0.4 < M < 0.85
PLS-U-REL-1	Mission shall use commercially available technology
PLS-U-SUS-1	Mission shall use sustainable clean fuels
PLS-U-PROP-1	Mission shall use a reciprocating type of engine for propulsion

From these requirements, in conjunction with the market analysis and technical risk assessment, 3 different concepts were developed. Each concept was designed to be developed around a unique propulsion system. The first concept is based on a piston powered bio fuel propulsion system. The second was a piston powered hydrogen UAV, while the third is a turbojet powered UAV, based on the Global Hawk[1]. A trade off was conducted, and resulted in the selection of the biofuel powered piston design.

Following the design selection, a multi stage design process was followed. This started with the selection of the initial design point, by means of an iterative tool. The iterative tool runs through a class I weight estimation, a wing and power loading diagram. The wing and power loading diagram leads into a trifecta of sizing modules that provide inputs into a class II weight estimation. These modules are run repeatedly until convergence is observed. This results in the initial design point. Following that, various subsystems conducted detailed design processes, where each department focuses on improving their section within the aircraft.

The detailed design process starts with the aerodynamic design. This includes aerodynamics. This includes the optimization of the airfoil, the design of the fuselage, the implementation of winglets as well as cooling and compression for the propulsion system. The propulsive design includes the

[1] https://www.northropgrumman.com/what-we-do/air/global-hawk/ [accessed 17/6/2021]

selection of an engine, the development of a turbocharger system to optimize performance for the flight condition and the matching between turbochargers and engines. Additionally the propeller is also designed in this process, leading to a 3-bladed outcome. The design of stability and control surfaces ensures the aircraft is stable, by use of a V-tail, which allows for coupled lateral motion. Finally, the structural design minimizes the weight of the aircraft, while ensuring that the expected load cases are dealt with sufficiently. Finally, the undercarriage was designed, so as to offer a wide range of runways that can be considered for the RePLASMA mission.

The completion of the detailed design phase allows for the final design integration. Key parameters are shown in Table 1.

Table 1: Summary of the dimensions of the basic design components.

Dimension Name	Dimension Value
Wing span	43.8 $[m]$
Wing area	77.6 $[m^2]$
Winglet height	1.5 $[m]$
Wing root chord	2.5 $[m]$
Wing tip chord	1 $[m]$
Fuselage length	8 $[m]$
Fuselage width	1 $[m]$
Fuselage height	1 $[m]$
V-tail halfspan	6.48 $[m]$
V-tail area	20.98 $[m^2]$
V-tail root chord	2.31 $[m]$
V-tail tip chord	0.93 $[m]$
Propeller diameter	3 $[m]$

Following this, the operational diagram was defined, considering the various procedures required by regulation and client requirements. A financial analysis shows that the operational cost of the RePLASMA mission is in the order of 3200 Euros, with an expected development cost of 16 million Euros. At the time of writing, the RePLASMA mission is able to conduct missions at altitude in excess of 18 kilometers, with early indications suggesting the possibility of achieving altitudes in excess of 25 kilometers is feasible, with an updated turbocharger configuration. The aim of the team is to focus on achieving this requirement, and lay a foundation for the future of the RePLASMA mission, including preliminary and detailed design.

Figure 1: The RePLASMA.

Abbreviations

Abbreviation	Definition
AERO	Aerodynamics
AoA	Angle of Attack
BSFC	Brake Specific Fuel Consumption
CAD	Computer Aided Design
CEA	Chemical Equilibrium Applications
CFD	Computational Fluid Dynamics
COMMS	Communications
CG	Center of Gravity
CS	Control and Stability
DOT	Design Option Tree
DSE	Design Synthesis Exercise
EIRP	Effective Isotropic Radiated Power
EL	Electrical
EU	European Union
FF	Fuel Fraction
FSC	Fuel Storage Complexity
HALE	High Altitude Long Endurance
HLD	High-Lift Device
MAC	Mean Aerodynamic Chord
MET	Methodology
MSE	Mean Squared Error
NASA	National Aeronautics and Space Administration
OPS	Operations
PERF	Performance
PLS	RePLASMA
PROP	Propulsion
REL	Reliability
STR	Structures
SUS	Sustainability
SWOT	Strengths, Weaknesses, Opportunities and Threats
TRL	Technology Readiness Level
UAV	Unmanned Aerial Vehicle
WBS	Work Breakdown Structure
WFD	Work Flow Diagram

List of Symbols

Symbol	Units	Definition
b	[m]	Wing span
b_{VT}	[m]	Span of the V-tail
$C_{L_{A-h}}$	[-]	Lift coefficient of tail-less aircraft
C_{L_h}	[-]	Lift coefficient of horizontal tail
$C_{L_{\alpha_{A-h}}}$	[rad^{-1}]	Lift coefficient gradient of tail-less aircraft
$C_{L_{\alpha_h}}$	[rad^{-1}]	Lift coefficient gradient of horizontal tail
$(C_{N_\beta})_{A-h}$	[-]	Change in yaw moment per sideslip, tail-less aircraft
$C_{m_{ac}}$	[-]	Moment coefficient around aerodynamic center
$C_{Y_{v_\alpha}}$	[-]	Gradient of the lateral force coefficient of the vertical tail per angle
$\bar{c}$	[m]	Mean aerodynamic chord
D_p	[kg]	Mass of a gaseous pollutant emitted during landing and take-off cycle
F_∞	[kN]	The maximum take-off thrust under ISA sea level static conditions
g	[m/s^2]	Gravitational acceleration
L_{AS}	[dB]	Slow A-weighted sound level
$L_{AS_{max}}$	[dB]	Maximum slow A-weighted sound level
l_h	[m]	Moment arm of the horizontal tail
l_v	[m]	Moment arm of the vertical tail
n	[mol]	number of moles
n_{ult}	[-]	Ultimate load factor
p_h	[Pa]	Pressure at altitude h
R	$[\frac{\text{J}}{\text{K·mol}}]$	Gas constant
S	[m^2]	Wing area
S_H	[m^2]	Horizontal tail area
S_V	[m^2]	Vertical tail area
S_{VT}	[m^2]	V-tail area
T	[K]	Temperature
$t_{r_{VT}}$	[m]	Thickness at the root chord of the V-tail
V	[m^3]	Volume
V_h	[m/s]	Air velocity at tail
V_{to}	[m/s]	Take-off velocity
$\bar{V}_h$	[-]	Volume coefficient of the horizontal tail
$\bar{V}_v$	[-]	Volume coefficient of the vertical tail
W_F	[kg]	Fuel weight
W_P	[kg]	Payload weight
W_{TFO}	[kg]	Weight of trapped fuel and oil
W_{TO}	[kg]	Maximum take-off weight
W_{VT}	[kg]	Weight of V-tail
x_{CG}	[m]	x-coordinate of the centre of gravity
x_h	[m]	x-coordinate of the horizontal tail aerodynamic centre
x_v	[m]	x-coordinate of the vertical tail aerodynamic centre

Continued on next page –

– continued from previous page

Symbol	Units	Definition
y_e	[m]	Distance from the engine to the y-axis plane of symmetry

Greek

β	[rad]	Sideslip angle
ΔT_e	[N]	Thrust of the operative engine
δ_r	[rad]	Rudder deflection
$\frac{d\epsilon}{d\alpha}$	[-]	Downwash gradient
η_v	[-]	Airspeed at vertical tail to airspeed ratio squared
ρ_h	[kg/m^3]	Air density at altitude h
σ_v	[rad]	Sidewash angle
τ_v	[-]	Rudder effectiveness

1

Introduction

For the design of an aircraft tailored for a high-altitude science mission, it is critical that each of the steps taken are firstly planned and then carried out carefully and effectively in order to achieve a successful design process in which project members' skills are enhanced. The project's procedure goes through analyzing the context in which the design is needed and will be used, followed by a brainstorm of possible solutions to the problem that is to be solved as concepts. Performing a trade-off among the options generated in the conceptual design phase paves the way into the initial design, where a design point to start with is obtained. This segues into the detailed design, which is the focus of this report, where every subsystem digs deep into how the corresponding requirements could be met. These subsystems are then amalgamated into one final design as other non-technical aspects of the procedure such as the cost, operations, and manufacturing is discussed and a foresight on what is to be expected and recommended given. The target of this report is to log the detailed design phase of the Remotely Piloted Atmospheric Science Unmanned Aircraft (RePLASMA).

The structure of the report is as follows. Chapter 2 and Chapter 3 provide the background of the project through what calls for such a mission and in which conditions it will be developed, as well as what the aircraft is expected to achieve. Chapter 4 depicts the initial ideas generated to tackle the given problem and Chapter 5 elaborate on the plans made in order to streamline the procedure. The initial sizing of the aircraft is explained in Chapter 6, where the idea of RePLASMA is first realized. From then on, the next chapters focus on subsystems and compartments of the aircraft, starting with aerodynamics in Chapter 7. The critical subsystem of propulsion that deals with providing power to succour the aircraft in its harsh conditions is explained after in Chapter 8. This is followed by the structures department in Chapter 9, ensuring rigidity, and control, stability & operations in Chapter 10, that guarantees the aircraft to remain in a firmly established state for the mission. Chapter 11 and Chapter 12 provide insight on the electronics system and the landing gear of the autonomous vehicle and Chapter 13 gives an overview on how the progress made in the aforementioned chapters unite into the final design. Next up, the operations and cost of the project is analyzed in Chapter 14 and the manufacturing and reliability aspects are discussed in Chapter 15. Finally, Chapter 16 provides a foresight on how the future is perceived and desired to be while Chapter 17 concludes this report.

2

Project Background

In this chapter the roots from which RePLASMA stems are explored, as several questions such as what a high-altitude long endurance unmanned aerial vehicle (HALE UAV) is, why atmospheric measurements at an altitude of 25 km is needed, and how RePLASMA fits in with the current level and trends in technology is answered. Firstly, Section 2.1 provides some insight on the context in which RePLASMA is fostered, and elaborate further on what requires such a project and how this could be made possible in the light of past developments. Next, Section 2.2 analyzes the market in which the aircraft will compete as well as how the past, current and expected future scenarios of this market leads to some advantages and disadvantages. Finally, the technical risk that is rooted in the project is discussed in Section 2.4 as the potential threats to the mission from an operational point of view has to be given in order to assess the reliability of the project effectively.

2.1. Project context

Climate change poses the single greatest threat to Earth as it currently exists. In order to mitigate the challenges posed by climate change, atmospheric science requires precise modelling and simulations of the chemical dynamics of the troposphere to be validated. Hence, precise in-situ measurements of pollutant samples and their impact are deemed valuable as they provide the most accurate results. Furthermore, since these collected data have to be analyzed as soon as they are obtained, there is a high need for subsonic HALE UAVs both because it allows for a large number of samples to be processed in real-time and some of the important and critical chemical species sampled could get destroyed by the aerodynamic heating and shock associated with supersonic flight. As a result, a novel science-oriented HALE UAV is in demand.

Despite some previous experimental aircraft achieved cruise at around 20 km altitude, coming up with propulsion systems that provide enough thrust to take and support the aircraft at higher altitudes have remained a challenge to this day. With the turboprop and turbofan engines suffering huge power drops at the altitude, the necessity for reciprocating engines become apparent. Although reciprocating engines seem favorable, the cooling in the thermal system and integration of the propulsion system in the airframe are the apparent issues that are to be tackled in this scenario.

Therefore the aim of this project is to design a cost-effective UAV driven by a novel piston engine to meet the following objectives: cruise at altitudes exceeding 25 km, remote controllability at very long distances, operating for at least 20 hours, and capability to transport a 150 kg payload for scientific measurements while remaining at a speed suitable for such measurements. The atmospheric samples collected and the data obtained from this mission can thus be used to validate climate models and eventually combat climate change.

2.2. Market analysis

Market analysis is performed for two main purposes: identifying strategic partners that can help bring the product to market and identifying market demands with regards to the payload. This section explains the identification of partners and resources, atmospheric parameters of interest, payload identification, and a SWOT analysis of the market.

2.2.1. Identification of key partners and resources

Analysis of the market, makes it possible to highlight certain key partners and resources. This subsection will aim to familiarize the reader with these domains and their subdivisions. This will serve as a useful precursor to constructing design options as it will enable the group to consider formally the specific uses of the design product.

The first category of partner are space agencies, such as NASA, ESA, and ISRO. These agencies have practical experience in measuring atmospheric conditions, both remotely and in-situ (using radiosondes or UAVs). These partners will likely be the ones providing the scientific payloads. Other technical partners include regulatory agencies (such as EASA) and contractors (such as Lockheed Martin and Raytheon) that have experience building UAVs. Regulatory agencies in particular provide a comprehensive framework that dictates the final design of the plane in the form of design regulations and compliance specifications. Finally, another useful technical partner that must be considered by the group are the researchers at TU Delft. These researchers will mainly act as in a supporting but driving role with the technical challenges that are encountered by the group during development. These partners are identified so that their prior research and development help streamline the design process. [1]

2.2.2. Atmospheric Parameters

The balance of the energy leaving and entering Earth regulates its temperature. Multiple natural and human factors affect the temperature of the planet. According to Oreskes [2], in the last 50 years the main cause of climate change has been 'greenhouse' gases resulting from human activity. Hence, it is vital to identify the gases which contribute to the greenhouse effect so they can be monitored and measured, but also to validate computer models that are able to predict their evolution in the long term. According to Prather et al. [3], the most relevant greenhouse gases include the following: CO_x, NO_x, CH_4, O_3 and N_2O. The same gases are subject to the atmospheric model proposed by Sudo et al. [4], meaning that measuring quantities of those pose a legitimate validation to their model.

Other relevant fields of interest for high-altitude studies are principally concerned with pollution and a changing photo-chemistry. According to Dedoussi et al. [5], the main pollutants associated with climate change, that originates in high-altitude emissions, are fine particulate matter and Nitrogen oxides. Additionally, it was found that fine particulate matter sensitivity to nitrogen oxide emissions is increasing rapidly. Given that nitrogen oxide emissions are expected to increase due to increasing combustor temperatures, it emerges as a particularly important class of chemicals to study.

Quadros et al. [6] propose two indicators to identify atmospheric conditions favorable to fine particulate and ozone formation. The first indicator measures the ratio between sulfates and nitrates which lead to fine particulate formation. The second measures the ratio of formaldehyde to reactive nitrogen which leads to ozone formation. Most importantly, it is the reaction with hydroxyl radicals (OH) which is responsible for removing many of the compounds from the stratosphere, therefore it must be carefully monitored in the future [7].

Over the last 10 years some effort has been made to model the chemical interactions in the stratosphere, resulting in models like IPSL-CM5 and GEOS-Chem. These models are expected to consider a large variety of trace gasses and chemical interactions, including those outlined in this section [8]. Since they have only been recently developed or updated for stratospheric simulations, the forcing and validation data might not necessarily be available, necessitating measurements that provide the according data.

Based on the above conducted literature study, the following atmospheric parameters have to be monitored [1]:

CO_x	- Carbon oxides	OH	- Hydroxyl radicals
NO_x	- Nitrogen oxides	PM	- Particulate matter
CH_4	- Methane	N_2O	- Nitrous oxide
O_3	- Ozone	CFC, HCFC, HFC	- Fluorinated gases

2.2.3. Potential Payloads

After identifying the important chemical components that would be of highest interest to measure, instrumentation that could perform the physical measurement of the gases is required. Since a single instrument cannot perform all the measurements, a selection is made to cover the widest range while minimizing the integration effort. To minimize cost and increase maintainability, preference is made towards already developed systems that can be readily integrated instead of investing time and funding into the development of new instrumentation. A selection of potential instruments, their capabilities and specifications can be found in Table 2.1. Most of the data used to compile Table 2.1 was found on NASA's Airborne Science Instrument Database, which lists instruments that have been used on high altitude airborne research before (such as on the Global Hawk, ER-2, and WB-57 aircraft).

Table 2.1: List of potential payloads, their capabilities and masses.

Instrument	**Capabilities**	**Mass [kg]**
Advanced Whole Air Sampler (AWAS)	In-situ measurements of CFCs, HFCs, HCFCs, Halons, VSLS, NMHCs, organic chemicals, nitrates, and CO.	146 [kg]
Airborne Compact Atmospheric Mapper (ACAM)	Remote measurement of NO2, O3, UV absorbing aerosols, SO2, and HCHO.	N/A
Meteorological Measurement System (MMS)	In-situ measurement of wind, turbulence, temperature, position, velocity, attitude, and airspeed.	26 [kg]
Harvard Hydroxyl Experiment (HOx)	OH (Hydroxyl radicals)	N/A
Cloud Aerosol and Precipitation Spectrometer (CAPS)	Remote measurement of aerosols, particle size distribution, temperature, pressure, and cloud liquid water content.	N/A

Given that the AWAS itself reaches the limits of our payload mass allocation, different mission configurations are implied from the selection of relevant payloads. As an example, a mission can be configured to carry one large payload, or alternatively, a mission can be configured that carries multiple smaller payloads. During development, integration considerations must be made to support different mission profiles [1].

2.2.4. Analysis of the Market

In order to effectively locate RePLASMA within the market of HALE UAVs, a SWOT analysis was performed on the market. This analysis lays down the marketable strengths and weaknesses of the design as well as the opportunities and possible threats it is expected to encounter within the HALE UAV market. The SWOT analysis of the targeted market for RePLASMA is given in Table 2.2. In Figure 2.1 the existing aircraft in the market currently are shown. It is clearly seen that RePLASMA is targeting a combination of endurance and altitude which has not yet been designed. Further, with many of the existing aircraft become phased out, the need for such an aircraft is becoming more important [1].

Table 2.2: SWOT analysis of the market.

	Helpful	**Harmful**
Internal	Strengths 1. Low development and operational cost 2. Suitable for subsonic measurements 3. Achieved sustainability through the use of green fuels	Weaknesses 1. Most information about high-altitude UAVs is concerning military use 2. There already exist UAV that fly for longer and carry larger payload 3. Due to its rarity, there isn't much research about such high-flying aircraft
External	Opportunities 1. Small amount of aircraft in the market that fly at such a high altitude -> high commercial value 2. Opportunity to develop innovative and sustainable technologies that can be used for future projects (e.g. engine) 3. Emerging need for data that will help against climate change	Threats 1. Unclear demand due to nicheness of the market 2. Could be easily adapted into reconnaissance use 3. Need for extra certification regulations to fit the market

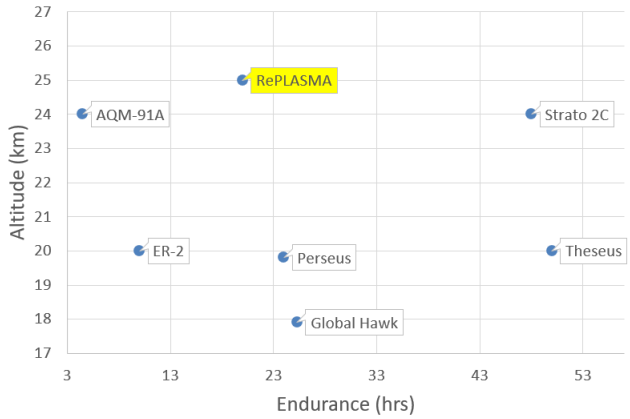

Figure 2.1: Altitude vs. endurance of current similar (subsonic HALE) aircraft in market.

2.3. Sustainable Development Strategy

As explained in Section 2.1, the birth of the RePLASMA mission is through the need for an overall movement towards a more sustainable development in the scientific community. Furthermore, in recent years, the aviation industry too is moving towards more sustainable solutions. RePLASMA aims to be a future-proof design and sustainability is a part of the ethos with which RePLASMA is designed. As a result, every stage of design includes considerations relating to sustainability and are outlined in this section. It also serves as a summary of the project flow from a sustainability perspective.

Pre-design phase

This is the phase that refers to the phase of planning and organization before any engineering begins. This is also the phase in which the requirements were specified and the design starting point of the design process was obtained. As such, this phase sets the foundation for the design and therefore the sustainability. Here, a member of the group in charge specifically for both sustainable engineering and sustainable practices in the design process was assigned. Furthermore, in the prescription of the requirements, regulation requirements were paid special attention to.

REQ-ID	Requirement
PLS-U-SUS-1	Mission shall use sustainable clean fuels
PLS-U-SUS-3	Mission shall be reusable or recyclable during decommissioning

Table 2.3: Key requirements relating to sustainability.

While regulation based requirements mean that the design is legal, RePLASMA aims to be leading the market segment in terms of sustainability. This necessitated further requirements which then came from the client requirements, shown in Table 2.3.

Conceptual design phase

This refers to the stage wherein multiple concepts are generated and traded-off. Here, the stress on the inclusion of sustainability lies mainly in the trade-off in form of the criteria used. Noise and emissions especially were used as key criteria in obtaining a design that was favorable from an environmental perspective. A more detailed view into the trade-off is provided in Section 4.2.

Furthermore, a detailed investigation into different fuel and material types was conducted in order to arrive at viable yet sustainable options before more detailed stages of engineering are commenced. This served to guarantee that sustainability does not remain an after-thought but at the forefront of decision making.

Preliminary and detailed design

This is the stage of design wherein sustainability is most important, however the least easy to keep track of. It was deemed important for the team to reintegrate the design and return to the high level goals in order to remain mindful of the overarching project themes, of which sustainability is a large part.

One great advantage was that the previous stages poised the project in a direction that was already geared towards a sustainable design. Strictly speaking, completing the requirements from the initial planning and the concept front the trade-off would already result in a sustainable design.

The stress on sustainability in the final design was mainly in the fields of propulsion, structures and ground operations. For structures and propulsion, the investigation into the possible materials and fuels respectively along with the key requirements from Table 2.3 were kept at the foreground of the design.

Finally for ground operations and logistics, great importance was given to using off the shelf components and already-in-use processes so as to minimize the extra effort and impact the development of new systems and processes would entail.

2.4. Technical risk assessment

In this section, the risks of the RePLASMA will be evaluated from a technical point of view. A SWOT analysis of the technical risks in Section 2.4.1 and a risk map in Section 2.4.2 will be used to provide an overview of the technical risks of the project.

2.4.1. SWOT analysis of risks

A SWOT analysis depicting technical aspects of the project that drive its technical characteristics and external factors was conducted. The result of the SWOT analysis is presented in item 2.4 [9].

Table 2.4: Technical SWOT analysis.

	Helpful	**Harmful**
Internal	Strengths 1. Unmanned aircraft 2. Endurant high altitude operation 3. In-situ data gathering 4. Controllable sampling location 5. Fast turnaround time for high altitude research 6. Engines work with green fuels	Weaknesses 1. Payload weight limited to at least 150 [kg] 2. Dependent on remote control 3. Design for high altitude flight is much more complicated 4. High altitude endurance of 20 hours requires complicated design
External	Opportunities 1. Climate change and research around it of increasing importance 2. All UAV components can be recycled and be possibly allocated for different use 3. Budget is minimized due to the use of commercially available parts 4. Technical components could be easily adapted into reconnaissance use	Threats 1. Potential for high development costs depending on the fuel and engine selection 2. Certification issues due to new aircraft configuration 3. Limitations with aircraft design due to use of commercially available parts 4. Production errors and fluctuating mission cost 5. Stricter emission regulations 6. Aircraft failure during operation

2.4.2. Risk map

In order to manage the technical risks, they first have to be plotted on a map which indicates the "risk level" of each, based on how likely they are to happen and how impactful they would be on the project. Likelihood and impact were measured on scales given in Table 2.5 and Table 2.6 respectively and the risk level is just the product of the two parameters. A list of possible risk events are provided in Table 2.9 alongside their likelihood, impact, risk mitigation, the updated likelihood and impact after risk mitigation, and the department that's responsible for the risk. The risk events are plotted in the risk map in Tables 2.7 and 2.8. Furthermore, only the risks in the red and orange part of the table are deemed mission-threatening. For this reason, risk mitigation strategies were only provided for these risks [9].

Table 2.5: Probability of risk event.

Rank	Likelihood
1	Very low
2	Low
3	Medium
4	High
5	Extremely high

Table 2.6: Consequence of risk event.

Rank	Impact
1	Negligible
2	Moderate
3	Critical
4	Catastrophic

Table 2.7: Technical risk map.

Likelihood \ Impact	Negligible	Moderate	Critical	Catastrophic
Extremely high				
High				
Medium		1,2	3,5	
Low		4	6	7
Very low		10	9,11	8

Table 2.8: Technical risk map after mitigation.

Likelihood \ Impact	Negligible	Moderate	Critical	Catastrophic
Extremely high				
High				
Medium		3,5		
Low	2	1,4		
Very low		10	6,7,9,11	8

Table 2.9: Technical risk table.

Risk Event	L	I	Risk mitigation	Updated L	Updated I	Risk owner(s)
1. All of the requirements are not met	3	2	Design systems with the goal of satisfying as many requirements possible, while also applying appropriate design thinking so that the design is practically feasible too.	2	2	ALL
2. Requirement is not extensive/specific enough to aid aircraft development	3	2	Adapt requirement for possible solutions	2	1	ALL
3. Initial sizing of aircraft is inaccurate	3	3	Conduct further more detailed sizing and research. Analyze affects of assumptions	3	2	ALL
4. Autopilot malfunction during flight	2	2	Remote pilot assumes control of the UAV and lands it for investigation/maintenance	N/A	N/A	CSO
5. Off-the-shelf products removed from market	3	3	Find similar products in market and iterate aircraft design for compatibility	3	2	ALL
6. Inability to maintain altitude for the duration of the mission	2	3	Design the aircraft for a service ceiling above the desired mission altitude to keep a safety margin.	1	3	AERO, PROP, FP
7. High emission levels	2	4	Check the emission level of the chosen propulsion system during the design phase. Furthermore, once the propulsion system is installed, the emission levels can be tested.	1	3	PROP
8. Permanent loss of connection between ground station and UAV during flight	1	4	The UAV lands autonomously for maintenance if a ground station signal is not received	N/A	N/A	CSO
9. Bird-strike during flight	1	3	Operate from airports that make use of bird strike preventative measures such as distress signals, add lights on the UAV to make it visible for birds, use the bird detection radar	N/A	N/A	PROP, SM
10. Engine failure during flight	1	2	Design the vertical tail to be able to remain laterally stable after engine failure	N/A	N/A	PROP, AERO
11. Landing gear failure during flight	1	3	Design the UAV such that the damage to the payload is minimized on rough landing	N/A	N/A	SE

3

Requirements

This chapter outlines the design requirements generated from client and stakeholder needs along those based on regulations. In addition, a functional breakdown of the mission and its operational flow are shown and discussed.

Section 3.1 presents the list of requirements that were derived from the initial stages of the DSE based on client needs, ranging from design-defining characteristics to operational restrictions. In addition, requirements generated from a functional analysis of the mission are provided. Section 3.2 presents the requirements considered to be the driving forces when further constraining the design space at each iteration of the design. These stem from user requirements and regulatory bodies that impose certain design restrictions to allow certification.

It is important to note that for the sake of brevity, the requirements presented this chapter constitute a subset of the full requirements list. Said requirements are considered to be the most defining design constraints.

User requirements are classified under six categories: operations (OPS), performance (PERF), reliability (REL), sustainability (SUS), cost (COST) and propulsion (PROP). Requirements highlighted in red, are those identified as driving for the whole project, and are considered to be the most important to be met. The following is a list of examples of said categories:

- **PLS-U-OPS-1** was identified as driving as the mission need statement and project objective statement are strongly linked to the need to operate at advanced altitudes.
- **PLS-U-PERF-1**, **PLS-U-PERF-2**, and **PLS-U-PERF-4**, are driving as they are dictated by the requirements of the scientific payloads that the mission aims to carry.
- **PLS-U-REL-1** considering the operational requirements, utilizing only commercially available technology is a very restricting factor, rendering it a driving user requirement.
- **PLS-U-PROP-1** is driving as the requirements pertaining to sustainability and propulsion are strongly linked, thus the requirement raises the importance of the use of sustainable fuels.

3.1. Client requirements

Based on the specifications and target mission profile and the set of the functions and services the UAV is meant to provide, requirements can be generated. Throughout the design iterations, the design space was further constrained. Table 3.1 lists the requirements derived from the client, with the driving requirements mentioned earlier written in red.

Table 3.1: User Requirements Table.

REQ-ID	Requirement
PLS-U-OPS-1	Mission shall facilitate sampling at an altitude above 25 km
PLS-U-OPS-2	Mission shall support in-situ processing of atmosphere samples
PLS-U-OPS-3	Mission shall meet its requirements at all latitudes all year
PLS-U-OPS-4	Mission shall not obey any take-off and landing distance requirements
PLS-U-OPS-5	Mission shall be operable from a remote base of operations
PLS-U-OPS-6	Mission shall be deployable from worldwide airfields without prejudice to **PLS-U-OPS-4**
PLS-U-OPS-7	Mission shall be operable by a ground crew by remote control
PLS-U-OPS-12	Aircraft shall be designed in a way that the safety of the operational personnel or of third parties in the air or on the ground, including property, can be satisfactorily demonstrated.
PLS-U-OPS-14	Information regarding diversion aerodromes and areas which allow the aircraft to land undamaged, without prejudice to **PLS-R-OPS-12**, shall be provided for each mission
PLS-U-OPS-15	Aircraft shall be capable of autonomous landing
PLS-U-OPS-15.2	Aircraft shall be recoverable after landing due to engine failure
PLS-U-OPS-15.3	Landing shall be performed without prejudice to **PLS-R-OPS-12** and **PLS-R-OPS-14**
PLS-U-PERF-1	Mission shall have cruise endurance of 20 hours
PLS-U-PERF-2	Mission shall support a payload mass of 150 kg
PLS-U-PERF-3	Mission shall be remote controllable up to a distance of 1000 km
PLS-U-PERF-4	Mission shall operate in an airspeed range of 0.4 < M < 0.85
PLS-U-PERF-5	Mission shall remain operational in moderate turbulence
PLS-U-PERF-6	Mission shall remain operational up to -100°C
PLS-U-REL-1	Mission shall use commercially available technology
PLS-U-SUS-1	Mission shall use sustainable clean fuels
PLS-U-SUS-2	Mission shall comply with the EU Waste Framework Directive
PLS-U-SUS-3	Mission shall be reusable or recyclable during decommissioning
PLS-U-COST-1	Mission shall establish no restrictions on budget
PLS-U-COST-2	Mission shall establish no restrictions on return of investment
PLS-U-COST-3	Mission shall aim to minimize maintenance and operational cost
PLS-U-COST-4	Mission shall provide an estimate of the operational cost of an exemplary mission
PLS-U-PROP-1	Mission shall use a reciprocating type of propulsion

In addition to those stemming from client needs, following a functional analysis of the type of mission the design is expected to operate, functional requirements were derived and listed in Table 3.2.

The functional analysis carried out in Baseline Report [1] revealed a more detailed layout of the relevant functions and procedures carried during a mission. This lead to a new set requirements arise deemed necessary to fulfill certain mission functions. An excerpt of said requirements is presented in Table 3.2 and are given the tag of **U** as well since the functional breakdown structure itself is derived from user requirements.

Table 3.2: Requirements derived from functional analysis.

REQ-ID	Requirement
PLS-U-SUS-2	The aircraft shall comply with the EU Waste Framework Directive.
PLS-U-AERO-2	The lift-to-drag ratio shall be <TBD>
PLS-U-AERO-3	The zero lift drag coefficient shall be <TBD>
PLS-U-AERO-4	The minimum lift force produced during cruise flight shall be <TBD> kN
PLS-U-AERO-05	The same airfoil shall be used in the span-wise direction
PLS-U-PROP-12	The propulsion subsystem shall not use more than <TBD> W of power
PLS-U-PROP-13	The propulsion subsystem shall provide <TBD> W of power
PLS-U-PERF-1-PROP-1.1	Propulsion shall have a fuel burn rate of <TBD> kg/s at critical thrust <TBD> kN.
PLS-U-PERF-3-COMMS-02	The downlink shall have an EIRP of <TBD> W.
PLS-U-PERF-3-COMMS-03	The uplink shall have an EIRP of <TBD> W.
PLS-U-PERF-3-COMMS-06	The communications shall achieve a S/N ratio of <TBD>.
PLS-U-COMMS-05	The communications subsystem shall be free of single point critical failure
PLS-U-OPS-15.1	The aircraft shall be able detect engine failure.
PLS-R-OPS-23	The operating limitations and essential speed and performance information including the flight envelope shall be clearly documented.
PLS-U-OPS-24	The aircraft shall be detectable with a maximum location position error of <TBD>
PLS-U-STR-19	The total structural mass should be no greater than <TBD>
PLS-U-STR-20	The structural subsystem shall be able to protect all other subsystems from environmental and operational hazards
PLS-U-STR-21	The structure shall the insulate the payloads and electronics at a temperature range of <TBD> to <TBD> C
PLS-U-STR-22	The structural subsystem shall be able to sustain all loads expected in its lifetime
PLS-U-STR-23	The structural subsystem shall be able to maintain <TBD> pressure during flight
PLS-U-FBS-4.1.2.1.2-STR-1	The structure shall facilitate landing gear.
PLS-U-FBS-4.1.3.3.3-STR-1	Complete documentation of the payload structural interfacing shall be provided.
PLS-U-FBS-4.1.3.3.3-EL-1	Complete documentation of the payload electrical and electronic interfacing shall be provided.
PLS-U-FBS-4.3.3.1-COMMS-1	The communication system shall facilitate communications between the pilot and ATC.
PLS-U-FBS-4.3.3.1-COMMS-1.1	The communication system shall be able to autonomously communicate with ATC.
PLS-U-FBS-4.2.3-CS-1	The aircraft shall be capable of autonomously conducting control surface displacement checks.

3.2. Driving regulations & requirements

For airworthiness and certification, regulations impose additional constraints to the design space. Table 3.3 contains requirements characterized as driving the design and either based on relevant regulation or subsystem requirements derived from client needs.

The regulatory requirements in question are mainly derived from Regulation (EU) 2018/1139 and Certification Specification CS-23. While formally only Annex IX on unmanned aircraft to Regulation (EU) 2018/1139 applies to the mission, a number of requirements are also adapted from Annexes II, III, and V. In addition to this, Regulation (EU) 2018/1139 also mandates environmental compliance with Volume I and II, on environmental protection and aircraft emissions, respectively, to Annex 16 of the Convention on International Civil Aviation. Additionally, Annex 14 of the convention is considered for aerodrome classification in order to restrict wing and gear span. Finally, under CS-23, the plane is classified as a high-speed level-1 aeroplane, therefore, the relevant requirements are adapted [9].

Table 3.3: Regulatory Requirements.

REQ-ID	Requirement
PLS-R-AERO-01	The aircraft shall not have a wingspan greater than <TBD>
PLS-R-PROP-06	Effects of cyclic temperature loading and environmental degradation shall not compromise structural integrity.
PLS-R-PERF-08	Stall speed safety margins and climb gradients shall be documented for take-off.
PLS-R-PERF-9.2	After critical loss of thrust on multi-engine aircraft, a climb gradient of 1% at 122 m with landing gear retracted and flaps in take-off configuration.
PLS-R-PERF-9.3	Climb gradient of 3% during balked landing with landing gear extended and flaps in landing configuration.
PLS-R-CS-03	Aircraft shall be stable such that loss of pilot input does not result in mission catastrophe.
PLS-R-CS-04	Limits for center of gravity that provide for stable and controllable operation shall be documented.
PLS-R-CS-05	Aircraft shall exhibit static longitudinal, lateral, and directional stability in normal operations.
PLS-R-CS-06	Aircraft shall have dynamic short period and Dutch roll stability in normal operations.
PLS-R-CS-07	Aircraft shall not exhibit divergent longitudinal stability so as to increase the pilot's workload or endanger the aircraft.
PLS-R-CS-08	Aircraft shall have controllable stall characteristics in straight and turning flight.
PLS-R-COMMS-1.1	The subsystems shall have a level of immunity to the electromagnetic disturbance which allows them to operate without unacceptable degradation of their intended use.
PLS-R-STR-04	The structure must be free from any aeroelastic instability and excessive vibration.

3.3. Functional breakdown

This section presents the construction of the functional breakdown diagram. The functions are presented to the lowest level, but unordered and without a logical flow. This diagram is used as a precursor to the functional flow diagram and also to the requirement generation process. The whole mission is divided into phases, which are further broken down into mission objectives that may need to be completed during the mission. It must be noted that while the phases themselves

are more-or-less chronological to allow for easier classification, the functions themselves are not ordered at this stage of design. An overview of the different phases of the functional breakdown can be seen in Figure 3.1. From the five phases presented above it is prudent to focus on the operational

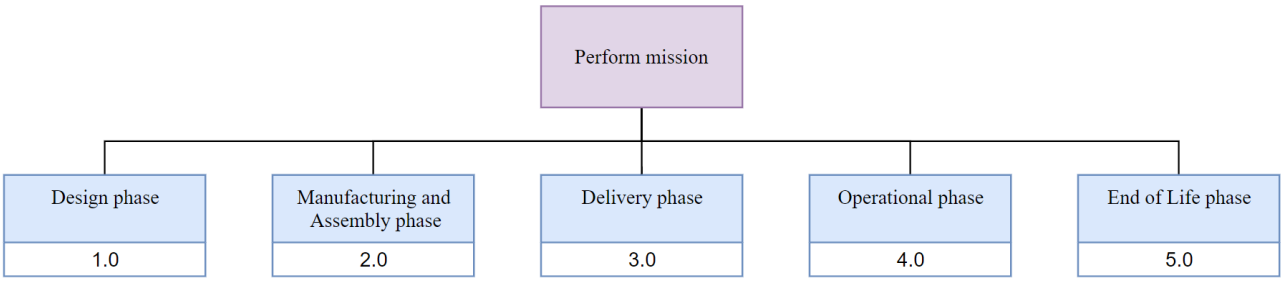

Figure 3.1: Phase division for Functional Breakdown.

phase, as this is where the majority of design is focused. Hence, an elaborate structure for phase 4.0 was made and presented as in Figure 3.2. Note that for a clearer overview of the functions, the operational phase was broken down into 4 more levels providing specific and detailed explanation of the function on every final level of functional analysis.With regards to the rest of the phases required to perform the mission, they were not considered of critical importance in the generation of requirements. Nonetheless, the reader may refer to [9] and [1] for the detailed breakdown of the phases.

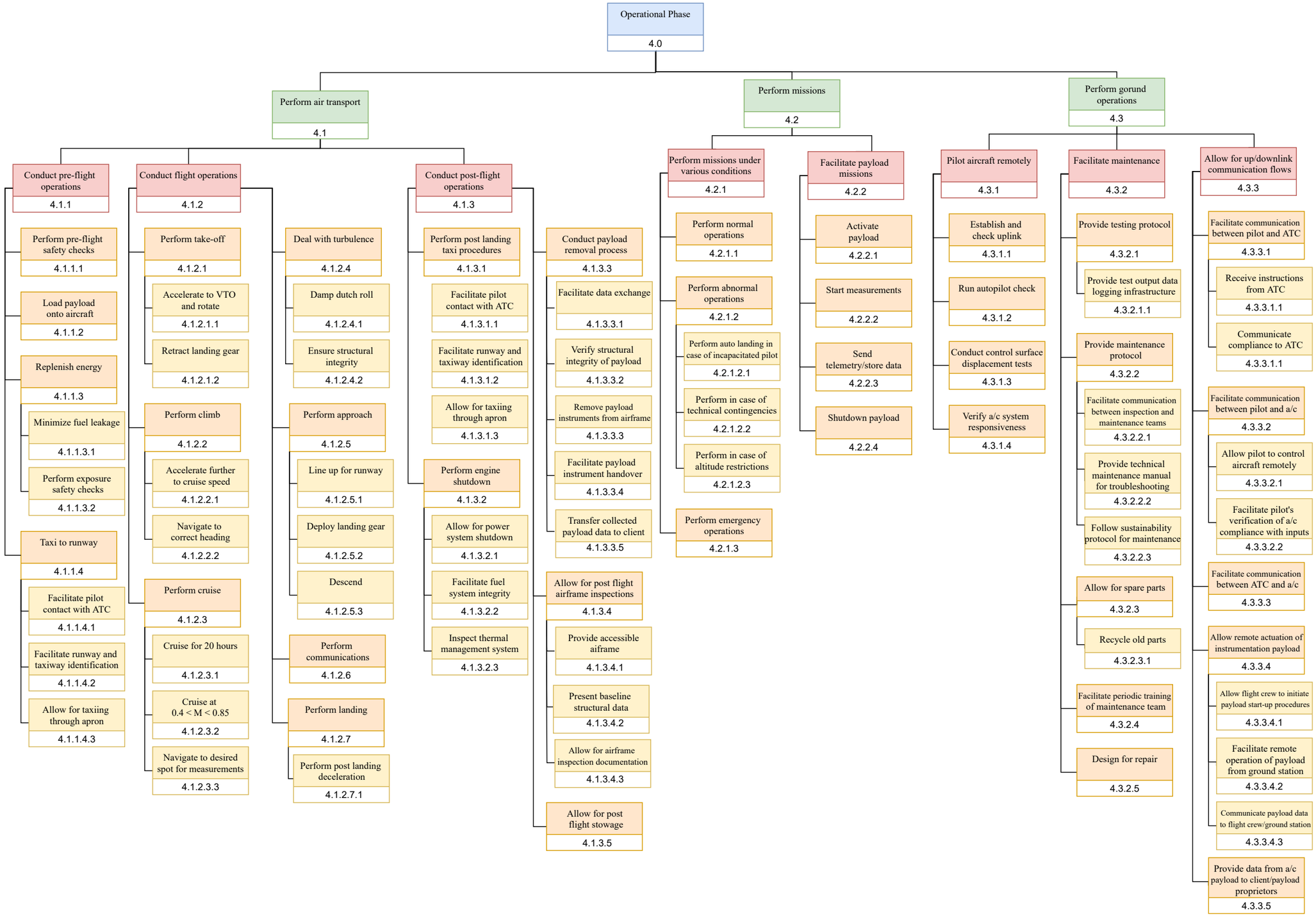

Figure 3.2: Functional Breakdown Structure of the Operational Phase.

3.4. Functional flow diagram

Following the demarcation of functions in the functional breakdown structure, the design team's next endeavour was the chronological organization thereof. This is depicted in a functional flow diagram, where functions are marked with numerical identifiers and connected with single headed arrows, used to indicate the passing of time. The aim of this section is to familiarize the reader with the functional flow diagram, the constituent phases as well as the intended flow and the rationale underpinning these.

3.4.1. Top level functional flow

The starting point for the flow diagram is the top level, as depicted in Figure 3.3. Considering the natural progression of a project, the design phase is the first block. Following design, the UAV must be produced and delivered to its operators. These first three blocks are considered non operational phases. The fourth block is linked to the entire operational life of the system, followed by a a fifth, non operational, block pertaining to the end of life phase.

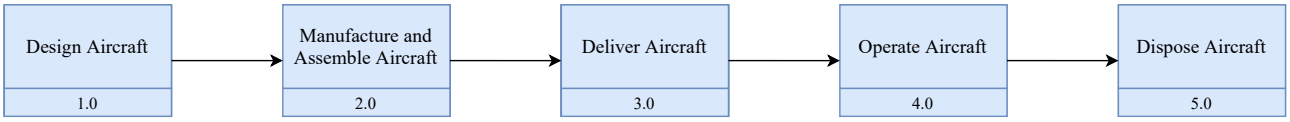

Figure 3.3: Flow diagram top level.

The initial stage of the design phase is the definition of parts and CAD models. Following this, the manufacturing of parts may start, contingent upon successful sourcing of materials. Naturally, the final stage after assembly is looking into quality control of the parts. The various sub phases of this phase have sub sub phases utilised to focus on sustainability and integration. The output of this phase is the final system, in a state that is ready to operate.

The delivery phase involves moving the assembled system to the operator, with stages divided chronologically. Following identification of a sustainable manner to transport the system, the system must be prepared for delivery. This is naturally contingent upon dimensional constraints, dictated by the mode of transport. Finally, the unloading and reassembly at delivery readies the system for the operational phase.

The operations phase contains all functions to be fulfilled, involving the system, from the time of it's reception by the operator, until the end of its final flight. This is shown in Figure 3.4. Naturally, as the project life cycle centers itself around operations, this is the largest functional flow diagram. In bold lines, the first stage of operations is the pre-flight activity. Following this, the remote piloting capability of the aircraft must be established, as well as the up and down-link communication flows. Following this, regular flight operations can be commenced. Following the commencement of flight operations, missions can be performed in two broad categories, either in a manner that facilitates the payload mission, or performing missions under various conditions. Following this, post flight operations commence. Upon the completion of these flight activities, the maintenance tasks can be initiated. The reader may note that the operations phase is carried out numerous times over the course of the system life cycle, following which the end of life protocols are initiated. The reader should note that the multi-level nature of the operational flow diagram is the result of the functional breakdown, and functions derived therein may be found within Figure 3.4.

Finally, the end of life phase is characterised by the processes and functions required to end the operational life of the system. In order to verify the start of the end of life phase, the aircraft's operational life must be assessed. This links to fatigue loading tests, inspections and compliance capabilities with regard to user needs. Following the end of life assessment, the system may be de-commissioned. Furthermore, following system disassembly, active effort must be taken to maximize the amount of material that can be recycled. Finally, the project life cycle ends following completion of documentation activities.

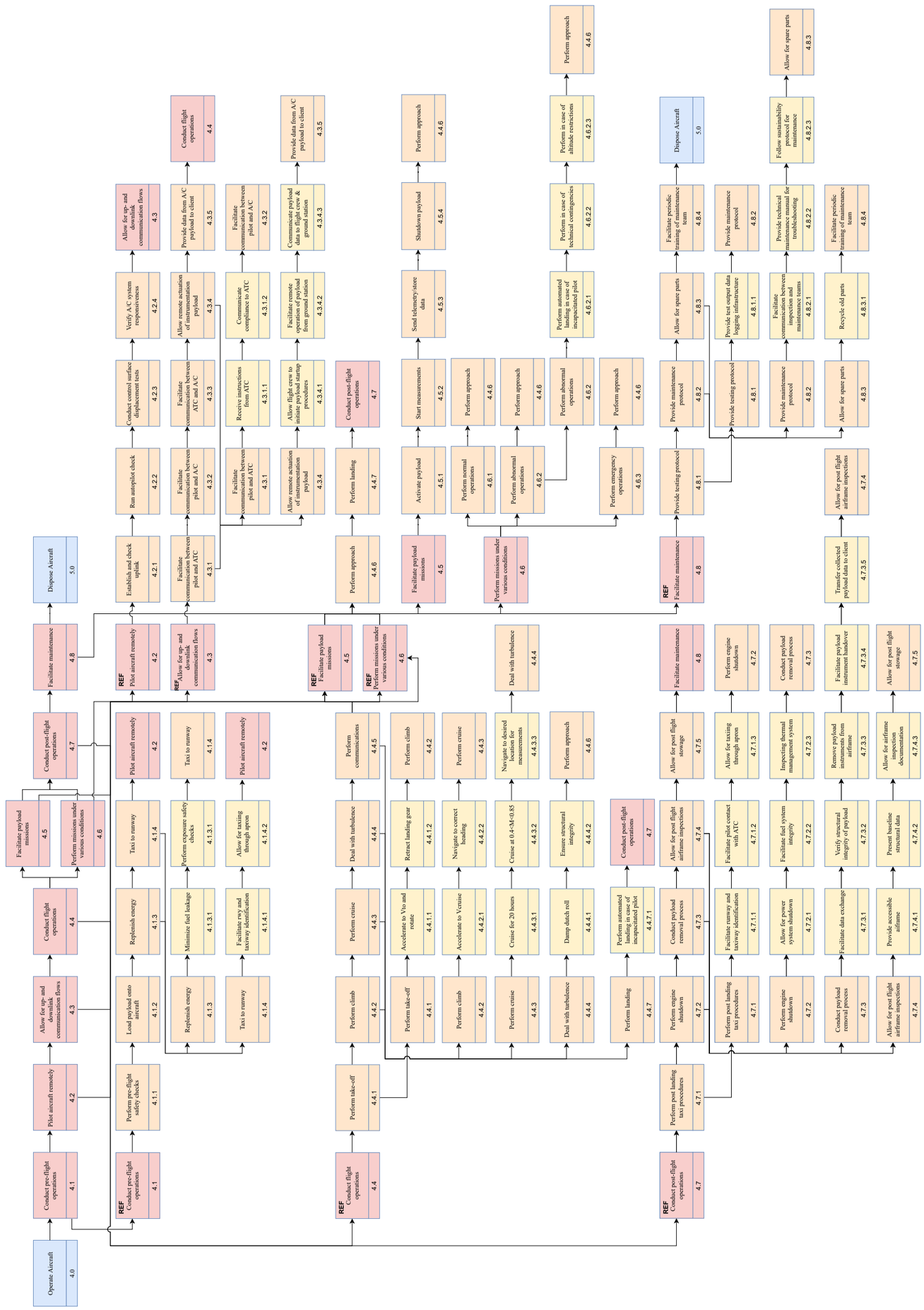

Figure 3.4: Functional Flow of the Operational Phase.

4

Concept Generation

This chapter explains the design concepts that were generated, elaborated on, and taken into trade-off in order to decide on the layout of the RePLASMA aircraft. Section 4.1 will briefly discuss the three main concepts that were considered, while Section 4.2 will define the trade-off process that was carried out and which factors were examined to pick the optimal design. Finally, Section 4.3 will get deeper into detail about these factors and how certain changes in the trade-off grading could impact the final decision about the concept choice.

4.1. Concepts

As described in the Midterm Report [9], the main philosophy that was followed during the initial design generation process was to make use of as wide and comprehensive variety of options as possible for all of the subsystems. Within the diverse range of options from various subsystems, priority was given to propulsion as the need to be able to provide lift and thrust at such a high altitude was identified as the driving issue. Hence, three main concepts were generated around the three main propulsion system types available: piston biofuel, piston hydrogen, and turbojet. The option for an E-fan as well as other fuel types were also considered but later deemed inappropriate either due to their insufficient readiness level or lack of environmental friendliness. This section lists and details the main characteristics of the conceptual designs that were brought about for the three propulsion types. For more detailed information regarding each concept in the initial phase, the reader is advised to refer to the Midterm Report [9]

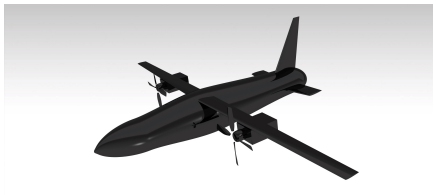

Figure 4.1: Biofuel concept

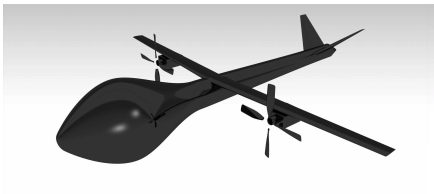

Figure 4.2: Hydrogen based concept

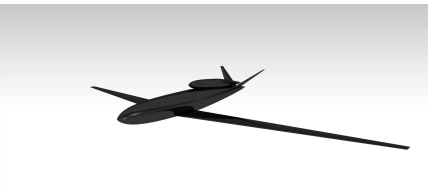

Figure 4.3: Turbojet concept

.

4.1.1. Concept I: Piston biofuel

Considering the user requirements of having a reciprocating engine and running on “green” fuels, propulsion system that was found to perform very well at high altitudes is a turbocharged piston engine system. A good example of that is the Boeing Condor, which reached an altitude of 67000 feet (~20 km) with a two-stage turbocharged piston engine. Therefore, for this design, a pair of these engines will be placed on a highwing with almost no sweep due to the low operational speeds. The difference, however, is in the fuel it uses. Due to the focus on sustainability, the traditional kerosene fuel is replaced with a biofuel in order to reduce emissions. As for the airframe, a blended wing body configuration with a conventional tail was chosen due to the increased lift over drag ratio it provides and simple and proven control system design. This concept utilizes an alternative fuel for two piston engines - biofuel, as well as a lift-generating fuselage. For the rest of the calculations a 20% blend ratio of biofuel to conventional fuel is used, however this is an assumption that is subject to change in the future when an actual analysis on the fuel will be performed. An image of this initial design concept is shown in Figure 4.1.

4.1.2. Concept II: Piston hydrogen

The second concept that passed our initial trade-off employs again a pair of piston engines, but the fuel utilized this time is hydrogen. From research it was concluded that the design changes needed to convert a reciprocating engine running on a petrol-derived fuel to hydrogen are insignificant, which was a good sign. To reach the desired operating pressure, the air will first be passed through a turbocharger system, which is yet to be designed. Fortunately, an aircraft that meets those specifications as well as the mission requirements very closely was identified. The Boeing Phantom Eye is a HALE UAV that flies at an approximate altitude of 20 km with a payload of 204 kg and an endurance of 4 days[1]. Its propulsion system consists of two Ford Fusion 2.3L engines modified to run on hydrogen and a multiple turbocharger system to compress the air[10]. Due to the relevance of this aircraft to the proposed design, much of the data available for the Phantom Eye will be used for the preliminary estimations. Initial visualization of this concept is given in Figure 4.2.

4.1.3. Concept III: Turbojet

The third concept considered for the trade off, was developed around the use of a traditionally powered turbojet. Turbojets suitable for high altitude applications are discussed in detail by Bents et al. [11]. Following a literature study into the use of traditional turbojets or turbofans for HALE applications, the Global Hawk emerged as a suitable baseline aircraft, with regard to airframe properties. In the domain of propulsion, the J97 turbojet, as well as newer derivatives thereof are presented [11]. One of these is the ERAST turbine, developed for use at 90000 feet (~27 km). The paper suggests that the development cost of such a turbine would border on prohibitively expensive. As such, the ERAST turbine can be developed from ‘a J97 rebuilt from remaining inventory of prototype hardware that never became a manufacturer-supported product’ [11]. The aim of this third concept is to utilize the immense potential of the turbojets described by NASA. This concept is depicted in Figure 4.3.

4.2. Trade off summary

Once an analysis of the three design options was carried out, their characteristics was compared in a logical manner to select the optimal design to take further into the detailed design. For each design option, a Class I weight estimation was carried out using a statistical approach. In order to assess the optimality of design, parameters were divided into engineering categories presented in Table 4.1 along with their relative weights. Within each category, a number of subcriteria were chosen, and given sub weightings. When the citeria weight is multiplied with the subweight, the final weight of the subcriteria is obtained and presented in Table 4.2.

[1] https://www.boeing.com/defense/phantom-eye/ [accessed [accessed 10/6/2021]]

Table 4.1: The trade-off categories along with their weighting.

Category	Group weighting [%]
General	15
Control, Stability & Operations	15
Propulsion	35
Flight Performance	15
Aerodynamics	15
Structures	5
Total	**100**

Table 4.2: Summary of trade criteria and subcriteria. The last column, 'Min/Max', describes whether it a higher or lower value is desirable for the specific criteria.

Category	Criteria	Weight (%)	Type	Min/Max
General	Investment cost	3	Qualitative	Min
	Operational cost	3	Qualitative	Min
	TRL	7.5	Quantitative	Max
	Ease of maintenance	1.5	Qualitative	Max
Control, Stability & Operations	Controllability	6	Qualitative	Max
	Stability	6	Qualitative	Max
	Operational risk & ground safety	3	Qualitative	Max
Propulsion & Thermal	Emissions	8.75	Qualitative	Max
	Noise	8.75	Quantitative	Min
	Thrust/Weight of propulsion system	10.5	Quantitative	Max
	Gravimetric energy density of fuel	7	Quantitative	Max
Flight Performance	Maximum proven altitude	7.5	Quantitative	Max
	Wing loading	7.5	Quantitative	Max
Aerodynamics	L/D ratio	15	Quantitative	Max
Structures	Fuel storage complexity	3	Quantitative	Min
	Propulsion induced vibrations	2	Qualitative	Min

Each concept is scored and the scores are normalised. This process is documented and explain in the Midterm Report [9] and readers are advised to refer to this document for more insight. The results of the trade-off are presented in Table 4.3. The piston biofuel design option is concluded as the most optimal and is moved forward into the detailed design phase which is presented in Chapter 5 onwards.

Table 4.3: Trade-off results. A higher score is favourable as it reflects that a design is more optimal based on the project engineering priorities.

Criteria	Piston Biofuel	Piston H_2	Turbojet
Total Score	71.3	68.8	69.0

4.3. Sensitivity analysis

The trade-off marks the end of the conceptual design phase, but it is still in the interest the project to perform a sensitivity analysis of the trade-off, both from a design team perspective and from a client perspective. The sensitivity of the trade-off result to changes in the trade-off weights (given in Table 4.1) has to be assessed. First, the weights are varied randomly within a margin of $\pm 5\%$ and the trade-off is conducted again. A tally is kept for each concept and a count is added every time a

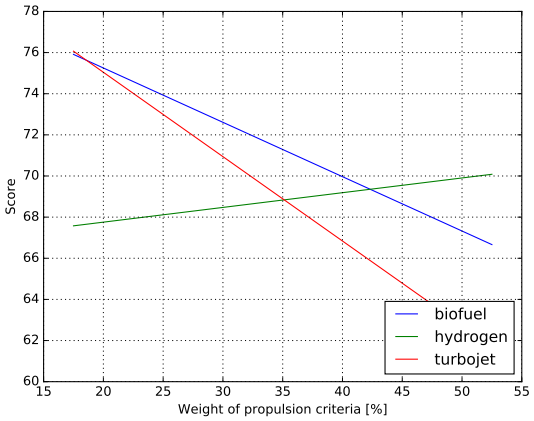

Figure 4.4: Trade-off scores as a function of the weighting given to the propulsion category. The weighting in the original trade-off is 35%.

concept is optimal in the iterative trade-offs. The results of this analysis is presented in Table 4.4. It is clear that as a result of this analysis, the piston biofuel design option it still most likely to be optimal.

Table 4.4: Results of the numerical sensitivity analysis.

Design option	**Proportion of alternate situations where design is optimal [%]**
Piston Biofuel	87.0%
Piston H_2	12.5%
Turbojet	0.5%

Following this, the sensitivity of the trade-off to each of the weights in Table 4.1 one-by-one was analysed. It was found that the most critical case was in that of the 'propulsion' category. The scores of the concepts as a function of the weighting given to 'propulsion' are plotted in Figure 4.4. It can be seen that only if the weighting given to propulsion is increased from 35% to approximately 42.5%, the hydrogen piston concept becomes optimal and if it is reduced to approximately 17.5%, the turbojet concept is optimal.

As a whole, it was concluded that apart from fringe situations such as the ones presented using Figure 4.4, the trade-off relatively stable in concluding that the piston biofuel concept is optimal. With this, this concept is moved to the detailed design phase.

5

Design Process Flow

The aim of this chapter is to introduce the reader to the technical design process, as undertaken following the selection of a concept from the trade off. The aim is to introduce the critical aspects of design, such as sizing and weight estimation, resulting in design point selection, followed by the detailed subsystem design, leading into the final integrated design.

5.1. Process overview

The first stage of understanding the design process flow is a global view of the design process, from its initial stages through to the final elements of the project. In order to do this, Figure 5.1 presents a high level overview of the design process from initiation to final analysis.

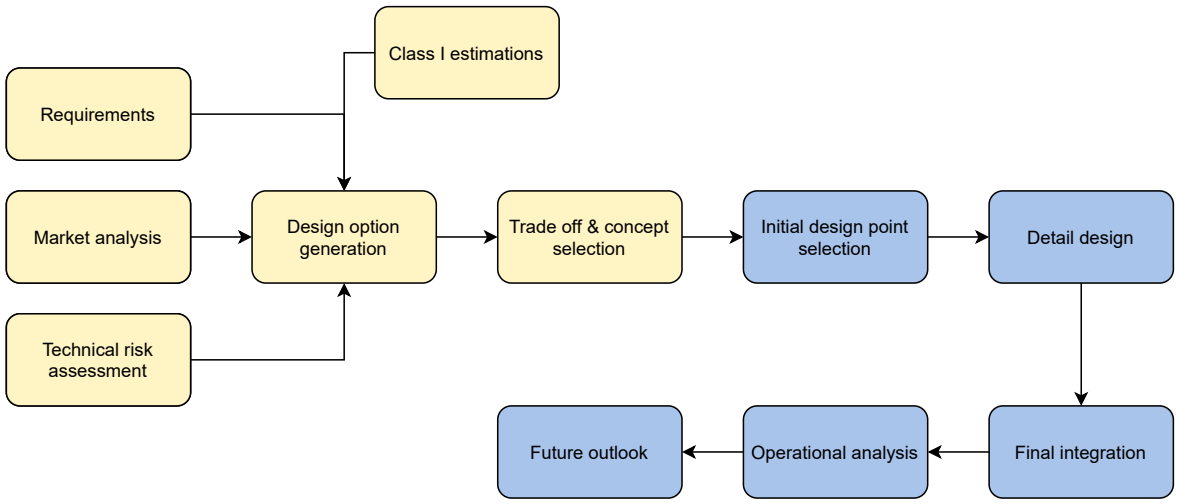

Figure 5.1: High level overview of design process flow.

The first stages of the process are conducted in parallel. Namely the analysis of requirements from clients, users, regulations and other source. Furthermore a market analysis and a technical risk assessment are conducted so as to demarcate the scope of the design space. Following this, class I estimations are utilized, as described in Section 4.1. These allow for the creation of the concepts described in Section 4.1.1, Section 4.1.2 and Section 4.1.3. In addition to the presentation of concepts in the prior chapters of this report, the avid reader will find a more elaborate explanation of the design generation process, as well as the resulting trade off and sensitivity analysis in the Midterm report of the RePLASMA mission. Note, that the stages highlighted in yellow are stages of the design process established in the prior midterm report. The phases highlighted in blue are those conducted through the final phase of design. This starts with the intial design point selection, as the result of an iterative process between a class I and class II weight estimation, as explained in Chapter 6.

Following this, detailed design of various subsystems is performed, with strong interlinking. A further explanation on the precise stages of the detailed design process may be found in Section 5.2. Following this, the final integration of the aircraft is performed to finalize the design of the vehicle, which further facilitates an operational analysis, such as that covered in Section 14.1. Finally, the stages described in the blue boxes in Figure 5.1 allow a plan to be developed for the future outlook of the RePLASMA project, as outlined in Chapter 16.

5.2. Detailed design breakdown

Following the high level description of the design process, the aim of this section is to familiarize the reader with a more detailed overview of the detailed design phase. This includes, in broad lines, the stages of design undertaken from the concept selection through to the final integration. Thus, Figure 5.2 presents a more detailed focus on the process between initial design point selection and final integration.

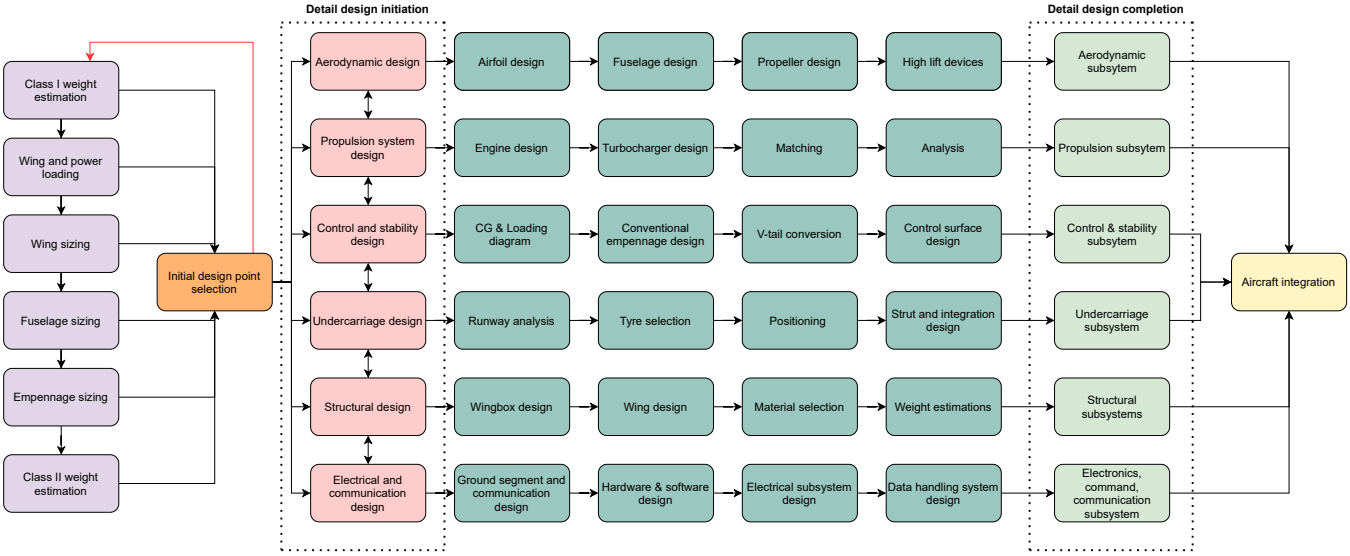

Figure 5.2: Detailed breakdown of detail design phase on a subsystem basis.

Consider the boxes highlighted in purple. These stages are described and explained further in Chapter 6. The outcome of these stages is a design whereby there is convergence to a specific design point. From here, six key subsystems are considered for detailed design, as shown in light red. These are aerodynamics, propulsion, control and stability, undercarriage, structures and electrical and communications. Each of these subsystems uses a chapter in order to elaborate further. The aerodynamic subsystem design looks at the airfoil design, fuselage design, propeller design and the use of high lift devices within Chapter 7. Additionally, the propulsion system design is considered in Chapter 8 where emphasis is laid on the engine design, turbocharger design, matching of components and analysis of the propulsion system. Thirdly, considering the control and stability subsystem, the loading diagram and center of gravity range feed into the design of a conventional empennage. This facilitates the conversion into a V-tail and finally the control surfaces, as presented in Chapter 10.The undercarriage design is discussed in depth in Chapter 12, while structural considerations are elaborated upon in Chapter 9. Finally, the electrical and communication subsystem design is presented in Chapter 11. The finalization of all 6 of these subsystems allows aircraft integration to take place. The reader should note that the stages described in Figure 5.2 are not exhaustive, and further detailed design may be conducted, as presented in the relevant design chapter.

6

Sizing & Weight Estimation

The aim of this chapter is to inform the reader about the initial stages of design undertaken following the selection of a concept. In order to facilitate this, the chapter will focus on 6 key modules (class I weight estimation in Section 6.1, wing & power loading in Section 6.2, wing, fuselage, & empennage sizing in Section 6.3, and class II weight estimation Section 6.4), as well as their overall integration with the aim of converging upon an initial design for the RePLASMA aircraft system.

6.1. Class I weight estimation

The class I weight estimation is a tool utilized in order to facilitate the start of the sizing and weight estimation process. The inputs to the class I weight estimation can be categorized into three classes. The first class is the set of mission parameters, the second is the design choice inputs, while the third and final set is the class of inputs derived from statistics. The set of mission parameters includes the payload mass, the endurance required of the mission, as well as the cruise mach number. The set of design choice inputs include the aspect ratio, Oswald efficiency factor, the ratio of wetted surface area to surface area, the propulsive efficiency and the power specific fuel consumption. It should be noted that in the preliminary stages of design, the design choice inputs are heavily influenced by aircraft of a similar nature, often referred to as a baseline aircraft. Finally, the third class of inputs are those derived from statistics. This includes the maximum take off weight, the operating empty weight and the various fuel fractions.

The class I weight estimation module has a plethora of outputs, that are utilized throughout various other inputs. These include the expected maximum take off weight, the zero lift drag, the efficiency, the cruise and non cruise fuel fractions, as well as the cruise velocity. The outputs of the class I weight estimation feed into the generation of the wing and power loading diagram, the sizing of the wing as well as the class II weight estimation.

6.2. Wing and power loading

The mission profile assigned to the RePLASMA mission cannot be classified as ordinary. The extraordinary nature of the mission, a combination of the required cruise altitude and speed, mean that the air frame design must meet a plethora of requirements, such that the aircraft is able to operate effectively in a multitude of conditions. As such, there are several flight regimes which constrain the design and 7 key parameters are considered, namely the take-off and landing distance, stall speed, cruise performance, climb rate and gradient and aircraft maneuvering. A brief explanation will be given for each of these parameters, to give an overview of which constraints are critical for the design point and why. For the method and formulas used throughout this section refer to the slides by Vos, R. and Melkert, J.A. [12].

Take-off distance

The take-off distance is a constraining factor since the take-off speed is usually associated with the runway length. Evidently, a small required runway length would imply that a larger number of airports would be able to facilitate the mission thus increasing the geographical possibilities of the mission. This specific constraint utilizes a statistical parameter associated with the take-off of similar aircraft known as the take-off parameter (TOP parameter) and Equation 6.1 presents the governing relationship.

$$TOP_{prop} = \left(\frac{W}{S}\right)_{TO} \left(\frac{W}{P}\right)_{TO} \frac{1}{C_{L_{TO}}} \tag{6.1}$$

The TOP parameter can be found from statistics based on a given runway length. In Figure 6.1 the take-off constraint was constructed using a runway length of 500 m and a maximum lift coefficient at take-off of 1.4. This rather low lift coefficient was chosen to showcase that even at low lift creating scenarios the take-off does not constrain the power and wing loading. The previous can be easily justified given the fact that the density at cruise altitude is 30 times lower than the one at take-off, thus making it significantly harder to generate lift at altitude. Moreover, able to perform a successful take-off on a 500 m long runway implies that the mission will be deployable even from small airports around the world.

Landing distance

Similar to the take-off constraint, the landing constraint also utilizes a statistical relationship between the approach velocity and the runway length required. Combining this with the lift formula Equation 6.2 is obtained, where f represents the fuel fraction over the course of the mission.

$$\left(\frac{W}{S}\right)_{TO} = \frac{C_{L_{max}} \rho \frac{s_{land}}{0.5915}}{2f} \tag{6.2}$$

Once again a runway length of 500 m and a C_L of 1.4 is assumed and Figure 6.1 clearly illustrates that this particular line is far from constraining. Furthermore, the low lift coefficient used for both take-off and landing turned out to be enough given the wing and power loading meaning that possibly no high-lift devices will be needed to produce excess lift. This will be discussed in more detail in Section 7.3.

Stall speed

In order to consider the ability of the aircraft to perform without stall posing a threat, one must consider the condition in which lift can be equated to weight.

$$L = W = C_L \frac{1}{2} \rho V^2 S \tag{6.3}$$

From this expression, the stall speed, V_s can be derived.

$$V_s = \sqrt{\frac{W}{S} \frac{2}{\rho} \frac{1}{C_{L_{max}}}} \tag{6.4}$$

At this stage, the designer must take a choice to assign values for both the stall speed and the maximum lift coefficient. As a result of this, the wing loading may be calculated.

$$\frac{W}{S} = \frac{1}{2} \rho V_s^2 C_{L_{max}} \tag{6.5}$$

In the case of RePLASMA, two key situations for which stall needs to be avoided were identified. The first is in cruise condition, where the wing must generate enough lift to negate the risk of stall. The second, is the case of landing, where the maximum lift coefficient is significantly higher. In the case of the landing stall speed, the choice was made to heed the stipulated values in CS-23 guidelines, whereby an aircraft attempting to be certified under the specification may not stall at a speed higher than 31.4 [m/s]. In the case of the first flight condition, the desired 'stall' speed was selected to

be the cruise velocity, with the maximum lift coefficient set to the target coefficient for the cruise phase. This was done so as to allow a constraint to preside over the ability of the aircraft to function appropriately in cruise conditions. Considering this, two wing loading constraints were identified, and are tabulated for the reader.

Flight condition	**W/S [N/m^2]**
Cruise	669
Landing	847

The values presented in the table illustrate that for the RePLASMA mission, the constraining stall line is that of the cruise condition.

Cruise speed

Another constraint present on the wing and power loading diagram is the curve pertaining to the cruise speed performance. By equating the available power and the required power, as well as the take off power with the brake horsepower available, the power loading required for adequate cruise performance can be presented as an equation.

$$\frac{W}{P_{TO}} = \eta_p \frac{\rho}{\rho_0}^{0.75} \left[\frac{C_{D0} \frac{1}{2}\rho V^3}{\frac{W}{S}} + \frac{W}{S} \frac{1}{\pi A e \frac{1}{2}\rho V} \right]^{-1} \tag{6.6}$$

From the equation above, the power loading as a function of wing loading is found, for given values of cruise speed. Furthermore, the constraints imposed by this curve are two-fold, as there are two additional terms relevant in influencing this. These terms are the power setting, as well as the percentage of the maximum take off weight at which cruise is performed. The equation above is then modified to:

$$\frac{W}{P_{TO}} = \frac{x}{y}\eta_p \frac{\rho}{\rho_0}^{0.75} \left[\frac{C_{D0} \frac{1}{2}\rho V^3}{\frac{yW}{S}} + \frac{yW}{S} \frac{1}{\pi A e \frac{1}{2}\rho V} \right]^{-1} \tag{6.7}$$

In this case, x represents the percentage of maximum power utilized during cruise, while y is the percentage of the maximum take off weight at which cruise occurs. Since the mass of the aircraft reduces significantly throughout the cruise phase, which lasts 20 hours, two curves are derived, one for the performance requirement at the start of cruise, and one at the end of cruise.

Climb rate

The climb rate represents the vertical velocity able to be achieved given a certain power output from the engine. Its importance is critical especially after take-off where for clearance purposes a high climb rate is preferred. The climb rate associated formula is given in Equation 6.8, derived from the difference of the excess power available to the power required. Note that η_P is the propulsive efficiency assumed to be 0.82, ρ the density at sea level since that is where the climb is assumed to start while c represents the climb rate and the $C_L^{3/2}/C_D$ ratio was calculated for maximum climb rate performance according to the data of the optimized airfoil (refer to Section 7.1).

$$\left(\frac{W}{P}\right)_{TO} = \frac{\eta_p}{c + \frac{\sqrt{\left(\frac{W}{S}\right)_{TO}}\sqrt{2/\rho}}{\frac{C_L^{3/2}}{C_D}}} \tag{6.8}$$

The team decided that a climb rate of 5 [m/s] would be a feasible value in order to fit clearance requirements and achieve a climb to cruise altitude within reasonable time. As visible in Figure 6.1 with the orange line, the climb rate turns out to be constraining and thus contributes directly to the choice of the design point.

Climb gradient

The climb gradient of an aircraft represents the ratio of horizontal distance covered to vertical altitude gained, often expressed as a percentage. Various constraints imposed upon the climb gradient can restrict the wing and power loading of an aircraft. Consider the following climb gradient requirements for aircraft with propellers:

$$\frac{c}{V} = \eta_p \cdot \frac{P_{br}}{W} \frac{1}{\sqrt{\frac{2W}{S\rho C_L}}} - \frac{C_D}{C_L} \tag{6.9}$$

Furthermore, for a given set of inputs, including a fixed climb gradient and other aerodynamic parameters, the power loading can be derived as a function of wing loading. This results in the following:

$$\frac{W}{P} = \frac{\eta_p}{\frac{W}{S}\left(\frac{c}{V} + \frac{C_D}{C_L}\right)\sqrt{\frac{2}{\rho C_L}}} \tag{6.10}$$

Plotting the climb gradient requirement on the wing and power loading diagram allows the design space to be demarcated appropriately.

Maneuverability

The final constraint imposed on the wing and power loading diagram is the maneuverability curve. This is linked to the load factor that the aircraft is designed to handle when maneuvering in various flight conditions. From CS23 regulations, a load factor of 3.5 was calculated as the required value. Furthermore, from performance analysis [12], the following relation is derived:

$$\frac{\eta_p P_{br}}{W} = \frac{C_{D_0}\frac{1}{2}\rho V^3}{\frac{W}{S}} + \frac{W}{S}\frac{n_{max}^2}{\pi A e \frac{1}{2}\rho V} \tag{6.11}$$

From this equation, it is possible to extract the power loading as a function of the wing loading. It should be noted that the maximum load factor is derived from regulations and requirements, and as such vary across designs.

Wing and power loading diagram

The inputs to the wing and power loading diagram, and consequent selection of a design point stem from three key sources. The first is the class-I weight estimation which provides a first order estimation of parameters like the drag coefficient and the fuel fractions. The second source is direct inputs derived either from literature or by guesses based on the team's engineering judgement. These inputs include the aspect ratio, the taper ratio as well as the lift coefficients (obtained through the airfoil choice and optimization as discussed in Section 7.1 on a later stage of the report). Final inputs stem from requirements and regulations constraining for instance the maximum allowable stall speed.

By creating a plot corresponding to each requirement stated previously using the aforementioned sources of inputs, the power loading diagram is constructed and it is shown in Figure 6.1. The constraining flight requirements turned out to be the ones designing for stall speed during cruise and the climb rate required at take-off. Having established all the viable power and wing loading combinations, a single design point was chosen based on maximizing both W/P and W/S parameters. This can be visualized as choosing the most top-right point on the feasible area created by the constraint lines, as illustrated in Figure 6.1 by a small circle.

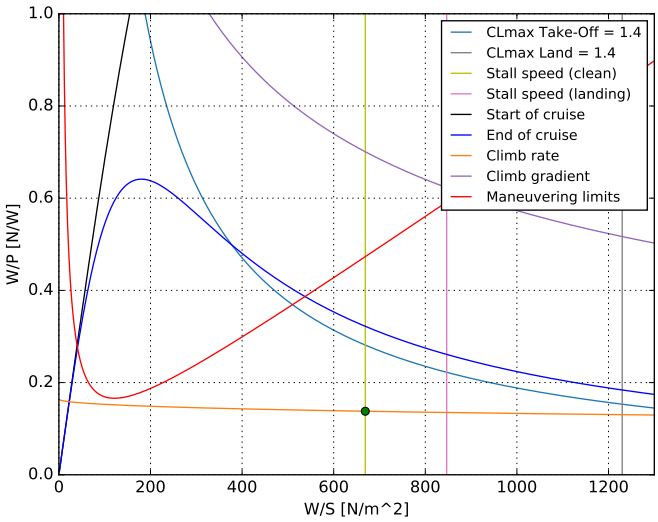

Figure 6.1: Power and wing loading diagram showing the various constraint lines and the final chosen design point marked with an 'o'.

This design point yields a wing loading of $\frac{W}{S} = 669$ [N/m^2] and a power loading of $\frac{W}{P} = 0.137$ [N/W]. These two values will be the ones carried over in the next design phases and will be the deciding factors for the wing sizing and planform as well as the power required and the selection of a corresponding propulsion system. Finally, it will be seen later that the wing loading no longer maintains a one-to-one correspondence with the take-off weight of the aircraft. This is because manual modifications will be performed on the wing surface area. Section 6.3.1 will explain the wing sizing procedure, delving deeper into why the surface area was altered.

6.3. Sizing

After a preliminary estimation was made on the weight of the aircraft and the loading expected for providing sufficient lift and thrust were calculated, the subsystems of the aircraft, namely the wing, the fuselage, and the empennage, were to be sized in more detail. This section elaborates on the initial sizing estimations for the wing planform in Section 6.3.1, the fuselage geometry in Section 6.3.2, and the horizontal and vertical tail layouts in Section 6.3.3.

6.3.1. Wing sizing

The wing sizing module of the program considers a variety of inputs to size an appropriate planform. A number of inputs are considered, including the calculated take-off weight, the aspect ratio, the taper, and the wing loading obtained from the wing and power loading diagram. Once again, the wing sizing methodology recommended by Vos and Melkert was followed [13]. Firstly, the wing area corresponding to the estimation of the take-off weight and the wing loading is calculated. Then, the aspect ratio, that had been set as a design choice and based on existing aircraft of similar mission profile, was used to obtain the wing span. Finally, geometrical calculations were carried out to calculate the root and tip chords as well as the mean aerodynamic chord and the wing sizing was concluded, with the outcome from the initial design being depicted in Figure 6.2.

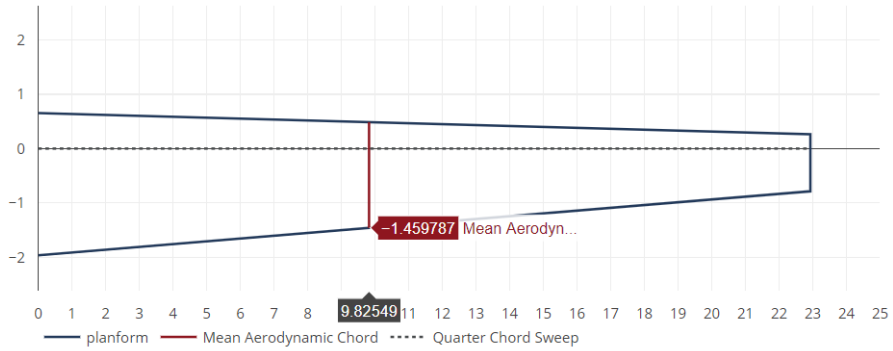

Figure 6.2: The wing planform obtained after initial wing sizing. [1]

However, after the initial sizing was completed, a discrepancy in the wing area and the aircraft weight was found such that the wing area would not be able to generate enough lift to support the aircraft's weight. This is due to the aircraft weight being updated after the wing area is calculated using the wing loading, which also takes into account the weight from the previous iteration. This problem was tackled by manually adding to the wing area before all other parameters of the wing is obtained. This amount was optimized manually, such that the addition of the surface area would be minimal while enabling the aircraft to lift its own weight. With this modification of the method, the wing sizing was finalized.

6.3.2. Fuselage sizing

Next, the fuselage, aircraft's main body on which the payload is located, was sized. The sizing of the fuselage was a different task compared to other sizing steps as it is not updated in iterations because it is only dependent on the payload size. Since the readiness is an important factor for the mission, research was conducted on commercially available/previously used pallets for the storage of the payload used in RePLASMA within the aircraft. The pallet that was concluded upon is the NASA WB57 due to its standard use in high altitude scientific measurement missions[2]. As the payload required for RePLASMA is relatively small and does not need pressurization, the 3 feet (0.9144 m) unpressurized pallet was chosen. Furthermore, in order to account for space in the fuselage, the height and the width of the fuselage were both chosen to be 1 m. For the length of the fuselage, Roskam's analysis [14] specifies that while a fuselage fineness ratio of 6 is optimal for fuselage drag, it is likely that it would require a relatively large horizontal stabilizer and lead to a more draggy aircraft as a whole. As a result, a total fuselage fineness ratio of 8 is optimal for the entire aircraft, to reach a final length of 8 m.In addition to this, the fuselage sizing module calculates the gross shell fuselage area. This is a crucial input to the class II weight estimation module, performed at the end of each iteration.

6.3.3. Empennage sizing

The final subsystem that remained to be sized was the empennage, consisting of the vertical and horizontal tails. A semi-empirical method by Roskam [15] was used for the preliminary sizing of both the vertical and the horizontal tails. In this method, the equations for the horizontal and vertical tail areas are given in Equation 6.12 and Equation 6.13 respectively.

$$S_H = \bar{V}_h \frac{S \cdot \bar{c}}{(x_h - x_{CG})} = \bar{V}_h \frac{S \cdot \bar{c}}{l_h} \qquad (6.12)$$

$$S_V = \bar{V}_v \frac{S \cdot b}{(x_v - x_{CG})} = \bar{V}_v \frac{S \cdot b}{l_v} \qquad (6.13)$$

The procedure to calculate the tail areas from these formulas start by assuming the values for $\bar{V}_h$ and $\bar{V}_v$ from statistics/literature. Since the mission profile of RePLASMA is considered significantly different from the statistically available aircraft given by Vos and Melkert [15], a research was made to find more accurate estimations for the parameters. Eventually, a HALE UAV design paper by Hwang et al. [16] was picked as a guideline. Hence, $\bar{V}_h$ was taken as 0.3 and $\bar{V}_v$ as 0.015. Then, the preliminary estimation of the lengths l_h and l_v had to be made, and for simplicity, both values were

[1] https://aerotoolbox.com/wing-plot-tool [accessed 17/6/2021]
[2] https://jsc-aircraft-ops.jsc.nasa.gov/wb57-design—integration.html [accessed 17/6/2021]

assumed to be the same as the lengthwise location of the aerodynamic centers of the horizontal and vertical tails are within negligible distance. From preliminary estimations on the wing positioning [15], this distance between the aerodynamic centre of the empennage and the aft CG position was calculated as 71.25% of the fuselage length calculated in Section 6.3.2. Finally, since the wing area, span, and the MAC were already obtained in Section 6.3.1, the areas of the horizontal and vertical tails were obtained, with initial values being 8.62 m^2 for S_h and 10.15 m^2 for S_v.

6.4. Class II weight estimation

The final module of the sizing and weight estimation tool is the class II weight estimation. In this module, the use of semi-empirical methods combined with an initially designed geometry allows for a more accurate estimation of the operating empty weight and maximum take off weight. For the purposes of the sizing and weight estimation module, the empirical methods developed by Torenbeek were utilized, as they were considered most appropriate for the class of aircraft that RePLASMA is. Torenbeek's methods are applied in a different manner for aircraft, with demarcation being formed on the basis of speed, or take off mass (derived from class I). The aim of this section is to illustrate the various formulas used to estimate component weights, from the wing through to avionics and aeronautics.

The first weight estimate is that of the wing planform.

$$\mathrm{W_w} = 0.00125\ \mathrm{W_{TO}} \left(\mathrm{b}/\cos\Lambda_{1/2}\right)^{0.75} \left[1 + \left\{6.3\cos\left(\Lambda_{1/2}\right)/\mathrm{b}\right\}^{1/2}\right] \left(\mathrm{n_{u1t}}\right)^{0.55} \left(\mathrm{bS}/\mathrm{t_r W_{T0}}\cos\Lambda_{1/2}\right)^{0.30} \quad (6.14)$$

Note that the take off weight remains an input, alongside the wingspan, the half chord sweep, the surface area and the maximum thickness of the airfoil at the root chord. Following this, the next two equations pertain to the empennage. The first refers to the horizontal tail, while the second allows the calculation of the vertical tail's weight.

$$W_h = K_h S_h \cdot \left\{3.81 \frac{S_H^{0.2} V_D}{1000\cos(\Lambda_{1/2_h})^{0.5}}\right\} \quad (6.15)$$

For a horizontal tail, S_h represents the surface area, while the dive speed is given by V_D.The coefficient K_h takes a value of 1 for fixed incidence stabilizers. For the vertical tail, the coefficient K_v takes n a value of 1 for a fuselage mounted horizontal tail.

$$W_v = K_v S_v \cdot \left\{3.81 \frac{S_V^{0.2} V_D}{1000\cos(\Lambda_{1/2_v})^{0.5}}\right\} \quad (6.16)$$

From the empennage, we can consider the fuselage for the purpose of estimating the weight. Consider the coefficient K_f. This coefficient holds a value of 1.07 for main gear attached to the fuselage, and 1.08 for a pressurized fuselage, or the product thereof for a combination of both. Additionally, the width and height (w_f and h_f) of the fuselage are of importance. Finally, the gross shell fuselage area is required, based on external dimensions of the fuselage.

$$W_f = 0.021 K_f \sqrt{\frac{V_D l_h}{w_f + h_f}} S_{fgs}^{1/2} \quad (6.17)$$

Consider now the nacelle weight. The sum of the masses of the nacelles on the aircraft are directly influence by the required take off power, which is a value that can be obtained from the wing and power loading module.

$$\mathrm{W_n} = 2.5\left(\mathrm{P_{TO}}\right)^{1/2} \quad (6.18)$$

In order to calculate the mass of landing gear, the same equation is applied to the main and nose gear, although the coefficients A_g through D_g take different values. In the case of main gear these values are: 40,0.15,0.019 and $1.5e-5$ respectively.

$$\mathrm{w_g} = \overline{\mathrm{K}}_{\mathrm{gr}} \left\{\mathrm{A_g} + \mathrm{B_g}\left(\mathrm{W_{TO}}\right)^{3/4} + \mathrm{C_g W_{TO}} + \mathrm{D_g}\left(\mathrm{W_{TO}}\right)^{3/2}\right\} \quad (6.19)$$

In order to estimate the weight of the engines, the take off power as well as the empty weight of the aircraft is needed, along with a coefficient of 1.35, according to Torenbeek, [17].

$$\mathrm{w_{pwr}} = \mathrm{K_{pg}}\left(\mathrm{W_e} + 0.24\mathrm{P_{TO}}\right) \quad (6.20)$$

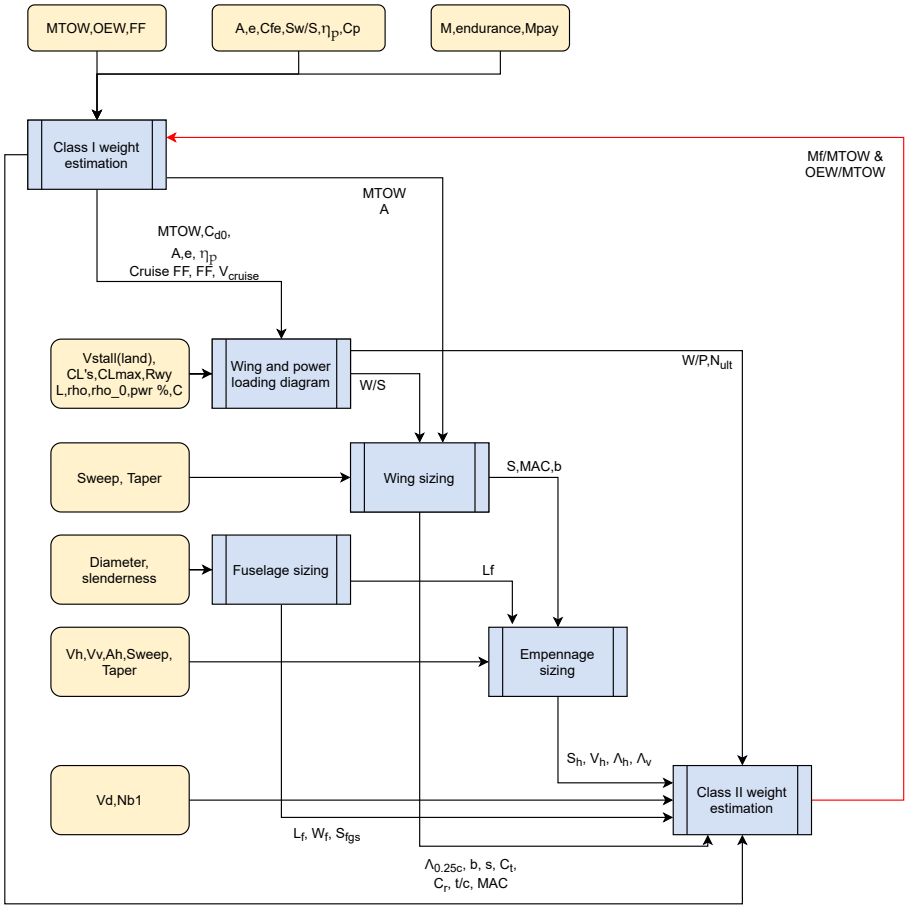

Figure 6.3: Schematic overview of aircraft iteration tool showing inputs and outputs.

Finally, the masses of the flight controls, hydraulics, electronics and instrumentation are all factors that depend on the take off weight and empty weight of the aircraft, as the following equations demonstrate.

$$W_{fc} = K_{fc} \cdot W_{to}^{2/3} \tag{6.21}$$

$$W_{hy} = 0.007 \cdot W_{to} \tag{6.22}$$

$$W_{el} = 0.325 \cdot W_{oew}^{0.8} \tag{6.23}$$

$$W_{iae} = 40 + 0.008 \cdot W_{to} \tag{6.24}$$

The numerous equations explained above are referred to as the class II weight estimation, and derive inputs from the modules explained earlier in this chapter. From the output of the class II weight estimation, a series of new inputs is provided for the next class I weight estimation, repeated until convergence is achieved.

6.5. Iteration & convergence

The methods explained in previous sections (Section 6.1 through Section 6.4) form the basis for the iterative design process. This iterative design process aims to converge upon a feasible aircraft design. In order to mark the completion of the convergence, the difference in weights estimated by the class I and class I weight estimates is used as the benchmark parameter. In industry, convergence is considered achieved when the difference between the two weight estimates is less than one percent. In order for the iterative tool to be developed, it is important to identify various outputs and inputs throughout the process. Prior sections have established this effectively, and it is now possible to integrate the aforementioned modules into an effective iterative tool.

Starting from the class I weight estimation in Figure 6.3, the inputs belong to three distinct categories. The output of the class I weight estimation leads to into the wing and power loading, the

wing sizing as well as the class II weight estimation. Following on from this, the wing and power loading feed parameters into the wing sizing and the class II weight estimation.

Following this, the wing and power loading diagram is generated, by means of inputs from the Class I weight estimation. Furthermore, there are external inputs that lead into the wing and power loading diagram generation module. These are the stall speed at landing, the various lift coefficients utilized at different phases of flight, the air density values at Cruise and sea level, the expected runway length as well as the power setting expected in cruise. The Wing and power loading forms an import part of the inputs into the wing sizing and the class II weight estimation.

The wing sizing module utilizes the wing loading derived from the wing and power loading module, as well as the maximum take off weight and aspect ratio from the class I weight estimation. Furthermore, the direct inputs of sweep and taper, allow the characterization of a wing planform.

In parallel to the wing sizing, the selection of the diameter and slenderness ratio's of the fuselage allow the fuselage to be sized.

Following the sizing of the fuselage and wing, the empennage is sized, using external inputs such as expected volumes, sweep and taper. Furthermore the length of the fuselage as well as the planform area, span and mean aerodynamic chord allow the empennage to be sized.

Finally, all the previous modules feed into the class II weight estimation. Through the methods described in Section 6.4, a new value for the maximum take off weight and the operating empty weight are found. In order to calculate a new MTOW to input back into the class I, the following formula is used:

$$MTOW_{i+1} = \frac{M_{pay}}{1 - \frac{M_{fuel}}{MTOW_i} - \frac{OEW_i}{MTOW_i} - M_{tfo}} \tag{6.25}$$

Following this calculation, the new values are fed into the class I weight estimation to restart the process. The modules are run until the difference between the class I and class II maximum take off weights are considered convergent, with a difference of less than 1%, as per the industry standard, with some leeway applied to account for the relative crudeness of the starting point, as caused by the low number of aircraft identified with similar mission profiles.

6.6. Results & initial design point

Following the running of the iterative tool, a series of results were obtained.For the purposes of the design process, these values are considered the baseline values, which form the crux of the detailed design process. The relation of this output to the final aircraft are explained further in Chapter 5. The relevant parameters are presented in the following table, and will be utilized in further design processes.

Parameter	**Value**	**Unit**	**Symbol**
Cruise velocity	149.18	m/s	V_{cruise}
Cruise lift coefficient	1.3	-	$C_{l_{cruise}}$
Cruise drag coefficient	0.045	-	$C_{d_{cruise}}$
Take off power	431.36	hp	P_{to}
Wing area	77.61	m^2	S
Wing span	43.81	m	b
Root chord	2.50	m	C_r
Horizontal tail area	7.52	m^2	S_h
Vertical tail area	8.85	m^2	S_v
Fuselage length	8	m	l_f
Maximum take off weight	4520	kg	MTOW
Operating empty weight	2795	kg	OEW
Fuel weight	1536	kg	M_{fuel}

7

Aerodynamic Design

The aerodynamic properties of the aircraft have a heavy impact on the final design. Efficiently producing lift directly dictates the wing size needed and thus, its weight, while the total drag produced by the wing planform and the fuselage sets requirements for the size of the propulsion system. Therefore, it is of upmost importance to select the correct aerodynamic shapes for the specific mission profile. In this chapter the design and analysis of the aerodynamic properties of the UAV is presented, starting with Section 7.1 where the airfoil optimization process is shown. Furthermore, Section 7.2 revolves around the process and results of designing the whole fuselage shape, Section 7.3 includes the analysis regarding the need for high lift devices on the aircraft, and Section 7.5 talks about the aerodynamic interface with the propulsion subsystem in the form of the design of the intake, exhaust and cooling functions of the aircraft. Finally, the design is analyzed as a whole and an aerodynamic overview is provided in Section 7.6.

7.1. Airfoil optimization

Practical aerodynamic design problems typically pose a trade-off between performance and constraints. In the case of airfoil selection, providing a high enough lift coefficient to support the UAV's weight while minimizing the drag could be seen as a prime example. This naturally can be formulated as an optimization problem where a certain *cost* function is maximized by tweaking the geometry of the airfoil iteratively. To do so, firstly a parametrization procedure will be presented. Following, the cost function describing how good an airfoil is at meeting the mission requirements will be described. Moreover, the aerodynamic solver allowing the computation of the cost function will be analyzed. Finally, the optimization algorithm that is needed to converge on an optimal solution will be described.

7.1.1. Parametrization

To parametrize the airfoil many schemes are available. Variables such as the airfoil coordinates could be used, but as Mukesh et al.[18] observed, this provides too many degrees of freedom, making the problem unintuitive and possibly unfeasible to solve. Therefore, the airfoil was parametrized using the PARSEC formulation[19], reducing the geometry to 11 geometrically intuitive parameters as presented along with their meaning in Table 7.1. They are also shown graphically in Figure 7.1.

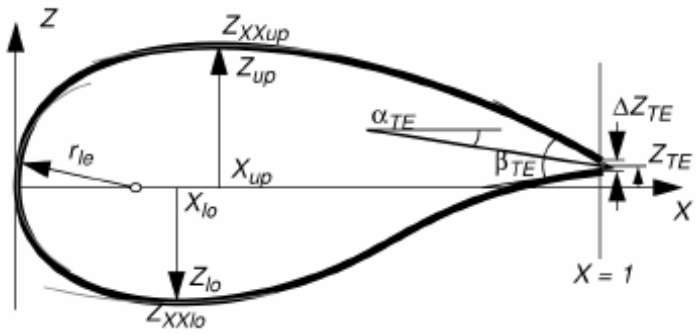

Figure 7.1: PARSEC parameters describing airfoil geometry[19].

Table 7.1: Description of PARSEC parameters[19].

Parameter	Definition
r_{le}	Leading edge radius
X_{up}	upper crest position in horizontal coordinates
Z_{up}	upper crest position in vertical coordinates
Z_{XXup}	upper crest curvature
X_{lo}	lower crest position in horizontal coordinates
Z_{lo}	lower crest position in vertical coordinates
Z_{XXlo}	lower crest curvature
Z_{TE}	trailing edge offset in vertical sense
ΔZ_{TE}	trailing edge thickness
α_{TE}	trailing edge direction
β_{TE}	trailing edge wedge angle

Having obtained the parameters for a specific airfoil, they can be converted to coordinates by means of polynomial curve fitting in the form of:

$$z_{up} = \sum_{i=1}^{n=6} a_{up}^{i} \cdot x^{i-\frac{1}{2}}, \quad z_{lo} = \sum_{i=1}^{n=6} a_{lo}^{i} \cdot x^{i-\frac{1}{2}} \tag{7.1}$$

where the coefficients a_{up}^{i} and a_{lo}^{i} are computed by solving a linear system of equations, formed using the 11 PARSEC parameters[19].

7.1.2. Cost function

Having obtained a parametrized version of airfoil, a certain criteria is needed to evaluate its fitness to the specific mission profile. The first and obvious criteria is the lift coefficient, C_l, produced during cruise. Due to the extremely high altitude at which the aircraft is operating, having as high as possible of a lift coefficient is of upmost importance in order to support the weight. Moreover, due to mission requirement constraining the endurance to be above 20 hours, attention has to be paid to the aerodynamic parameters involved in the endurance equation:

$$E = \frac{\eta_p}{c_p}\sqrt{2\rho S}\frac{C_L^{3/2}}{C_D}\left(\frac{1}{\sqrt{W_2}} - \frac{1}{\sqrt{W_1}}\right) \tag{7.2}$$

where it can be seen that the endurance is directly proportional to C_l^3/C_d^2. Therefore, airfoils that maximize this parameter will be rated higher. Moreover, a general aerodynamic parameter that is key is the ratio between C_l and C_d. Although, providing enough lift is the main requirement for an airfoil, reducing the drag, which has massive impact on the propulsion system is also vital, and C_l/C_d encapsulates exactly this. Finally, if the aircraft is flying at a high angle of attack during cruise, if the stall point is close to it, a sudden wing gust could possibly push the aircraft into stall, which is undesireable. Therefore, the final criteria considered is the range between the operative angle of attack, which in this case was chosen to be the angle of attack where C_l^3/C_d^2 is maximum, and the stall angle of attack, resulting in the following cost function.

$$C = 0.6 \cdot C_{l_{cruise}} + 0.2 \cdot \frac{C_l^3}{C_d^2} + 0.1 \cdot \frac{C_l}{C_d} + 0.1 \cdot (\alpha_{max} - \alpha_{cruise}) \tag{7.3}$$

where the weights placed before the parameters are used to impose relative importance as per the mission requirements as explained previously.

7.1.3. Aerodynamic Solver

To be able to compute the cost attributed to an airfoil as defined beforehand, a way of estimating the aerodynamic polar is needed. Today's standard for computing aerodynamic properties with high accuracy is by using Computational Fluid Dynamics (CFD), but due to its extreme computational cost, research was put into other tools. A prime candidate for the occasion is the potential flow solver XFOIL[1], which is particularly suited for the analysis of low Reynolds number (< 1 x 10^6) applications. XFOIL is a panel based solver that is also able to model viscous phenomena such as boundary layer effects and transition and thus, is particularly suited for the computation of airfoil polars based on geometry, Reynolds number and Mach number. It has been shown to produce accurate estimates for C_l, C_d and C_m for angle of attack ranges between -5° and 12° for a fraction of the computational power needed compared to CFD methods [20].

7.1.4. Optimization Algorithm

In order to reach to an optimal value, an optimizer prescribing a set of rules that guarantee convergence is needed. Due to the fact that the problem cannot be formed analytically and is also very discontinuous, no gradient function can be formulated, rendering modern gradient descent algorithms useless and therefore, research was put into other methods. As reported by Dina et al.[21], optimal solutions can be achieved by utilizing genetic algorithms. These types of algorithms draw analogy from nature by starting off with an initial population consisting of a number of solutions and evolving this population through a set of rules, namely - crossover and mutation, which occur on each iteration based on a set probability. Crossover is an operator used to combine data from two airfoils from the previous generation to produce an "offspring" that potentially carries the best parameters of its parents while mutation is an operator meant to diversify the population by randomly altering a parameter of an existing airfoil to create a new one.

7.1.5. Procedure and Results

In the case of airfoil optimization, the sections listed above can be combined to produce an optimal result in the following way.

Firstly, an airfoil is chosen as an initial design point from which all iterations stem. In this case, that airfoil is the NLF1015, which was chosen in the preliminary airfoil trade-off [9]. Due to the fact that PARSEC parameters were not directly available for this specific airfoil, they were obtained manually through a non-linear least squares fit as shown in Table 7.2.

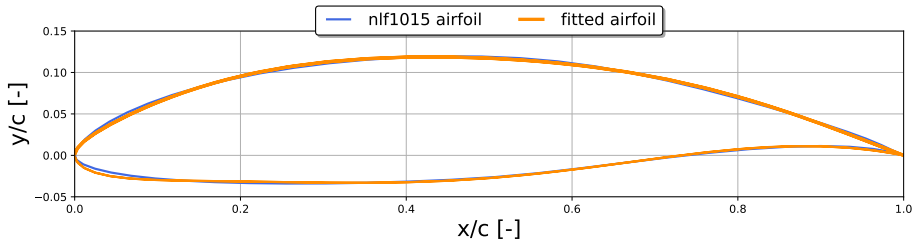

Figure 7.2: PARSEC airfoil fitted to the original NLF1015 airfoil.

Table 7.2: Parsec parameters for initial fitted airfoil.

Parameter	Value
r_{le}	0.011
X_{up}	0.430
Z_{up}	0.119
Z_{XXup}	-0.667
X_{lo}	0.341
Z_{lo}	-0.033
Z_{XXlo}	0.316
Z_{TE}	0.0
ΔZ_{TE}	0.0
α_{TE}	-16.1
β_{TE}	9.54

Following that, an initial population of 500 airfoils was created by uniformly changing each of the initial 11 PARSEC parameters, with a maximum allowed change of 15%. By invoking XFOIL's viscous analysis capabilities, each of the 500 solutions were evaluated by the cost function and a pool of 50 was selected based on the result, ranking the ones with the highest cost function at the top. These airfoils were processed with crossover and mutation to produce a new population and the

[1]https://web.mit.edu/drela/Public/web/xfoil/ [accessed 13/6/2021]

process was repeated for a total of 15 times, keeping track of the best airfoil at each iteration. A block diagram of the procedure can be seen in Figure 7.3.

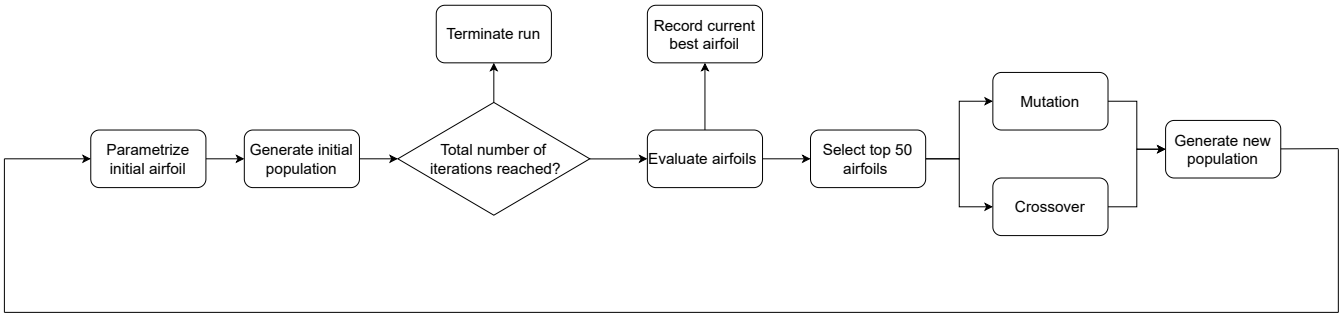

Figure 7.3: Block diagram of genetic algorithm.

The algorithm was run with a Reynolds number of 7.68 x 10^5, corresponding to a flow Mach of 0.5 and a reference chord of 2.0 m (initial MAC estimate). After running the algorithm, the following geometry was obtained as seen in Figure 7.4.

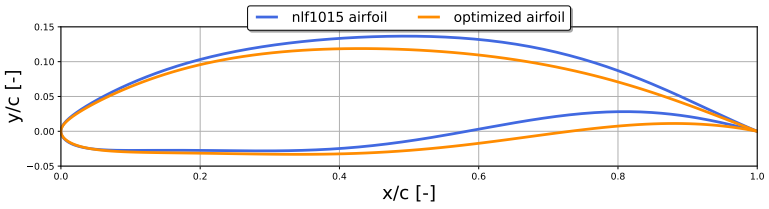

Figure 7.4: Geometrical comparison between the original and optimized airfoils.

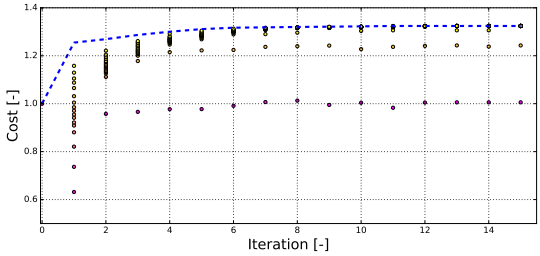

Figure 7.5: Cost function progression with respect to iteration number.

A progression of the cost functions based on the number of iterations can be seen in Figure 7.5. Moreover, comparing the aerodynamic properties of the optimized airfoil to the original NLF1015 airfoil, the following changes were observed as seen in Figure 7.6.

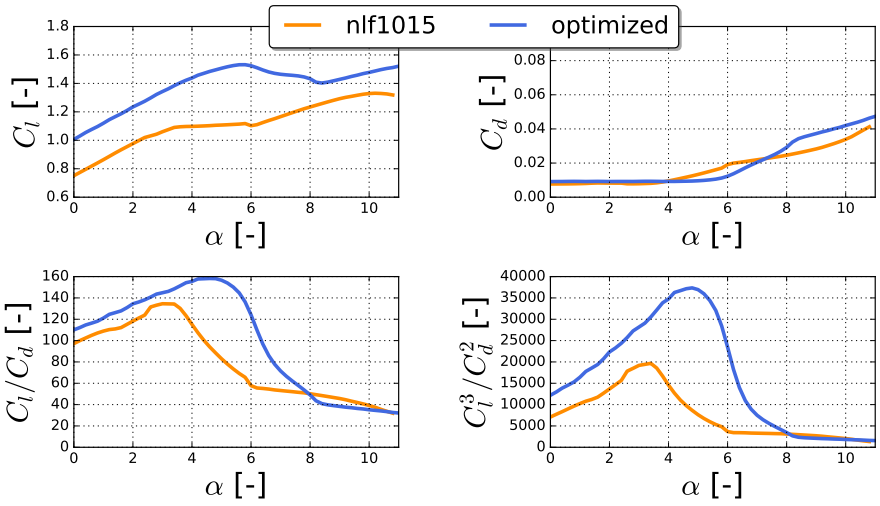

Table 7.3: Comparison of cost function components between initial and optimized airfoils.

Parameter	Initial	Optimized
$C_{l_{cruise}}$	1.09	1.50
C_l/C_d	134	158
C_l^3/C_d^2	19700	37400
AoA_{range}	6.8	11.2

Figure 7.6: Comparison of aerodynamic polars between original and optimized airfoils.

Firstly, looking at the C_l vs α graph, it can be seen that for the same angles of attack, the optimized airfoil produces more lift, reaching almost 50% more at cruise conditions, while the drag remains almost equal for angles of attack smaller than 8°. Furthermore, the drag bucket is extended by 1.5°, allowing operation at minimal drag up to AoA's of almost 6°. These changes are also reflected

in the C_l/C_d and C_l^3/C_d^2 graphs, with the latter increasing by almost a factor of two and thus, doubling the theoretical endurance and proving the importance and the effectiveness of the optimization procedures.

7.2. Fuselage design

The fuselage will primarily hold payload, flight systems, communication systems and fuel. From the sizing in Section 6.3.2, the required volume for the fuselage was determined. Moreover, due to the nature of the mission, the design of the fuselage must take into account aerodynamics and potential interactions with the wing and empennage. In the initial phase of design a lifting body fuselage was considered but was not practical due to a significant increase in wetted area (thus more drag) and structural mass that did not outweigh the aerodynamic gain. Therefore, a standard 'tube' configuration was chosen. Firstly, the choice of fuselage cross section is presented in Section 7.2.1, following with the nose and tail cone design in Section 7.2.2 and Section 7.2.3 respectively. Finally, the synthesized design it presented in Section 7.2.4.

7.2.1. Fuselage cross-section

Front an aerodynamics perspective, the cross sectional shape of the fuselage can have a great effect on the performance of the fuselage. In the case of RePLASMA, minimization of drag while allowing ample volume for payload and fuel along with enough of an arm for the tail to be effective was of highest priority.

A triangular cross section was considered as it had a slightly better L/D [22] but was not feasible as the aircraft is configured with a high wing, and on ground turnover requirements need to be satisfied for the landing gear. As a result, an upright triangular cross section would not be feasible for the integration of the wing and fuselage from a structural viewpoint. Vice versa, the landing gear would have to be made larger and longer to have the same turnover angle.

As a result, only two shapes were considered in further analysis, square and ovular. For a given volume it can be proven that square-sectioned prism has a smaller surface area than a circular sectioned prism (cylinder). The surface area of the square section is 11% less than that of the traditional circular sectioned fuselage. Since the drag of the fuselage is mainly driven by the skin friction drag, a smaller surface area greatly affects the drag characteristics of the fuselage. Therefore, since there is not a need for pressurization a square sectioned fuselage is chosen. Indeed, due to structural concerns, the corners of the section cannot be sharp. As a result, an r/w value of 0.25 is used. The definition of r and w in the context of the fuselage cross-section is shown in Figure 7.7.

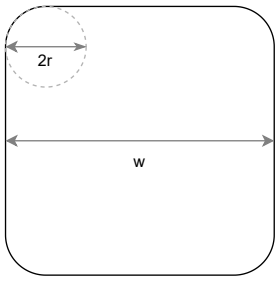

Figure 7.7: The definitions of r and w. r is the radius of curvature of the corners and w is the width/height of the fuselage section.

Furthermore, according to simulation based research carried out by Mahjoob et el. [23], a square cross section is more desirable in terms of arodynamic efficiency. Digitised graphs from Mahjoob et al. are presented in Figure 7.9 and Figure 7.8. Thus the final section of the fuselage is decided to be a rounded square with a r/w value of 0.25. The full fuselage design is presented in Section 7.2.4.

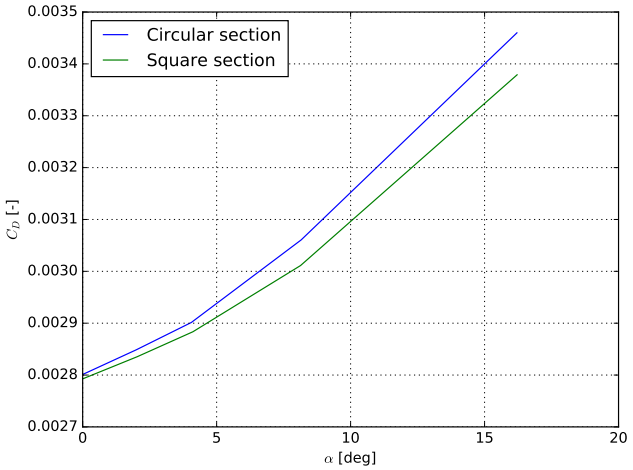

Figure 7.8: C_D shown as a function of α shown for a square and circular sectioned fuselage. It can be seen that for every positive angle of attack, the square section has lower drag. The plot was obtained from Mahjoon et al. [23] and normalised with the wing area instead of the fuselage cross section.

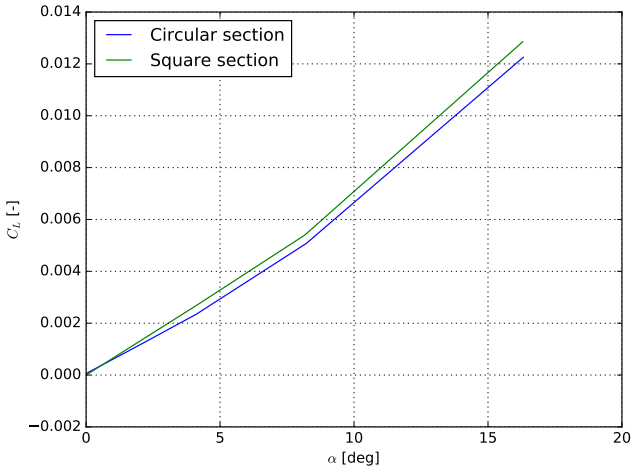

Figure 7.9: C_L shown as a function of α shown for a square and circular sectioned fuselage. It can be seen that at all non-zero positive angles of attack, the circular section has less lift than the square section. The plot was obtained from Mahjoob et al. [23] and normalized with the wing area instead of the fuselage cross section.

7.2.2. Nose design

At the stated mach number and altitude the aircraft must fly at, the parasitic and induced drag are low. Parasitic drag refers to the drag created due to viscous forces between the fluid and surface of the body. This is also confirmed by the low Reynolds number found for the aircraft in Section 7.1 that can be interpreted as the ratio of inertial to viscous forces. It can therefore be inferred that the surface characteristics and the wetted area of the nosecone drive the determination of the drag losses caused due to it as the induced drag is negligible and mostly found on the wing. Another concern relating to the design of the nose of the fuselage is the accommodation of payload and radar equipment. In the case of the payload, it is useful to situate some of the measurement instrumentation in the nosecone to enable measurement of free stream air. Furthermore, it is usual in case of airliners to have a weather radar situated in the nosecone but in the context of the mission profile of RePLASMA this will not be necessary due to the fact the majority of the flight takes place at an altitude much above most weather phenomena.

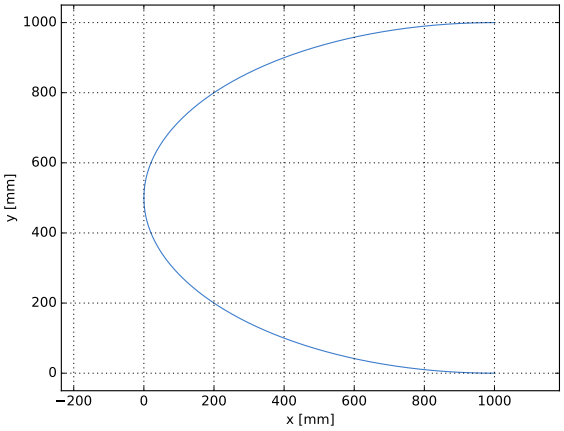

Figure 7.10: Nosecone profile of RePLASMA.

In order to then choose the shape of the nosecone, a literature study was carried out. The scope of the study was to determine the shape and dimensions of the nosecone of the fuselage so as to produce a design which has a relatively optimal drag performance while still being structurally feasible. It was found that an elliptical contour for the nose would be appropriate as this provides the least drag for $0.4 < M < 0.6$ [24]. To reduce the wetted area a smaller fineness ratio would be preferred. The fineness ratio is the ratio of the length of the nose to its base diameter [24]; thus a shorter nose length would be favorable, and as a result a fineness ratio of 1 was chosen. The contour is depicted in Figure 7.10; the left hand side of the plot is the tip of the nose.

7.2.3. Tail design

The tail will also have an elliptical contour but with a tail angle to allow for sufficient rotation at take-off. Unlike the nose cone, the fineness ratio of the tail cone does not need to be minimized, but optimized to provide the least drag from the fuselage and tail surfaces. Having a longer tail cone allows for a smaller tail control surface reducing tail drag, but this benefit can be outweighed by the additional structural weight. According to a study into tailcone shape and performance for maximised lift-to-drag conducted by Oktay et al.[25], a fineness ratio of 2 is used for the tail cone.

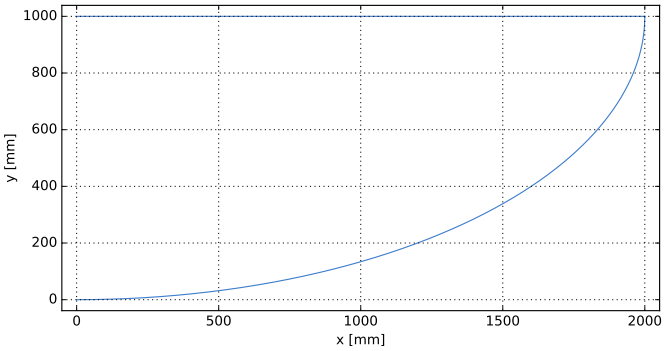

Figure 7.11: Tailcone profile of RePLASMA.

The side profile of the tailcone is finally presented in Figure 7.11. Here, the right hand side of the image is the tip of the tailcone. Of course, considering the producibility, it is likely not optimal to employ the full ellipsoid contour and as a result some alterations are made. The profile is reduced in length by 20 cm in order to avoid the pointed trailing edge of the fuselage. While this shortens the tailcone and reduces the fineness ratio to 1.8, the contour from Figure 7.11 is still used, and it is just stopped at a distance of 1800 mm from the start of the tailcone.

7.2.4. Final fuselage design

Following the design of the cross-sectional shape, nosecone geometry and tailcone geometry, the fuselage can be synthesised. A variable that remains undecided is the overall fineness ratio. The fineness ratios of the nosecone and tailcone were determined to be 1 and 1.8 respectively in Section 7.2.2 and Section 7.2.3 respectively. In Section 6.3.2 it was discussed and concluded that a total fuselage fineness ratio of 8 is optimal for the entire aircraft. Therefore, since the nose and tailcone already have a prescribed fineness ratio from the analysis of their shape, the central section of the fuselage is made to have a fineness ratio of 5.2 in order for the full fuselage to have a fineness ratio of 8. Finally, a drawing along with some of the relevant dimensions of the cross section and profile are shown in Figure 7.12.

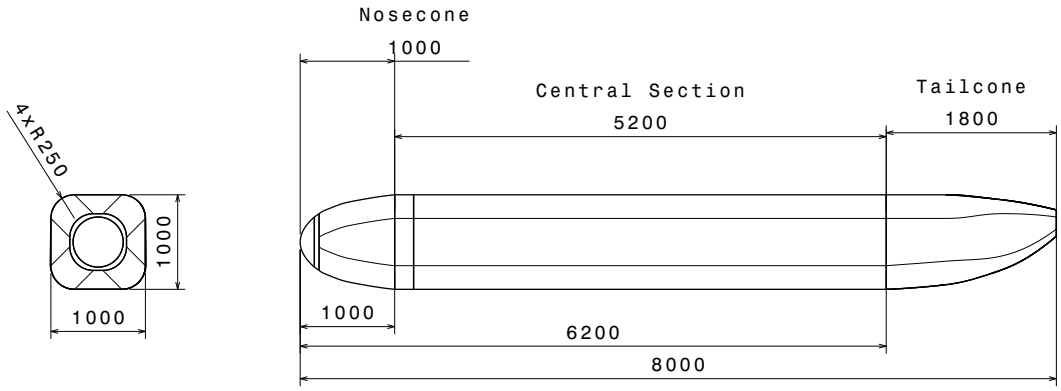

Figure 7.12: The RePLASMA fuselage. Above the side view, the length of each section is provided while below the side view, the position of the start of each section is provided relative to the tip of the noes, which is used as a datum point.

Theoretical Drag Calculation

The form factor of a fuselage, which is a function of its geometry, is a good indicator for its drag when utilised in conjunction with the skin friction coefficient. This relation is shown in Equation 7.4. Due to aircraft design majorly revolving around the shape of circular or ovular fuselage section shapes, most relations for form factor are geared to these cases. In the niche case of RePLASMA where the fuselage shape is rather unconventional, a different approach must be employed. From Bil et al. [26] an improved formulation for the form factor of the fuselage for rounded square section shapes

can be obtained and is presented in Equation 7.5 through Equation 7.6.

$$\mathrm{FF} = cs_1 \cdot \left(\frac{l}{w}\right)^{cs_2} + cs_3 \tag{7.5}$$

$$cs_1 = -0.825885 \cdot \left(\frac{2r}{w}\right)^{0.411795} + 4.0001 \tag{7.6}$$

$$C_D = C_f \cdot \mathrm{FF} \cdot \frac{S_{\mathrm{wet}}}{S_{\mathrm{ref}}} \tag{7.4}$$

$$cs_2 = -0.340977 \cdot \left(\frac{2r}{w}\right)^{7.54327} - 2.27920 \tag{7.7}$$

$$cs_3 = -0.013846 \cdot \left(\frac{2r}{w}\right)^{1.34253} + 1.11029 \tag{7.8}$$

The intermediate and final values obtained for the calculation of the drag is presented in Table 7.4. The skin friction coefficient is obtained from a statistical analysis of skin friction coefficients C_f of several aircraft carries out by Brandt et al. [27], a value of 0.012 is used. This value is listed as typical for high altitude solar UAVs and it was concluded that the mission profile and aerodynamic goal of RePLASMA is in enough commonality with that of high altitude solar UAVs to use this value. As a result, a drag coefficient of 0.00478 was obtained for the $\alpha = 0°$ condition. This is greater than the value obtained through CFD analysis by Mehjoob et al. [23] as shown in Figure 7.8. This is likely due to the slightly differing flow conditions and nose and tail shape relative to RePLASMA. Furthermore, the model used to calculate drag using form factor is a statistical regression and is not necessarily applicable to HALE UAVs such as RePLASMA due to the dearth of data available for such missions. Resultantly, the simulation based study from Figure 7.8 and Figure 7.9 is trusted relatively more and used in subsequent calculations.

Table 7.4: A summary of the parameters and their values used in and obtained through Equation 7.5 and Equation 7.4.

Parameter	Value
l/w	8.0
r/w	0.25
C_f	0.012
S_{wet}/S_{ref}	0.350
cs_1	3.923
cs_2	2.281
cs_3	1.105
FF	1.139
C_D	0.00478

7.3. High-lift devices

Having established an initial layout and weight for each basic subsystem of the aircraft, the next step is to design the moving surfaces of the plane required in order to be able to function on flight conditions other than steady level flight. In this section focus is given on the HLDs which are used during phases of flight that require an excess in lift coefficient to be performed, for instance the landing where one needs to minimize the approach velocity to land in a smooth manner. Frequently used HLDs include the flaps attached on the trailing edge and the slats attached in the leading edge of the main wing.

In general the use of HLDs is trivial on commercial aircraft however the RePLASMA UAV does have substantial differences which require to be examined in order to test the need for flaps. It is important to keep in mind that the UAV is designed to sustain a cruise altitude of 25 km, where the air density is almost 30 times lower implying that lift generation is significantly easier at sea level. This means

that the aircraft during the lift-dense flight conditions which are performed closer to sea level may by default be able to produce the required excess lift, scrapping the need for HLDs.

In order to effectively examine this, 3 flight phases were chosen to be the ones deciding the need for HLDs. These are the take-off, the initial climb and the landing.

Take-off

For the take-off performance as seen in Figure 6.1, there was a large margin between the constraint line and the design point even though the maximum lift coefficient was assumed to be 1.4 at take-off. The previous means that according to Equation 6.1 the aircraft can achieve a take-off from a runway with length of 500 m as long as it can achieve the aforementioned lift coefficient. By looking at the optimized values for the airfoil in Table 7.3 one can see that the updated $C_{l_{max}}$ reaches a value of 1.5 for the airfoil while applying an empirical factor of 0.9 translates to a value of 1.35 for the $C_{L_{max}}$ of the 3D wing. For the sake of completeness, Equation 6.1 was recalculated with the given wing and power loading but now assuming an even smaller $C_{L_{max}}$ of 1.3. Results yield a required runway length of around 250 m and a take-off speed of around 30 m/s which are both acceptable values. Of course, the statistical relation used for the take-off parameter can be very inaccurate since the take-off and landing distances are usually hard to estimate (as mentioned by Vos, R. and Melkert, J.A. [12]). However, the margin that was taken throughout these calculations should ensure that there is no need for HLDs at least for take-off.

Climb rate

For the estimation of the climb rate given the power and wing loading calculated at Section 6.2 and certain other inputs, Equation 6.8 is used. The results using a $C_L^{3/2}/C_D$ of 37400 according to Table 7.3 yield a climb rate of approximately 5.8 m/s at sea level. Note that by substituting the air density for that at cruise altitude Equation 6.8 gives a climb rate of 5 m/s at cruise altitude which means that the plane will be able to sustain the acceptable climb rate throughout the entire range of altitudes. That also implies that the climb from sea level to 25 km would require approximately 75 minutes which is an acceptable time for climbing to such a high altitude. Furthermore, given that the entire mission is over 20 hours, the percentage of time spent for climbing to cruise altitude was also considered acceptable by the team. Hence it was decided that there was no need for HLDs in order to increase the climb rate of the aircraft since it was already enough.

Landing

With regards to the landing requirement, similar things hold as in the requirement for take-off. Figure 6.1 clearly shows the high margin on the landing constraint and the design point. In the figure a $C_{L_{max}}$ of 1.4 was assumed and the constraint was constructed assuming a runway length of 500 m. As mentioned previously, a safe assumption for the lift coefficient of the 3D wing as translated by the one found for the optimized airfoil is a $C_{L_{max}}$ of 1.35. Thus calculations were performed using Equation 6.2 where all the values came from the design iteration and a $C_{L_{max}}$ of 1.35 was used. The resulting required runway length turns out to be around 270 m which corresponds to a landing speed of 13 m/s according to the statistical relation mentioned by Vos, R. and Melkert, J.A. ([12]). This value, however, is way below the stall speed at landing of 21.5 [m/s] which means that it is not feasible. Instead, the landing speed was manually assumed as 23 m/s to result in a landing distance of around 900 m Once again the calculations performed are accompanied with a high uncertainty since the utilized statistical relations vary significantly from aircraft to aircraft. These rough estimations therefore were only performed in order to test the need for HLDs and do not provide accurate estimations of the aircraft characteristics and the required runway length.

Since the aircraft can achieve the required lift characteristics to perform the lift-intense phases of flight, no HLDs are needed. This influences the design positively since HLDs introduce not only extra weight on the design but also structural and manufacturing complexity. Thus, although small flaps could still be considered in order to increase the performance (especially during climb), the team decided that the weight and complexity benefit would outweigh the extra performance factor introduced by HLDs and so they were discarded as a design consideration.

7.4. Winglet design

Winglets have been widely used in aviation to reduce the lift induced drag of the aircraft by means of increasing the effective aspect ratio of the wing which causes a minimization of the wing tip vortices that disturb the flow from the top and bottom side of the airfoil. They are used in a big part of the aircraft industry however after analyzing similar missions to RePLASMA one can spot the lack of winglets in almost all the HALE designs. Instances include the Boeing Phantom Eye, NASA's Altus II as well as the Global Hawk by Northrop Grumman. The previous fact raised concerns on why the seemingly beneficial winglets are not widely used in similar missions and so Table 7.5 was constructed in order to compare the advantages and disadvantages on the team's design.

Table 7.5: Advantages and disadvantages of winglets on RePLASMA's design.

Advantages	**Disadvantages**
Reduced lift-induced drag / Efficiency increase	Added design and manufacturing complexity
Redirection of wing-tip vortices	Structural difficulties and induced vibrations
Increased lateral stability	Extra weight

Directly from inspection, some entries of the table do not form an important factor for the team's design choice. Firstly, since the span of the wing is considerably larger than that of the tail, no interference between the wing tip vortices and the tail is expected even without winglets. Furthermore, in case winglets are attached, due to the structural constraints they impose, their size will be limited which means that there is limited contribution to the lateral stability. For the same reason, however, the extra weight as well as the added complexity will not be significant with respect to the overall design. Henceforth, the decision will be made solely on a trade-off between the decrease in drag and the structural difficulties induced.

To start off, it was decided that a design for the winglets would be derived using methods from literature and afterwards the impact of that specific design on the overall performance would be estimated.

The geometry of a winglet can be fully defined by some basic parameters. These are, excluding the airfoil, the taper ratio, the height, the sweep and the angle with respect to the wing. A value for each of these parameters will be given below, using relevant sources for justification.

- **Taper ratio:** To minimize the tip vortices usually a pointy edge is used for the winglet. However, the lift distribution should preferably match the elliptical one of the wing to achieve the optimal efficiency. For the winglets, according to the analysis of Whitcomb, an elliptical distribution is found to be achieved for a taper ratio of 0.3 [28]. Thus this value will be used.
- **Height:** The lift-induced drag reduction is almost linearly dependent on the winglet's height so from an aerodynamic perspective maximizing it would give the greatest benefit [29]. However the height is restricted by the structural loads it induces so the aerodynamic benefit is also limited. Due to the lack of high-precision structural analysis on the effect of winglets on the load path, an estimate of the height was made by the team using an acceptable ratio of winglet height to wing half-span of approximately 1:14. This resulted in a height of approximately 1.5 [m].
- **Sweep:** The sweep was decided to be adjusted in order to have the trailing edge of the winglet match the trailing edge of the wing, as suggested by F. George [30].
- **Wing-winglet angle :** This parameter was manually chosen as 90° (vertical) so as to not increase the horizontal span of the wing which is already high.
- **Airfoil:** The choice of the airfoil was reconsidered since the wing's airfoil was optimized for endurance. In the case of winglets, research by Robert J. McGhee and William D. Beasley provide reasoning behind the use of the NASA/LANGLEY LS(1)-0413 airfoil for winglets [31]. Since the winglet is already a very specific part of the design, the team decided to continue with that airfoil and not to perform a trade-off.

Taking heed of the previous, the effect of the winglets on the lift induced drag can be found using Equation 7.9, with the oswald factor e being 0.82 and assuming a lift coefficient at cruise of 1.35.

$$C_{D_i} = \frac{C_L^2}{\pi e A} \tag{7.9}$$

Initially, using the aspect ratio of 25, the induced drag is 0.0283. Introducing the winglets, the effective span increases by 3 m while the surface area increases only by 1.95 m^2 which causes the effective aspect ratio to become 27.8. Using Equation 7.9 once more but now with the effective aspect ratio and assuming a slightly lower Oswald efficiency factor value of 0.8 to account for the less optimal lift distribution introduced by the winglets yields a lift induced drag of 0.0261. This accounts an 8% decrease in lift induced drag and approximately a 3% decrease in overall drag of the wing.

In order to estimate the structural impact of the winglets, a quick analysis of the forces induced was made, using the dimensions chosen before and assuming that the airfoil was vertically placed at 0° angle of attack with respect to the freestream. Moreover, given that the UAV is made for long endurance and that most of the wing loading will be applied during cruise, the loads induced were calculated for cruise conditions although they are not the most critical on an absolute sense. It was found that the normal force (pointing towards the fuselage) was in the order of 200 N, thus inducing a moment of 90 Nm to the tip of the wing. Note that throughout this analysis it was assumed that the forces act on the mean aerodynamic chord of the winglet which is located at 41% of the height of the winglet resulting in a 0.62 m moment arm from the wing tip. Furthermore, it was calculated that the winglet will experience a drag force of approximately 3.3 N which induces a negligible moment around the wing. As will be seen in Chapter 9 in more detail, the loads applied on the wing are at least 2 orders of magnitude above the loads calculated for the winglet which means that they are negligible in a purely structural sense. The previous also neglects the weight of the winglet which is beneficial during flight since it counteracts some of the lift forces, meaning that the assumption is even more valid if one accounts for the weight as a structural force.

The previous estimations illustrate clear benefits from the use of winglets while introducing very small structural loads. Therefore it was decided that winglets with the aforementioned geometry will be used in the RePLASMA design and an initial illustration is given in Figure 7.13.

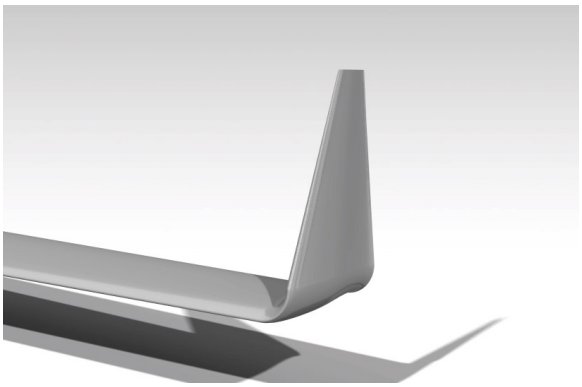

Figure 7.13: A CAD render of the vertical winglet design as attached to the aircraft's wing tip.

To close this section off, it is important to mention the uncertainty of the choice made, as well as how the choice could be re-adjusted. Firstly, recalling the fact that similar HALE UAV's avoid the use of winglets on their design raises concerns that factors not discussed in this section take a big part in the design choice. An important factor not considered due to the complexity of its analysis is the induced vibrations. By introducing extra surfaces on an already slender wing, one runs the risk of inducing unwanted vibrations that can influence the effective loading the wing has to withstand during flight. This may thus be a limiting factor on the size or even the choice of winglets. On the other hand, since the geometry of the winglet was taken mostly from literature, there is plenty of room for optimization. By performing a deeper analysis on the effects of the winglet, also taking into

account vibrations, a better estimate of the structural impact could be obtained and the dimensions of the winglets could be re-adjusted to fit the constraints.

7.5. Cooling & compression

With regards to the propulsion system (of which the design is presented in Chapter 8), there is a sizable interface with aerodynamics. Firstly, the propulsion system requires an inflow of air and an expulsion of emissions in order to operate. Secondly, the engine, along with the compression system both need cooling and therefore a sufficient airflow through the radiators and intercoolers. As a result, both of these aspects must be incorporated and in such a fashion that their aerodynamic implications are the most optimal for the full system. The air-breathing setup of the propulsion is presented in Section 7.5.1 and cooling system is presented in Section 7.5.2.

7.5.1. Intake & exhaust

This section presents the design choices, assumptions and results of the air breathing design of the propulsion system. It presents the intake and exhaust design.

Intake

The intake diameter can be defined in many ways. Amongst these, one possibility is to model the intake and its internal viscous drag for the venting such that the inflow velocity in cruise is equal to free stream velocity in order to minimize pressure drag. While this would likely provide the most optimal design, the scope of the intake design does not involve the design of the venting, and the computation to model the drag losses in the intake would be rather expensive. As a result an approach is applied that is rather rudimentary yet relatively informed. Through the study of similar aircraft (piston powered, high altitude), such as the Boeing Phantom Eye and the Aurora Perseus, and through consulting typical sizes for turbomachinery for piston engines, it was concluded that an inlet area 30% greater than that of the first turbine inlet would suffice as a first order approximation. In subsequent design iterations and elaborations, this value can be used as a starting point and is not expected to change by a substantial proportion.

Once the inlet area (A_{in}) is chosen, and because of the fact that the air mass flow ($\dot{m}_{engine}$) is known as mentioned above, if air density at the air inlet (ρ_{in}) is known, the velocity of the flow into the inlet (V_{in}) can be trivially calculated using the relation Equation 7.10.

$$\dot{m}_{in} = V_{in}\rho A_{in} = \dot{m}_{engine} \tag{7.10}$$

The positioning of the intake directly affects the density of the flow into the intake. The positioning should be such that the flow is as undisturbed as possible and therefore it was decided to place the intake atop the engine cowling, where it can be assumed that the flow conditions are the same as the free stream flow. Finally, using the worst case scenario wherein the flow that reaches the first compressor still has the same density as the free stream flow, and the fact that $\dot{m}_{comp,1}$ (mass flow into the first compressor) should equal the expression Equation 7.10, the ratio w/V_{in} can be calculated to be 0.77. Here w is the velocity of the flow into the compressor.

These results can then be used to determine an optimal shape for the inlet. A condition set for the inlet geometry is to minimise the drag for the given area and w/V_{in} while also ensuring that the boundary layer atop the engine cowling is not ingested into the inlet. The boundary layer thickness on the midpoint of an engine cowling 1 m long is approximated using Equation 7.11. This is the equation presented by Schlichting [32] to estimate the thickness of the boundary layer of a turbulent flow. δ represents the thickness. x is given a value of 0.5 m, and the Reynold's number is calculated to be $3 \cdot 10^5$ using a characteristic length of 1 m. The boundary layer height is then calculated to be 0.015 m. Therefore an inlet that is higher than this level will ensure to a satisfactory level that the flow entering it will be free of the low energy air from the boundary layer.

$$\delta(x) \approx 0.37\frac{x}{\mathrm{Re}_x^{1/5}} \tag{7.11}$$

Finally, a shape can be chosen for the air inlet. For this, Hoerner's work regarding the Fluid Dynamic drag of bodies [33] is consulted. Values for C_D for each inlet geometry are provided as a function

of the w/V_{in} ratio. Hoerner prescribes that the inlet drag can be characterised by two separate coefficients: the momentum drag $C_{D,m}$ and the external drag $C_{D,ext}$. The total drag is then simply shown in Equation 7.12. In order to find the external drag, the plot from Hoerner can be consulted. A digitised version for the chosen geometry in Figure 7.14 is presented in Figure 7.15.

$$C_{D,in} = C_{D,m} + C_{D,ext}$$
$$\text{where} \tag{7.12}$$
$$C_{D,m} = 2 \cdot \frac{w}{V_{in}}$$

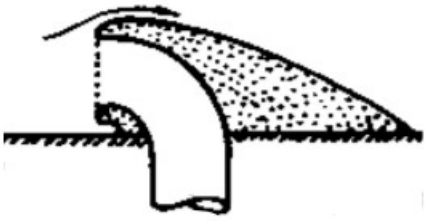

Figure 7.14: Geometry of the inlet for the propulsion system. The inlet is raised from the surface so as to avoid boundary layer ingestion into the compression system. The profile also shows a lip above the intake in order to minimise separation and the formation of an adverse pressure gradient.

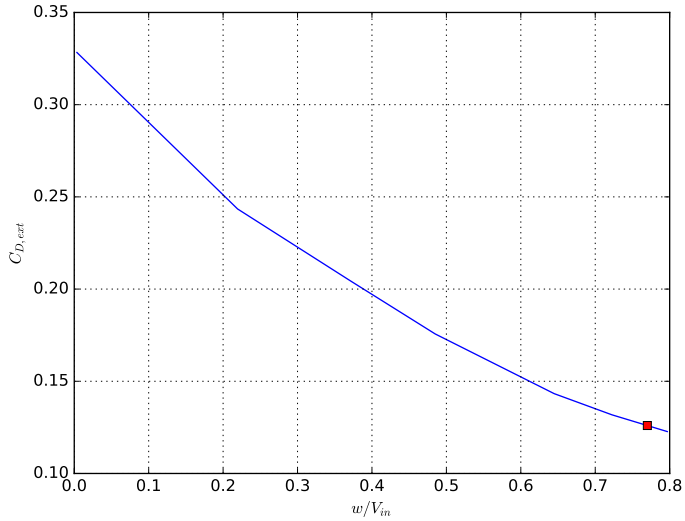

Figure 7.15: The external drag created by the inlet as a function of the w/V_{in} ratio which has the value of 0.77 in this design case. Therefore, the design point, shown by the marker where $C_{D,ext}$ has the value of 0.126.

Finally, the total coefficient of drag for the inlet can be calculated using Equation 7.12 to be 1.67.

Exhaust

The design of the exhaust vent is carried out in a similar fashion to that of the inlet scoop. Again, Hoerner [33] is consulted. The model used to estimate the drag from the outlet is shown in Equation 7.13. w/V, as before, is the ratio of velocity in the outlet to the free stream velocity, $C_{D,ext}$ the external drag which Hoerner provides for each geometry based on experimental data, and $C_{p,out}$ is the suction pressure coefficient at the outlet. The pressure difference at the outlet can greatly affect the drag created by it. The geometry chosen for the outlet is presented in Figure 7.16.

Finally, the drag coefficient of the outlet can be calculated by assuming a value of w/V of 0.5 which mimic some assumptions also made by Hoerner. This can be justified by the fact that while the flow is highly energised as it leaves the cylinders after combustion, it must pass through multiple stages of turbines and it thus loses its velocity such that it is significantly slower than the free stream flow at cruise. As a result, $C_{D,ext}$ and $C_{p,out}$ can be obtained and are equal to 0.1 and -0.2 respectively. The total drag coefficient is then calculated to be 0.8.

$$C_D = 2 \cdot \frac{w}{V} - 2 \cdot \left(\frac{w}{V}\right)^2 + C_{D,ext} - C_{p,out} \tag{7.13}$$

7.5.2. Cooling

The propulsion system of the aircraft requires cooling both for the engine itself, and for the intercoolers in the compression subsystem. For both of these, one cowling is mounted on the wing, located spanwise at the same location as the engine. A cowling is used in order to minimize the air that bypassed the heat exchangers.

Figure 7.16: Geometry of the outlet for the propulsion system. The inlet is not raised from the surface in order to minimise drag and since boundary layer concerns do not apply here.

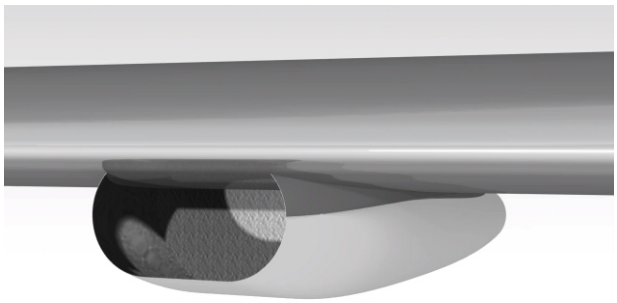

Figure 7.17: A CAD render of the cooling cowling designed.

A divergent-convergent tunnel is employed in order to house the cooling system. The divergence is in order to retard the flow to an extent where the heat exchangers reach their optimal efficiency and the re-convergence is so that the flow can more closely match the velocity outside the cowling to minimize drag losses due to a pressure gradient with a steep change.

In order to maximise the cooling effectiveness of the heat exchangers, the density of the air passing through needs to be maximized. Given that at an ISA altitude of 27 km, the ambient air density is 0.029 kg/m^3, any pressurisation of the air, leading to greater air density, helps. As a result, the cowling is placed on the pressure side (bottom side) of the wing. Furthermore, through the use a simulation based study carried out by Drela [34], it is concluded that it is most effective from a cooling and drag perspective to place the inlet of the cowling at the leading edge of the wing rather than further down the chord length. This study deals specifically, with high altitude, low Reynold's number situations which are directly applicable to RePLASMA. Furthermore, Drela further presents the sensitivity the performance of the cooling has to even small changes in geometry so it can be concluded that a relatively high accuracy model would be needed to design the cooling setup with certainty. As a result, a design reflective of what is expected is produced for sizing purposes, but not to complete the objective of detailed design with calculated interactions.

7.6. Aircraft aerodynamic analysis

After all components of the aircraft are sized, a final lift and drag analysis of the aircraft can be conducted. The components analyzed and the sections in which their aerodynamic design was dealt with are presented in Section 7.6.1. The aerodynamic performance of the aircraft as a whole is presented in Section 7.6.2. The reader should note that all the zero-lift drag coefficients presented for each subsystem are normalized with respect to the wing surface area so as to be able to add them in the end to one final value for C_D that can be directly multiplied by the standard wing surface area to give the total aircraft drag force. This was done by calculating the wetted area of the individual components and dividing it by the wing surface area.

7.6.1. Subsystem analysis

For the subsequent analyses the wetted areas of the individual components had to be estimated in order to be used for the calculation of the skin friction drag. The estimation was initially performed roughly using first-level approximations of the component dimensions. However, since the RePLASMA design is a highly iterative process, at a more converged stage of the design the entirety of the aircraft was made in the CAD software CATIA which was able to accurately calculate the individual wetted areas. The aerodynamic analyses were hence performed twice, with the second time being fairly more accurate. Both of the estimations are given in Table 7.6 for the sake of comparison, however the CAD calculated wetted areas provide a much more accurate estimate and they will be the ones used hereafter.

Table 7.6: Assumed wetted areas and wetted areas given from the precise CAD model for the individual aircraft components in $[m^2]$.

	Wetted area assumed [m^2]	**Wetted area from CAD [m^2]**
Wing	153	147.7
Empennage	43.8	41.7
Engine nacelles	4.3	8.4
Cooling nacelles	3	3.4

Wing and tail system

The estimation of the aerodynamic parameters of the lift-creating surfaces of the aircraft can be performed analytically by using semi-empirical formulas that correct the coefficients of the airfoil for the ones of the 3D wing. For instance Equation 7.14 can be used to correct the airfoil lift coefficient gradient to account for the finite wing span, the wing sweep and other characteristics that are not considered in a 2D airfoil analysis.

$$\frac{dC_L}{d\alpha} = C_{L_\alpha} = \frac{C_l A}{2 + \sqrt{4 + \left(\frac{A\beta}{\eta}\right)^2 \left(1 + \frac{\tan^2 \Lambda_{0.5c}}{\beta^2}\right)}} \tag{7.14}$$

Although the previous formula provides a good estimate for the lift gradient of the wing, it is still semi-empirical and can deviate from case to case. Therefore, it was decided to follow another, more reliable method to estimate the wing-tail group characteristics through the use of a well established testing and simulation software for aviation, AVL. AVL is an extended vortex lattice method solver, finding usage for thin lifting surfaces. Its prime application is for estimation of lift and induced drag, due to the fact that it does not model viscous effects. The wing and the empennage were designed and placed in the program, while the conditions were adjusted manually to fit the mission's cruise conditions.

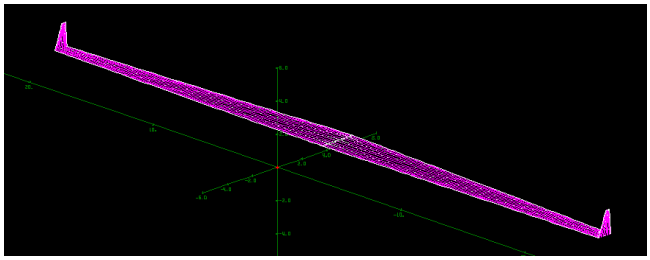

Figure 7.18: AVL model of main wing used to obtain aerodynamic parameters of interest.

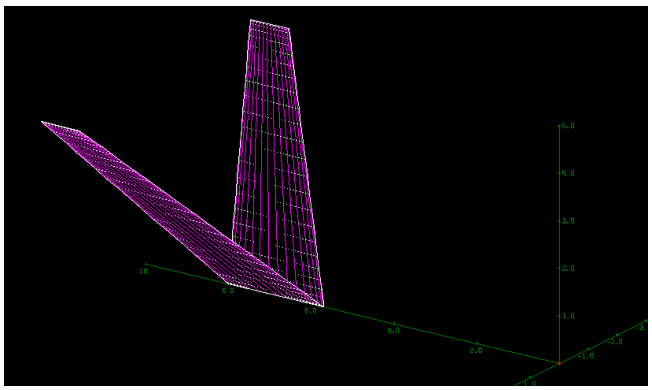

Figure 7.19: AVL model of V-tail used to obtain aerodynamic parameters of interest.

Simulations were then performed for the wing and empennage individually, as well as for their combination, resulting in the graphs presented in Figure 7.20 and Figure 7.21. It should be highlighted that the analysis of the systems individually as well as combined was done purely for verification purposes. It should be noted the the coefficients for the combined wing and tail are the weighted average of the contributions of the wing and tail individually. The weight used for the wing is the planform area and that of the tail in case of lift is the component of area upwards, and for drag is the total planform area of the wing. This is why the difference between the plot for the wing and tail system is not very different from that of solely the wing. There is also the interference the wing causes on the tail that affects the total system, but the main cause of the behaviour of the plots is the weighted average.

The reader should also note that although the lift coefficient is accurate for the mission's realistic range of angles of attack, the drag coefficient only includes the drag induced by lift because skin friction and parasitic drag can not be modeled by AVL. Hence, a different, more empirical approach will be taken to estimate the C_{D_0} of the wing-empennage system.

At this point it is prudent to consider the way the wing is mounted on the fuselage. More specifically, the angle at which the wing is placed with respect to the fuselage, also referred to as the incidence angle, will be discussed. Firstly, an estimate was made of 3.5°, as this provides the optimal lift coefficient for cruise while the fuselage stays at approximately 1° with respect to the freestream flow, thus eliminating the lift induced drag of the fuselage to a high extend. This educated estimation was afterwards verified by using a semi-empirical formula as given by Roskam, which calculated a similar incidence angle [35]. Henceforth, a 3.5° incidence angle will be applied to the design.

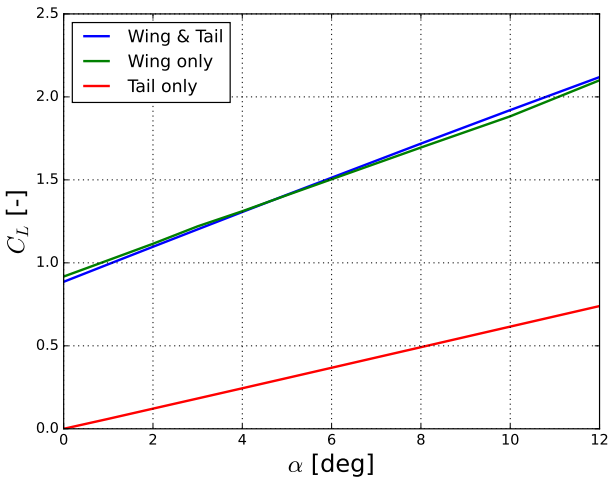

Figure 7.20: Lift coefficient of the wing-tail system for different angles of attack generated by AVL.

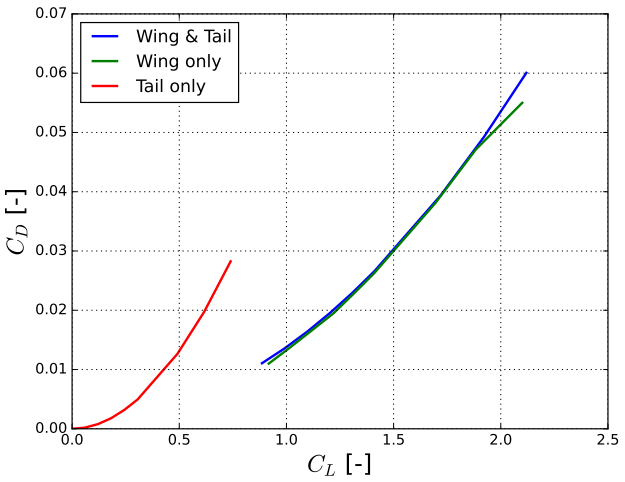

Figure 7.21: Drag coefficient of the wing-tail system for different lift coefficients generated by AVL.

Assuming cruise conditions, the aircraft will be flying with an angle of attack from 4° to 5° which corresponds to a lift coefficient of approximately 1.3 for the wing-tail system according to Figure 7.20. Then from Figure 7.21 the induced drag for that certain C_L is found to be 0.02 and that will be used for the consequent calculations.

With regards to the parasite drag of the wing and the empennage, a statistical approach was followed by assuming the skin friction coefficient based on data from similar aircraft and then multiplying by the wetted area as given in Table 7.6 and then normalizing. Brandt et al. on their paper about semi-empirical models in aircraft design provide a range of friction coefficients with 0.012 being the one chosen for the RePLASMA mission representing high altitude aircraft with a cruise Reynolds number of $5 \cdot 10^5$ [27]. Using Equation 7.15 with the reference wing area being 77 m^2, the wetted area from Table 7.6 for the wing-tail group and the skin friction coefficient C_{fe} discussed above, the normalized zero-lift drag coefficient is calculated and presented in Table 7.7 later.

$$C_{D_0} = C_{fe} \cdot \frac{S_{wet}}{S_{ref}} \tag{7.15}$$

Fuselage

As already discussed in Section 7.2 the square fuselage was chosen in order to minimize drag while concurrently increasing volume area inside it. Figure 7.8 taken from literature showcased the drag coefficient for different angles on attack [23]. Since the fuselage is generally parallel to the freestream, for the sake of simplicity it was assumed that the fuselage does not contribute to lift creation which also implies that induced drag can be neglected with respect to the parasite drag. Hence for the fuselage the value of 0.0028 was taken from Figure 7.8 as the drag coefficient and that will be the value used for consequent calculations.

Propulsion system

The propulsion system includes the nacelles covering the engine and the cooling system, as well as the inlet and outlet ports. Once more, these parts are assumed to not be related to any lift creation so only their zero-lift drag was taken into account.

With regards to the estimation of the drag of the entire propulsion system there are two main assumptions. First assumption is that the impact of the inlet and outlet ports on the overall drag is negligible. This is because although their aerodynamic characteristics are sub-optimal, as discussed in Section 7.5.1, the area they cover is 2 orders of magnitude below the rest of the components which implies that the contribution of the inlet and exhaust to the drag can be neglected[2]. Second assumption applied is that the momentum of the air through the cooling cowlings as well as its losses are neglected. This assumption was taken due to the fact that the mass flow at cruise altitude is little given the very low density. Furthermore, the area of the cowling exit can be adjusted so as to speed the air up to a point where the pressure of the used air matches the ambient. This is done to prevent inflow or outflow from the sides of the exit due to the pressure differences and to ensure smoothness of the outlet air. By doing this, the velocity difference of the cooling air can be minimized thus moderating the momentum drag even more. The reader should note that since the exit velocity of the air after the cooling is unknown, no numerical estimation could be given to support the assumption apart from the theoretical argumentation. Thus, in future stages of the design, this specific assumption should be revisited and, depending on the results, should be implemented in the calculations of the overall drag.

Given the previous, the parasitic drag of the propulsion system can be found using Equation 7.15 where the skin friction coefficient was taken to be 0.012, as justified in the wing-tail group section using statistical data by Brandt et al. [27]. Once again, both the areas of the engine and cooling nacelles given in Table 7.6 were summed up and normalized with the wing surface area to yield the normalized drag coefficient of the entire propulsion system.

7.6.2. Overall aerodynamic performance

All the drag coefficients, zero-lift and lift-induced, calculated previously are summarized in Table 7.7.

Table 7.7: Summary of the aerodynamic drag coefficients of the aircraft.

	C_{D_0}	C_{D_i}
Wing-Tail system	0.0295	0.02
Fuselage	0.0028	-
Propulsion system	0.0018	-

By adding the individual contributions to the drag, the overall drag coefficient can be calculated for the entire aircraft.

$$C_D = C_{D_0} + C_{D_i} = 0.034 + 0.02 = 0.054$$

Evidently, almost 2/3 of the drag arise from skin friction and parasite while slightly more than 1/3 accounts for the drag induced by the lift.

The total lift coefficient, since only the wing-tail contributions were accounted for, is the one given in Figure 7.20 as a function of the angle of attack. The value of the C_L of the entire aircraft is thus

[2]Area approximately 0.2 m^2 compared to 11.8 m^2 of the cooling and engine nacelles as shown in Table 7.6.

strictly calculated with following formula for a given angle of attack measured in degrees [◦]. Note that since AVL is not able to model stall behavior, this formula holds only as the linear part of the lift coefficient thus holding true for the smaller angles of attack.

$$C_L = 0.104 \cdot \alpha + 0.861$$

Figure 7.22 showcases the drag polar of the entire aircraft. The zero-lift drag coefficient as well as the quadratic behavior of the line are clearly visible. Finally, given an angle of attack at cruise of 4.5°, the lift coefficient at cruise is 1.3 resulting in a lift-to-drag ratio at cruise of 23.2.

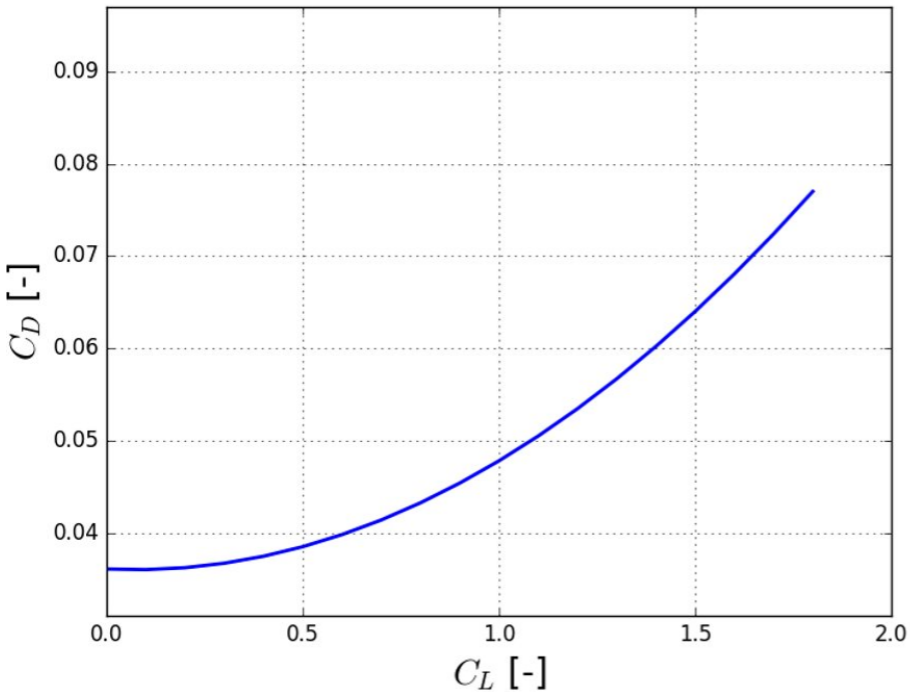

Figure 7.22: The drag polar of the entire aircraft after combining the zero-lift drag with the lift coefficients derived using AVL.

8

Propulsion

The RePLASMA will be designed for intense conditions that not many existing aircraft operate in. At a minimum of 25 km altitude, temperatures drop down to -56.5°C along with air pressure and density which drop to 2.511 kPa and 0.0394 kg/m^3. With such a restricted supply of air, the propulsion system's performance will be severely impacted. Thus a system was designed involving a set of turbocharging stages and a sufficiently powerful engine in order to provide the aircraft sufficient power and thrust at take-off but also to carry on operations for the target endurance of 20 hours.

This chapter starts off with Section 8.1, where a commercially available engine is selected. Following this, Section 8.2 describes the methods used to derive a model for all of the elements of the turbocharging system. The approach to selecting an optimal configuration of these components is then discussed in Section 8.3. An analysis of the selected configuration is presented in Section 8.4. Finally, the development of a fitting propeller is described in Section 8.5.

8.1. Engine

In this section, the selection process for the RePLASMA's propulsion system is discussed. Once the final engine choice is made, its performance under the established mission conditions is analyzed and discussed. Furthermore, the methodology behind the performance modeling is discussed for the sake of verification.

8.1.1. Potential candidates

Continuing from the previous phases, the winning design from the concept trade-off was an aircraft powered by a piston engine running on biofuel. The search for potential engine candidates was then focused on reciprocating engine which make use of alternative fuels to standard hydrocarbon based options. The choice of propulsion system was narrowed down based on off-the-shelf availability in the market. An ideal choice would be an engine that satisfies the operational power requirements and functions efficiently on bio-fuel with a certified service ceiling as high as possible However, due to the uniqueness of this mission and lack of existing designs for this mission, the best choice would be an engine unit that complies with most of these requirements with minimal investment or modifications needed. Table 8.1 shows a subset of the total list of candidates.

During the market analysis, rotary or Wankel engines were previously considered as potential candidates. Wankel engines have a handful of advantages such as a high specific power ratios, high RPMs and more compact compared to standard piston engines [36]. Thanks to their design, the Wankel engines has less moving parts compared to conventional piston engines thus more mechanically efficient and more reliable. It also allows for smoother power delivery and operating at high RPMs for long periods of time [1]. Wankel engines however do suffer from higher heat transfer between the

[1] https://www.carthrottle.com/post/engineering-explained-why-the-rotary-engine-had-to-die/ [accessed 17/6/2021]

Table 8.1: Subset of full list of engine candidates

Engine	Rated Power [hp]	Compression Ratio	Weight [kg]	Bore [mm]	Stroke [mm]	Max RPM	Rated RPM	Num. Pistons	Fuel Type
Ford 5.0L Ti-VCT V8	400	12	180	0.0922	0.0927	6000	6000	8	E87
GM 3.6L V6 LFX	300	11.5	157	0.094	0.0856	7200	3800	6	E86
GM 5.3L V8 Vortec LMF	326	9.6	200	0.09601	0.092	5300	5200	8	E85
TSIO-520-G, M, R	310	7.5	206	0.1334	0.1016	2700	2600	6	100/100LL
TSIO-520-P	310	7.5	206	0.1334	0.1016	2700	2600	6	100/100LL
IO-550-A	300	8.5	207	0.1334	0.108	2700	2700	6	100/100LL,B95/130 CIS, RH95/130
GTSIO-520-D, H	375	7.5	261	0.1334	0.1016	3400	3400	6	100/130
CD-300	296	15.5	265	0.083	0.092	3880	3880	6	Jet A-1
O-470-R, S	230	7	193.6	0.127	0.1016	2600	2600	6	80/87
L/TSIO-360-RB	220	7.5	185.4	0.1127	0.0984	2600	2600	6	100/100LL
CD-230	234	15	198.8	0.126	0.1	2200	2200	4	Jet-A, Jet A1, TS-1
TSIO-550-E	350	7.5	307	0.1334	0.108	2700	2700	6	100/100LL

walls than within the volume resulting in reduced thermal efficiency, further worsened by their lower compression ratios. In addition, their non-optimal combustion chamber shape can lead to quenching; rapid cooling of fuel which prevents burning, resulting in poor emissions [36]. Combined with sealing and leakage issues, making maintenance more complicated, the Wankel engine design was thus removed from consideration in favor of more proven technology.

8.1.2. Selection criteria

The engine selection was conducted based on a set of quantitative criteria and assigned weights. The scores for each option were attributed using the same approach used in the Midterm Report [9]. The quantitative criteria are given scores relative to the parameters allowing them to be used as inputs. For criterion where the maximum value is needed, Equation 8.1 is used, whereas Equation 8.2 is used if the criteria is to be minimised. $\bar{S}_i$ is then the normalised score of candidate i and S_i is the score or value for each option i. The goal of this method is to normalise the scores and to any bias. As a result, in the case of minimizing a criteria such as Engine Weight (in kg), the option with the largest Weight will have a score of 0 being the least favorable and acts as a reference to judge the rest. Similarly, in the case of maximizing a criteria such as Power (in hp), at least one concept will have a score of 1, denoting the best option. Therefore, the best option when maximizing will have a score of 1 and the worst when minimizing will have a score of 0.

$$\bar{S}_i = \frac{S_i}{\max S_i} \tag{8.1}$$

$$\bar{S}_i = 1 - \frac{S_i}{\max S_i} \tag{8.2}$$

In addition to the quantitative criteria, a set of qualitative criteria was also established. These criteria are instead used more as qualitative discussion points in order to assess a certain option outside of its technical aspects. The reason is that a criterion such as emissions is an important factor to consider given the context of this design. However, it also the hardest to quantify outside of the design process. In order to make a more informed technical decision on a certain engine's emission characteristics, extensive testing of said engine in controlled conditions is required, thus outside the scope of this DSE. That being said, certain qualitative conclusions can be made based on the available literature and existing research.

Quantitative Criteria

A trade-off was conducted in order to identify the best option based on the following selection criteria and the assigned weights out of 100:

- **(20) Maximize power:** In order to provide the aircraft with sufficient power to take-off, climb, overcome drag and maintain lift at the target altitude, the powerplant must be able to provide a significant amount of power due to the significant MTOW. Hence, the most powerful engine possible within weight restrictions is favorable.
- **(20) Maximize operable RPM:** During the cruise phase (largest flight segment), the engine should not be operating at maximum RPM for the sake of engine life. Therefore, the engine with the highest RPM rated for continuous operation is more favorable for thrust generation.
- **(20) Choice of Fuel:** One of the goals of this design is to provide a sustainable platform for high altitude missions. Therefore, in the context of engine selection, the candidate that can

provide the right amount of power while compatible with an existing and available biofuel is the more favorable option. As of 2021, there are biofuels with a wide selection of percentages with varying sources of biomass. However, in order for the design to remain in-line with what is commercially available, biofuel such as Synthetic Kerosene, Ethanol of varying percentage such as E85 and Aviation Gasoline Ethanol or AGE-85 are considered. The scoring system regarding fuels is explained in Section 8.1.3

- **(15) Minimize weight:** Along with brake power, a certain engine can weigh considerably while having a significant power output. Therefore, weight as an individual criteria will help avoid selecting an option later considered too heavy.
- **(15) Maximize compression ratio:** Another key parameter when considering a powerplant is how efficiently the system can convert thermal energy in a given fuel via combustion into mechanical energy to rotate the shaft. Thermal efficiency can be assessed based on the the relation shown in Equation 8.3:

$$\eta_{th} = 1 - \frac{1}{\epsilon^{\gamma-1}} \tag{8.3}$$

where γ can vary between 1.2 and 1.4 depending on the fuel-air mixture. However, the key variable is the compression ratio ϵ. The higher the engine's compression ratio, the more thermally efficient the system is, leading to more power extracted and less heat lost to the surroundings which improves the system's cooling capability.

- **(10) Minimize BSFC** The brake specific fuel consumption is a metric that shows how much fuel is burned per work done over a period of time, with units of kg/J or g/kWh or lb/hp-hr. The best engine option is one with the lowest value for BSFC.

Qualitative Criteria

- **Reliability:** Due to the nature of the mission and significant endurance target of 20+ hours of flight time, the powerplant will be subject to high loads for extended periods of time and can lead to operational concerns such as long-term reliability and longevity of the system. Therefore, sufficiently modern propulsion units built with high performance materials are considered in this selection.
- **Technology Readiness Level:** During the previous phases, TRL was a widely used criteria in order to identify and select systems and components that were favorable to the design but also available off-the-shelf. Therefore, only existing propulsion systems readily available from manufactures are included in the list. Engine choices undergoing certification, testing or still in the detailed design phases were not considered as they were internally labeled as "Low TRL".
- **Emissions:** In addition to the choice of a biofuel as part of the design's goals in sustainability, the propulsion system is also expected to produce reduced emissions compared to existing powerplants running on conventional aviation fuels.

8.1.3. Scoring choice of fuel

The market analysis in the previous design phases revealed that synthetic kerosene may be the more favorable choice of alternative aviation fuel as of 2021 compared to aviation gasoline and largely ethanol-based fuels. As of now, aviation kerosene has a viable alternative in the form of synthetic kerosene, which has already been used by airlines like KLM [2]. This alternative fuel seems to be gaining much more traction in the industry compared to AVGAS [37]. The only viable alternative to AVGAS is AGE-85 or ethanol based motor gasoline or MOGAS, primarily used for land vehicles. The main disadvantage of ethanol-based fuel as alternative to low-leaded AVGAS is the modifications a given aircraft piston engine requires to allow efficient combustion. Due to its additives, AGE-85 can cause increased corrosion and damage to certain components, primarily where rubber is found [38]. Thus additional inspection and maintenance is required and the longevity of the engine

[2]https://www.bloomberg.com/news/articles/2021-02-08/klm-makes-first-regular-flight-with-sustainable-synthetic-fuel [accessed 15/6/2021]

may be reduced. As for synthetic kerosene, aircraft which made use of it have reported that little maintenance and modifications were required to operate efficiently with it, hence making it a more compatible alternative to powerplants running on Jet A-1. In addition, the increasing infrastructure and availability for synthetic kerosene can render the RePLASMA design more future-proof.

As for E85, a variety of land vehicles are already certified to use it and operate at nominal conditions. However, compared to kerosene, E85 has a smaller (specific) energy density both in terms of volume and weight. Fischer-Tropsch synthetic kerosene sits at 44.2 MJ/kg and 35 MJ/L where as E85 holds 33.1 MJ/kg and 25.6 MJ/L [39]. This translates to more weight and volume required for E85 compared to synthetic kerosene.

Taking into account all of the above points, the choice of fuel for the engine selection was attributed the following score system: engines running on AVGAS are given a score of 0, E85 a score of 0.5 and engines running on kerosene a score of 1.

8.1.4. Engine selection

Using the previously established criteria, the selection was performed on a reduced list of applicants. The first round of elimination was conducted based on the updated Power & Wing Loading diagram (Section 6.2 Figure 6.1) which revealed a power loading of $\frac{W}{P}$ N/W. Using this value, design's MTOW and converting to horsepower using Equation 8.4 yields the following value.

$$P_{req}\ [\text{hp}] = \frac{MTOW \cdot g}{\frac{W}{P} \cdot \frac{1}{745.7}\frac{[\text{W}]}{[\text{hp}]}} = 434.13\ \text{hp} \tag{8.4}$$

Therefore a total of 434.13 hp is required or a minimum of 217.06 hp per engine. Thus all engines with a power output below 217.1 hp were eliminated.

The second round of eliminations involved removing all engine units that came with a built-in turbocharger. Due to the mission's extreme altitude and operational requirements, the turbocharger configuration needed to be configured in-house using existing compression systems in the market. The closest unit that fit the propulsion system's requirements was the one equipped on the Grob Strato 2C, which reached an altitude of 24 km and was able to break 26 km for a short period of time. Since the Strato 2C's turbocharger was specifically designed for this mission and the unit is not available commercially, the same had to be done for the RePLASMA design. Hence all engines with turbochargers equipped had to be removed in order to accommodate the design's required configuration.

At the third round, candidates were reduced down to three engines initially designed and sold for land vehicles such as cars and SUVs, and three designed for aircraft. These final candidates are shown in Table 8.2 along with their respective specifications.

Table 8.2: Final engine candidates for trade-off

Engine	Brake Power [hp]	Weight [kg]	BSFC [g/kWh]	Max RPM	Compression Ratio	Fuel Type
Ford 5.0L Ti-VCT V8	400	190	318	6000	12	E87
GM 3.6L V6 LFX	300	165	299	7200	11.5	E86
GM 5.3L V8 Vortec LMF	326	200	349	5300	9.6	E85
IO-550-A	300	207	250	2700	8.5	100/100LL,B95/130 CIS, RH95/130
O-470-U	230	191.5	248	2400	8.6	100/100LL
O-470-R, S	230	193.6	283	2600	7	80/87

The trade-off was then performed using the weights listed above in the quantitative criteria list. The scores attributed to each engine unit was calculated using the normalized min-max method previously outlined. Following this procedure, the following results were reached and compiled in Table 8.3.

The winning candidate then revealed to be the GM 3.6L V6 VFX [3] engine block, used in vehicles such as the Cadillac ATS and Chevrolet Impala , both running on E85 as biofuel[4]. The full specifications

[3]https://gmauthority.com/blog/gm/gm-engines/lfx/ [accessed 17/6/2021]
[4]https://afdc.energy.gov/vehicles/flexible_fuel_availability.html [accessed 17/6/2021]

Table 8.3: Results of engine trade-off.
NOTE: The following values are not technical parameters but the score of each engine based on its parameters

Engine	Power	Max RPM	Fuel Type	Weight	Compression Ratio	BSFC	TOTAL
GM 3.6L V6 LFX	***0.75***	***1***	***0.5***	***0.202***	***0.958***	***0.143***	***0.638***
Ford 5.0L Ti-VCT V8	1	0.833	0.5	0.057	1	0.088	**0.634**
GM 5.3L V8 Vortec LMF	0.815	0.736	0.5	0.033	0.8	0	**0.535**
IO-550-A	0.75	0.375	0	0	0.708	0.283	**0.359**
O-470-U	0.575	0.333	0	0.07	0.716	0.289	**0.329**
O-470-R, S	0.575	0.361	0	0.064	0.583	0.189	**0.303**
Weights	20	20	20	15	15	10	**100**

are show below in Table 8.4.

8.1.5. Engine mission performance modeling

Now that a suitable candidate for the RePLASMA's main propulsion system component has been identified, the next step is to simulate the engine's performance under conditions it will certainly meet during a typical mission. To reiterate, according to NASA the main issue any propulsion system at such altitudes is the restricted air supply which in turn will have a major negative effect on the available power output. In other words, the higher the UAV will go, the more the engine will struggle to provide sufficient power and thrust. The goal of the following methodology is to simulate parameters such as power output, shaft torque, required mass flows and fuel consumption at different altitudes and how the system will behave when crossing layers of the atmosphere. The conclusions pulled form this method will also serve as either starting points or design constraints for the propeller design and turbocharger subsystem.

Modeling the performance of a given engine depends on many factors and data that is either not publicly disclosed and readily available or difficult to reconstruct and associate with the RePLASMA's configuration. Therefore, in order to analyze the performance of the engine throughout the mission profile, the starting point had to be based on the most prevalent specifications disclosed by manufacturers. During the market analysis, engine specifications were found to be the most available and reliable as they are either directly provided from the manufacturer or disclosed from reliable sources. For the case of the GM 3.6L V8 LFX, the relevant technical data is shown in Table 8.4 and was provided by GM Authority[5].

Figure 8.1: Winning engine option: GM 3.6L V6 LFX

Table 8.4: Relevant technical specifications for performance modeling

Engine	GM 3.6L V6 LFX
Rated Power [hp]	300
Compression Ratio	11.5
Weight [kg]	157
Bore	0.094
Stroke	0.0856
Max RPM	7200
Rated RPM	3800
Num. Pistons	6
Fuel Type	E85

Using the above as a starting point, performance curves and data was derived using the following procedures based on relations and parameters stated by Ruijgrok [40] and X-Engineer[6].

[5]https://gmauthority.com/blog/gm/gm-engines/lfx/ [accessed 22/6/2021]
[6]https://x-engineer.org/automotive-engineering/internal-combustion-engines/performance/brake-specific-fuel-consumption-bsfc/ [accessed 23/6/2021]

PV Diagram Simulation & Power Output: Based on the bore and stroke of the engine's cylinders, the pressure and temperature of the air at the intake and an assumed maximum temperature of $1200°K$ inside the cylinder during combustion, the work done per cylinder W_i can be found by taking the area under the curves during compression and expansion. Using the work done per cylinder, the indicated power P_i is found using the engine speed or RPM and the number power strokes in one second, which in this case is two. Then, the brake power of the engine is the indicated power per cylinder multiplied by the number of cylinders. In addition, the effective pressure and output torque is computed, where n_r and n_m are the number of power strokes per second (2 in the case of a 4-stroke engine) and the mechanical efficiency of the engine respectively, assumed to be 0.9. The PV diagram was recreated in Python[7] following principles in literature.

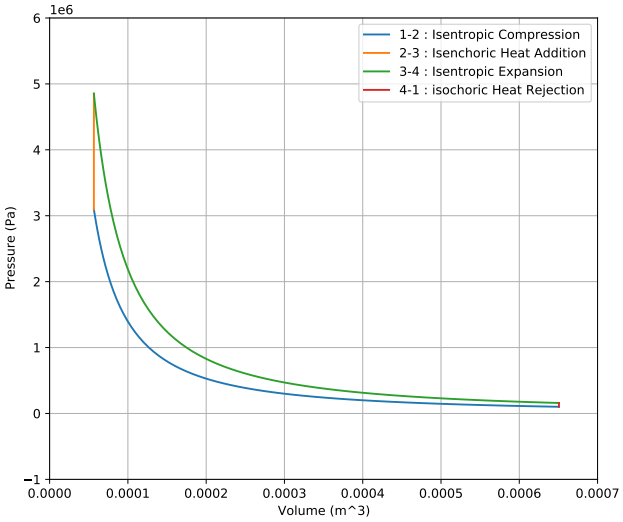

Figure 8.2: P-V diagram of simulated power stroke within cylinder.

$$W_i = \oint pdV \tag{8.5}$$

$$P_i = W_i \frac{n}{2} = W_i \frac{RPM}{2 \cdot 60} \tag{8.6}$$

$$P_{br} = N_{pist} P_i = N_{pist} W_i \frac{RPM}{2 \cdot 60} \tag{8.7}$$

$$BMEP = n_r \frac{n_r P_{br}}{V_d \frac{RPM}{60}} \tag{8.8}$$

$$T_e = \frac{p_{me} V_d}{2\pi n_r} \tag{8.9}$$

Intake Manifold: A recurring issue when computing the brake power output was that the power found at sea level conditions was consistently lower than the rated power given by the manufacturer. Rated power is documented after testing and certification under real conditions and not found analytically, thus should be the starting power when computing power output at sea level. After consulting Heywood [41], based on engineering judgment, the propulsion team then concluded that certain pressure losses before reaching the piston are the culprit and thus the function of the engine's intake manifold must be accounted for. Since the exact compression ratio of the intake manifold is not stated and may vary in certain conditions, it is assumed that the manifold is simply a convergent duct that further passively pressurizes the air by a relatively small factor. The method involved taking the initial power output and correct it by multiplying the intake pressure by a factor ranging from 1 to 2 found via iteration until the difference between the two power outputs was within 1%. The resulting intake manifold compression factor was approximately 1.1525.

Engine Consumption: Carrying over the indicated power Pi, the next steps is to calculate the air mass flow at a certain RPM. The mass flow is a function of the number of pistons and volume, RPM, gas parameters of air and volumetric efficiency of the piston, as outlined by Equation Equation 8.10. Subsequently, the fuel mass flow required, Equation 8.11, is based on the given fuel's stoichiometric air-fuel ratio AFR_{st}, which is 9.733 for E85. Hence the model assumes that combustion continuously takes place with the minimum amount of air, not lean (more fuel) nor rich (more air). Burning rich results in a colder and less pollutant combustion but less efficient and converse is true when burning rich. A balance of efficiency and reduced pollution can be reached if the AFR within the piston is maintained at the stoichiometric ratio as much as possible [41]. Furthermore, using the mass flows and power output, the brake specific fuel consumption or BSFC can be computed using

[7] https://skill-lync.com/student-projects/OTTO-CYCLE-PV-DIAGRAM-AND-THERMAL-EFFICIENCY-69250 [accessed 23/6/2021]

Equation 8.12, which is a measure of fuel consumed per unit of work done. The lower this value, the more fuel efficient the system is.

$$\dot{m}_{air} = \frac{N_{pist} \cdot V_{pist} \cdot RPM \cdot P_s \eta_{vol}}{120 \cdot R \cdot T_s} \quad (8.10) \qquad \dot{m}_{fuel} = \frac{\dot{m}_{air}}{AFR_{st}} \quad (8.11) \qquad BSFC = \frac{\dot{m}_{fuel}}{P_{br}} = \frac{\dot{m_{fuel}}}{T_e \omega_{eng}} \quad (8.12)$$

Mission Performance: The engine's performance, provided by the previous relations, is then plotted for every condition as a function of altitude and RPM. The first series of plots show the brake power and engine mass flows as a function of operating altitude and RPM for the target altitude of 25 km.

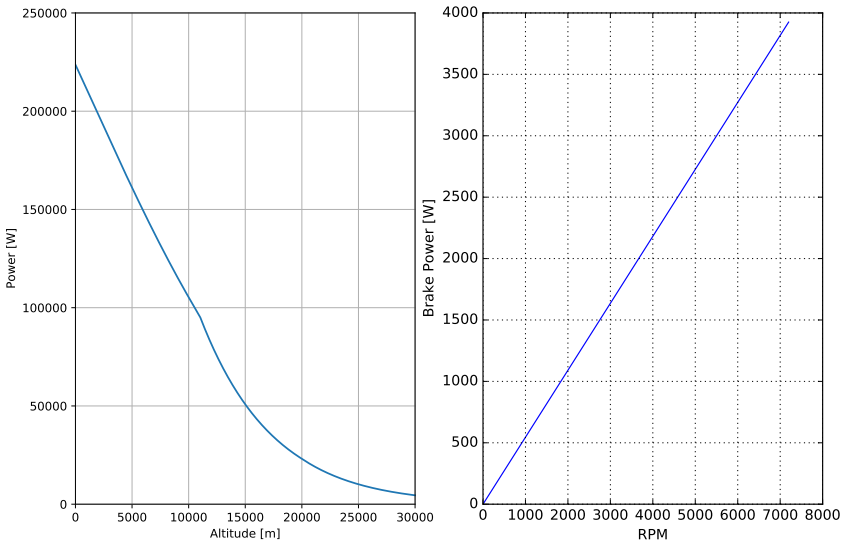

Figure 8.3: First series of engine performance as function of altitude and RPM.

Looking at the first (left) plot, it can be seen that the power output does decrease with altitude quite rapidly and levels off when reaching the mission's maximum altitude. This is due to the exponentially decreasing air supply when climbing which is generally the most significant constraint when operating at high altitude. During the turbocharger design, a key parameter will be the power required from the engine throughout the flight. Power required is based on aircraft parameters and signifies the required power needed to overcome aerodynamic drag and is found using Equation 8.13.

$$P_{req} = \frac{1}{2}\rho V^3 S C_{D_0} + \frac{W^2}{\frac{1}{2}\rho V S}\left(\frac{1}{\pi A e}\right) \quad (8.13)$$

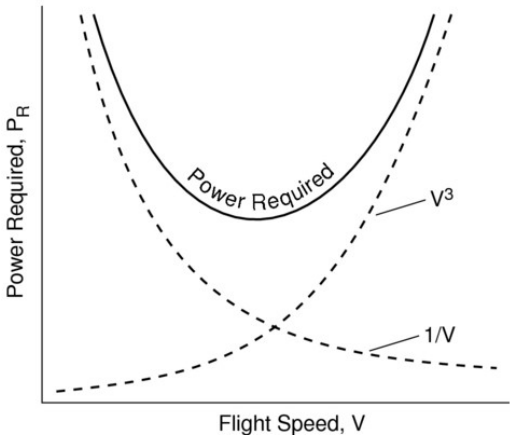

Figure 8.4: Power required as a function of airspeed according to Equation 8.13

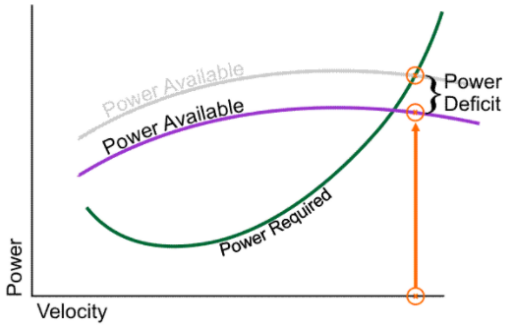

Figure 8.5: Power available vs power required as a function of airspeed

As can be seen from Equation 8.13 and Figure 8.4[8], the power required is mostly dependent on airspeed since it is proportional to V^3. It does decrease with decreasing density but at a much slower rate compared to the influence of airspeed since the increasing power required is due to the increasing magnitude of parasitic drag (the V^3 curve). Hence there is a certain altitude where the decreasing power output and increasing power required will match and power available is insufficient beyond that. This is shown on Figure 8.5[9]. This is considered to be the absolute ceiling; when the aircraft cannot generate enough power to avoid stalling due to the increased drag. Luckily, due to the aircraft's relatively low weight (compared to the Grob Strato 2C) and highly optimized aerodynamics, the power required will decrease due to the decreased C_{D_0} term in Equation 8.13, however the driving factor will remain the airspeed. Given conditions at an altitude of 25km and a target cruise speed of Mach 0.5, the power required will be in the order of 200 kW; leaving only a small margin of 22 kW. To overcome this issue, increased power delivery is achieved by pressurized air equivalent to sea level conditions fed into the engine inlet during operations [42]. Said air mass flow will be provided by the turbocharger system, explained in Section 8.2.

The second (right) plot shows how the power output varies with RPM at the target altitude. As can be seen the power output is linear with RPM, as expected from Equation 8.7. Note that at maximum RPM for this altitude, the highest power output reached remains about 85% of the maximum rated power due to the restricted air supply. Continuous operation near maximum RPM is highly detrimental to the longevity of the engine. Therefore, the cruise segment will be conducted at the rated RPM between 4800 and 6500, thus providing between 220 to 300 kW depending on thrust and propeller design restrictions, assuming the turbocharger can provide sufficient pressurized air to reach power outputs equivalent to sea level.

The second series of plots shows relations between Brake Mean Effective Pressure or BMEP, BSFC and Engine Mass Flows. The first (left) plot shows the relation of BSFC with BMEP. BMEP is a parameter, independent of piston displacement, used to assess the piston's capacity to produce work [41] and can be interpreted as a sort of "specific torque". According to Heywood [41], optimal values of BMEP for naturally aspirated 4-stroke engines lies within the range of 10 and 12 bar when operating at the maximum RPM for maximum Torque, which is where the lowest fuel consumption can be seen in Figure 8.6.

The second (left) plot show the mass flow of air (blue) and fuel (orange) as a function of altitude assuming the engine operates at maximum RPM. This plot will serves to identify the maximum mass flows the engine will experience to determine not only the fuel consumption but also provide mass flow requirements for the turbocharger system to satisfy to maintain mass flow continuity throughout the altitude profile. Assuming the turbochargers must provide air mass flows equivalent to sea level conditions, then the air mass flow requirement shows to be 0.27 kg/s for a power output near 300 hp (223 kW). As for fuel, the associated mass flow is assumed to continuously remain at

[8]https://web.mit.edu/16.unified/www/FALL/thermodynamics/notes/node97.html [accessed 23/6/2021]
[9]https://flightacademy.info/aviation-power-curves [accessed 23/6/2021]

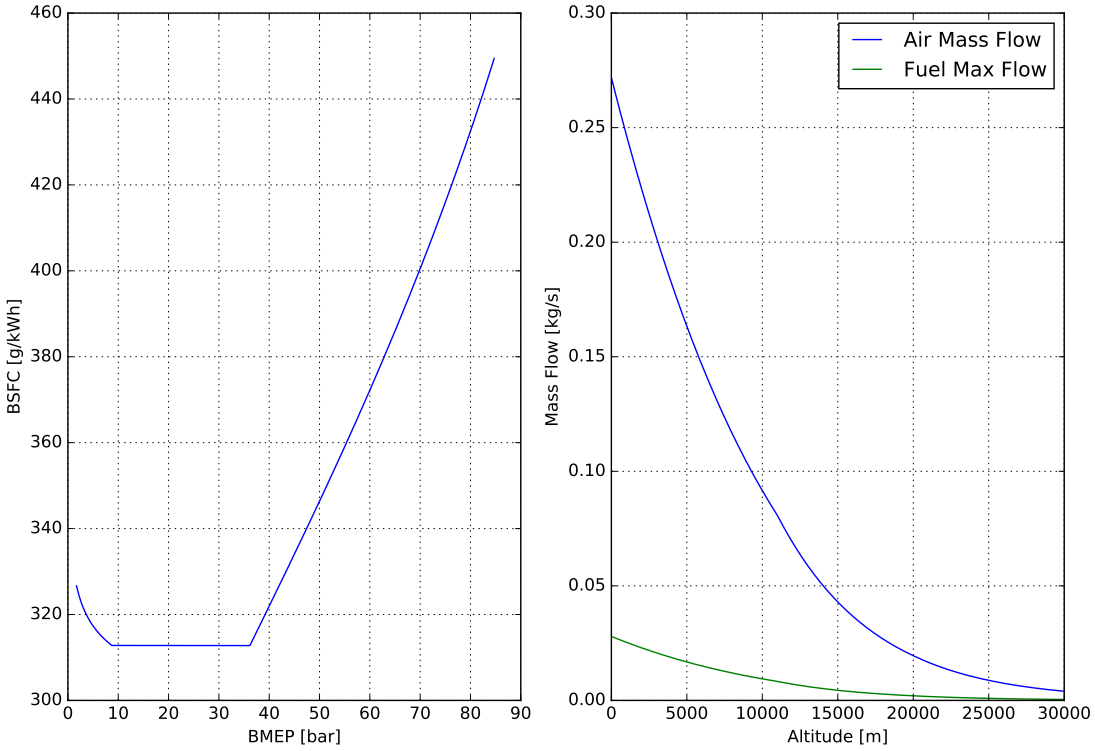

Figure 8.6: Second series of engine performance plots showing BSFC, BMEP, RPM and Power output.

the stoichiometric ratio of the fuel, which is 9.733 to 1.

BSFC Contour Map: An additional method was implemented to simulate the BSFC's contour map. This is generally used to identify the point of lowest consumption during engine operations. Figure 8.7 is BSFC contour map simulated for the GM 3.6L V6 LFX using the relations shown in Equations 8.10, 8.11 and 8.12.

The BSFC contour map serves to identify which engine conditions result in the best fuel economy. Referring back to Equation 8.12, when plotting against RPM and Torque, the ares with the lowest values of BSFC can be identified and allow for a more precise definition of the engine's operating profile in order to properly assess the amount of fuel required to achieve 20 hours of endurance for the cruise segment. BSFC remains constant with RPM while increasing when output torque is decreased. The lowest areas, highlighted in purple show the operating conditions where minimum fuel consumption is reached. The design's fuel consumption will depend on the propeller requirements, later discussed. However, a preliminary estimate on the maximum BSFC required to achieve the mission's requirements is made here below:

$$BSFC_{limit} = \frac{\dot{m}_f}{P_{req_{cruise}}} = \frac{0.01388}{200 \cdot 10^3} \frac{[\text{kg/s}]}{[\text{W}]} \cdot 3600 \cdot 10^6 = 249.84 \text{ g/kWh} \tag{8.14}$$

assuming a power required of approximately 200 kW when in cruising at Mach 0.5 at 25 km with an air density of 0.0394 kg/m^3 and assuming 1 ton of fuel is available at the start of the 20+ hour cruise segment. A value lower than that above will lead to less fuel consumption and more left in reserve.

Despite providing a useful perspective on engine performance, the fuel consumption contour in this form is quite limited and does not completely reflect reality. The limitations of this tools are explored in Section 8.1.6.

Emissions and E85: One of the driving requirements behind the RePLASMA design is the use of

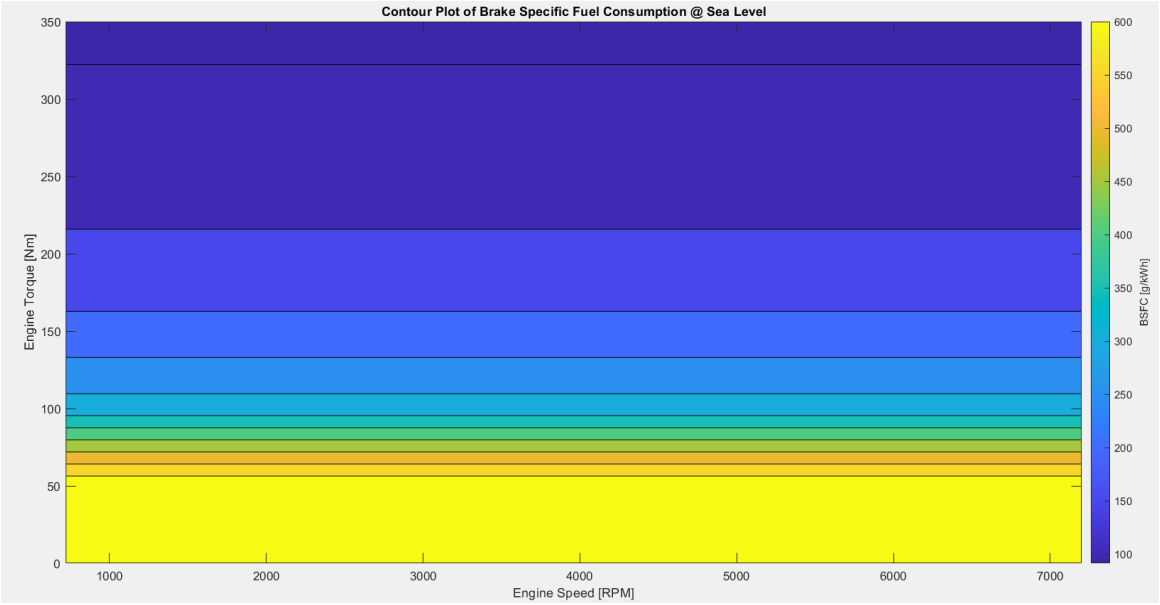

Figure 8.7: Simulated contour map of BSFC as function of Torque and RPM.

alternative fuel source. As stated in previous chapters and sections, the winning design was a reciprocating engine running on biofuel. Options included synthetic kerosene, ethanol mixtures of gasoline and hydrogen. While the gran majority of piston engines used in general aviation, the dominant fuel source in the market was AVGAS 100 or 100LL (Low Lead). However, after much research, there is yet to appear a suitable biofuel alternative to AVGAS which completely eliminates lead and has existing infrastructure. This is one of the criteria that worked ion favor of the GM 3.6L V6 LFX; a mass-produced and available piston engine certified to run on Ethanol E85 as biofuel. The use of a higher blend of ethanol with gasoline such as 85% for E85 according to G. Martini et al [43], showed a significant decrease in CO, NO_X and other volatile organic compounds emissions compared to conventional gasoline, further stating that said emission are well below the limit of the relatively stringent Euro 4 emission regulation. That being said, it was stated that the repeatability of these measurements was considered poor, most likely due to the complex engine management systems found in certain models. For a more precise analysis of the potential emissions of this design, testing and experimental data will be required.

8.1.6. Modeling limitations and assumptions

Despite performance data being within adequate ranges, the modeling methodology above is not a one-to-one representing of real-life conditions. Certain assumptions were made to simplify calculations and results do not account for other potential losses, transient behaviors and other unforeseen fluctuations in the system. The following points will discuss the assumptions and likely sources of error which could have affected the results.

Modeling combustion: The performance information derived from the specifications of the engine(s) is all based on the simulated Otto Cycle using the P-V diagram and relations. This is not however fully representative of the process within a piston stroke. The combustion process taking place is generally not perfect; other chemical interactions and products can appear due to trace amounts of other substances that may be found within a given volume of air at the intake. Combustion within a piston engine takes place between fuel and oxygen. However within the atmosphere, air is not purely made of oxygen; a significant percentage is nitrogen, leading to NO_X, and other gases are present in small amounts. Therefore, the combustion process is rarely ”clean” due to new products appearing and affecting the fuel conversion efficiency. In addition, the air-fuel mixture within the piston may not be completely homogeneous which then leads to unburnt hydrocarbons in the exhaust and contribute to further energy loss[10]. Due to the fact the performance models used in during this

[10]https://x-engineer.org/automotive-engineering/internal-combustion-engines/performance/engine-combustion-process-explained/ [accessed 24/6/2021]

design process, the energy extracted and exhaust properties will carry some level of error.

Modeling BSFC: When comparing contour maps from existing engines, it is clear that the fuel consumption does not behave continuously. When comparing the following contour map from experimental data, Figure 8.8[11], to that of the GM V6's contour map found numerically, Figure 8.9, it can be seen that the simulated map has a more homogeneous surface since it depends on linear relationships between engine torque and RPM. Though the magnitude of the fuel consumption does sufficiently coincide, exact areas of minimum fuel consumption are harder to discern since they seem to occupy the entire surface band at higher torques, which is not fully the case in Figure 8.8 where discernible "islands" can be seen on the surface denoting the optimal operational regime. This disparity between the two surfaces is due to the fact that the numerical model used cannot fully account for inefficiencies throughout the system, further emphasizing the BSFC contour map's dependence on experimental data as tool for performance insight. A discussion on whether these results are sufficiently valid is found in Section 8.1.7.

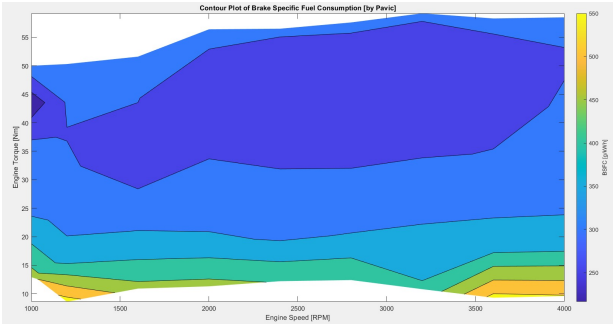

Figure 8.8: BSFC contour from experimental data

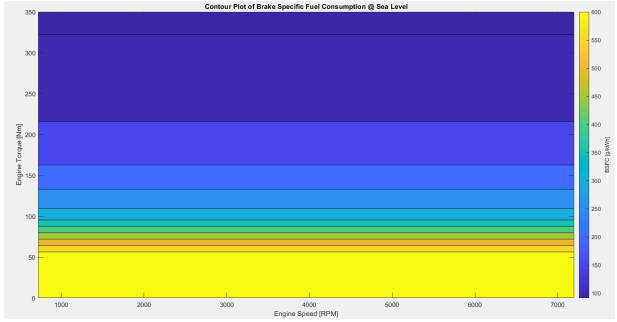

Figure 8.9: Simulated contour map of BSFC as function of Torque and RPM.

Pressure losses within engine: Referring back to the method of simulating the intake manifold, this solution was implemented to match the initial conditions and outputs provided from the engine's specifications. In other words, the output power at sea level under maximum RPM is assumed to be the maximum brake power the engine can provide. Hence an initial power loss was considered error and correct by accounting for the engine's internal characteristics. Applying a small compression factor attributed to the engine manifold did manage to bridge the power gap to within 1% of the specified maximum. However, the Propulsion Dept. does acknowledge that other potential pressure losses are possible.

Estimation of increased fuel consumption: Referring back to the issue of other potential losses, such fluctuations can also alter the air-to-fuel ratio within the piston at a given stroke. In reality, the mixture within the piston may not always exactly equal to the stoichiometric AFR; some fluctuations occur due to additives in the fuel that can increase oxygenation in the process or contaminants in the air that can affect the chemical process during combustion and result in wanted or foreign particulates within the engine and in the exhaust. That being said, most engine management system come equipped with sensors to monitor oxygenation rates and offset the difference by increasing the fuel mass flow, thus affecting fuel consumption[12].

8.1.7. Verification

This subsection focuses on results of verification procedures performed on the numerical methods outlined in the previous section. Simplifications were made and assumptions taken in order to aid the design process and are discussed in Section 8.1.6. The following paragraphs will explain certain tests and supporting data in order to justify that the results of the numerical model follow the expected relations and are sufficiently within the bounds of accuracy in the context of the design process.

ISA model via ADRpy: During performance modelling, when looking at parameters as a function of altitude, the atmosphere gas state variables are required; pressure, density, temperature and speed

[11] https://nl.mathworks.com/matlabcentral/answers/6071-how-to-create-a-contour-plot-for-bsfc-using-the-data-for-rpm-torque-and-bsfc-on-matlab [accessed 23/6/2021]
[12] https://www.bosch.com/stories/40-years-of-bosch-lambda-sensor/ [accessed 24/6/2021]

of sound. These parameters are retrieved from a numerical model of the International Standard Atmosphere written in Python as part of the ADRpy[13] package. For this unit test, parameters at sea level, 1 km, 10 km and 25 km provided from ISA data[14] will be compared with the output of the ADRpy Atmosphere model. If the outcomes are within 1%, then the test is passed.

Table 8.5: Results on verification of ADRpy atmosphere model.

State Variable	Value from ISA	Value retrieved from ADRpy	% Difference
Temperature [K]	221.65	221.65	0
Pressure [Pa]	2511	2511.0134	5.3365 x 10-4
Air Density [kg/m^3]	0.0395	0.039465	0.088

As can be seen from the results in Table 8.5, the Atmosphere model provided by ADRpy is sufficiently accurate as a source for atmospheric state parameters.

PV Diagram simulation The work done by piston during combustion follows the dynamics of an Otto Cycle. This cycle is best presented in the form of a PV diagram, where the pressure and volume of the space inside the cylinder is plotted at each stage of the combustion cycle. From principles of thermodynamics, it is expected to see an isentropic (constant entropy) contraction of the volume, followed by an isochoric (const. volume) pressurization and heat release, rapidly followed by an isentropic expansion where no heat is lost and only work is performed, ending with an isochoric heat and pressure release, returning to the original starting point[15].

This unit test will involve a qualitative comparison between the program's output and PV diagram generated for a 4-stroke diesel engine [44].

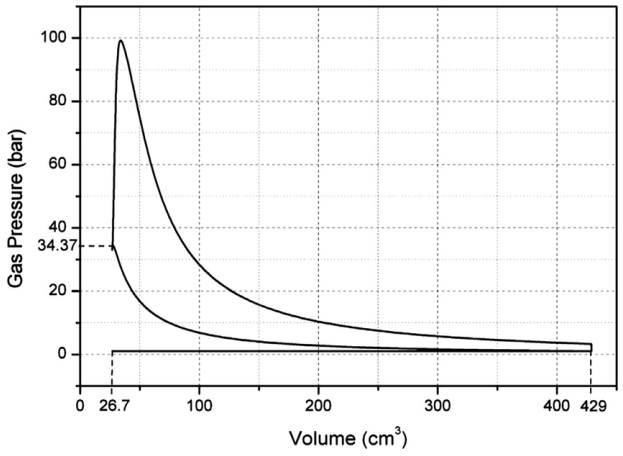

Figure 8.10: PV diagram of four-stroke diesel engine

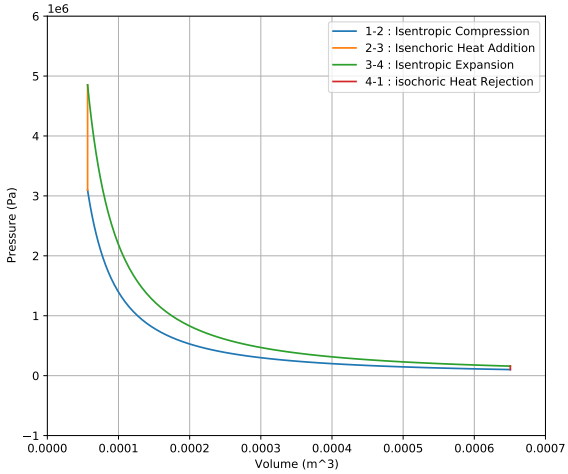

Figure 8.11: PV Diagram simulated by numerical model

When comparing both diagrams, all phases of the Otto Cycle can clearly be observed during the engine strokes. In addition, the combustion and heat release phases also occur without any (major) volumetric expansion, thus suggesting that the model does maintain a (sufficiently quasi-) isentropic process. Based on the large similarity with the results above and that the PV diagram shows the expected behaviour, it can be concluded that the PV diagram simulation is sufficient in order to model a given piston engine's power output with reasonable accuracy for the design process.

Intake Manifold The role of the "intake manifold" component is to compensate for any pressure loses from the engine intake to the piston. Power outputs lower than the expected max brake power were seen and thus need to be corrected. Since the intake manifold is just a passive component and

[13] https://github.com/sobester/ADRpy [accessed 24/6/2021]
[14] https://www.eoas.ubc.ca/courses/atsc113/flying/met_concepts/03-met_concepts/03a-std_atmos/index.html [accessed 24/6/2021]
[15] https://www.grc.nasa.gov/www/k-12/airplane/otto.html [accessed 25/6/2021]

assumed to act as a convergent duct, based on engineering judgement the equivalent compression ratio required is expected to be no larger than 1.5.

The following unit test will verify that the numerical model does output a given engine's maximum power output within 1% of the expected rated power. For this test, a random set of engines will be chosen from the previously extensive candidates list.

Table 8.6: Verification of intake manifold component in model.

Engine	Rated Power [kW]	Corrected Power Output [kW]	% Difference	Intake Manifold Ratio
Ford 5.0L Ti-VCT V8	298.3	298.2068	0.0312	1.314
TSIO-520-P	231.2	231.07	0.0562	1.554
TSIO-520-EB	223.7	223.562	0.0616	1.504
O-470-U	171.5	171.421	0.0460	1.349
IO-550-A	223.7	223.591	0.0487	1.340

From these results, it can be seen that the all engines' power outputs match their rated brake power within 1% while the intake manifold compression ratio remains well between 1.0 and 1.5 with the exception of engine models equipped with turbocharges which are just slightly above 1.5. Based on these results, the propulsion team agreed this is an acceptable correction method.

Engine performance The engine performance plots do also suffer from the same inherent inaccuracies. Most of the limitations behind the methodology revolves around the issue of lack of experimental data and factors not accounted by analytical relations that can be observed in real-life conditions. However, most relations do sufficiently hold in order to acquire a first-order approximation of an engine's characteristics in certain operating conditions. The following is a series of comparisons with the resulting plots above and plots obtained from experimental data.

Looking at the pair of plots below,Figure 8.12[16] shows Power (in red) as a function of RPM for a 6.2L HEMI Hellcat engine. Though the line is not completely smooth, it does show a linear relationship and an extremely similar slope, as implied by Equation 8.7. The main difference is the behaviour at the end points, where Figure 8.12 does not completely cover, Figure 8.13 does extend to zero, most likely due to unsustainable combustion at lower RPM.

[16]https://gomechanic.in/blog/bhp-vs-torque-difference-explained/ [accessed on 2021-06-19]

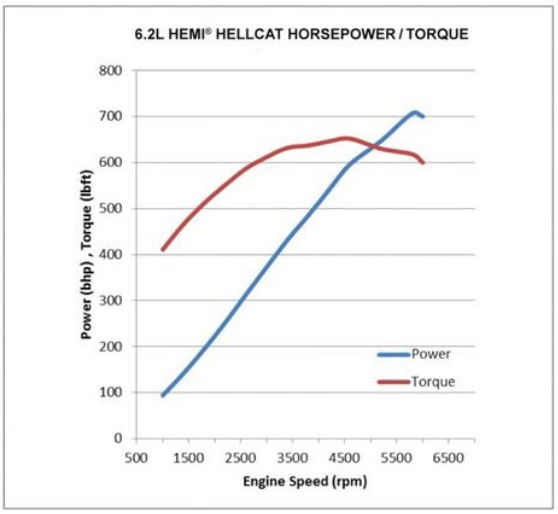

Figure 8.12: Power vs RPM plot for 6.2L HEMI engine.

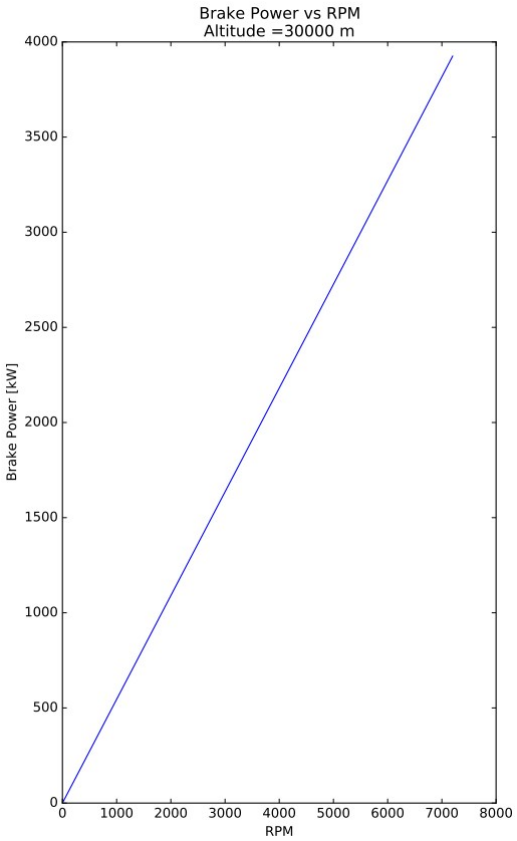

Figure 8.13: GM V6 Brake power as function or RPM.

Furthermore, looking back at Figure 8.6, the BSFC-BMEP plot follows similar characteristics. Below is a side-by-comparison between the same plot and one generated on experimental data on an diesel engine running on hythane gas [45]. Both plots show values of BSFC quickly followed by a decrease as the BMEP increases. Eventually a plateau is reached at a certain BMEP range, where the most fuel efficient operating condition is found. Both of these characteristics can be observed in Figure 8.15. However, one differentiating attribute is the fact that the BSFC suddenly starts to climb at high values of BMEP, specifically past 30 bar. In practice, conditions past 30 bar are not reached and not for extended periods of time; Figure 8.14 does not exceed a BMEP past 4 bar. That being said, this does offer insight on which conditions are considered optimal and which potential conditions can be highly detrimental to the mission. All in all, the numerical model's ability to approximate said relations given the selected engine is considered to be acceptable based on the above.

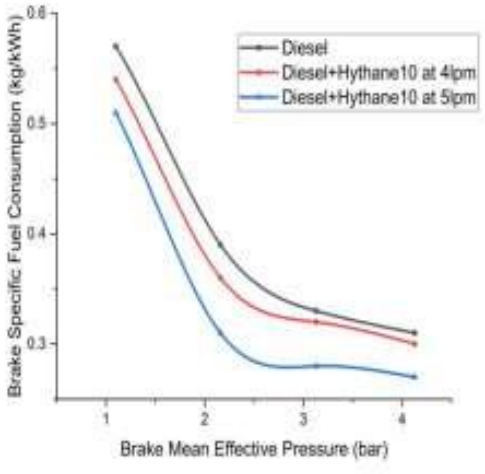

Figure 8.14: BSFC as function of BMEP of hythane-fueled engine.

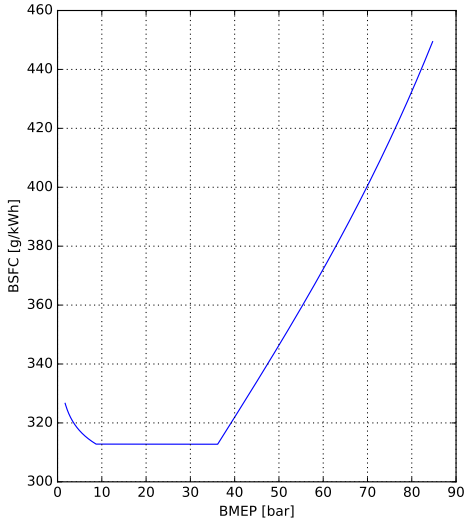

Figure 8.15: GM V6 BSFC as a function BMEP.

BSFC Contour Map: Further study into the literature revealed that despite BSFC having a straightforward relations with other parameters, those equations do not fully represent real-life conditions and that generating a contour map heavily relies on experimental data and measurements acquired during testing, as mentioned previously in Section 8.1.6 and which the team sadly does not have access to since it is out of the scope of the DSE. That being said, the contour map generated for the GM V6 engine is a more simplified approximation. The following is a side-by-side comparison of a contour map generated during an EPA benchmark of a Toyota engine [46] and a map simulated for the GM 3.6L V6 LFX.

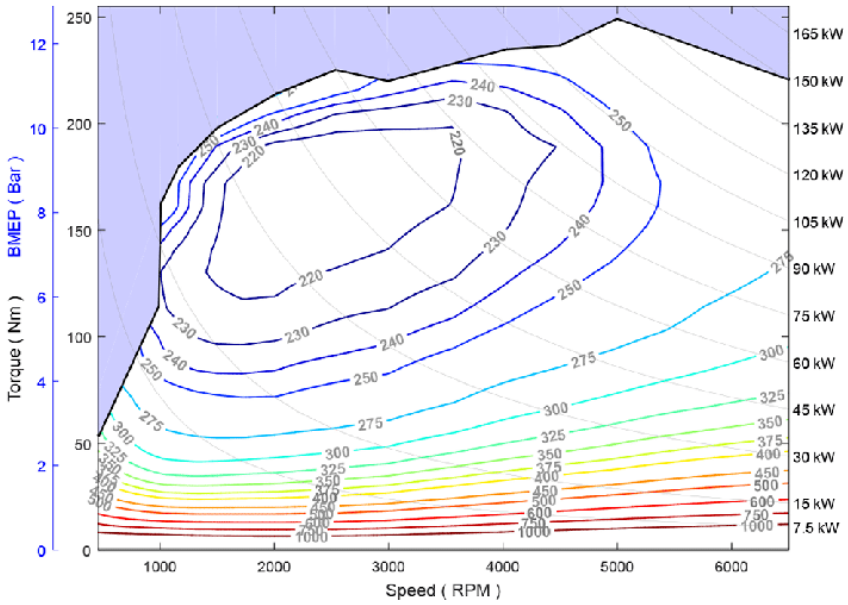

Figure 8.16: Contour map of BSFC as function of Torque and RPM from EPA tests of Toyota engine

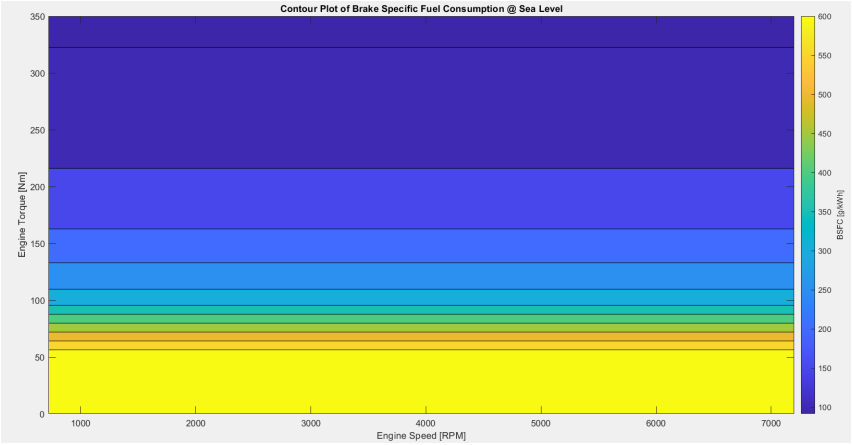

Figure 8.17: Simulated contour map of BSFC as function of Torque and RPM.

As can be seen, the BSFC of the GM V6 follows the same general physical behaviour as that seen in [46]. BSFC remains relatively constant with RPM at lower torque values. The lowest areas, highlighted in purple show the operating conditions where minimum fuel consumption is reached, generally found in the upper half of the Torque axis. The same areas can be seen in Figure 8.17 relatively within the same region of RPM and torque. However, it must be noted that the model in Figure 8.17 only represents ideal conditions, resulting in the smooth continuous surfaces and requires experimental data in order to be properly validated. The contour map shown in Figure 8.16 is plotted the same way but the points were recovered from measurements retrieved during emission benchmark tests, thus show more sudden dips and a more precise definition of the contour surface due to fluctuations, intake fluid properties and likely mechanical and thermal losses usually seen in real-life operating conditions. That being said, given the output magnitude and relations of the GM V6's contour map with these parameters and its significant similarity with Figure 8.16, the

Propulsion Dept. concluded that this model does provide useful insight and information regarding fuel consumption within an acceptable margin of error for the sake of the design process.

8.2. Turbocharger system

The established engine model suggests that the performance of the engine will decrease significantly with decreasing intake pressures and increasing temperatures. Due to the extreme altitudes at which RePLASMA will operate, a high-performance turbocharging system is necessary to compress the air in such a way that the engine can develop the power required. For the case of a reciprocating engine, the turbocharger system will have to provide a certain mass flow of pressurized air at the engine inlet equivalent to sea level conditions to allow the proper functioning of the engine at flight altitude [42].

According to the ICAO atmosphere model, the air pressure at 25km is a factor of 40 smaller than at sea-level. Current high-performance compressors can efficiently reach pressure ratios of around 2-4[17].

The total pressure ratio can be computed with Equation 8.15, where i is the amount of stages. Using this information, the amount of serial stages can be estimated to be at least three.

$$\Pi_{C_{tot}} = \Pi_{C_n}^{i} \tag{8.15}$$

Furthermore, due to the temperatures generated during compression, the air flow must be additionally cooled by intermediate inter-coolers in order to maintain a high power output. The justification for inter-coolers is provided in Section 8.2.5.

Figure 8.18 presents a tentative compressor configuration with two parallel compressors at the intake, being the assumed design for the parallel 3-stage option. An alternative configuration could be one where there is only one compressor at the intake, which is the assumed serial 3-stage design option. Both of these configurations and more will be taken into account during the design.

[17] https://www.garrettmotion.com/racing-and-performance/performance-turbos/ [accessed 25/6/2021]

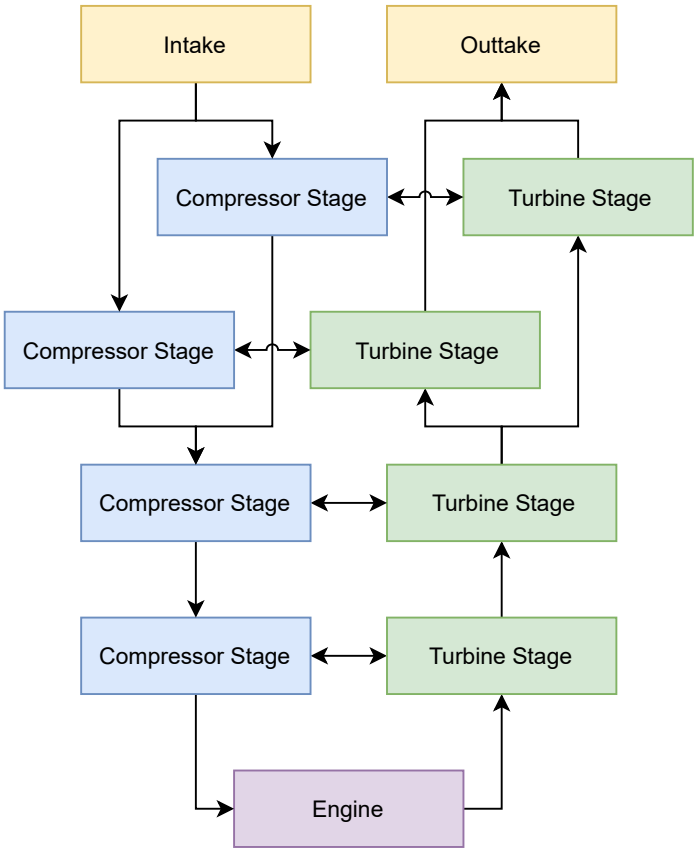

Figure 8.18: Tentative 4-stage turbocharger configuration for a compressor option.

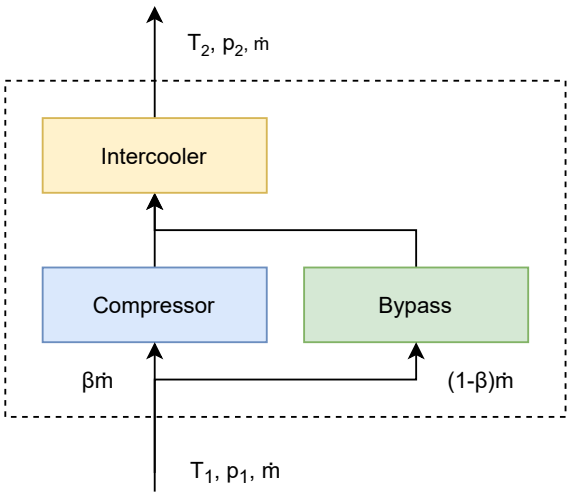

Figure 8.19: Overview of a compressor stage, which includes a bypass and inter-cooler.

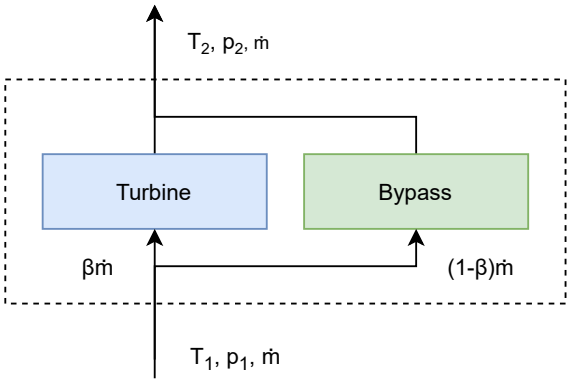

Figure 8.20: Overview of a turbine stage including a bypass.

Figure 8.19 and 8.20 show exploded views of the compressor and turbine stage respectively. The rest of this section will cover the mathematical model of every component and the numerical implementation of these models.

The reason for implementing the entire multi-stage turbocharger model numerically is to be able to optimize the compressor models, bypass ratios and compression ratios as is described in Section 8.2.9.

8.2.1. Thermodynamic calculation software

To perform thermodynamic calculations for the propulsion system, the python module pyCycle was used[18]. This module uses the same calculation methods for thermodynamic properties as the NASA Chemical Equilibrium Applications (CEA) program[19], which has the pressure, temperature and gas mixture as main inputs, with the option of adding more. Since the gas mixture is an input, this can be used both for air before and in the compressor, as well as in the turbine where the gas will be a mixture of exhaust gases.

8.2.2. Compressor Stage

In order to determine which compressors have an operating range which is compatible with the upstream and downstream air intakes, an analytical model to simulate a compressor model shall be established. This subsection will present the analytical and numerical models for the compressor and their corresponding verification.

[18]https://github.com/OpenMDAO/pyCycle [accessed 25/6/2021]]
[19]https://cearun.grc.nasa.gov/ [accessed 25/6/2021]

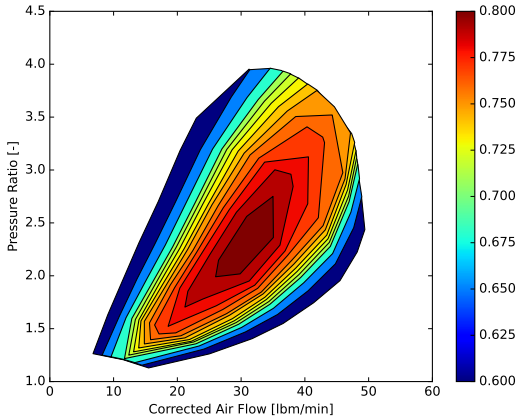

Figure 8.21: G25-550 Compression Map. The colorbar indicates the efficiency of the compressor at each operating condition.

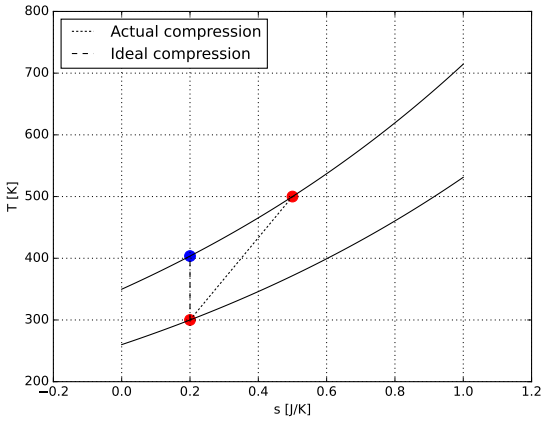

Figure 8.22: T-s diagram showing compression in an arbitrary compressor. The path between the two red dots shows the actual compression, whereas the blue dot is where the process ends up if it is idealized.

Compressor performance statistics are often provided by manufacturers in the form of a compression map, an example of which is presented in Figure 8.21. The compression map can be used to evaluate the airflow properties across a turbocharger, however, it is difficult as the relation between the pressure ratio and efficiency is a complex function of the mass flow [42].

Analytical model

An analytical model is established to provide a theoretical base for the development of a numerical model, and establish the inputs and outputs of the compressor model. Input variables are denoted as x_{1,C_n} for variable x in the n_{th} compressor stage, outputs as x_{2,C_n}. Π_{C_n} and η_{C_n} are the nth compression and efficiency ratios respectively.

γ_{C_n} is the specific heat ratio of gas is taken from the flows in the pyCycle module. The calculation of this inside of pyCycle is calculated using the CEA model, which is inline with the approach that Jung et al. [47] propose and later verified in Section 8.2.8.

$$p_{2,C_n} = p_{1,C_n} \cdot \Pi_{C_n} \tag{8.16}$$

$$T_{2,C_n} = T_{1,C_n}\left[1 + \frac{1}{\eta_{C_n}}\left(\Pi_{C_n}^{(\gamma_{C_n}-1)/\gamma_{C_n}} - 1\right)\right] \tag{8.17}$$

The power required to drive the compressor is provided by Jung et al. [47] and shown in Equation 8.18. $T_{2,C_n}/T_{1,C_n}$ is derivable from Equation 8.17.

$c_{p_{C_n}}$ is the constant pressure heat capacity of gas, which can be determined from the flow properties by the CEA model, just like the specific heat ratio.

$$W_{C_n} = \frac{1}{\eta_{C_n}} \cdot \dot{m}_a \cdot c_{p_{C_n}} \cdot T_{1,C_n}\left(\Pi_{C_n}^{(\gamma_{C_n}-1)/\gamma_{C_n}} - 1\right) \tag{8.18}$$

Π_{C_n} is the only variable which remains unknown, where it is heavily dependent on the mission profile. It is necessary for calculating the operating envelope of a turbocharger, as shown in Figure 8.21. The methodology to determine Π_{C_n} is presented in Section 8.3.

In order to evaluate compression and exhaust flow maps the corrected mass flow rate is required, which is presented in Equation 8.19. Corrected mass flow is the mass flow that would flow through the component at sea-level, and must be used when the component is operating at altitude. Corrected mass flow is evaluated the same way for compressors as for turbines, there P_1 and T_1 denote the input pressure and temperature, and $P_{h=0}$ and $T_{h=0}$, the sea level reference values.

$$\dot{m}_{corr} = \dot{m}\frac{P_{h=0}}{P_1}\sqrt{\frac{T_1}{T_{h=0}}} \tag{8.19}$$

Numerical model

Initially, an attempt was made at developing a system using Ordinary Differential Equation (ODE) modelling. Using this approach, however, led to a problem where the output power of the turbine could not be coupled to the compressor.

Another issue that quickly arose was the inability to directly model the inefficient non-isentropic compression that the compressor performs. To get around this problem, Figure 8.22 was used to identify a different approach in modeling the compression. This new approach consists of two steps: first, ideal compression is modeled for the certain pressure ratio, followed by an addition of enthalpy to reach the final point of actual compression. Figure 8.23 presents this approach as a block diagram.

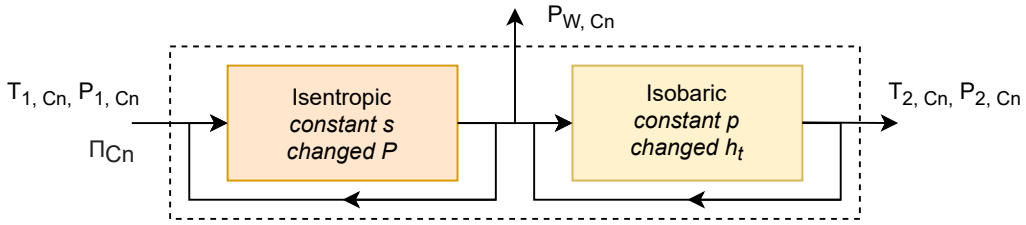

Figure 8.23: Two-step approach used to numerically determine the pressure and temperatures after the compressor stage.

The amount of enthalpy change required was then derived using the fact that after the ideal compression, the second part of the compression model takes place on an isobar for which Equation 8.20 holds.

$$\Delta h_t = C_p \Delta T \tag{8.20}$$

$$\Pi_{C_n}^{(\gamma_{C_n}-1)/\gamma_{C_n}} = \frac{T_{2,ideal,C_n}}{T_{1,C_n}} \tag{8.21}$$

Then, combining this with Equation 8.21 and 8.17, Equation 8.22 can be derived for this isobaric process. The power required to drive the compressor is derived from the enthalpy change $\Delta h_{t_{ideal_{C_n}}}$.

$$h_{t_{2,C_n}} = \frac{h_{t_{ideal_{2,C_n}}} - h_{t_{1,C_n}}}{\eta_{C_n}} + h_{t_{1,C_n}} \tag{8.22}$$

Verification

To verify the numerical model and its implementation, the temperature ratio as a function of the compressor ratio was investigated. Figure 8.24 shows the results of the pyCycle model and the analytical results of Equation 8.17.

The model results were obtained by running the pyCycle model at sea level conditions with the G25-550 compressor, for a mass flow of 0.2 kg/s. For the analytical results Equation 8.17 was used with $\gamma = 1.4$ and η_{C_n} derived from the compressor map.

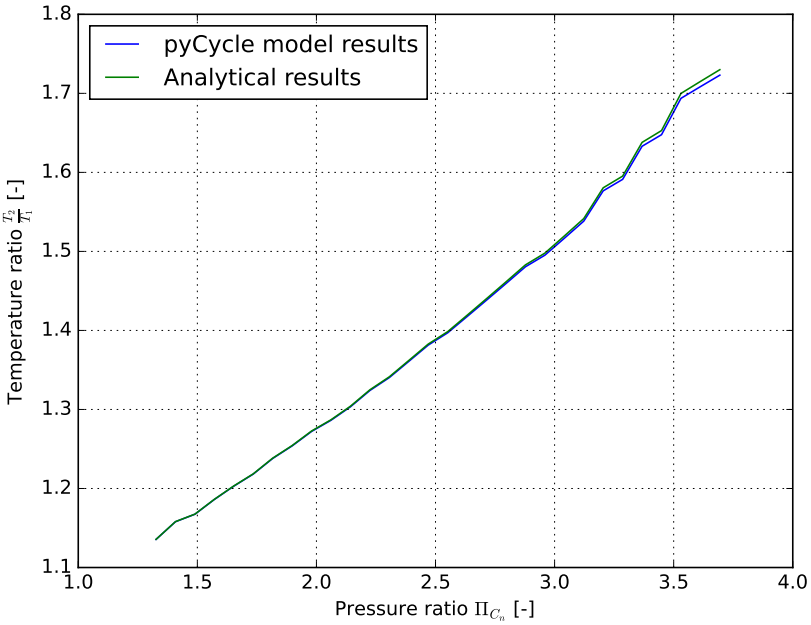

Figure 8.24: Verification of the compressor pyCycle model. The pyCycle model was run at sea level conditions with the G25-550 turbine, for a mass flow of 0.2 [kg/s]. Analytical results were obtained using Equation 8.17, where the efficiency η_{C_n} is taken from the model and the specific heat ratio γ is taken to be 1.4.

In Figure 8.24, two observations can be made: at higher temperature ratios a slight deviation between the two models starts to occur, and both models output not completely smooth curves.

The first observation can be explained by the fact that for the analytical results, a constant γ = 1.4 is used, whereas the pyCycle model uses the CEA model for its thermodynamic properties in which case the γ has a dependency on temperature. A more detailed discussion about the CEA model can be found in Section 8.2.8.

The second observation can be explained by the fact that both of the plots were made using manufacturer data for the efficiency. These efficiencies are given in a discrete way, which is also why the same pattern can be recognized for both plots.

8.2.3. Turbine stage

Each compressor needs a turbine component which can provide the power necessary to drive the compressor. This subsection will present the analytical and numerical models for the turbine and their corresponding verification.

Analytical model

An analytical model is established to provide a theoretical base for the development of a numerical model, and establish the inputs and outputs of the turbine model.

Similarly to compressors, turbine input variables are denoted as x_{1,T_n} for the input and x_{2,T_n} for the output.

$$p_{2,T_n} = p_{1,T_n} \cdot \frac{1}{\Pi_{T_n}} \tag{8.23}$$

As opposed to the compressor stage where Π_{C_n} remained undetermined, Π_{T_n} can be determined by matching the power generated by the turbine to that used by the compressor. The power generated by a turbine is provided by Jung et al. [47] and shown in Equation 8.24.

$$W_{T_n} = \frac{1}{\eta_{T_n}} \cdot \left(\dot{m}_a + \dot{m}_f\right) \cdot c_{p_{T_n}} \cdot T_{1,T_n} \left(1 - \Pi_{T_n}^{(\gamma_{T_n}-1)/\gamma_{T_n}}\right) \tag{8.24}$$

Therefore the power balance can be denoted as in Equations 8.25 and 8.26.

$$W_{C_n} = \eta_{mech} \cdot W_{T_n} \tag{8.25}$$

$$\Longrightarrow \Pi_{T_n} = \left[1 - \frac{1}{\eta_{C_n} \cdot \eta_{T_n} \cdot \eta_{mech}} \cdot \frac{\dot{m}_a}{\dot{m}_a + \dot{m}_f} \cdot \frac{C_{p_{C_n}}}{C_{p_{T_n}}} \cdot \frac{T_{1,C_n}}{T_{1,T_n}} \left(\Pi_{C_n}^{(\gamma_{C_n}-1)/\gamma_{C_n}} - 1\right)\right]^{\gamma_{T_n}/(1-\gamma_{T_n})} \tag{8.26}$$

Numerical modeling

The numerical modeling of the turbine stage is quite similar to that of the compressor stage. In the same way as in Figure 8.23, expansion is split up into two parts: ideal expansion followed by an addition of enthalpy.

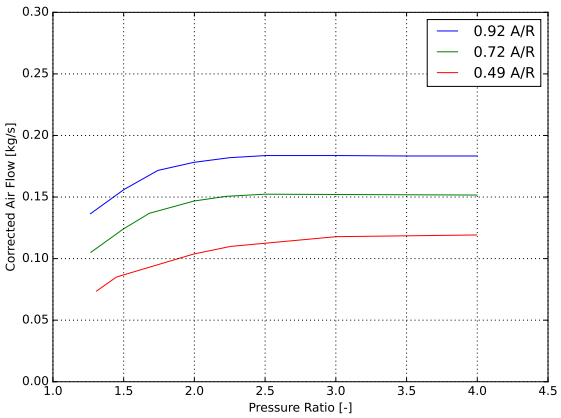

Figure 8.25: G25-550 exhaust flow diagram for different aspect ratios (A/R).

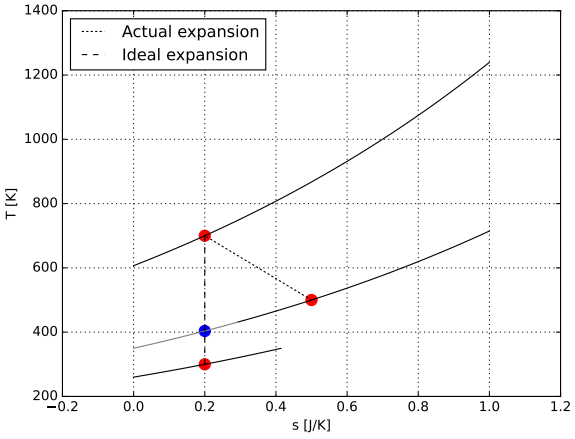

Figure 8.26: T-s diagram of the actual and ideal expansions within a turbine. The lowest red dot would be reached in case of perfect efficiency and the blue dot is the point reached in isentropic expansion before adding enthalpy.

In the numerical model, first the pressure ratio is calculated using Equation 8.26 which leads to the blue dot in Figure 8.26. The heat generated due to the inefficiency is then added to the flow by correcting the enthalpy as shown in Equation 8.27.

$$h_{t_{2,T_n}} = h_{t_{1,T_n}} - \eta_{T_n}(h_{t_{1,T_n}} - h_{t_{ideal_{2,T_n}}}) \tag{8.27}$$

This equation was derived by combining Equation 8.28, taken from the approach of Jung et al. [47], Equation 8.20 and 8.29.

$$T_{2,T_n} = T_{1,T_n}\left[1 - \eta_{T_n}\left(1 - \Pi_{T_n}^{(\gamma_{T_n}-1)/\gamma_{T_n}}\right)\right] \tag{8.28}$$

$$\Pi_{T_n}^{(\gamma_{T_n}-1)/\gamma_{T_n}} = \frac{T_{2,ideal,T_n}}{T_{1,T_n}} \tag{8.29}$$

The airflow through a turbine is limited by the pressure ratio across it, as shown in Figure 8.25, where A/R represents the aspect ratio of the turbine. It can be reasonably expected that the exhaust mass flow exceeds the permissible mass flow through the turbine, therefore each turbine shall include a bypass valve. The mass flows through the turbine under a bypass are defined in Equations 8.30 and 8.31, where β, $\dot{m}_t$, and $\dot{m}_b$ are the bypass ratio, mass flow through the turbine, and mass flow bypassed around the turbine respectively.

$$\dot{m}_b = \beta \dot{m}_{tot} \tag{8.30}$$

$$\dot{m}_t = (1 - \beta)\dot{m}_{tot} \tag{8.31}$$

Verification

To verify the numerical model and its implementation, the temperature ratio as a function of the pressure ratio was investigated. Figure 8.27 shows the results of the pyCycle model and the analytical results of Equation 8.28.

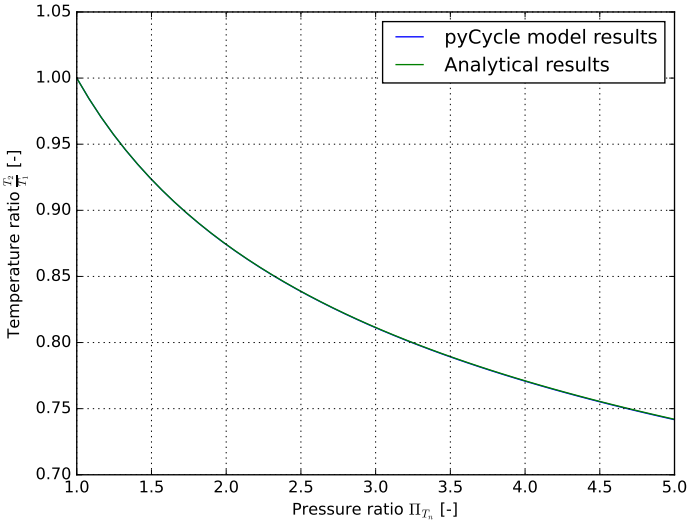

Figure 8.27: Verification of the turbine pyCycle model. The model results were obtained by running the PyCycle model at sea level conditions with the G25-550 turbine, for a mass flow of 0.2 kg/s and A/R of 0.72. For the analytical results Equation 8.28 was used with γ = 1.4 and η_{T_n} taken from the turbine data, which is a constant 0.7 as provided by the manufacturer.[20]

The two lines of the pyCycle model and analytical results perfectly match, proving the pyCycle model was implemented correctly. In contrast to the verification of the compressor model in Figure 8.24, no discrepancies were found between the pyCycle turbine model and the analytical results. There are two reasons for this: the temperatures stay relatively low, leading to little variation in gas properties, and the turbine efficiency is constant.

The verification was performed at sea-level conditions and the air is expanded in the turbine, lowering the temperature, which is why low temperatures were observed. Due to the low temperatures, γ is not influenced significantly, therefore, no discrepancy is observed as for the compressor. The plots in Figure 8.24 were not completely smooth due to the discrete values that were taken for the compressor efficiencies. In Figure 8.31 this effect is not present, as the turbine efficiency was taken as a constant value.

8.2.4. Bypass stage

The numerical model for turbine necessitates the use of a bypass component in order to control the amount of power being generated by the turbine. The bypass consists of two components, a splitter and a mixer. The splitter simply splits the flow into two flows based on the bypass ratio and the mixer mixes two flows together. First, the splitter is described and verified, followed by the same procedure for the mixer.

Splitter model

The splitter was implemented in a very simple way, where the mass flows are split based on the bypass ratio and other flow parameters are left untouched. Equation 8.30 and 8.31 show these relations, with $\dot{m}_b$ as the mass flow through the bypass, $\dot{m}_t$ the mass flow through the turbine/compressor and $\dot{m}_{tot}$ the total mass flow.

It is important to note that this definition is fundamentally different from the common definition of the bypass ratio for axial engines, $\beta = \dot{m}_t/\dot{m}_b$. The justification behind developing a new model

[20] https://www.garrettmotion.com/racing-and-performance/performance-catalog/turbo/g-series-g25-550/ [accessed 25/6/2021]

is that the model must be well behaved when all the flow goes through the turbine or is bypassed entirely.

Mixer

For mixing the two flows after a bypass, a model exists within the pyCycle module. This model relied on the areas corresponding to each flow which is not a property that is being considered for the team's model. Therefore, a new model was developed that does not depend on flow areas. This subsection discusses the assumptions made and workings of the new model. Figure 8.28 shows a schematic view of the situation at hand.

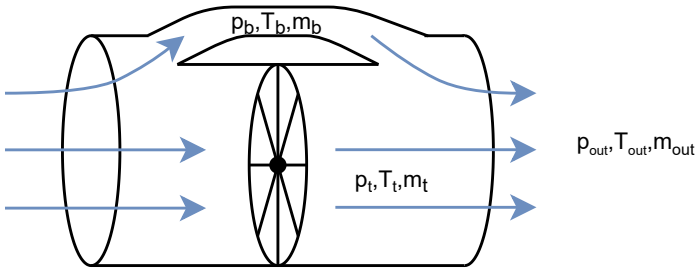

Figure 8.28: Schematic overview of a compressor/turbine with a bypass. In each station, the flow variables are given with their respective subscripts used in further derivations.

Mixer analytical model

The main assumption made for the derivation of the numerical mixer model is that the gas is ideal, and that the output volume is an addition of the volume passed through the turbine/compressor and the volume passed through the bypass, as shown in Equation 8.32.

$$V_{out} = V_t + V_b \tag{8.32}$$

A limitation of this model is the fact that any possible backward flows due to pressure differences are not taken into account. In a real mixer pressure valves that maintain equal pressure in the inputs of the mixer would be necessary.

The second assumption made is that the amount of moles n in these assumed volumes is proportional to the mass flow $\dot{m}$. implying $n = c\dot{m}$. This constant c would in that case depend on the time interval considered, as the flow is moving and thus also the volume would depend on this time interval. As shown in the derivation following this, however, the value of neither this constant c or the volumes considered is relevant for the actual model.

Combining the ideal gas law and 8.32 with the defined variable names in Figure 8.28 leads to Equation 8.33.

$$\frac{c\dot{m}_{out}RT_{out}}{p_{out}} = \frac{c\dot{m}_tRT_t}{p_t} + \frac{c\dot{m}_bRT_b}{p_b} \tag{8.33}$$

Equation 8.34 is obtained using $\dot{m}_b = \beta\dot{m}_{tot}$ and $\dot{m}_t = (1-\beta)\dot{m}_{tot}$ and rearranging Equation 8.33 to output p_{out}, also canceling all c and R terms.

$$p_{out} = \frac{T_{out}p_tp_b}{(1-\beta)T_tp_b + \beta T_bp_t} \tag{8.34}$$

In this equation, the T_{out} is an input meaning this already needs to be known when calculating p_{out}. Like in previous sections, conservation of energy was again implemented using the enthalpies of the flows. Equation 8.35 shows the relation that was derived to implement this.

$$h_{out} = (1-\beta)h_t + \beta h_b \tag{8.35}$$

After this calculation step in the model, T_{out} can be taken from the flows properties and p_{out} can be calculated, enabling the full model to run.

Mixer numerical model

The mixer numerical model is structured similarly to the compressor and turbine components, using a two-step approach to calculate the flow properties, as shown in Figure 8.29.

Since Equation 8.34 requires the mixed temperature, the temperature has to be first calculated as an isobaric process and its output used as input into the isentropic process that calculates the final pressure.

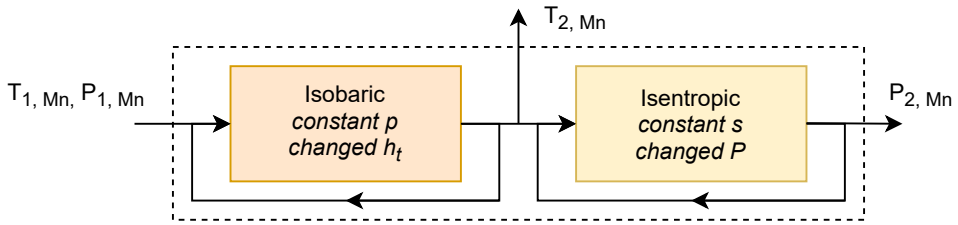

Figure 8.29: Two-step approach used to numerically determine the pressure and temperatures after the mixer.

The previously described turbine and compressor models establish mass flow requirements based on their operating conditions, for example when the compressor becomes choked. This establishes an implicit relationship in the mass flow across a component, necessitating the introduction of a residual that must be driven to zero for the model to converge. This residual is defined in Equation 8.36.

$$\mathcal{R}_{E_n} = \dot{m}_{2,E_n} - \dot{m}_{1,E_n} \tag{8.36}$$

In this relation, $\dot{m}_{2,E_n}$ is dependent on the state of the system E_n, which will be denoted as S, leading to $\dot{m}_{2,E_n} = f(S)$. This state of the system refers to either the compression ratio or the pressure ratio for compressors and turbines respectively. The incoming mass flow depends on the bypass ratio β, which can then be shown as $\dot{m}_{1,E_n} = g(\beta)$. When this residual is successfully brought to zero, conservation of mass is achieved across the subsystem.

Mixer verification

The verification process was performed by calculating the properties of a mixed flow given two input flows. The results are presented in Figure 8.30 and were derived using a turbine output temperature and pressure of 400 K and 1 bar respectively. The bypass flow had a temperature and pressure of 500 K and 2 bar respectively.

It can be clearly observed that for a bypass ratio of $\beta = 0$, the output flow is the same as the turbine flow, which is to be expected. The same holds for $\beta = 1$, where the output flow is identical to the bypass flow.

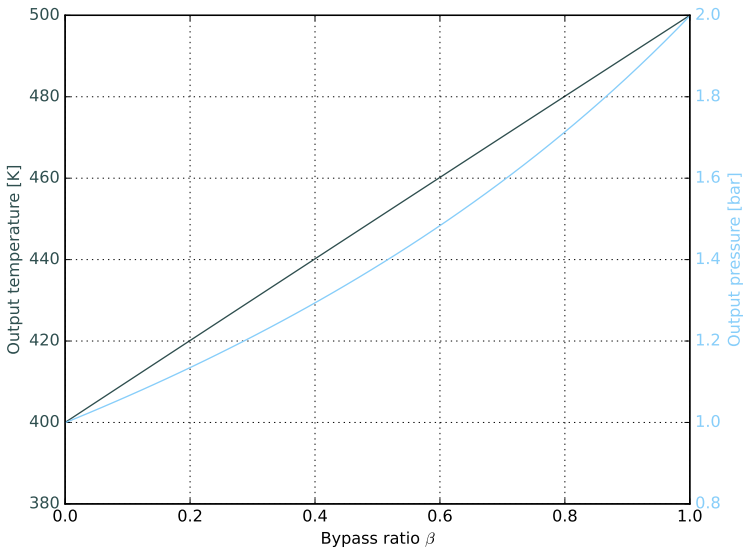

Figure 8.30: Output pressure and temperature of the mixer plotted against possible bypass ratios between 0 and 1.

The linearity of the temperature with the bypass ratio is to be expected, since the temperature is dependent on the enthalpy which is linear with the bypass ratio, as visible in Equation 8.35. In contrast to the temperature, the pressure is non-linear, which can again be explained by the calculation method shown in Equation 8.34. This equation is clearly non-linear with respect to the input pressures, solidifying the results of Figure 8.30.

8.2.5. Engine model

For the engine model, no actual combustion is modeled. Instead, it is treated as a 'black box', for which the inputs and outputs are specified and the physical process in between is omitted.

The pressure and temperature of the flow at the exhaust is based on the outcome of the engine Otto cycle in Figure 8.2. The PV diagram simulation showed a piston exhaust pressure of approximately 16 kPa.

Equation 8.37 shows a relation of power output of the engine with input flow density as given by Torenbeek [17]. The ideal gas law is used to rewrite Equation 8.37 to demonstrate the power relationship with temperature and pressure.

$$\frac{P_h}{P_{h=0}} = (1+c)\frac{\rho_h}{\rho_{h=0}} - c = (1+c)\frac{p_h}{p_{h=0}}\frac{T_{h=0}}{T_h} - c, \; c \approx 0.132 \tag{8.37}$$

The relationship demonstrates that in order to increase power, temperature must also be kept low, and this is indeed the behavior that the Otto cycle model exhibits. Due to this relationship, inter-cooler stages after each compressor become necessary in order to guarantee a cool enough flow.

The temperature of the flow coming out of the engine was then found 420 [°C] based on the exhaust pressure and the fluid density approximated to be 0.08 kg/m^3 when exiting. To account for this in the energy of the flow, Equation 8.38 is used where T_{out} = 420 [°C].

$$h_{t,out} = h_{t,in} + C_p(T_{out} - T_{in}) \tag{8.38}$$

The engine establishes a requirement for intake air mass flow that is required in order to ensure stoichiometric combustion of the fuel. This establishes an implicit relationship in the mass flow across the engine, necessitating introducing a residual that must be driven to zero for the model to converge. This residual is defined in Equation 8.39, and is controlled by the atmospheric intake.

$$\mathcal{R}_E = \dot{m}_a - \dot{m}_{1,E} \tag{8.39}$$

In this, $\dot{m}_a$ is dependent on the RPM of the engine, $\dot{m}_a = f(\text{RPM})$. As for $\dot{m}_{1,E}$, this is simply equal to the total mass flow, $\dot{m}_{1,E} = \dot{m}_{tot}$.

8.2.6. Inter-cooler stage

The G-Series Garrett lineup of compressors is particularly interesting for this project, due to their superior performance characteristics. However, their capabilities remain limited, rated up to a temperature of 1323 [K] [21]. Therefore, it can be justified that multiple inter-cooling stages will likely become necessary. The efficiency of an inter-cooler is provided by Jung et al. [47], presented in Equation 8.40, where they assume that $\epsilon_{T,I_n} = 0.7$.

$$T_{hot,2,I_n} = T_{hot,1,I_n}\left(1 - \epsilon_{T,I_n}\right) + \epsilon_{T,I_n} T_{cold,1,I_n} \tag{8.40}$$

Loth et al. [48] also consider that there is a pressure drop of 1 to 10 percent across the inter-cooler stage, reflected in Equation 8.41, where the value for ϵ_{p,I_n} is taken about the average at 0.05.

$$P_{2,I_n} = P_{1,I_n}\left(1 - \epsilon_{p,I_n}\right) \tag{8.41}$$

Numerical modelling

To model this in pyCycle, the same method is used as for the compressor and turbine. First, the pressure drop is implemented using Equation 8.41, followed by a change of enthalpy. This change of enthalpy is, again, assumed to be at isobaric conditions which leads to Equation 8.42.

$$h_{t_{hot,2,I_n}} = h_{thot,1,I_n}\left(1 - \epsilon_{T,I_n}\right) + \epsilon_{T,I_n} h_{tcold,1,I_n} \tag{8.42}$$

In order to minimize the size of the intakes for cooling air, the same cold air flow will be used by all of the inter-coolers. This means the output cold flow of the first inter-cooler becomes the input cold flow to the second inter-cooler. To take this into account in the simulation, a need arises for a model that is able to calculate how much the cold flow heats up in the process of cooling the hot flow. This is done by adding the amount of energy removed from the hot flow to the cold by as shown in Equation 8.43. As the enthalpies used in calculations are specific, a ratio of the hot mass flow to cold mass flow appears in this calculation. $\xi = \frac{\dot{m}_h}{\dot{m}_c}$ will be used for the rest of this chapter to refer to this ratio.

$$h_{tcold,2,I_n} = h_{t_{cold,1,I_n}} - \xi \Delta h_t \tag{8.43}$$

Verification

The model, when only considering the energy transfer, does not have a limitation on how much energy can be transferred. Because of this, in the verification of the first iteration of this model, situations would occur where the cold output flow was at a higher temperature than the hot output flow which is not physically possible. These situations would occur for high inter-cooler effectiveness ratios combined with low hot to cold mass flow ratios $\frac{\dot{m}_h}{\dot{m}_c}$.

To ensure the model does not output physically impossible results, a limit was set such that the cold output temperature does not exceed the hot output temperature. Using Equation 8.20, Equation 8.43 can be used to derive an analytical expression for the temperature of the cold output flow. Δh_t is taken as $h_{thot,2,I_n} - h_{t_{hot,1,I_n}}$ from Equation 8.42, leading to Equation 8.44.

$$T_{cold,2,I_n} = T_{cold,1,I_n} + \xi \epsilon_{T,I_n}(T_{hot,1,I_n} - T_{cold,1,I_n}) \tag{8.44}$$

[21] https://www.garrettmotion.com/racing-and-performance/performance-catalog/turbo/g-series-g25-550/ [accessed 25/6/2021]

This can then be equated to Equation 8.40, to solve for which *epsilon* is critical. Any *epsilon* higher than this will lead to the situation mentioned previously, where the cold output flow temperature is high than the hot output flow temperature.

$$\epsilon_{crit} = \frac{1}{1+\xi} \tag{8.45}$$

By implementing ϵ_{crit} as a limit to the inter-cooler effectiveness, Figure 8.31 is the result.

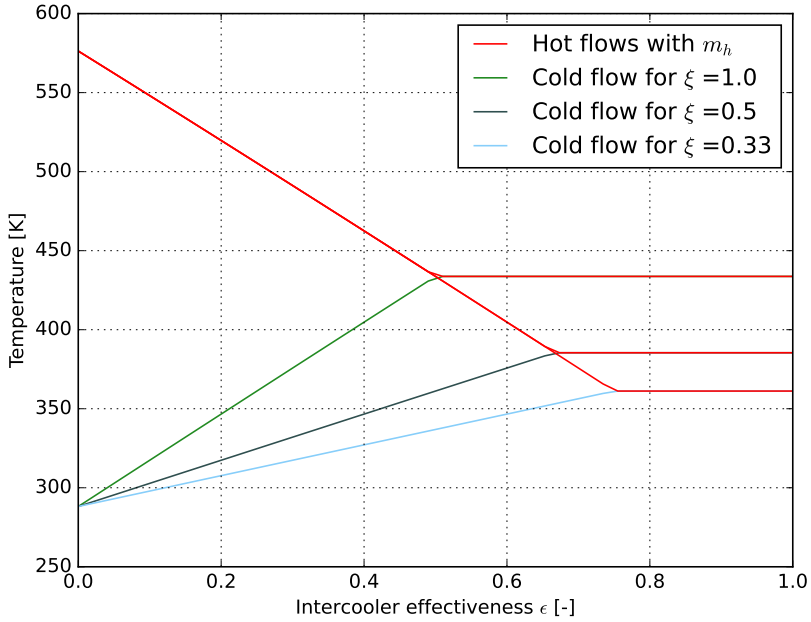

Figure 8.31: Relation between hot and cold flow output temperature shown for three different mass flow ratios ξ, plotted against the inter-cooler effectiveness ϵ

.

In this figure it is clearly visible that the cold output flow temperature correctly gets limited as soon as it reaches the hot output flow temperature. In addition, for a mass flow ratio of $\xi = 1.0$ and an inter-cooler effectiveness of $\epsilon = 0.5$, the final temperature of both the cold and the hot flow ends up exactly in the middle of the two starting temperatures.

It is however worth noting that the methodology used above to compute the flow temperature within the inter-cooler does not make use of the flow pressure. Though the temperature change in the inter-cooler is based on the enthalpy exchange needed to achieve the target temperature drop, a better physical representation is assessing the enthalpy exchange based on the actual flow properties. Hence the resulting temperature must be a function of the enthalpy exchange given the flow's initial temperature and pressure when entering the inter-cooler and the flow properties when traversing the inter-cooler, as opposed to the method above which computes the enthalpy exchange based on the target temperature at the inter-cooler exhaust.

Defining the inter-cooler component concludes the description of all components that are necessary to evaluate a multistage turbocharging system.

8.2.7. Mass flow preserving components

When creating a certain turbocharging system configuration, it is important that any such system can be reliably evaluated. A problem that occurred during the implementation of the model was that the engine mass flow residual could not be driven to zero, due to compressors requiring too much power for a given mass flow in order to match its required compression ratio. To get around this problem, a solution was adopted to integrate the bypass relations directly into the compressor and turbine, yielding an explicit relationship, rather than the implicit one.

Mass flow preserving compressors and turbines have the bypass ratio as an output, such that the ratio is set to such a value that conserves mass flow across the component given any compression or pressure ratio and mass flow. An advantage of this is that the bypass ratios do not have to be implicitly determined for each iteration, therefore the residuals defined in Equations 8.36, and 8.39 are no longer required. However, a disadvantage is that the bypass ratio cannot be set on the compressor.

Numerical model

The implementation of the bypass turbine is relatively simple. With this new explicit method for the bypasses, given any pressure ratio, the mass flow limit through the turbine will be provided by the model. The implementation for the compressor is not trivial, as any mass flow in its operational range can be selected. In order to select the mass flow through the compressor, it is assumed that the maximum mass flow is desirable as it achieves the highest compression. Alternative formulations can be considered, such as one that balances mass flow and efficiency. Some preliminary tests proved that the maximum mass flow lead to the best results, however.

For each compression ratio a min $\dot{m}_{C_n}$ and max $\dot{m}_{C_n}$ can be established where the compressor is still operational. The final flow through the compressor is then determined using Equation 8.46.

$$\dot{m}_{C_n} = \begin{cases} 0, & \dot{m} < \min \dot{m}_{C_n} \\ \dot{m}, & \min \dot{m}_{C_n} \leq \dot{m} \leq \max \dot{m}_{C_n} \\ \max \dot{m}_{C_n}, & \max \dot{m}_{C_n} \leq \dot{m} \end{cases} \tag{8.46}$$

Verification

In order to verify the proper behavior of the bypass ratios returned by the mass flow conserving components, the mass flow of the bypass and component flows were investigated with a changing input flow. Figures 8.32 and 8.33 show the result of the verification.

The verification displays expected behavior in both verified components, where the turbine, once activated, retains a fixed mass flow limit, and the compressor matches until it would otherwise choke.

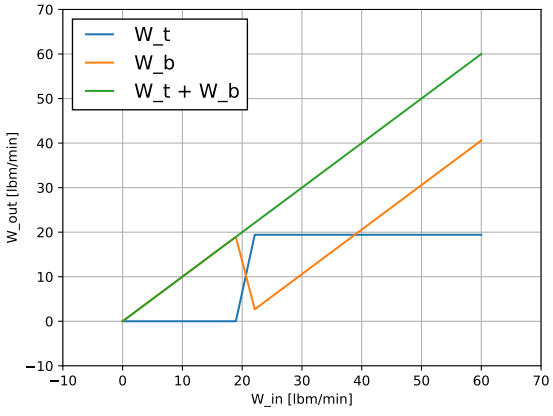

Figure 8.32: Mass flows in turbine bypass under varying input mass flow.

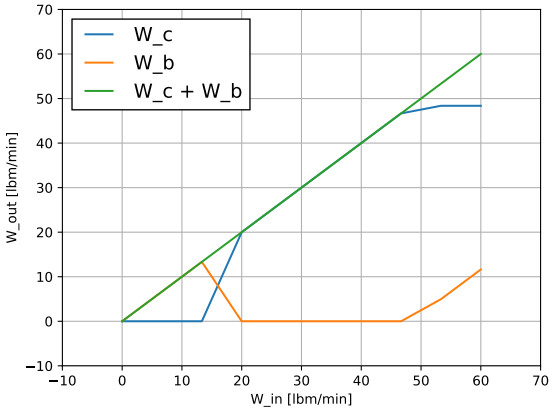

Figure 8.33: Mass flows in compressor bypass under varying input mass flow.

8.2.8. Thermodynamic verification

All of the components that the model is structured out of require the calculation of multiple initial value and gas property problems. To perform the calculations pyCycle delegates work to the NASA CEA software package.

The NASA CEA model was found to only use temperature to determine thermodynamic properties. For example, C_p is computed as shown in Equation 8.47 [49] and from this also the specific heat

ratio γ is calculated. This raises a potential issue for the analysis of RePLASMA as it operates within a wide range of pressures, therefore, a verification of the CEA model is deemed necessary.

$$\frac{C_p^0(T)}{R} = a_0 + a_1 T + a_2 T^2 a_3 T^3 a_4 T^4 \tag{8.47}$$

To ensure the pressure does not have a significant effect on these data, the model was verified using a model that does include pressure terms. This model by Bahadori and Vuthaluru (B&V)[50] is only valid for air, so this specific verification is only done for the case where air is the used gas. The exact methods used in their model can be found in the reference.

This reference model has coefficients for either up to 100 bar or from 100 to 1000 bar, both tuned for temperatures ranging from 200 to 1000 K. For the RePLASMA project, only the first model is relevant, as the pressure values of the second model will simply never be reached in either the compressor or turbine.

As a general verification, first the entire range up to 100 bar is compared to the CEA model in Figure 8.34.

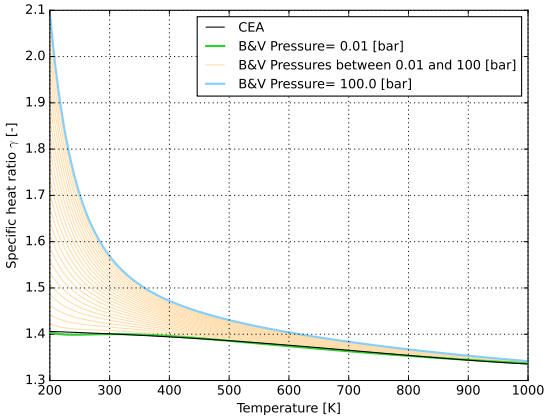

Figure 8.34: This figure shows different graphs plotting the specific heat ratio against temperature for different pressures, compared to the CEA model which does not take pressure into account. The lowest and highest pressure considered for the B&V model, 0.01 and 100 bar respectively, are highlighted in different colors.

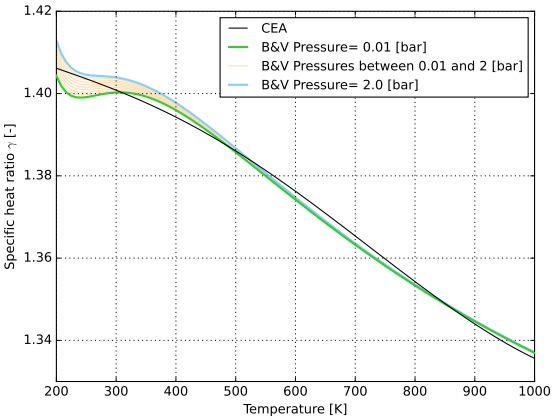

Figure 8.35: Figure 8.34 Specific heat ratios for a combination of temperatures and pressures for the B&V model, compared to the CEA model in which pressure is not used as a parameter. The lowest and highest pressure considered, 0.01 and 2.0 bar respectively, are displayed in green and blue.

In this figure it is visible that for low temperatures at high pressures, the CEA model is quite inaccurate. For low pressures, however, it can be seen the two models line up well. For the verification of the application to specific project, the pressure in the compressor and turbine is assumed to not exceed 1.2 and 2 bar respectively. Following this, the CEA model is presumed to be verified if the errors with respect to the B&V model are negligible up to a pressure of 2 [bar]. The same starting point of 0.01 bar is taken, this is below the pressure at the target altitude of 25 km which implies the full range of possible pressures is considered. The results that follow from this are shown in Figure 8.35.

The order of magnitude of the MSE is 10^{-6}, from which the conclusion was drawn that the CEA model was indeed precise enough for this application. In addition, the maximum absolute error of the CEA model with respect to the B&V model in this data set is 0.48%, which is deemed acceptable as well. For perspective: if the pressures were to go up to 100 [bar], for example if the processes within the engine were to be analyzed, the MSE would be in the order of magnitude of 10^{-2} and maximum absolute error 33%, which would not be deemed acceptable.

An interesting note after a further analysis of Figure 8.35 is that the CEA model appears to have the least error with respect to the B&V model around a pressure of 1 bar. This implies that the CEA

model is calibrated for pressure values around that of the atmosphere on the Earth's surface, which makes sense for general usage of the model.

8.2.9. Turbocharger implementation

Using all of the components established during this chapter, a full model of the turbocharger was setup in pyCycle in which all of the components are connected together. Each configuration takes as an input the turbocharger models that should be present on each stage as well as their prescribed compression ratios.

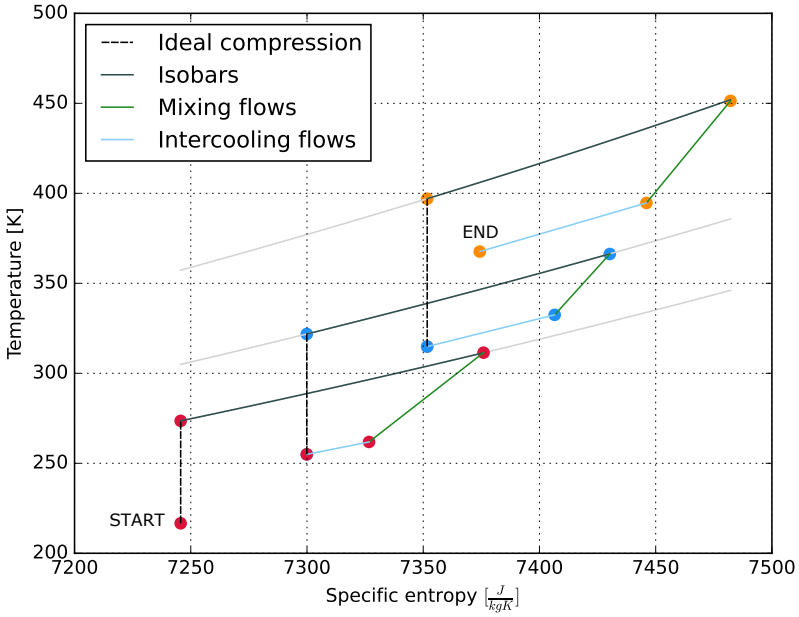

Figure 8.36: T-s diagram of a 3-stage compressor, including bypasses and inter-coolers. This specific example shows a configuration that uses a G35-1050, G57-2550 and G57-2350 in order from ambient flow to the engine intake. Inter-cooler cold air mass flows were set to $\dot{m}_c$ = 0.05 [kg/s], and the altitude was set to 19 [km]. The indicated start point shows where the ambient airflow enters the first compressor and the end point is the flow where it is about to enter the engine. Compression is shown in the way it is implemented in the model, which is a combination of ideal compression followed by isobaric enthalpy increase, similar to the T-s diagram in Section 8.2.2. Finally, the red, blue and yellow points indicate the first, second and third stage respectively.

Figure 8.36 presents a T-s diagram, for an example 3-stage configuration, that encapsulates the entire compression part of the turbocharger, from air intake to engine intake. The figure only depicts the flow through the compressor, to which the bypass flow is then added in the mixing. For high enough cool mass flows $\dot{m}_c$, the specific entropy actually starts to go down while the air progresses through the stages. This is, however, not a breach of the second law of thermodynamics as this entropy is added to the cold flow of the inter-cooler, meaning the total system entropy does not go down. Inter-cooler flows pass through each inter-cooler serially in order to minimize induced drag due to the intake.

In order to evaluate the system, an initial guess of the state of all components must be established since at the starting point all compressors will be outside of their operating range. Due to the flexibility of the mass-flow conserving components, the initial input requires only the compression ratios and a guess for the corresponding pressure ratio. When evaluating a parallel stage, all parallel components are chosen to be the same model with mass flow split equally between them.

In order to determine the pressure ratio that a turbine must operate at a residual that must be driven to zero is established. The turbine is connected to the compressor via a shaft component whose net power must be driven to zero. This residual is denoted in Equation 8.48. P_{C_n} is dependent on the input compression ratios, $P_{C_n} = f(\Pi_{C_n})$, while P_{T_n} is dependent on the pressure ratio, $P_{T_n} = g(\Pi_{T_n})$. Π_{T_n} is varied until the residual is driven to zero, thus balancing the power across the shaft.

$$\mathcal{R}_{S_n} = P_{C_n} + P_{T_n} \tag{8.48}$$

Pressure ratios are re-evaluated at each iteration of the system, and are evaluated using Equation 8.49. This relationship is identical to Equation 8.26 except that it assumes that the gas thermal properties do not change and $\gamma = 1.4$.

$$\implies \Pi_{T_n} = \left[1 - \frac{1}{\eta_{C_n} \cdot \eta_{T_n} \cdot \eta_{mech}} \cdot \frac{\dot{m}_a}{\dot{m}_a + \dot{m}_f} \cdot \frac{T_{1,C_n}}{T_{1,T_n}} \cdot \left(\Pi_{C_n}^{(\gamma-1)/\gamma} - 1\right)\right]^{\gamma/(1-\gamma)} \tag{8.49}$$

Because the compression ratio Π_{C_n} of each stage remains undefined, the matching process assumes that the work done by each stage of compressors is equal. Watson and Janota [51] state that the dual stage turbocharging system performs optimally when work is split between compressors, therefore we extend the idea to a multiple stage system.

For any guess of compression ratios the system performance can be evaluated. A consequence is that the compression ratios can be externally optimized to meet some desired property. When evaluating a configuration at a certain altitude the team looks to identify the maximum power that can be developed by the turbocharger and engine configuration, in order to verify that the required power can be met.

To choose the compression ratios the objective function in Equation 8.50 is minimized. $f(\bar{\Pi}_{C_n})$ is the power developed by the engine. The product term in the equation is responsible for penalizing the configurations whose residuals are not driven to zero. It is important to note that the pressure developed at the engine intake can exceed sea level conditions for additional power.

$$\min_{\bar{\Pi}_{C_n}} \; -f(\bar{\Pi}_{C_n}) \cdot \prod_n g(1 - |\mathcal{R}_{S_n}|), \; g(x) = \begin{cases} x, & x \leq 0 \\ 0, & \text{otherwise} \end{cases} \tag{8.50}$$

8.3. Turbocharger matching

In this section the methodology for selecting a turbocharger configuration is discussed. The section will cover how each configuration is scored, how new configurations are discovered, and the results of the matching process.

A genetic algorithm was then set up that evaluated a number of configurations and determine the best possible combination of commercially available compressors. Initially, the search for viable configurations begins with the parallel at intake 3-stage design option, depicted in Figure 8.18. Such a layout shall be denoted as 1-1-2, where the left digit indicates the number of parallel stages at the engine. The genetic algorithm starts off by assuming a set of random combinations of compressors to form the multi-stage turbocharger, which it scores using the objective function defined in Equation 8.50 at 25 [km]. The configurations are then mutated and combined with additional fully randomized combinations, until an upper limit is reached.

Mass and price estimation is performed using data provided by TurboMaster S.L.[22]. It is assumed that the inter-cooler model used is 703521-6003, as it is the smallest model that supports the required horsepower of RePLASMA.

The final configuration that was identified by the genetic algorithm is shown in Table 8.7. This is a 1-1-2-2 configuration, which outperformed all three stage configurations, and was more mass efficient than candidate 1-2-2-2 configurations. In a 1-1-2-2 configuration, stages 2-3 and 4-5 are placed in parallel at the environmental intake.

[22] https://www.turbosbytm.com/ [accessed 25/6/2021]

Table 8.7: Final configuration for 1-1-2-2 design

Stage	Compressor model	Super-core model	Turbine model	Mass [kg]	Price [€]
Stage 0	G57-2550	880547-5033S	761208-0084	31.8	4210
Stage 1	G57-3000	880547-5030S	761208-0085	32.7	4565
Stage 2/3	G57-2550	880547-5033S	761208-0085	64.1	8510
Stage 4/5	G57-2550	880547-5033S	761208-0084	62.9	8420
			Inter-coolers:	24	824
			Total mass and price:	215.5	26529

8.4. Analysis

In this section an analysis of the selected design is presented, covering the variation of engine power with altitude, compressor operating points, bypass ratio variation, and the thermal limits of the compression system.

8.4.1. Performance

Evaluating the chosen configuration, a performance diagram that plots the power developed by the engine can be derived. This performance diagram is presented in Figure 8.37, complemented by Figure 8.38 which shows the pressures developed at the outlet of each compressor. Two observations can be made from these diagrams. First of all, the naturally aspirated engine power falls below the mission profile required power at an altitude of 15 [km]. It can be seen that at around 12 [km] the turbocharging system kicks in to raise the maximum operational altitude to 25 [km]. This can be recognized by the point where the power required line is crossed by the turbocharged configuration. Secondly, power is actually decreased for lower altitudes with the turbocharging system. This power loss is caused by the pressure losses over the inter-coolers.

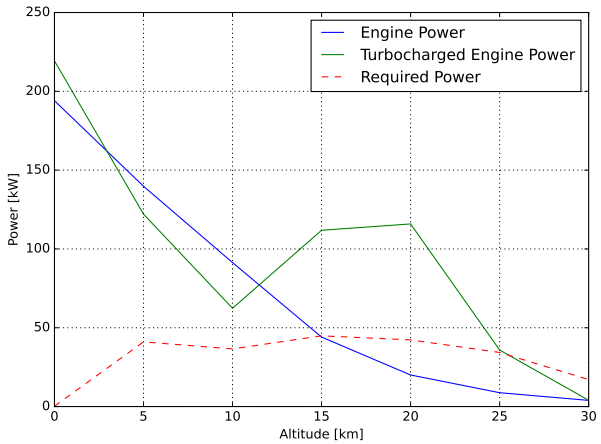

Figure 8.37: Turbocharged and naturally aspirated engine power with altitude

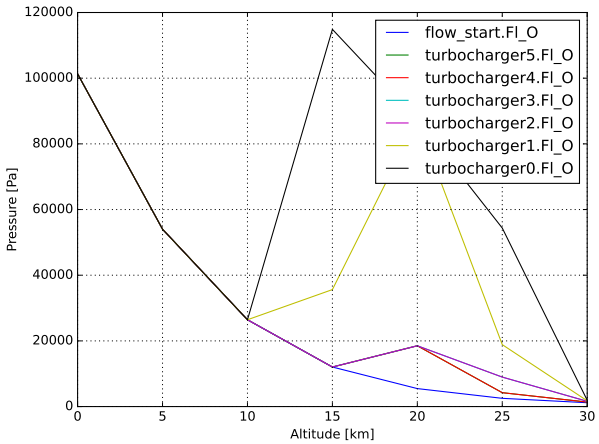

Figure 8.38: Output pressures of each compressor stage plotted against altitude.

Figure 8.38 shows the output pressures of each turbocharger component. For this configuration, the first two stages are composed of two parallel compressors. This was optimized by the genetic algorithm and makes sure the turbocharged engine power stays above the required power for the entire operational range.

Figure 8.39 shows the compression ratios of each compressor, which were derived from the objective function defined in Equation 8.50. The compression ratios are not one-to-one related to the output pressures in Figure 8.38 due to the bypass ratios imposed by the model, shown in Figure 8.40. When a large part of the air is bypassed, the compression ratio is not relevant seeing that only a small part of the air is actually compressed. Figure 8.41 shows the operating points of each stage.

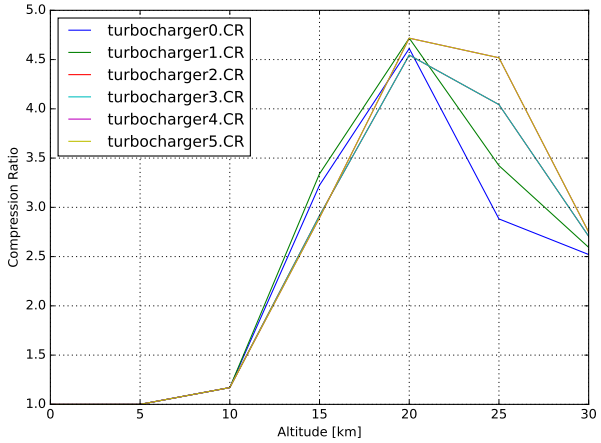

Figure 8.39: Compression ratios of each compressor plotted against altitude.

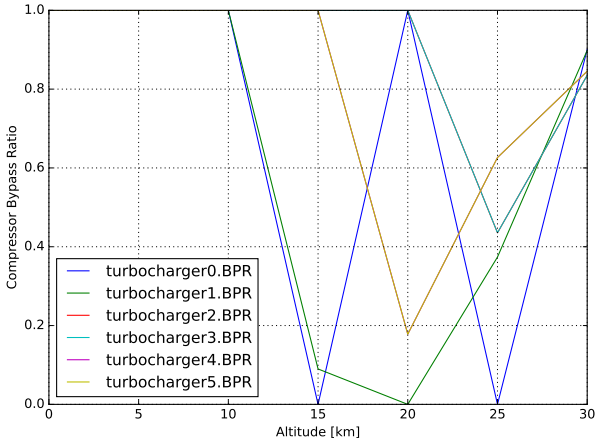

Figure 8.40: Mass flows in compressor bypass under varying input mass flow.

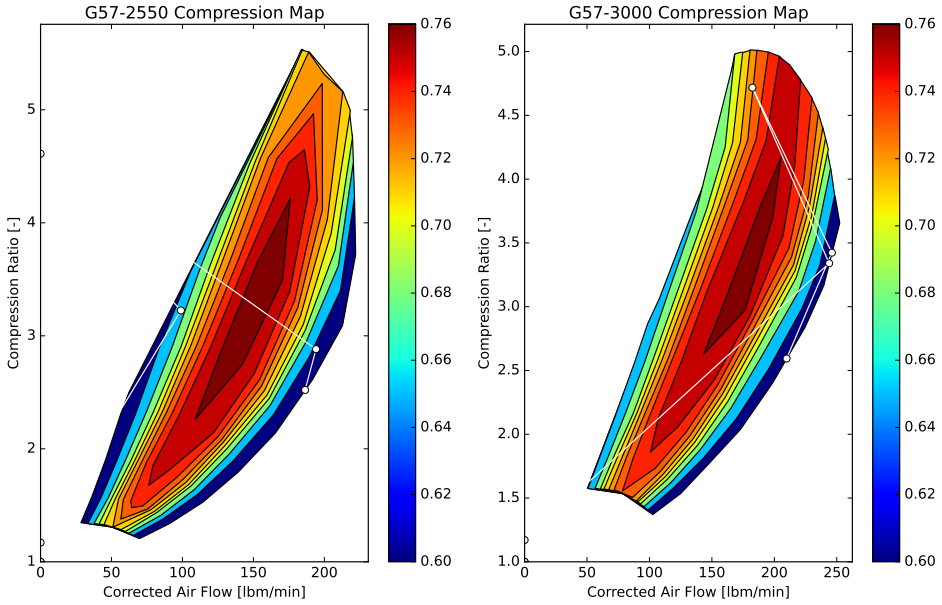

Figure 8.41: Compressor operating points, where the left-most operational diagram is the zero-th stage.

8.4.2. Thermal Limits

The physical compressor components have a maximum operational of 1323 [K][23]. Figure 8.42 and 8.43 show the pressures developed in the compressor and inter-cooler flows respectively.

It can be clearly concluded that this maximum operational temperature is not exceeded in the compressors, and that there is room for decreasing the air flow through the cold inter-cooler flow. On the turbine side energy is extracted from the flows rather than added. When extracting energy from a flow it can be reasonably assumed that the maximum operational temperature will not be exceeded in the turbine flow.

[23] https://www.garrettmotion.com/racing-and-performance/performance-turbos/ [accessed 22/6/2021]

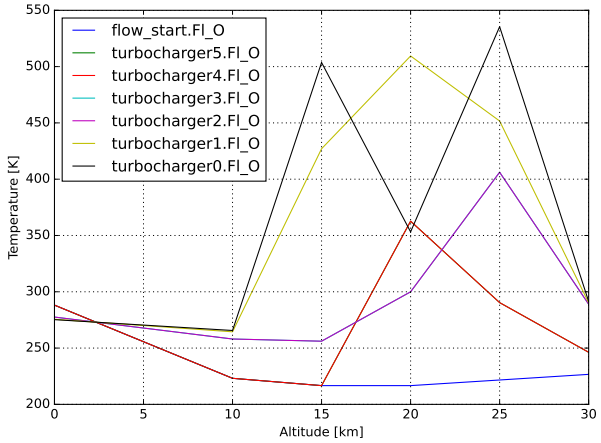

Figure 8.42: Temperatures reached in output flows of each compression stage for altitudes up to 30 [km], compared to the maximum allowable temperature of the compressor stages.

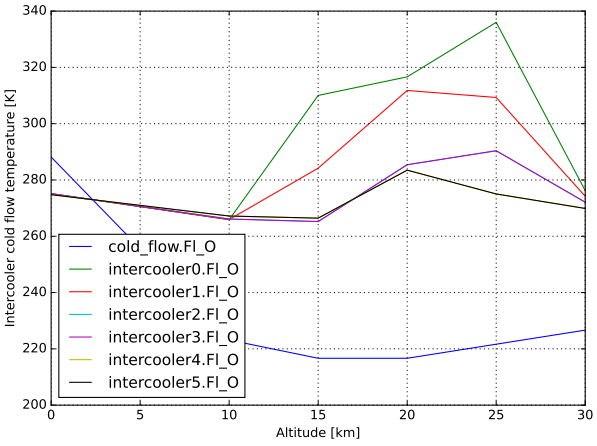

Figure 8.43: Inter-cooler flow temperatures of each turbine stage for altitudes up to 30 [km].

8.4.3. Further work

The methodology for compressor evaluation and matching, while capable of selecting a preliminary configuration, is not suitable for detailed control and optimization of configurations. This subsection shall discuss the remaining problems to be tackled before the method can be used effectively.

The critical issue is present when evaluating turbine pressure ratios, in that the method is unable to correctly iterate the pressure ratio, such that the shaft power residual is driven to zero. This problem is evidenced in Figures 8.44 and 8.45 where the turbine is operating outside of its operational range as evidenced by the high pressure ratios and completely bypassed turbines. This occurs due to the low slope of the turbine performance curve, where the guess of Newton's method is often far outside the bounds of the turbine operational domain. Despite proper bounds for backtracking being set, the pyCycle solver did not respect them for complex systems, resulting in a lot of time wasted searching for a solution in a range where one didn't exist. To tackle this problem, a simplified custom solver should be implemented. Additionally, in order to ensure that a turbocharger state can always evaluate, the mass preserving compressor component has to be modified to enforce a Π_{max,C_n} which is determined by the maximum power of the turbine.

In the current implementation, in order to ensure that thermal limits are met and to maximize power, the inter-cooler mass flow is taken at an unreasonably high value. Therefore, for any future implementation, to ensure that the configuration is operational at reasonable cooling mass flows the cooling flow must be incorporated into the objective optimization function.

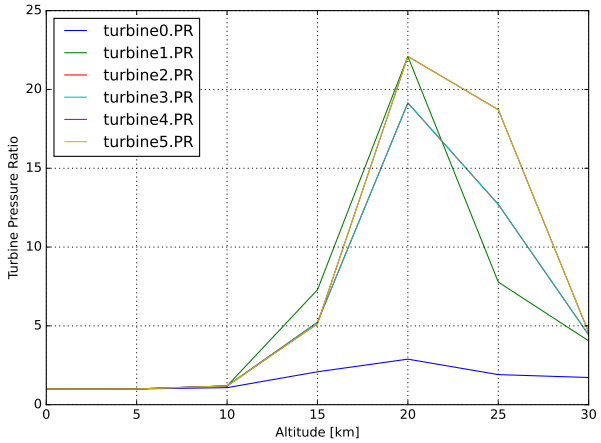

Figure 8.44: Turbine pressure ratios plotted against altitude.

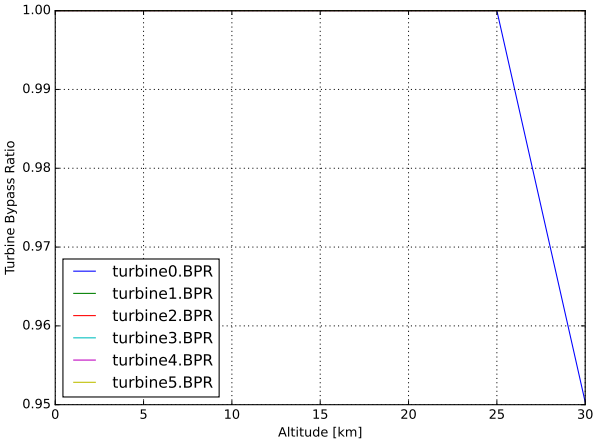

Figure 8.45: Turbine bypass ratios plotted against altitude.

8.5. Propeller design

For the design of the propeller, firstly an airfoil was chosen in Section 8.5.1. Then according to the thrust, and engine requirements the propeller diameter, number of blades and propeller pitch were determined in Section 8.5.2. The propeller was designed for cruise and take off (sea level) conditions as they were found to be the most critical.

8.5.1. Airfoil selection

The airfoil was chosen by a literature study and analysis of the airfoil in XFOIL for Reynolds numbers of $2{\cdot}10^5$ - $9{\cdot}10^5$ to examine its performance for take off and cruise. The two most important parameters included: high $C_{L\alpha}$ values and a large drag bucket with low drag to be able to operate the airfoil at different angles of attack. It was decided to use CLARK Y as it has been widely used in propeller designs [24] [52] [53] [54] and provided an adequate drag bucket.

8.5.2. Sizing and configuration

In propeller design the blade element momentum theory (BEMT) [25] was utilized to determine propeller geometry and performance. In BEMT, the propeller is divided into to a number of elements in the spanwise direction. The characteristics of each element are found and summed to determine the total thrust, torque and power. Due to its simplicity and computational time this method was preferred as it provides a quick first order estimation of the propellers configuration. Assumptions made in the method which reduce its accuracy include:

- No flow interaction and wake: there are no aerodynamic interactions between the different blades and blade elements. This causes the results to be overestimated as flow interaction and wake reduce total output thrust and propeller efficiency.
- All three dimensional aerodynamic effects are neglected: any aerodynamic effects that is not normal or tangential to the blade sections is neglected.
- Propeller is a rigid body: no aeroelastic effects are taken into account. This assumption, can overestimate the performance as losses due to of the propeller as material choice and structural design of the blade is not taken into consideration.
- No tip losses: Some flow is lost/bypasses the tip on propeller blades. It was assumed that this phenomenon does not occur. As a result this would overestimate the results as its assumed the propeller performs the same in the spanwise direction, even though it does not perform as well near the tips in reality.
- Steady flow (static condition): the free stream air is assumed to not change with respect to time. This does not hold in reality as turbulence and the propeller intake region can be affected by aerodynamic interactions with other parts of the aicraft. Therefore, the actual airflow is unsteady.

Before the sizing of the propeller, the thrust requirements at sea level and cruise were determined from Chapter 6 . Assuming a speed of 27 m/s (M = 0.079) and 120 m/s (M = 0.41 at 25km altitude) respectively, Table 8.8 was derived.

Table 8.8: Required thrust levels at sea level and cruise.

Flight condition	Total thrust [N]	Thrust per engine [N]
Sea level	1884	942
Cruise	839	419

The diameter, number of blades and propeller pitch were the main variables for choosing an appropriate propeller configuration. Secondly, the chord distribution was found to ensure the thrust

[24] https://www.sciencedirect.com/science/article/pii/S1270963819323375#bbr0230 [accessed 17/6/2021]
[25] https://glingram.webspace.durham.ac.uk/wp-content/uploads/sites/104/2021/04/wind_turbine_design.pdf [accessed 17/6/2021]

requirement was satisfied. Multiple factors were in consideration for choosing the propeller diameter. These include:

- Maximum torque by the engine: By increasing the diameter, the moment of inertia increases with quadratic growth. As a result, the torque required increases with diameter. This can be understood intuitively as a larger diameter will have greater inertia, thus a larger torque requirement. This can be seen in Equation 8.51, where T is the torque [Nm], m is the mass [kg], and d is the diameter [m] of the propeller:

$$T = m(d/2)^2\alpha \tag{8.51}$$

  with the aircraft sizing data shown in Chapter 6, it was determined a maximum of 3m diameter blade would be viable, to keep the landing gear as short as possible and to reduce the tail surfaces sizing. The tail surface sizing is affected by propeller diameter as a larger propeller would position the engine further away from the fuselage. Consequently, during one engine operative conditions, a larger tail surface would be required to balance the moment generated. Therefore, by interface management it was agreed to not exceed 3m diameter to satisfy the constraints put by other subsystems.

- Blade tip speed: with increasing diameter and at fixed rotations per minute (RPM) the tip speed increases. If the tip speed reaches near sonic speeds this will result in noise, vibration, and a large increase in drag. This is taken into consideration for both sea level and cruise conditions as is a major limiting factor in the sizing of the blades. From Equation 8.52 and Equation 8.53 and adjusting the mach number with respect to sea level and cruise conditions Figure 8.46 and Figure 8.47 were determined

$$V_{rot} = 2\pi r\text{rps} \tag{8.52}$$

$$V_{tip-helical} = \sqrt{V_{rot}^2 + V_{trans}^2} \tag{8.53}$$

  where r is the radius and rps is revolutions per second and V_{trans} is the airspeed and V_{rot} is the rotational velocity.

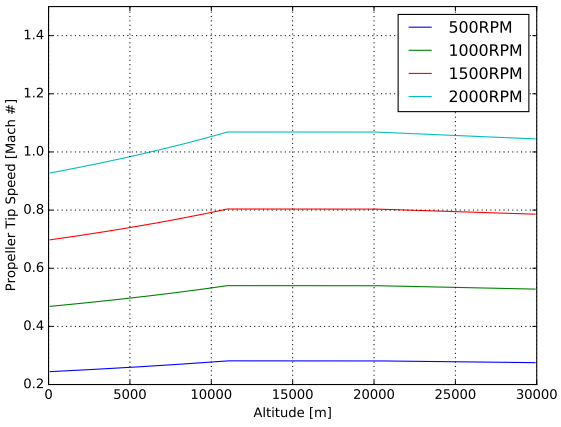

Figure 8.46: Blade tip mach number for varying RPM with respect to altitude, M = 0.0794 (27 m/s) and diameter = 3 m.

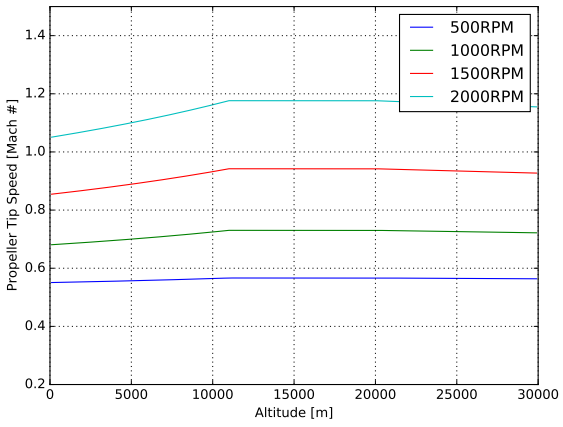

Figure 8.47: Blade tip mach number for varying RPM with respect to altitude, M = 0.41 (120 m/s) and diameter = 3 m.

It is seen clearly from Figure 8.46 that the sea level and cruise conditions are severely limiting the maximum RPM. As a result, the propeller pitch and chord will need to be designed to ensure enough thrust is produced.

- Material and structure: by increasing the diameter, the centripetal force increases causing more stress in the blades. The material choice should be made keeping in mind the environmental conditions and propeller configuration.

- Ground clearance: the diameter of the propeller should not affect the safe operation of the aircraft on ground and in flight. Moreover, the landing gear design is affected as a larger

diameter will require a longer landing gear, resulting in more weight on the aircraft which will have a snowball effect on all subsystems.

By increasing the number of blades, the propeller can generate more thrust as more power is extracted from the engine. On the other hand, due to the engine's torque limit, placing more blades also increases the torque requirement. Therefore, the number of blades should be minimized to not exceed engine torque limit during all operational phases. Moreover, using less blades minimizes weight. Blade pitch primarily affects the torque required and RPM. A low pitch propeller will rotate with a higher RPM and require less torque. Whereas a high pitch propeller will rotate slower and require more torque. Due to the tip speed constraint, especially at both conditions, RPM should be minimized. Also due to low air density at cruise, pitch should be maximized to be able to 'cut' through more air; thus generating sufficient thrust. Finally, the chord length of the blade affects the torque and thrust generated. By increasing the chord, more surface area is available and the airfoil will generate more normal (thrust) force. Though this will increase the torque requirement as well due to more drag generated on the airfoil. An optimization shall be used to determine the right balance. The use of a smaller chord length or anhedral at the tip is preferred to reduce any potential wake and improve efficiency [55]. Therefore, the chord distribution shall be designed in way such that the chord tapers at the tip.

With the use of pyBEMT a python module[26], an iterative procedure was performed to proceed to a feasible configuration. The iterative procedure follows:

- Estimate the number of blades, diameter, propeller pitch and chord distribution with the above given constraints on these parameters.
- Determine if the required thrust is produced at sea level.
- Determine if the configuration satisfies the torque and power limits by the engine at sea level.
- Check if the configuration satisfies the conditions and cruise.

If the design does not meet the requirements at sea level or cruise, the procedure is repeated until a configuration is found. Figure 8.48 below shows the thrust, torque and power coefficients and propulsive efficiency with respect to the advance ratio. As seen in Figure 8.48, the propeller still has room to be further optimized to have greater efficiency which can be refined as the propeller is equipped with variable pitch (12°for sea level, 43°for cruise). It was decided to use a variable pitch propeller. As the take off and cruise conditions are very distinct, determining a fixed pitch propeller which is equally efficient in both scenarios is unlikely. By allowing a variable pitch, it can be made certain that the efficiency will be greater by allowing more control over the RPM of the propeller, thus making sure the the blade tip mach number is in a range where aerodynamic effects are not a concern. To implement a variable pitch system, centrifugal weights, by means of oil pressure, or an electro-mechanical system could be utilized. The electro-mechanical system is advantageous as it will potentially have the least weight and can be made highly reliable (up to 99.95%) [56].

[26] https://pybemt.readthedocs.io/en/latest/index.html [accessed 23/6/2021]

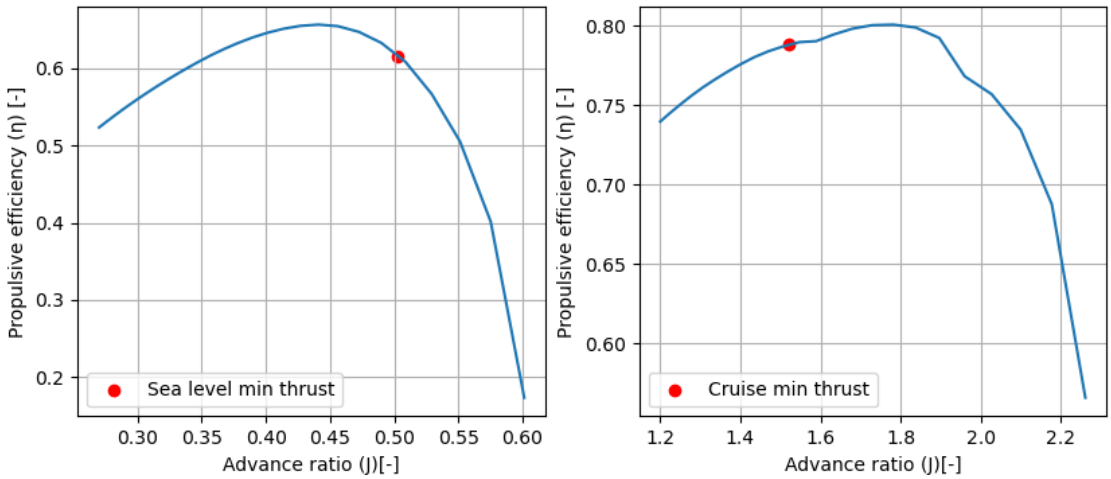

Figure 8.48: Propeller efficiency vs. advance ratio. Right: Sea level conditions, Left: cruise conditions

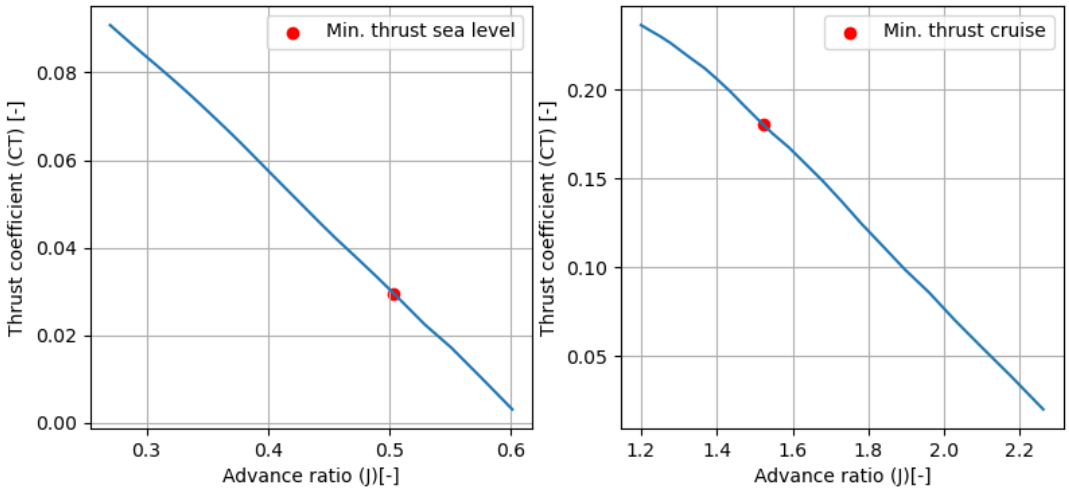

Figure 8.49: Thrust coefficient vs. advance ratio. Right: Sea level conditions, Left: cruise conditions

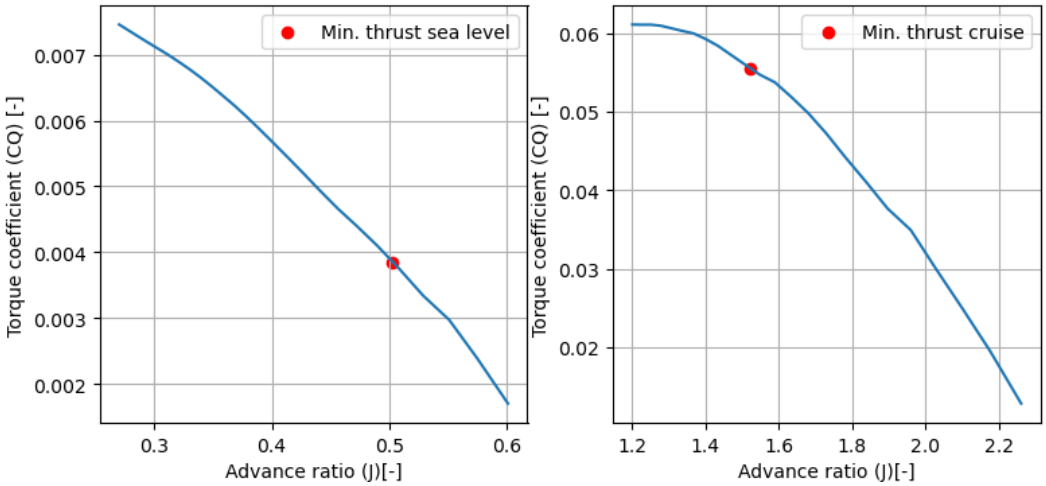

Figure 8.50: Torque coefficient vs. advance ratio. Right: Sea level conditions, Left: cruise conditions

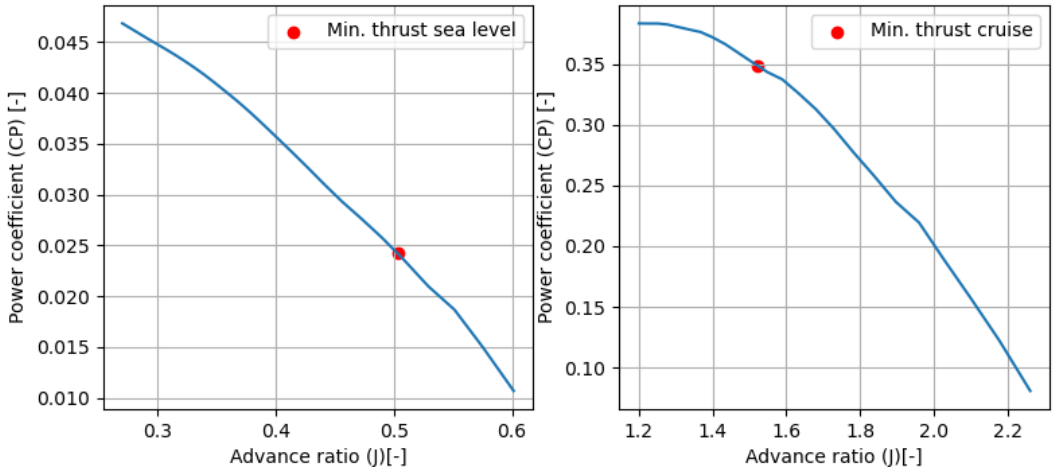

Figure 8.51: Power coefficient vs. advance ratio. Right: Sea level conditions, Left: cruise conditions

Where the advance ratio is defined as:

$$J = \frac{V}{nD} \tag{8.54}$$

where V is the free stream velocity, n is the revolutions per seconds and D is the diameter. Lastly, the thrust, torque and power coefficients, and propulsive efficiency are defined as [27]:

$$C_T = \frac{T}{\rho n^2 D^4} \tag{8.55}$$

$$C_Q = \frac{Q}{\rho n^2 D^5} \tag{8.56}$$

$$C_P = \frac{P}{\rho n^3 D^5} \tag{8.57}$$

$$\eta = \frac{J C_T}{2\pi C_Q} \tag{8.58}$$

where ρ is the density of the air. Though a verification of the results was not possible due to lack of reference data, the pyBEMT module has been validated against [28] where characteristics of six propellers were found experimentally. Hence, the results found provide a good first order estimate for further analysis of the design. The final values mentioned in Table 8.9 provide the propeller characteristics at sea level and cruise conditions. For take off, the RPM required was found to be 1072, which results in a tip blade mach number of 0.51. For cruise at an RPM of 1591, the tip blade mach number is 0.93. As a result, the tip blade mach number will be less than M = 1 during the complete operation. However, for efficiency, and mitigation of shock waves and other sonic region phenomenon, the tip blade mach number should never exceed 0.9 [29]. Due to this, the current design must be further optimized specifically to reduce the RPM to below 1500. As the diameter of the propeller is fixed, this analysis could be performed by defining a cost function to optimize pitch and chord length/distribution. If this does not provide a solution, further research could be performed on airfoil selection to obtain better aerodynamic characteristics.

Table 8.9: Note: Values provided are shown for one engine. The pitch is assumed to be constant spanwise.

	Thrust per engine [N]	Pitch [°]	RPM	Torque [Nm]	Power [kW]	J	C_T	C_Q	C_P	η
Sea Level min. thrust	942	12	1072	367	41.22	0.503	0.0296	0.00385	0.0242	0.616
Sea Level at max torque	969	12	1077	373	42.23	0.501	0.0303	0.00389	0.0245	0.619
Cruise min. thrust	419	43	1591	373	61.7	1.522	0.181	0.0555	0.349	0.788

[27] http://www.aerodynamics4students.com/propulsion/blade-element-propeller-theory.php [accessed 19/6/2021
[28] https://digital.library.unt.edu/ark:/67531/metadc66252/m2/1/high_res_d/19930091669.pdf[accessed 25/6/2021]
[29] http://www.trylam.com/files/ARO-103L_tlam_Week2.pdf [accessed 25/6/2021]

From Table 8.9 it can be seen that at cruise, maximum torque is utilized, thus more thrust cannot be generated and the fixed cruise speed is M = 0.41. For sea level conditions, the difference between the minimum thrust and thrust at max torque is minor. This was done intentionally as the upper limit of the torque allowed for the design of longer and larger chord lengths which are able to produce more thrust at lower RPM's. The chord distribution in the current design is of 0.3m and the tip of the blade is tapered to 0.2m. This was found by performing multiple iterations in pyBEMT to satisfy the RPM and torque limits. As stated, it is usually recommended to maintain the tip mach number below 0.9 [30] to avoid reduction in propulsive efficiency and excessive drag. Also, as the tip reaches M=1, shock waves, and noise is produced which can affect the structural integrity and airport noise requirements respectively. However, due to the requirement that the propellers shall produce an appropriate amount of thrust (shown in Table 8.8) the tip speed was comprised marginally to satisfy both sea level and cruise thrust requirements. For further design phases, a more detailed analysis using PowerFLOW (CFD) is recommended. By conducting a further analysis, some of the assumptions used in BEMT could be quantified and its effects on the design could be assessed to determine if the design still remains viable. Additionally, to reduce the tip speed and its effects, raked [57] and/or split tip [31] designs could be implemented which could also be analyzed using PowerFLOW.

[30] http://www.trylam.com/files/ARO-103L_tlam_Week2.pdf [accessed 25/6/2021]
[31] https://stacks.stanford.edu/file/druid:dk871sj7273/thesis-augmented.pdf [accessed 25/6/2021]

9

Structures & Materials

In this chapter, the structural analysis and design of the main aircraft components will be presented. In Section 9.2, the materials selection of the main components will be elaborated upon. Next, the structural analysis and design of the wing structure will be presented, allowing for a more accurate wing weight estimation. Finally, the structural weight of the main aircraft components will be elaborated upon in Section 9.3.

9.1. Material selection

The materials that are mainly used in the field of aerospace are metal alloys, such as aluminum and titanium alloys, or even composite materials, such as carbon fiber reinforced polymer or fiberglass. They all have in common that they all have a relatively high stiffness-to-weight ratio compared to other materials, while also having great thermal properties. The materials that have been taken into consideration for the RePLASMA aircraft can be found in Table 9.1, along with some of their main mechanical properties and prices. Carbon Fiber Reinforced Polymer (CFRP) has been selected because of it being ultra lightweight and stiff. The reason that Aluminum 7075 has been taken into consideration is that it is the most common aluminum alloy in today's aerospace industry. Ti-6Al-4V has been opted for because it has slightly better mechanical properties than aluminum and also better thermal properties. On a final note, the property "thermal performance" has been scored on a qualitative basis, with a scoring system of 1 to 5 with 1 being poor and 5 being great. [1][2][3][4][5][6]

Table 9.1: Some materials with their mechanical properties. [58]

	Density (ρ) [kg/m3]	**Young's Modulus (E) [GPa]**	**Specific stiffness (E/ρ) [kPa·m^3/kg]**	**Thermal performance [-]**	**Price [$/kg]**
Carbon Fiber Reinforced Polymer (CFRP)	1,600	85	53.125	Poor (1/5)	$21
Ti-6Al-4V titanium alloy	4,430	113.8	25.7	Great (5/5)	$21
Aluminum 7075	2,810	71.7	25.5	Good (4/5)	$8.1

From the table can be concluded that the carbon fiber reinforced polymer has the best stiffness-to-weight ratio E/ρ, with Ti-6Al-4V coming in second just before Aluminum 7075. The only downside of the CFRP is that its performance drastically decreases at temperatures below -50°C [59], which approximately equal to the temperature at which the RePLASMA UAV is supposed to fly. However,

[1] http://www.performance-composites.com/carbonfibre/mechanicalproperties_2.asp [accessed 25/6/2021]
[2] http://asm.matweb.com/search/SpecificMaterial.asp?bassnum=MA7075T6 [accessed 25/6/2021]
[3] http://asm.matweb.com/search/SpecificMaterial.asp?bassnum=MTP641 [accessed 25/6/2021]
[4] http://www.metalspiping.com/titanium-alloy-ti-6al-4v.html [accessed 25/6/2021]
[5] https://www.indiamart.com/proddetail/aluminum-alloy-7075-4049470448.html [accessed 25/6/2021]
[6] https://www.infosys.com/engineering-services/white-papers/documents/carbon-composites-cost-effective.pdf [accessed 25/6/2021]

one of the top-level requirements states that the aircraft should be able to operate up to temperatures of -100°C, which instantly makes the use of CFRP unfeasible. The stiffness-to-weight ratios of Ti-6Al-4V and aluminum 7075 are nearly equal, but the titanium alloy is slightly better as stated previously. The bigger differences lie in the in the pricing and thermal performance. It is therefore better to use aluminum 7075 as much as possible, and Ti-6Al-4V if it is really necessary.

The fuselage and tail of the RePLASMA UAV are not conventional, meaning that structural analyses of these components are complex. It is outside the scope at this stage of the design, as structures & materials only make up a small part of this project. The decision has therefore been made that the fuselage is set to 2 mm and the tail skin is set to 2.5 mm, because in general, fuselage and tail skin thicknesses are about 1.5 - 2.5 mm [60]. The tail skin thickness is set to be slightly higher than the fuselage skin thickness, because the torsional loads at the root of the V-tail is higher than for a conventional tail. The reason for this is that for a V-tail, the same loads are distributed over two connection points, whereas a conventional tail has three.

The skin materials for both fuselage and tail is selected to be aluminum 7075, mainly because it is the cheaper option. Besides, the fuselage and tail are not significantly influenced by the hot exhaust gases from the engine. Lastly, the materials in the wing are still to be determined; they will be finalized in Section 9.2.

9.2. Wing structural analysis & design

The wing box is the main load-bearing component in the wing. It also accounts for the largest part of the wing weight. Therefore, it is helpful to make a preliminary design of the wing box to obtain a better estimate for the wing weight. In the preliminary design, the driving requirement on the wing box is the deflection of the wing tip in the vertical z-direction, which should be smaller than 1.095 m (5% of semi-span of the wing). The reason for this is that the aircraft aerodynamic performance decreases rather drastically in case the wing tip bending exceeds this value.

The first step in the design is then to find a relation for the wing tip deflection. This is not straightforward, because the wing has a taper ratio of $\lambda = 0.4$. However, there exists an approximation for the wing tip deflection v, depending on the geometry of and the loads on the wing. This relation is presented in Equation 9.1 [61]. In this equation, κ_0 is the beam curvature at the wing root, M_0 is the bending moment at the wing root, E is the Young's modulus of the wing material, I_0 is the moment of inertia at the wing root and b is the wing span.

$$v \simeq \frac{1}{2}\kappa_0 \left(\frac{b}{2}\right)^2 = \frac{M_0}{EI_0}\frac{b^2}{8} \tag{9.1}$$

When analyzing Equation 9.1, it becomes clear that there are three steps in determining the wing tip deflection. Particularly, determining the internal bending moment, defining the wing box geometry and selecting a wing box material. These three steps are heavily dependent on each other: the wing box geometry and material influence the weight of the wing, which then influences the bending moment of the wing. Therefore, an algorithm must be built, which uses the wing box geometry and material as an input to determine the bending moment, which ultimately leads to a wing tip deflection. The best option in this case will be the option with the lowest weight and best material characteristics.

9.2.1. Wing Geometry

Thus, the initial step in determining the geometry of the wing box is to determine the outline of the wing box. The outline of the wing box consists of a front and a rear spar, as well as a top and a bottom panel. The location of the front spar is fixed to $x = 0.2c$, whereas the rear spar location is fixed to $x = 0.75c$ [13]. It must be noted that the rear spar is placed at this location to allow for enough space for the ailerons. The top and bottom panels follow the contour of the airfoil.

As stated above, the cross-section of the wing box will not be symmetrical. This will complicate the analysis of the bending of the wing to a degree that falls outside the scope of preliminary design. Therefore, several assumptions have been made. For the structural analysis, the top and bottom

panels will be straight so that the outer shell of the wing box is rectangular. This will slightly alter the moments of inertia of the wing box, meaning that the analysis will also be slightly off. However, the perimeter of the original and the simplified wing box are equal, which implies that the weight of both wing boxes will in fact also be equal. All of this is visualized in Figure 9.1, where the cross-section of the airfoil including the outlines of the wing boxes is presented.

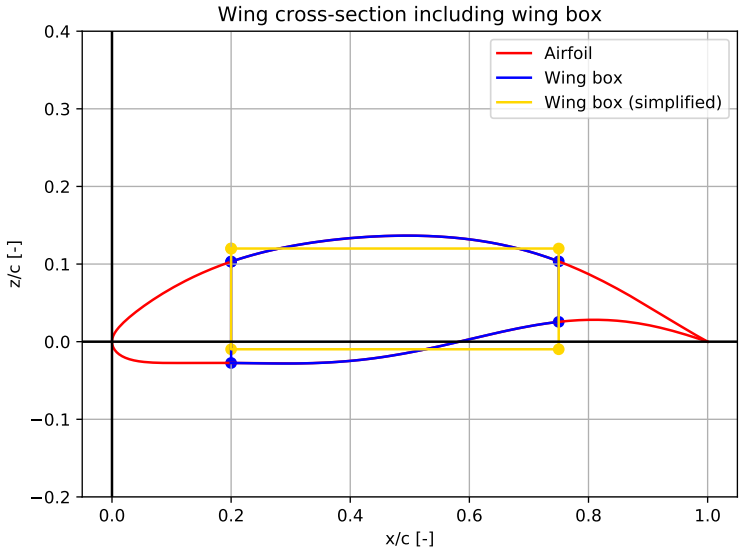

Figure 9.1: Wing cross-section including wing boxes.

For the preliminary design, the wing box also consists of stringers. Stringers are thin-walled structures that transfer the loads of the skin and are therefore good at taking up the bending loads on the wing. They come in different shapes and size, as can be seen in Figure 9.2. Out of these five options, a compromise must be made between manufacturability, bending stiffness and weight. The I-shaped and Hat-shaped stringer are dropped, because they are simply more complex than the other options. The Z-shaped stringer is then also dropped, because fastening it will probably cause more problems than with the other shapes. Considering that the loads in the vertical direction are greater than in other directions, the extra horizontal part of the C-shaped stringer will not bring more advantages into the design with respect to the L-shaped stringer. It will only make the wing unnecessarily more heavy, which is why the L-shaped stringer was ultimately chosen.

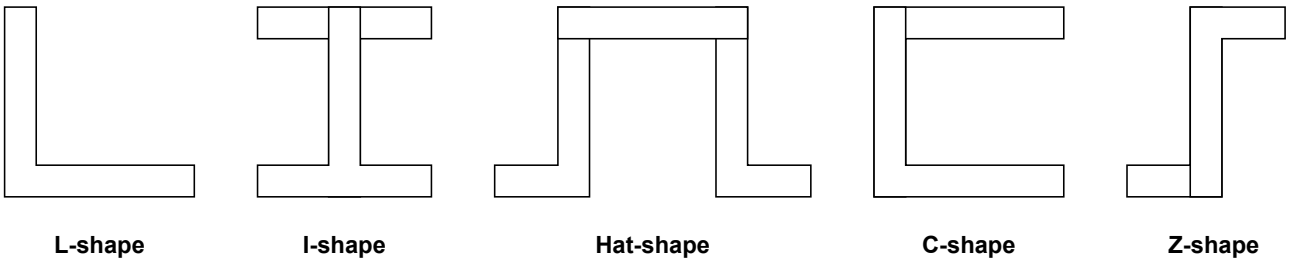

Figure 9.2: Different stringer shapes.

The sizes out of which the algorithm can choose must also be determined. The best option is to make a few standard sizes, because the program will otherwise be too compute-intensive. These standard sizes can be found in Table 9.2, next to the stringer cross-section in Table 9.3. On other thing that should be noted is that the size of the stringer does not vary along the wing span, because that will be too complex to manufacture. Furthermore, only one option will be used throughout the whole wing box.

Table 9.2: Different standard stringer sizes.

	Width [mm]	Thickness [mm]
Option 1	25	1
Option 2	20	1
Option 3	15	1.5
Option 4	20	1.5

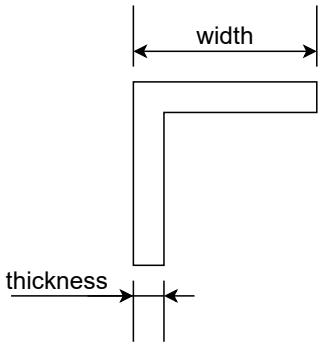

Figure 9.3: Cross-section of the L-shaped stringer).

The last part of the wing geometry is the wing skin. The moment of inertia of the wing skin is rather difficult to determine. For this purpose, XFOIL has been used, and in particular XFOIL's BEND function. This function gives an approximation for the bending properties of the airfoil.

9.2.2. Loads on wing

The next step in the process is to analyze the loads acting on the wing in vertical direction. For this purpose, the wing will be modelled as a tapered beam with rectangular cross-section. Moreover, the design load case must be determined. The two different load cases that have been analysed can be found in Table 9.3. As can be seen in the table, the loads during take-off are higher than during cruise, but not too significantly. Hence, the loads will be analyzed during take-off. Now that the load case has been determined, the free body diagram of the wing in z-direction can be drawn, which can be found in Figure 9.4. One assumption that was made in the free body diagram is that the lift is equally distributed over the wing, simplifying the analysis of the loads.

Table 9.3: Different load cases.

Load case	Wing lift [kN]
Take-off	40.6
Cruise	39.9

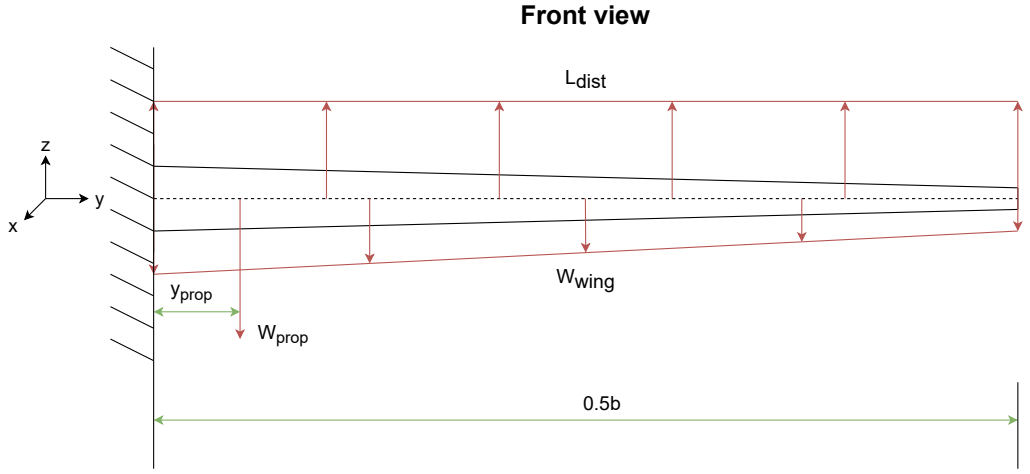

Figure 9.4: Free body diagram of the left wing in z-direction. The positive x-direction point out of the paper.

In Figure 9.4, $y_{prop} = 2$ m, $W_{prop} = 3649$ N, $b_{hs} = 21.9$ m and $L_{dist} = 928$ kN/m. The weight of the wing can not be assigned a fixed value, because it varies with the wing geometry and material.

9.2.3. Optimization Algorithm and Results

The optimization algorithm is a Python program written especially for the purpose of generating the best possible wing configuration. A flow chart of this algorithm can be found in Figure 9.5. The program chooses a wing configuration using the parameters found in Table 9.4. In this table, the range in which every parameter is also given. After choosing a configuration, the program calculates the moment of inertia I_0 in parallel with choosing a material. It then calculates the wing weight W_{wing}, after which it calculates the internal moment at the wing root M_0. The last step is then to calculate the wing tip deflection v. When all configurations have been analyzed, the lightest configuration will be selected for the final design. The results of the optimization algorithm can also be found in Table 9.4.

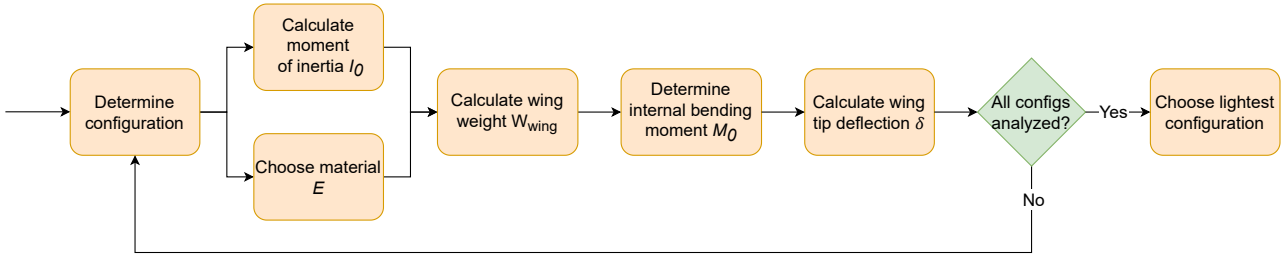

Figure 9.5: Flow of the wing structural design.

Table 9.4: Parameters that are varied in the algorithm, together with optimized configuration.

Parameter	Optimization range	Final value
Panel thickness	0.5 - 2 mm	1.5 mm
Spar thickness	0.5 - 2 mm	0.5 mm
# of stringers on top panel	2 - 20	9 (selected stringer is option 2)
# of stringers on bottom panel	2 - 20	8 (selected stringer is option 2)
# of spars	2 - 5	3
Wing skin thickness	0.5 - 2 mm	0.6 mm
Material	aluminum 7075 or Ti-6Al-4V	Ti-6Al-4V

9.2.4. Internal loads

Now that the geometry of the wing has been established, the internal loading diagrams and deflection diagrams in z-direction can be set up. The loading and deflection diagrams of the other directions can also be set up, but for this design, it will not be of any added value. The internal loads can directly be derived from the free body diagram, starting with the bending moment M_x. The bending moment about the x-axis is positive such that it creates tension in the xz-plane. Thus, in this case it will be clockwise positive. Once the bending moment along the wing span has been determined, the shear force V_z can be determined using the relation as can be seen in Equation 9.2.

$$V_z = \frac{\mathrm{d}M_x}{\mathrm{d}y} \tag{9.2}$$

Equation 9.3 must be integrated once to obtain the slope of the wing in z-direction v', and twice to obtain the deflection of the wing in z-direction v.

$$\frac{\mathrm{d}^2 w}{\mathrm{d}y^2} = -\frac{1}{EI_{xx}} M_x(y) \tag{9.3}$$

The internal loading and deflection diagrams can now be set up. They are presented in Figure 9.6. In the top left graph, it can clearly be seen at which point the propulsion system is located along the wing. Furthermore, the wing deflection looks quite significant in the bottom right graph, while in real life this would not be the case. Also note that in this method, the wing tip deflection is calculated differently than in Equation 9.1. However, using this method the wing tip deflection is only 4.7% larger. It can therefore be said that the relation of Equation 9.1 is quite accurate.

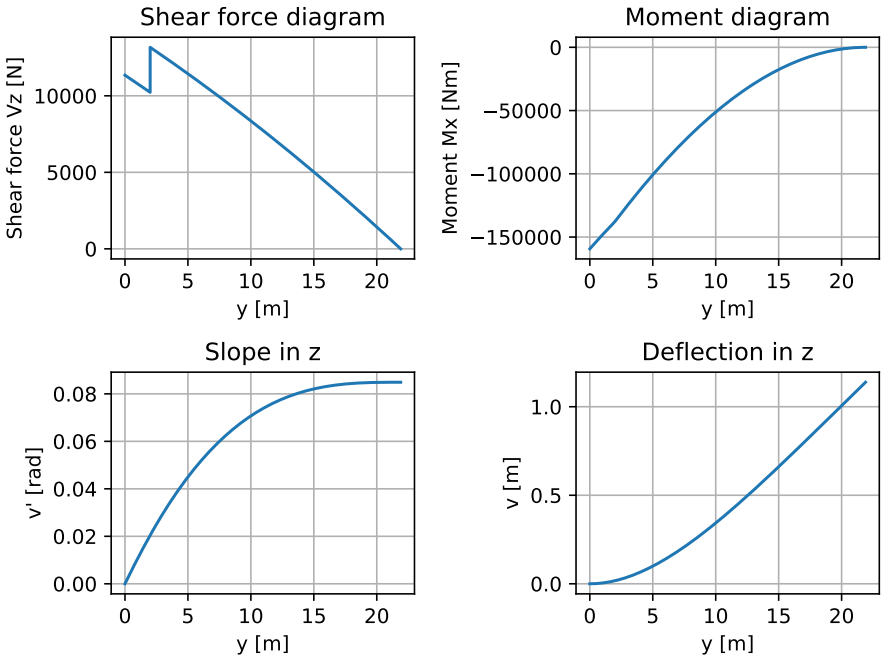

Figure 9.6: Internal force, moment and deflection diagrams in z-direction.

9.2.5. Verification

The verification of the wing design program has been performed as follows. The bending moment at the wing root has been verified by calculating it by hand and comparing it to the moment at the wing root that the program calculates. The same procedure has been performed for the moment of inertia. Furthermore, the loading diagrams have been verified by drawing them by hand. Other assumptions, such as the rectangular outline of the wing box as well as the evenly distributed lift are also plausible, because as stated in the previous subsection, the wing tip deflection determined by the method using Equation 9.3 is only 4.7% larger than the one approximated by Equation 9.1.

9.3. Weight estimations

The final important task of task is the weight estimation of the fuselage, tail and wing. This is not particularly complex in case of the wing, because it is an output of the optimization algorithm. However, for the fuselage and the tail, it is also not that difficult, but it requires a few more steps. The thicknesses and materials of both components are already known (see Section 9.1), but the shell areas are still unknown. This is where the CAD models come in useful, because they automatically generate the outer area. The only task left is to multiply it by the thickness of the desired component and density of the desired material. The weight of the fuselage, wing and tail are presented in table Table 9.5.

Table 9.5: Weight estimations for fuselage, wing and tail.

	Volume [m^3]	**Material density [kg/m^3]**	**Component weight [kg]**
Fuselage	0.096	2810	261.2
Wing	0.23	4430	1019
Tail	0.108	2810	304.7

10

Stability & Control

In this chapter, the analysis and assessments regarding the controllability and stability of the design will be presented. Firstly, Section 10.1 will examine the centers of gravity of the aircraft at various conditions and elaborate on how it varies, as knowing where the center of gravity of the aircraft is critical to ensure stability. Then, Section 10.2 and Section 10.3 will explain the methodology and criteria that were taken into account for horizontal and vertical tail sizing respectively. Section 10.4 will introduce the innovative V-tail concept that is to be utilized in RePLASMA due to its benefits for overall controllability and stability of the UAV. Finally, Section 10.5 will explain the empennage control surfaces required to adjust and control the flight attitude, and Section 10.6 will describe the autonomous flight control system that the UAV will possess.

10.1. CG and loading analysis

The first step to analyzing the stability of the aircraft is determining the position of its center of gravity throughout its mission profile, starting off with CG location at Operational Empty Weight (OEW). Without having a detailed plan of the aircraft configuration along with all of its subsystems, CG estimation for separate subsystems is predominantly based on statistical approaches such as the Torenbeek method [14]. The coordinate system adopted for this section is centered at the nose of the vehicle with the x-axis pointing along its length, the z-axis pointing upwards and the y-axis completing the right-hand rule. Firstly, the wing center of gravity was estimated to lay at about 40% of the chord from the leading edge of the wing, placing it at approximately 4.31 m from the nose of the fuselage. While for the fuselage, the estimation was based on formulas for a twin propeller aircraft with engines mounted on the wing as per Torenbeek, putting the fuselage's CG at 4.00 m. This method was also employed for the remaining subsystems as well resulting in the values found in Table 10.1.

Table 10.1: Center of gravity positions for main subsystems.

Subsystem	**CG location [m]**
Wing group	4.31
Fuselage group	4.00
Empennage	6.80
Landing gear	4.60
Propulsion group	3.56

Here it should be mentioned that even though mass estimations were done for many more subsystems, their exact contributions to the CG were spread across different groups due to the high uncertainty of their placement. For example, the fuselage group includes the fuselage, electrical and instrumentation subsystems while the wing group includes the wing and the hydraulic sys-

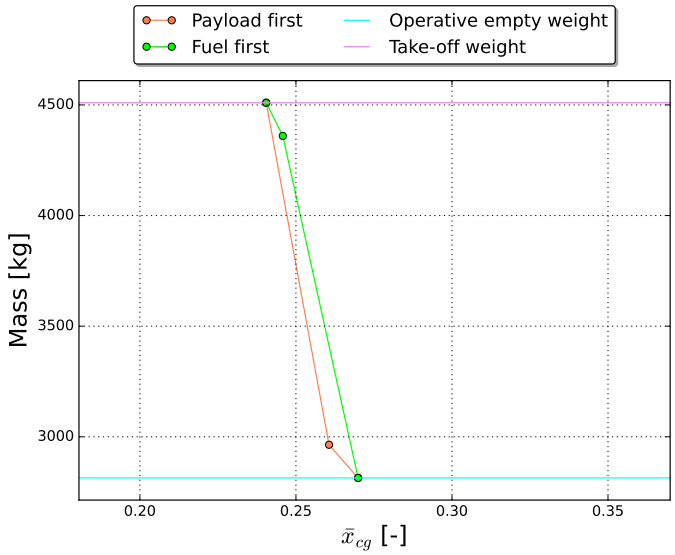

Figure 10.1: Loading diagram for RePLASMA.

tem. All of this resulting in a center of gravity location of 4.27 m from the nose at Operative Empty Weight.

The next step is to analyze the CG movement after loading the fuel and the payload of the UAV. Starting off with the fuel, since its placed both inside the fuselage and inside the wings, its contribution will be split 50/50 between the two subsystems. As for the payload, its position is fixed at 50% of the fuselage length. After using standard loading procedures, the following loading diagram was generated as presented in Figure 10.1.

where it can be seen that the most forward CG position is at about 57% of MAC while the most aft position lays at around 63%, resulting in a 6% CG shift during the mission profile. Of course, to size the horizontal stabilizer for the minimum area, this range should be as minimal as possible. One way to achieve that is by shifting the position of the wing, which due to its weight, has a considerable impact on the UAV's center of gravity. This effect can be explored by continuously translating the wing along the fuselage and recording the CG range that is produced. The results of this procedures can be seen in Figure 10.2.

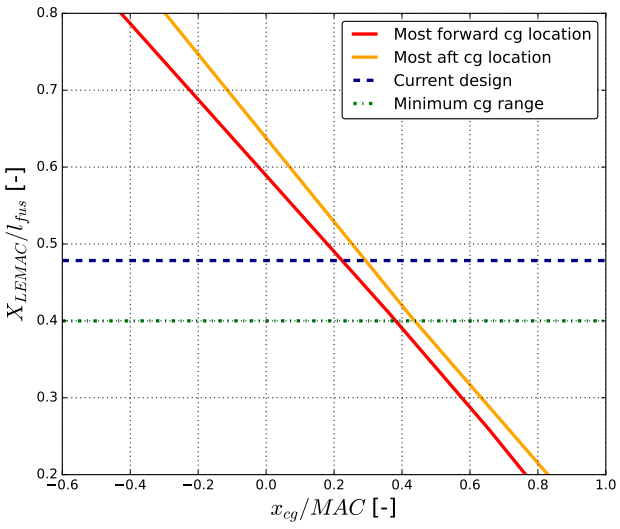

Figure 10.2: Effect of wing position on the center of gravity shift during the mission profile.

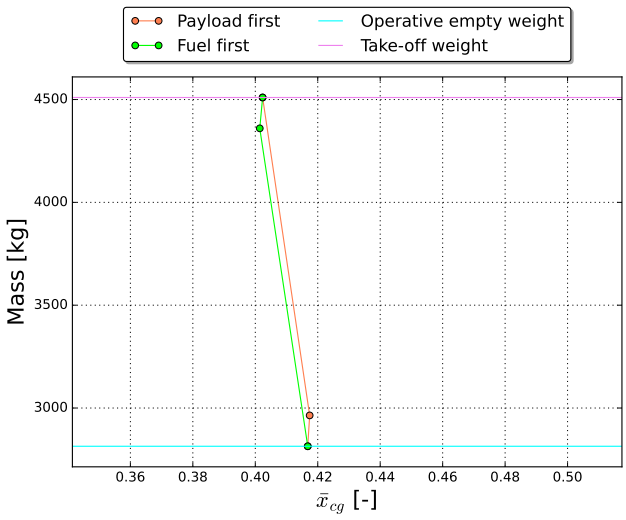

Figure 10.3: Loading diagram generated after updating the wing position to its optimal location.

By moving the wing's leading edge MAC position to 40% of the fuselage, the maximum CG range decreases to about 2% as seen in Figure 10.3.

10.2. Horizontal tail detail design

Having positioned the wing and estimated the movement of the center of gravity during the UAV's mission, the horizontal stabilizer responsible for stabilizing and controlling it can be designed. The two equations that dictate the required tail area for stability and controllability of an aircraft with a conventional tail are the following [62]:

$$\frac{S_h}{S} = \frac{1}{\frac{C_{L_{\alpha_h}}}{C_{L_{\alpha_{A-h}}}}\left(1-\frac{d\epsilon}{d\alpha}\right)\frac{l_h}{\bar{c}}\left(\frac{\bar{V}_h}{V}\right)^2}\bar{x}_{cg} - \frac{\bar{x}_{ac} - S.M.}{\frac{C_{L_{\alpha_h}}}{C_{L_{\alpha_{A-h}}}}\left(1-\frac{d\epsilon}{d\alpha}\right)\frac{l_h}{\bar{c}}\left(\frac{\bar{V}_h}{V}\right)^2} \tag{10.1}$$

$$\frac{S_h}{S} = \frac{1}{\frac{C_{L_h}}{C_{L_{A-h}}}\frac{l_h}{\bar{c}}\left(\frac{\bar{V}_h}{V}\right)^2}\bar{x}_{cg} + \frac{\frac{C_{m_{ac}}}{C_{L_{A-h}}} - \bar{x}_{ac}}{\frac{C_{L_h}}{C_{L_{A-h}}}\frac{l_h}{\bar{c}}\left(\frac{\bar{V}_h}{V}\right)^2} \tag{10.2}$$

A myriad of parameters affect the final output of both equations. An important aspect that affects those parameters is the horizontal tail's airfoil. The first criteria to consider when selecting the airfoil is that it must be able to produce both positive and negative lift due to the CG shift and therefore, it must have a symmetrical shape. Moreover, it is of upmost importance that the horizontal tail stalls after the main wing, and thus, the airfoil must be usable at very high ranges of AoA. For those reasons, the airfoil chosen for the horizontal stabilizer is the NACA 0012.

It is also important to note that those two conditions were investigated at different operative points. The stability condition was explored assuming that the aircraft is in cruise flight due to the fact that the neutral point is in its most forward position at maximum speed. On the other hand, the controllability condition was investigated during the landing phase, because that is when the maximum $C_{L_{A-h}}$ is achieved.

To obtain values for the parameters involved in Equation 10.1 and Equation 10.2 both analytic and semi-empirical methods were used. For example, to obtain the lift gradient of the horizontal tail - $C_{L_{\alpha_h}}$ - firstly, the polar for the 2D airfoil was generated using XFOIL for the respective flight condition, the lift gradient was extracted and then converted to wing lift gradient using Equation 7.14. As for the aerodynamic center of the wing-fuselage system, the following equation was used [62]:

$$\left(\frac{x_{ac}}{\bar{c}}\right)_{wf} = \left(\frac{x_{ac}}{\bar{c}}\right)_{w} - \frac{1.8}{C_{L_{\alpha_{A-h}}}}\frac{b_f h_f l_{fn}}{S\bar{c}} + \frac{0.273}{1+\lambda}\frac{b_f c_g (b-b_f)}{\bar{c}^2(b+2.15b_f)}\tan\Lambda_{1/4} \tag{10.3}$$

For the sake of conciseness, a detailed derivation of all the parameters is omitted and summary of all relevant numerical values can be found in Table 10.2.

Table 10.2: Main parameters involved in stability and controllability analysis.

Parameter	CLah	CLaAh	deda	VhV	xac	lh	CLh	CLmax	Cmac
Value	3.93	6.93	0.321	0.850	0.242	6.44	-1.00	1.46	-0.250
Unit	[-]	[1/rad]	[-]	[-]	[-]	[m]	[-]	[-]	[-]

With those values, the stability and controllability can now be analyzed, resulting in Figure 10.4.

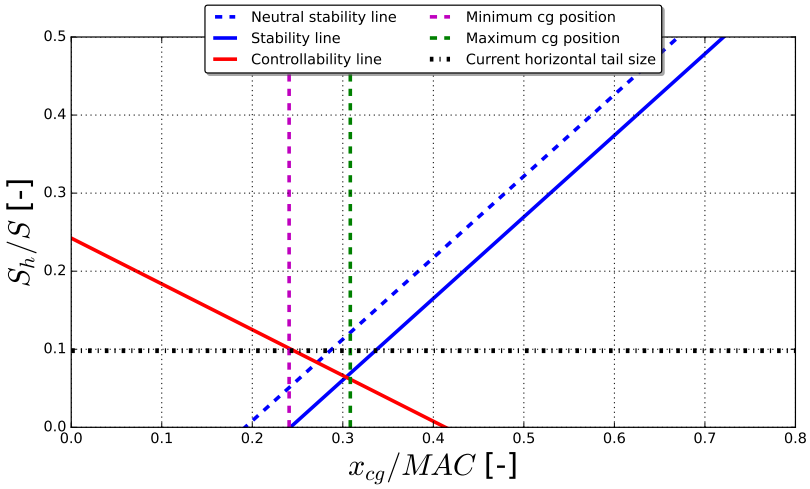

Figure 10.4: Scissor plot for RePLASMA, containing stability and controllability requirements.

As seen, despite meeting the controllability requirement, the current horizontal stabilizer design does not meet the neutral stability requirement and therefore, the area has to increase from 7.6 m^2 to 9.4 m^2. And with this, the sizing for the horizontal tail can be concluded.

10.3. Vertical tail detail design

The stability and controllability criteria assessed so far are regarding the longitudinal forces and moments, however lateral stability and controllability of the aircraft is also very important. This is especially the case for RePLASMA, considering that a client requirement demands the aircraft to have autonomous landing capability in case of an engine failure. Therefore, the estimate of 8.85 $[m^2]$ for the vertical tail size obtained in Chapter 6 must be carefully evaluated to ensure dynamic lateral stability for the UAV.

The lateral control and stability of an aircraft is examined in four main requirements, which are about the cross-wind, directional stability, engine failure, and spin. Moreover, for aircraft that operate with wing mounted engines, the critical design case for the vertical tail is reported to be at the one engine out situation rather than the other three considerations that were mentioned. [63] Hence, the evaluation of the vertical tail was done in accordance with the inoperative engine scenario although remarks have to be made regarding the other lateral stability criteria.

The case for having a dorsal fin is definitely a modification of the vertical tail that must be discussed. A dorsal fin is a fillet that connects the front of the vertical tail to the upper part of the fuselage, as shown in Figure 10.5. The benefit of having a dorsal fin is that it postpones the stall angle for the vertical tail, thus keeping the aircraft laterally stable and controllable at high sideslip angles [64]. Although it has a negligible impact for sideslip angles of up to 20 degrees, it is proven that the vortex generated by the dorsal fin is heavily influential at higher angles [65]. Furthermore, it is reported that this prevention of stall at relatively low sideslip angles is also beneficial to mitigate rudder lock, which is a deflected rudder suddenly reversing due to a vertical tail stall. [66]. Another advantage of the dorsal fin is that it reduces the lateral instability of the fuselage in yaw moment, hence allowing the vertical tail to be smaller in size (to be discussed further later in this section).

Figure 10.5: Illustration of a dorsal fin (marked in red) [66].

10.3.1. One engine out situation

The case of an engine failure in an engine of the UAV causes the moment equilibrium to be broken as a torque is generated by the operative engine. The role of the vertical tail in this situation is to restore the lateral balance by generating forces and moments by making use of the rudder and sideslipping flight. This leaves four sources of forces and moments that have to be taken into consideration [64]: thrust asymmetry, side force & yawing moment of the aircraft without the vertical tail, aircraft weight, and side force & yawing moment of the vertical tail. Combining these factors and solving for equilibrium with dimensionless coefficients leads into Equation 10.4:

$$\eta_v C_{Y_{v\alpha}} \frac{S_v}{S} = \frac{C_L \frac{y_e}{l_v} \frac{\Delta T_e}{W} + \beta (C_{N_\beta})_{A-h} \frac{b}{l_v}}{\tau_v \delta_r - (\beta - \sigma_v)} \tag{10.4}$$

In Equation 10.4, all parameters except for the rudder deflection (δ_r), sideslip angle (β), and the sidewash angle (σ_v) are set, with the parameter for the vertical tail area (S_v) being assessed. Firstly, for the current size of the vertical tail, the required rudder deflection to maintain equilibrium for varying sideslip angles were examined. Sideslip angles between the extremes at ±25 degrees were taken into consideration as it has been reported as the possible transient peak value [64]. With the linear relationship as stated in Equation 10.4, the maximum required rudder deflection remained below 30 degrees, a value which has been the maximum possible deflection for many reference aircraft [64]. The critical value of 29.2 degrees was reached at 25 degrees of sideslip and it is noteworthy that for sideslip angles lower than 20 degrees, the equilibrium rudder deflection is computed to be less than 25 degrees, which is a capability of most aircraft. Furthermore, for comparison the same relation was plotted for a range of vertical tail sizes, as shown in Figure 10.6:

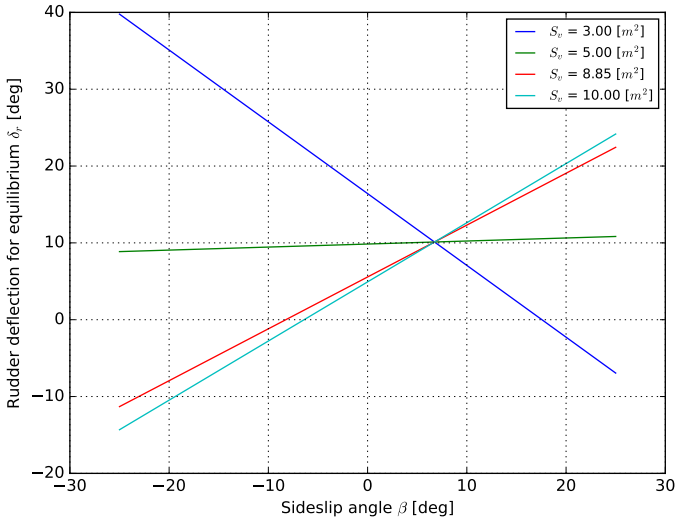

Figure 10.6: Required rudder deflection for equilibrium for varying sideslip angles, plotted for various vertical tail sizes.

Using this plot, it was looked to optimize the vertical tail size such that the rudder movements are minimized in case sideslip angles are observed due to crosswinds. From Figure 10.6, it is seen that among the plotted sizes, a vertical tail area of 5 m^2 results in the flattest line and thus is the closest to the optimal vertical tail size. After performing calculations with a more detailed variety of sizes, it was concluded that 4.87 m^2 is the best for minimal rudder deflection to maintain lateral stability.

10.3.2. Weathercock stability

Despite the criterion assessed in the previous subsection suggesting for a downsize of the vertical tail, another significant criterion, namely the weathercock stability must also be taken into consideration while designing the vertical tail for one engine inoperative scenario. The previous subsection had

already made use of the weathercock stability of the aircraft excluding the vertical tail, C_{N_β}, and now an elaboration of the weathercock stability of the whole aircraft has to be done by adding the parameter for the vertical tail. The weathercock stability coefficient of the vertical tail is given in Equation 10.5.

$$(C_{N_\beta})_v = C_{Y_{v_\alpha}} \left(1 - \frac{d\sigma}{d\beta}\right) \left(\frac{V_v}{V}\right)^2 \frac{S_v l_v}{Sb} \tag{10.5}$$

From literature [63], it is known that for an aircraft to be considered laterally stable, as per regulations, the $(C_{N_\beta})_{A-h}$ value has to be positive, with typical values ranging around 0.4. Hence, an initial assessment of the C_{N_β} was made with a vertical tail area of 4.87 $[m^2]$ and the total weathercock stability was calculated to be 0.0015. As this value is not considered safe enough, the vertical tail was resized so that a C_{N_β} value of at least 0.4 is reached. The corresponding vertical tail area was 11.05 $[m^2]$, and even though this is more than double the optimal area obtained in Figure 10.6, it is not a large change on the initial sizing estimate. Also, the required rudder deflections for the considered sideslip angles remain within a controllable margin and thus it was concluded to have a vertical tail area of 11.05 $[m^2]$.

10.4. The V-tail concept

After the horizontal and vertical tailplanes required for longitudinal and lateral stability were found, a brainstorm on the layout of the empennage was conducted. A brief consideration of various conventional and also outside-the-box options paved the way into the V-tail configuration, shown in Figure 10.7, to be the leading option. This is due to several significant advantages brought by the V-tail configuration: since the amount of components are reduced, the weight of the aircraft is expected to decrease, and less interference between the fuselage and empennage inspiring a better aerodynamic performance. Some other advantages caused by the V-tail are the reduction of debris impact and engine effect on downwash/sidewash. On the other hand, this novel configuration also brings some disadvantages, mainly due to its complexity: decoupling lateral and longitudinal control is more difficult and torsional loads on the fuselage is increased. However, for the considered UAV design, the advantages brought on by the V-tail configuration far outweigh its disadvantages, and thus was chosen as the empennage layout.

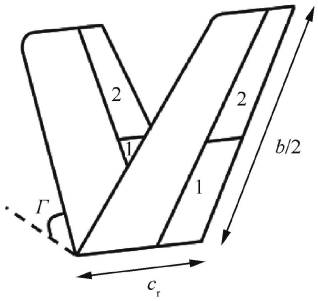

1—For pitching; 2—For yawing; *b*/2—Semi span;
c_r—Root chord; *Γ*—Dihedral angle

Figure 10.7: An example illustration of a V-tail, with its key geometric features[67].

For the conversion of the existing conventional empennage design to a V-tail, the methods described by Oliviero [63] and Gómez-Rodríguez et al. [68] were used. From this, the area of each of the two tailplane and the V-tail dihedral were calculated in Equation 10.6 and Equation 10.7, respectively:

$$S_{VT} = 0.5(S_H + S_V) \tag{10.6}$$

$$\Gamma_{VT} = \arctan\left(\frac{S_V}{S_H}\right) \cdot \frac{180}{\pi} \tag{10.7}$$

The area of each V-tail planforms were calculated to be 10.49 m^2 and the dihedral at 48.04 degrees. Furthermore, for the determination of other key geometric parameters of the V-tail such as the aspect ratio, taper ratio, the values from the original horizontal tail were considered as is recommended

by literature [68] and the sweep was taken the same as the original vertical tail. Thus, the final geometric parameters of RePLASMA's V-tail empennage is given in Table 10.3:

Table 10.3: Key geometric parameters of the V-tail of RePLASMA.

Parameter	**Value**
Empennage area (each of the two)	10.49 m^2
Dihedral angle	48.04°
Span	6.48 m
Root chord	2.31 m
Tip chord	0.93 m
Half-chord sweep	20.0°

Finally, for the detailed design, the weight of the empennage has to be updated. This will also be used as a verification tool for the foresight made earlier in this section that the V-tail will result in a lower weight. From Chapter 6 it is known the the preliminary weight of the whole empennage is 199.36 kg, 88.18 kg of which is from the horizontal tail and the vertical tail weighing 111.18 kg, although Section 10.2 and Section 10.3 have since found that larger tail areas are needed for longitudinal and lateral stability, which implies that the empennage weight will be increased for a conventional tail configuration. Since the weight estimation of a V-tail, especially for a HALE UAV, is not mentioned in the previously used literature [64], research was conducted to find accurate V-tail weight estimation methods. A statistical regression method proposed by Z. Yi and W. Heping [69] was deemed useful for RePLASMA due to its credibility and accuracy in terms of mission profile. The suggested formula for the weight of the V-tail is given in Equation 10.8:

$$W_{VT} = 0.022\left[W_{TO}^{0.813} \cdot n_{ult}^{0.813} \cdot S_{VT}^{0.584} \cdot \left(\frac{b_{VT}}{t_{r_{VT}}}\right)^{0.033} \cdot \left(\frac{MAC_{wing}}{l_v}\right)^{0.28}\right]^{0.915} \tag{10.8}$$

Combination of these values in this equation gives an empennage weight of 123.50 kg, which is a significant reduction from the preliminary weight despite the surface areas of the original horizontal and vertical tails increasing. This result hence justifies the design choice for a V-tail instead of a conventional layout.

10.4.1. Verification

To verify that the design of the V-tail still meets the stability requirement that was already met by the conventional tail design, further analysis has to be carried out. Since the complexity of the design couples the longitudinal and lateral dynamics of the UAV, the analysis was carried out using AVL by first modelling the geometry of the wing and tail systems and disregarding the fuselage and all other systems. Of course, this simplification removes some of the complex interactions between the lift generating surfaces and the other systems, but for this case their contribution was considered negligible. The modelled body can be seen in Figure 10.8.

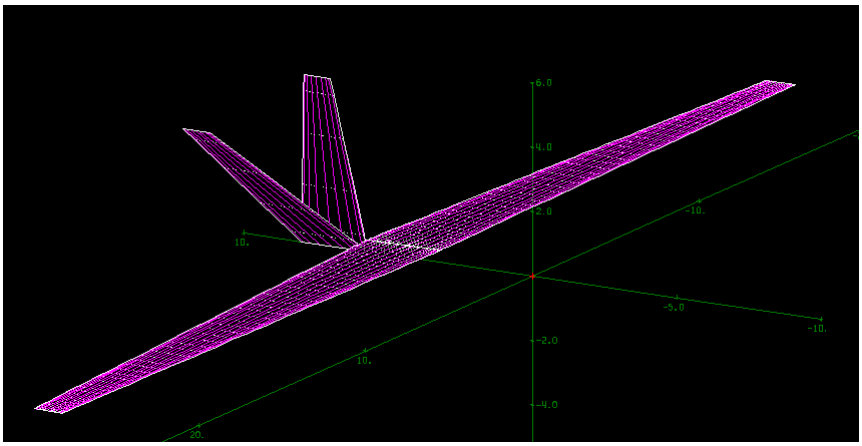

Figure 10.8: AVL model of the RePLASMA main wing and V-tail.

Beginning with longitudinal stability, when the aerodynamic center of the main wing is more forwards than the center of gravity of the vehicle, to guarantee static longitudinal stability, the gradient of the moment coefficient with respects to the AoA, C_{m_α} has to be negative and the total moment coefficient at zero lift has to be positive. To analyze the first quantity, the AVL model was run at a zero AoA at zero free-stream velocity, resulting in C_{m_α} of -0.41 rad^{-1}. As for C_{m_0}, the model was trimmed for a C_L of zero and ran again, outputting a total moment coefficient value of 0.15, thus proving the longitudinal stability of the vehicle.

As for directional stability, the coefficient of importance is the weathercock coefficient, C_{n_β}, which was analyzed at zero free-stream velocity and sideslip angle, resulting in a value of 0.15 rad^{-1}, which is reasonably above negative value, indicating yaw stability. Therefore, by switching from a conventional tail to a V-tail of similar dimensions, the aircraft remains still statically stable both in the longitudinal and lateral directions.

10.5. Control surface sizing

Having sized the empennage in order to make the aircraft both longitudinally and laterally stable, it is also vital to design the flight control surfaces that will enable the aircraft to reach any desired attitude by the mission profile. For that case, firstly, ailerons, placed on the main wing, will be needed in order to allow the vehicle to bank and turn. Moreover, a combination of an elevator and a rudder - a *ruddervator* - will be needed to provide pitching and yawing capabilities.

10.5.1. Ailerons

Currently, there are no mission requirements dictating the roll performance of the vehicle while in flight and therefore, research was done in order to identify potential certification specifications that will drive the design. It was found that low-to-medium maneuverability aircraft below 6500 kg, which is quite applicable to the current design, are required to achieve a bank angle of 30° in less than 1.8 s during landing conditions[70] and therefore, this was set a the driving requirement.

To start off the design process, firstly, the main aerodynamic control parameters that affect the dynamic behaviour of the vehicle need to be identified. Those are aileron control derivative $C_{l_{\delta a}}$ and the roll damping derivative C_{l_p}. To estimate the aileron control derivative, the following equation can be used[70]:

$$C_{l_{\delta_A}} = \frac{2C_{l_\alpha}\tau}{S_{ref}b}\int_{y_i}^{y_o} c(y)ydy \qquad (10.9) \qquad c(y) = C_r\left[1 + 2\left(\frac{\lambda - 1}{b}\right)y\right] \qquad (10.10)$$

where C_{l_α} is the lift gradient of the wing's airfoil, S_{ref} is the total area covered by the ailerons, c is the local chord length, y is the span-wise distance and τ is the aileron effectiveness parameter. As for S and y, these parameters can be obtained straightforwardly from geometry. C_{l_α} is dependant on the airfoil and can be obtained via polar analysis with XFOIL while τ is a function of the aileron's chord length over the wing's chord length as displayed in Figure 10.9

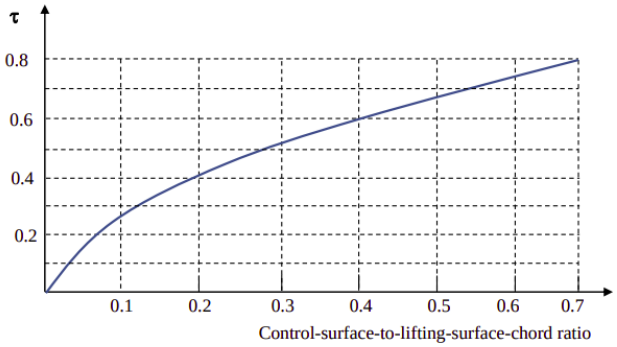

Figure 10.9: Relationship between control surface effectiveness and chord ratio[70].

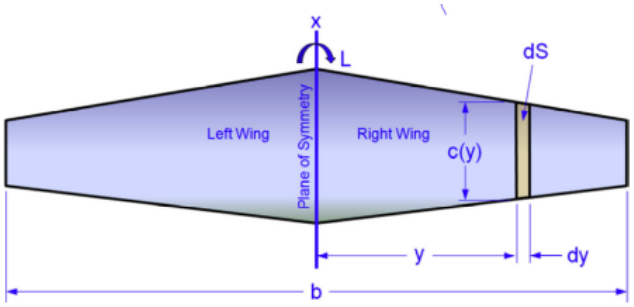

Figure 10.10: Diagram representing main geometrical parameters involved in aileron sizing[13].

Since the rear spar of the wing is positioned at 75% of the wing chord, the aileron can be attached at exactly this position, resulting in a aileron chord to wing chord ratio of 0.25 and an aileron effectiveness of 0.45.

As for the roll damping derivative, its contribution can be modeled with[70]:

$$C_{l_P} = -\frac{4\left(C_{l_\alpha} + C_{d_0}\right)}{S_{ref} b^2} \int_0^{b/2} y^2 c(y) dy \tag{10.11}$$

with C_{d_0} being the airfoil's parasite drag coefficient, which can again be estimated via XFOIL analysis.

Finally, to calculate the time needed to reach a 30° bank angle based on a maximum aileron deflection - δa - of 20° the following scheme can be used:

$$P = -\frac{C_{l_{\delta a}}}{C_{l_P}} \delta a \left(\frac{2V}{b}\right) \tag{10.12}$$

$$\Delta t = \frac{\Delta \phi}{P} \tag{10.13}$$

Since for both derivatives to be estimated, the start and end position of the aileron along the span of the wing is needed, a tool that computes the optimal position by iteratively changing the aileron's location and computing the time needed to bank, was set. This resulted in a starting position of 53% of the span and an end position of 87% of the span and a time needed to reach a 30° bank angle of 1.798 s thus, meeting the requirement.

10.5.2. Ruddervator

A ruddervator is a combination between a traditional elevator and a rudder providing both longitudinal and later control of the aircraft and is mainly found as a control surface on V-tail aircraft such as the early Beechcraft Bonanza[2].

To achieve pitch and yaw control, the mixture of control inputs is used as seen in Figure 10.11. Due to the dynamic coupling between the pitch and yaw, the design between such a system is usually very complex and limited methods exist for it. As shown by Raymer [71], a possible direction that would allow for independent pitch and yaw analysis, is to design the control surfaces as if a conventional tail is used, that is, to design an elevator and a rudder, an combine them in a final step to produce a ruddervator. Therefore, this is the methodology that will be used for the design.

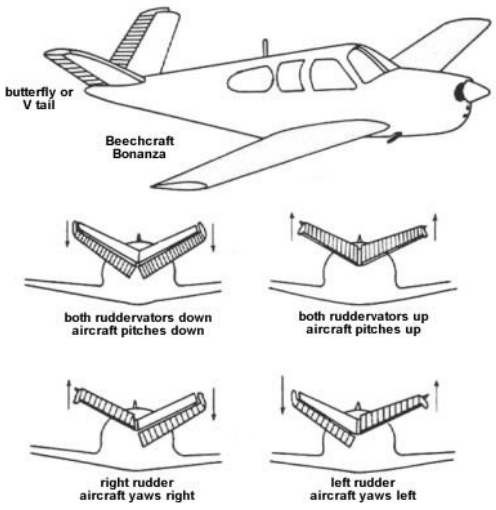

Figure 10.11: Pitch and yaw control achieved via a ruddervator. [1]

[1]http://www.pilotfriend.com/training/flight_training/fxd_wing/emp.htm [accessed 24/6/2021]
[2]https://beechcraft.txtav.com/en/bonanza-g36 [accessed 24/6/2021]

10.5.3. Elevator design

The first step in this endeavour is of course to reflect on the relevant requirements or specifications dictating pitch performance of the UAV. Since no direct mission requirements are applicable in this case, research was put into regulatory specification, identifying that for a remote controlled aircraft of this type, the pitch angular acceleration upon take-off should be between 10 and 15°/s^2 [70]. To analyse the dynamic motion of the aircraft at take-off, the following FBD was produced as seen in Figure 10.12.

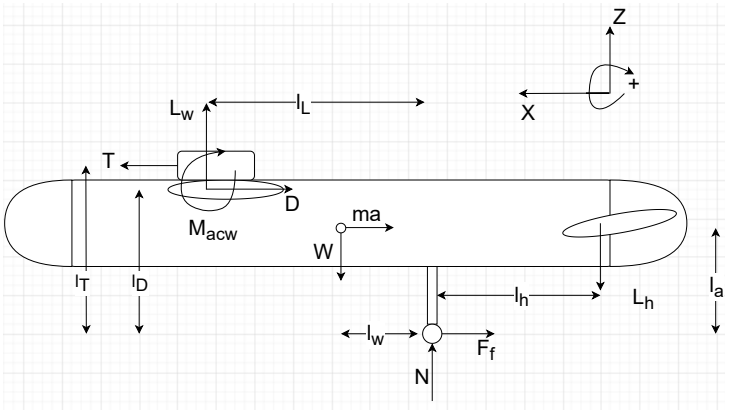

Figure 10.12: Free body diagram of aircraft at the moment of take-off.

resulting in the following set of equations:

$$\Sigma F_x = T - D - F_f = ma \tag{10.14}$$

$$\Sigma F_z = L_w - L_h + N = W \tag{10.15}$$

$$\Sigma M_g = -Tl_T + Dl_D + L_w l_L + M_{ac_w} - Wl_W + mal_a + L_h l_h = I_{yy}\ddot{\Theta} \tag{10.16}$$

where moments were taken about the point where the main landing gear touches the ground with the respective moment arms displayed in the figure. These equations describe the motion of the aircraft just at the moment of take-off when the nose gear has lost contact with ground. Solving for the required tail lift reduces the system to:

$$L_h = \frac{I_{yy}\ddot{\Theta} + Tl_T - Dl_D - L_w l_L - M_{ac_w} + Wl_W - mal_a}{l_h} \tag{10.17}$$

Let us analyse the components on the right-hand side one by one, starting with $I_{yy}\ddot{\Theta}$. I_{yy} represents the moment of inertia of the UAV about its pitch axis, where an initial estimate of 76319 kgm^2 was made. This estimate was computed by assuming all relevant subsystems of the aircraft as point masses and summing their contribution about the center of gravity as per:

$$I_{yy} = \Sigma m_{subsystem} r^2 \tag{10.18}$$

using mass and moment arm estimates provided by class II and initial sizing methods. As for $\ddot{\Theta}$, as mentioned earlier, this value represents the pitch angular acceleration and is set to 12°/s^2 based on requirements. Next up is the thrust contribution to the moment, with T being the take-off thrust of about 12600 N. The aerodynamic components were naturally found using:

$$D = 0.5\, C_d\, \rho\, V_{to}^2\, S \tag{10.19}$$

$$L_w = 0.5\, C_L\, \rho\, V_{to}^2\, S \tag{10.20}$$

$$M_{ac_w} = 0.5\, C_{m_{ac_w}}\, \rho\, V_{to}^2\, S\, \bar{c} \tag{10.21}$$

with C_L, C_d and $C_{m_{ac_w}}$ developed through airfoil, wing and mission analysis. Finally, W represents the aircraft's maximum take-off weight placed at the most aft CG position and a is the aircraft's linear acceleration computed via:

$$a = \frac{V_{to}^2}{2S_{to}} \tag{10.22}$$

Plugging everything into Equation 10.17, the required negative lift generated by the tail is 9344 N, or a tail lift coefficient C_{L_h} of 0.87, based on current estimates of tail geometry. Finally, we can analyze the independent tail and size its elevator so that the desired lift coefficient is achieved, starting with the formulation dictating the aerodynamics of the tail:

$$C_{L_h} = C_{L_{\alpha_h}}(\alpha_h + \tau_e \delta_E) \tag{10.23}$$

$$\alpha_{\mathrm{h}} = \alpha + i_{\mathrm{h}} - \varepsilon \tag{10.24}$$

with τ_e being the elevator angle of attack effectiveness parameter, which will be the parameter dictating the elevator size as will be seen shortly. Since the airfoil is known, $C_{L_{\alpha_h}}$ can be easily obtained by polar analysis with a value of 6.04 rad^{-1} while computation of the AoA of the tail is a little more involved, requiring computation of the angle of downwash caused by the main wing and can be found in Table 10.2. As for δ_E, it represents the maximum deflection angle of the elevator and was set to 25° after thorough look into existing aircraft and literature [70]. This leads to a τ_e value of 0.51, which can be related to the control surface over tail surface ratio by addressing Figure 10.9, resulting in a S_E/S_h value of 0.29 that was deemed reasonable after consultation with literature[70]. As for the span ratio, looking at existing aircraft of similar category and mission profile such as the Global Hawk [72] and the Phantom Eye [3], an elevator span over tail span ratio of 1 was chosen. To verify that the designed elevator does indeed generate the required lift coefficient, lifting line theory was used, and the lift distribution over the tail was estimated at full elevator deflection angle as presented in Figure 10.13

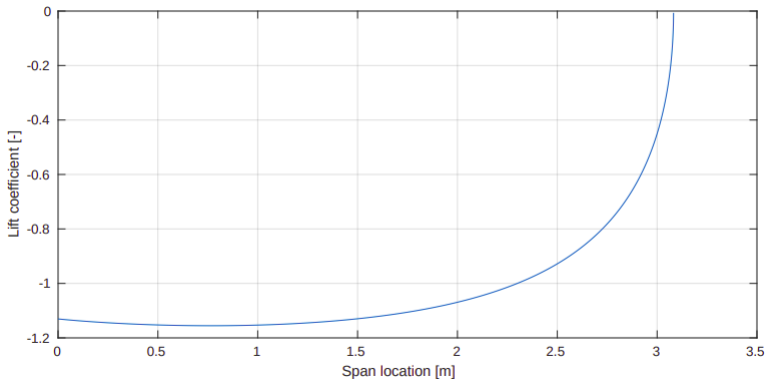

Figure 10.13: Lift distribution versus span for horizontal tail at maximum elevator deflection.

while the total 3D tail lift coefficient was found to be 0.89, which is slightly above the required C_{L_h} of 0.87 and therefore, the current size of the elevator proves to be sufficient and within bounds of already existing aircraft.

10.5.4. Rudder design

The rudder is the primary control surface responsible for yaw control of the vehicle. When the a rudder deflection is applied, a lift force is generated by the vertical tail and a yawing moment, rotating the vehicle about its vertical axis. To size its dimensions with respects to the vertical tail, firstly a consultation with requirements should be carried out. As mentioned in Section 10.3, the critical case for this mission is the one-engine-inoperative scenario, with the dynamics presented in Figure 10.14.

[3]https://www.boeing.com/defense/phantom-eye/ [accessed 22/6/2021]

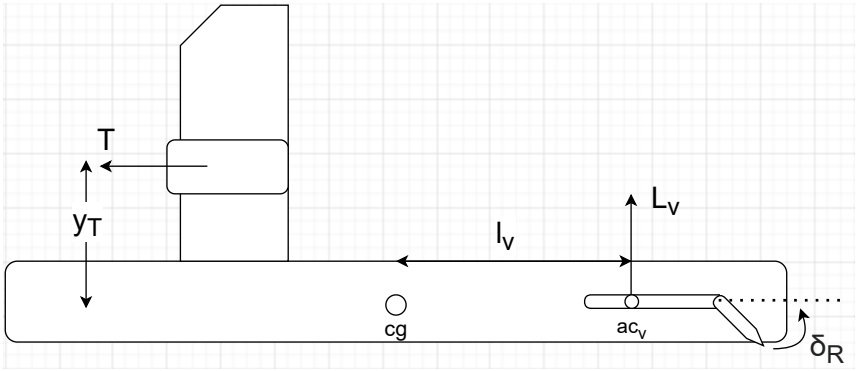

Figure 10.14: Diagram displaying forces acting the vehicle when an engine fails.

Summing the moments about center of gravity and solving for equilibrium:

$$\Sigma N_{cg} = T y_T + L_v l_v = 0 \tag{10.25}$$

$$L_v = \bar{q} S b \left(C_{n_0} + C_{n_\beta} \beta + C_{n_{\delta A}} \delta_A + C_{n_{\square R}} \delta_R \right) \tag{10.26}$$

Now onto the coefficients that dictate vertical tail lift production, C_{n_0} is the moment coefficient about the aerodynamic center of the vertical tail and since a symmetric airfoil is used, it is equal to zero. C_{n_β} is the moment coefficient derivative with respect to sideslip. The term associated with it can be put to zero, solving for zero sideslip. $C_{n_{\delta A}}$ is the yaw moment coefficient derivative with respect to the aileron deflection, but since no aileron is employed, this whole term is set to zero as well. The final coefficient and the one that the design process of the rudder affects is $C_{n_{\delta R}}$. Solving for that coefficient results in:

$$C_{n_{\delta R}} = \frac{T y_T}{-\bar{q} S b \delta_R l_v} \tag{10.27}$$

Exploring the parameters that affect it and analyzing for the worst case scenario, T is the maximum thrust produced per engine, being equal to 6.3 kN. y_T is the moment arm between the engine and the center of gravity having a value of 3 m. The dynamic pressure, $\bar{q}$ will be analyzed at 80% of stall speed at ground conditions as per requirements [70]. S and b are the geometrical parameters of the vertical tail, being the area and the span. The maximum deflection, δ_R, is set to 25° by looking at already existing aircraft [70]. Finally, l_v is the moment arm between the center of gravity and the aerodynamic center of the vertical tail and can be obtained through geometrical inspection equalling 3 m, thus resulting in a value for $C_{n_{\delta R}}$ of 0.24. Now in order to design the actual size of the rudder, an expression of $C_{n_{\delta R}}$ is used with respect to the size of the rudder as per[70]:

$$C_{n_{\delta R}} = -C_{L_{\alpha_v}} \bar{V}_V \eta_V \tau_r \frac{b_R}{b_V} \tag{10.28}$$

$$\bar{V}_V = \frac{l_V S_V}{b S} \tag{10.29}$$

Firstly, after looking at existing aircraft [70], a rudder span over vertical tail span ratio of 1 was assumed. $C_{L_{\alpha_v}}$ is the lift gradient of the wing, which can directly be obtained from airfoil analysis of the NACA 0012 airfoil used. $\bar{V}_V$ is the tail volume ratio, which can be straightforwardly computed using the already estimated parameters. Finally, η_V is the ratio between the freestream airspeed and the airspeed at the vertical tail having a value of 0.97. This results in a τ_v value of 0.43, which is converted to a S_r/S_v ratio of 0.25 by looking at Figure 10.9.

10.5.5. Final V-tail design

Having independently sized the dimensions of the elevator and the rudder in order to meet the control requirements imposed on the vehicle, their parameters can now be combined to create a final ruddervator design to be attached to the V-tail as explained in Section 10.4. Firstly, the estimated S_e/S_h ratio was found to be 0.29, which when multiplied by the original horizontal stabilizer area

results in an elevator area of 2.85 m^2. As for the rudder, S_r/S_v was computed as 0.25 and therefore, the area of the rudder is equal to $0.25 \cdot 11.05 = 2.75$ m^2. Utilizing the method described in Section 10.4, the total ruddervator area needed is 2.8 m^2 and with this, the sizing of the control surfaces attached to the V-tail can be concluded. The final V-tail design including the ruddervator is presented in Figure 10.15.

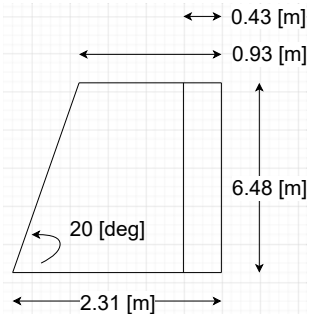

Figure 10.15: Final dimensions of V-tail with integrated ruddervator.

Table 10.4: Geometrical parameters of designed ruddervator.

Parameter	Value
Ruddervator Area	2.80 [m]
Span	6.48 [m]
Chord	0.43 [m]

10.6. Autopilot design

Modern autopilot system are not only capable of maintaining static processes such as altitude, attitude and heading, but also perform complex maneuvers such as turning and guiding between waypoints describing a route. These capabilities greatly aid pilots and alleviate their effort, especially for long mission profiles such as RePLASMA's one. Moreover, these capabilities are especially useful for UAV's in emergency scenarios such as loosing connection to ground, allowing them to autonomously cruise until connection is regained or potentially land. As per mission requirements, the RePLASMA aircraft must be able to autonomously land in case of an engine failure and therefore, designing a control system capable of that is of upmost importance.

Autopilot system typically consists of interconnected systems, acting together to control the vehicle. These systems provide state estimation, guidance, navigation and control algorithms and are generally referred to as the Flight directory system.

10.6.1. Flight director system

Controlling the vehicle firstly requires an accurate estimation of the state of the aircraft. This state includes parameters such as position, velocity, attitude and angular rates. Moreover, all on-board instrumentation has to be redundant in order to provide trustworthy data even in the case of a single sensor failure and since cost and availability are of great importance to RePLASMA, preference is put in low-cost, off-the-shelf instruments.

One way to go about satisfying all requirements mentioned beforehand is by using sensor fusion of multiple sensors using state reconstructors such as the Kalman filter. This techniques makes use of multiple measurements of the same state by sensors with different noise characteristics to produce a new and more accurate estimate. For example, by combining the measurements of an accelerometer, that suffers from high-frequency noise and a gyroscope that experiences low-frequency noise, real-time estimation of the attitude of the vehicle can be achieved as shown by Wang et al. [73]. Furthermore, to localize the UAV in 3D space, GPS data can be mixed with an accelerometer data to produce estimates of its position and velocity [74]. Finally, an Air Data Measurement(ADS) system will be needed to extract measurements for the angle of attack and the sideslip angle. A visual representation of the filtering scheme can be seen in Figure 10.16.

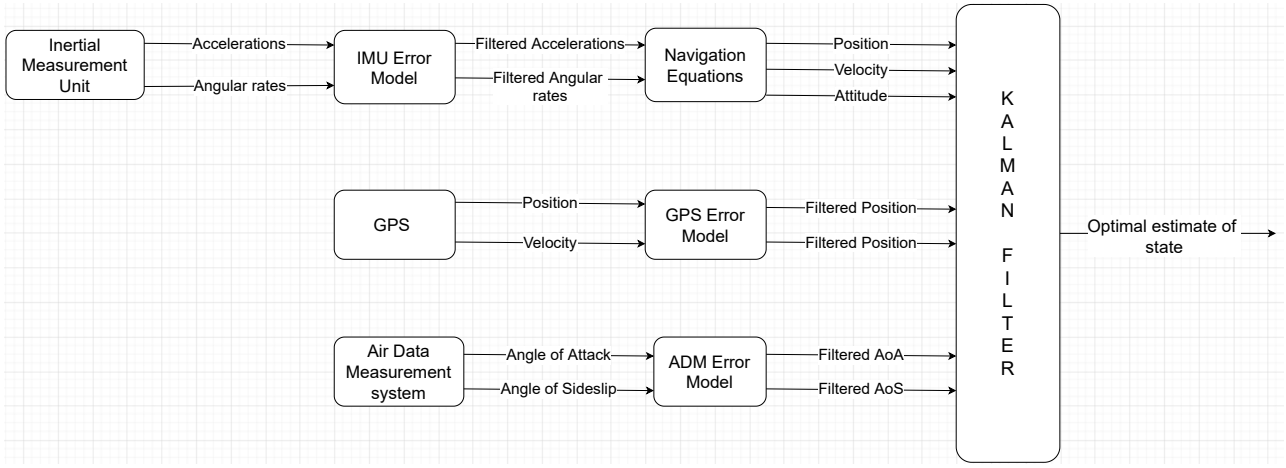

Figure 10.16: State estimation procedure converting from raw instrument measurements to optimal state estimate via Kalman filtering.

Having obtained an accurate estimate of the state of the vehicle, this can now be fed into guidance algorithms in order to bring the vehicle to a desired point by generating a feasible trajectory. Since the mission requirement in terms of autonomy is to perform an unpiloted landing in case of an engine failure, research was direction in this area.

Fallast et al. have described a way of generating landing trajectories that satisfy the aircraft's dynamics based on a rapidly-exploring random tree(RRT) algorithm [75]. To do so, firstly the maximum range achievable by the aircraft is computed using its equations of motion and an internal aerodynamics model. All possible landing locations within this range are explored and trajectories are generated using an optimized RRT algorithm, complying with the UAV's constraints such as maximum climb and descent rates. Based on a number of criteria such as runways risk, meteorological conditions and availability of on-site facilities, an optimal landing location is selected from the initially generated ones. An example of a generated trajectory can be seen in Figure 10.17.

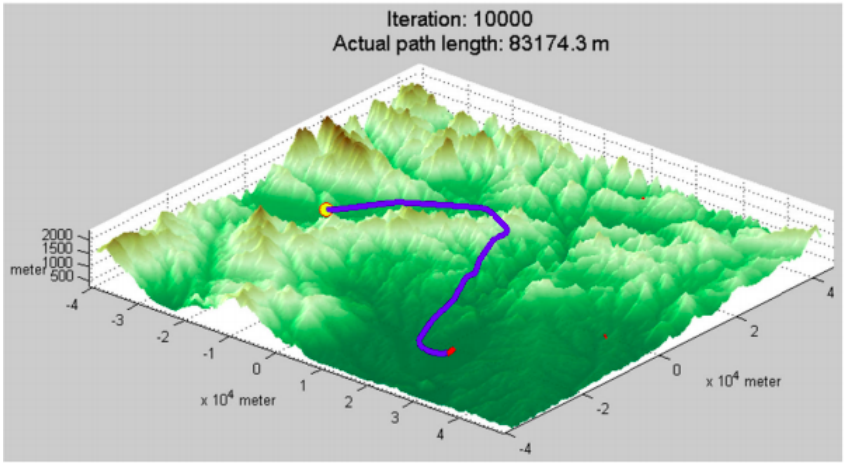

Figure 10.17: Flight trajectory generated using the algorithm proposed by Fallast et al.[75].

The final trajectory can be fed into a control law to bring the aircraft back to ground. Traditionally, Proportional Integral Derivative(PID) control systems are preferred in the aerospace industry due to their reliability and proven performance. As shown by Albaker et al. [76] by using a model of the aircraft and its powerplant and nested PID loops that control the airspeed the turn-rate, and the altitude, a pre-computed trajectory can be optimally followed even in the presence of stochastic processes such as turbulence and wing gusts. Therefore, this control system will be adopted for the RePLASMA aircraft.

11

Electronics, Command & Communication

For the success of the RePLASMA mission, it is essential that the command, communication and electronic subsystem of the UAV are sufficiently able to relay, interpret and respond to data links. Furthermore, the various subsystems on board requiring electrical power also need to be supplied with sufficient power. Thus, the aim of this chapter is to explain to the reader the design process of the communications link, the layout of the electrical subsystem as well as the flow of hardware and software interactions within the RePLASMA UAV.

11.1. Ground segment & communication link

The success of a HALE UAV's mission is often contingent upon the ability of the UAV to receive and process as well as respond to inputs from a source, such as a ground station. Within the context of the RePLASMA mission, there are a number of key elements required for communication. These are the ground station, the UAV, air traffic control as well as satellite communications infrastructure.

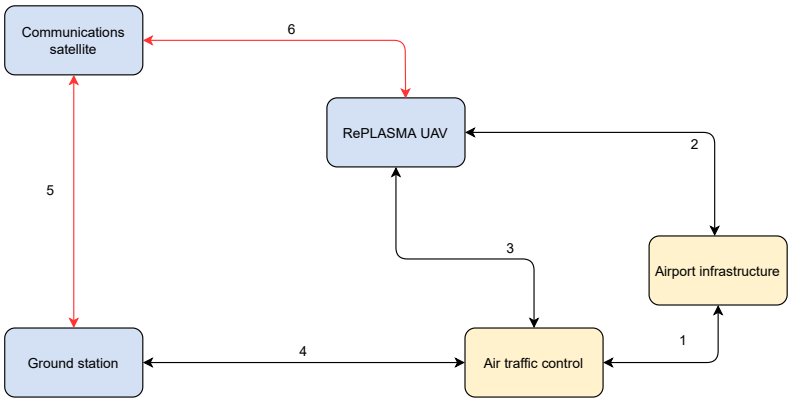

Figure 11.1: Schematic overview of various communication interfaces and links.

It is prudent to note the existence of 6 links of communication. Link one represents the communication link between airport infrastructure such as instrument landing system (ILS) beacons and air traffic control. This is a link that exists in an established manner at airports that are equipped to handle ILS landings. Furthermore, link two represents the interaction between the airport infrastructure, excluding ATC, and the UAV. This can include glideslopes being communicated automatically, as well as ILS beacons and other similar systems. The main purpose of this communication link is to ensure adequate data flows to the UAV in the case an autonomous landing is performed. Link three is between the UAV and air traffic control. The aim of this link is to ensure the UAV is able to receive instructions and display compliance with orders of air traffic control when flying through controlled airspace, such as in the early stages of climb and the latter stages of approach.

The final three links, numbered four through six form the crux of the communications link within the scope of this section. Link four allows air traffic control to issue commands to the manned ground station, with a reverse link allowing confirmation of compliance. Secondly, link five and six form the communications link between the ground station and the UAV, through the communications satellite system.

11.2. Communication architecture

Before all the data link sizing can begin, a clear communication architecture needs to be established. To do that, it should be explored whether a direct link will be able to support requirement **PLS-U-PERF-3**, stating a maximum operational distance of 1000 km. Looking at Figure 11.2, it can be seen that to reach a certain operational distance - d -, the aircraft must be flying above a certain altitude to enable a direct line-of-sight.

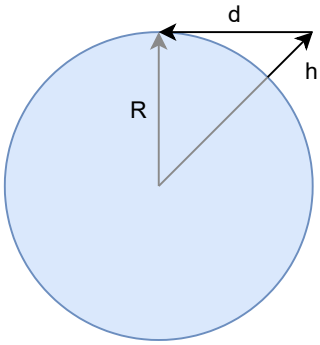

Figure 11.2: Communication range diagram.

Using Pythagoras' theorem, it can be seen that the relationship between h and d is the following: $h^2 + 2 \cdot R \cdot h - d^2 = 0$. Using a distance of 1000 km and Earth radius of 6,371 km, the equation can be solved, resulting in a required altitude of 78 km. Since the operating altitude in this case is around 25 km, a direct link will not be a viable option and therefore, a satellite link will be needed.

In order to size the communication system, now it is important to set the requirements to which it should adhere. These requirements do not come only from the data rates generated on-board the vehicle, but also from the data packets coming from the ground station. Therefore, the up-link and down-link communication flows will be investigated individually.

Starting with the UAV itself, the set of data generated on-board and sent to the ground station via the down-link needs to allow the pilot to effectively operate the aircraft by providing information about the aircraft's environment and its internal operation. As per regulations, the so-called "six pack"[1] avionics set consisting of an Airspeed Indicator, an Altimeter, a Vertical Speed Indicator, an Attitude Indicator, a Heading Indicator and a Turn Coordinator are the basic flight instruments needed to operate an aircraft. Their data is already encompassed by the 12-state vector produced by the state estimation system explained in Section 10.6. Moreover, due to nature of the mission, a camera will be needed to provide visual information to the pilot on-ground. As for the internal state of the aircraft, this includes information such as the engine's current throttle setting, deflection of control surfaces and so on. Of course, the dictating output for the communication system is the camera's data rate due to the fact that all other mentioned parameters can be stored as a single value. Assuming a resolution of 640x480p at 30 fps and a H264 compression, the required bitrate to transfer the video feed is 470 kbps. To support this data rate, commercially available transceiver solutions such as the Iridium network were considered. A prime candidate for that turned out to be the Iridium Certus transceiver[2], being able to provide data transfer rates of up to 352 kbps on up-link and 704 kbps on downlink, and therefore supporting the aircraft's down-link rate.

In order to approve the transceiver, the up-link from the ground station, air traffic control and

[1] https://www.mcico.com/resources/flight-instruments/six-pack-aircraft-instruments-explained [accessed 25/6/2021]
[2] https://www.iridium.com/services/iridium-certus-700-2/ [accessed 25/6/2021]

airports to the UAV has to be analyzed as well. The data generated by these facilities consists mainly of control inputs sent by the pilot as well as payload inputs from the payload operator on-ground. Those control inputs include the throttle level, aileron and ruddervator deflections, but also things such as landing gear deployment, etc. Assuming they are stored as a 4-byte floating point number and an update rate of 2 Hz, an estimate for the required up-link rate is 15 kbps, which is again met by the Iridium Certus transceiver, and is therefore chosen as the primary transceiver of the aircraft. Moreover, the Iridium Satcom link is also used by the Global Hawk aircraft, whose range spans 20000 km and is of similar mission profile to RePLASMA, thus proving the availability of the link. A final communication flow diagram between the aircraft and all external elements can be seen in Figure 11.3.

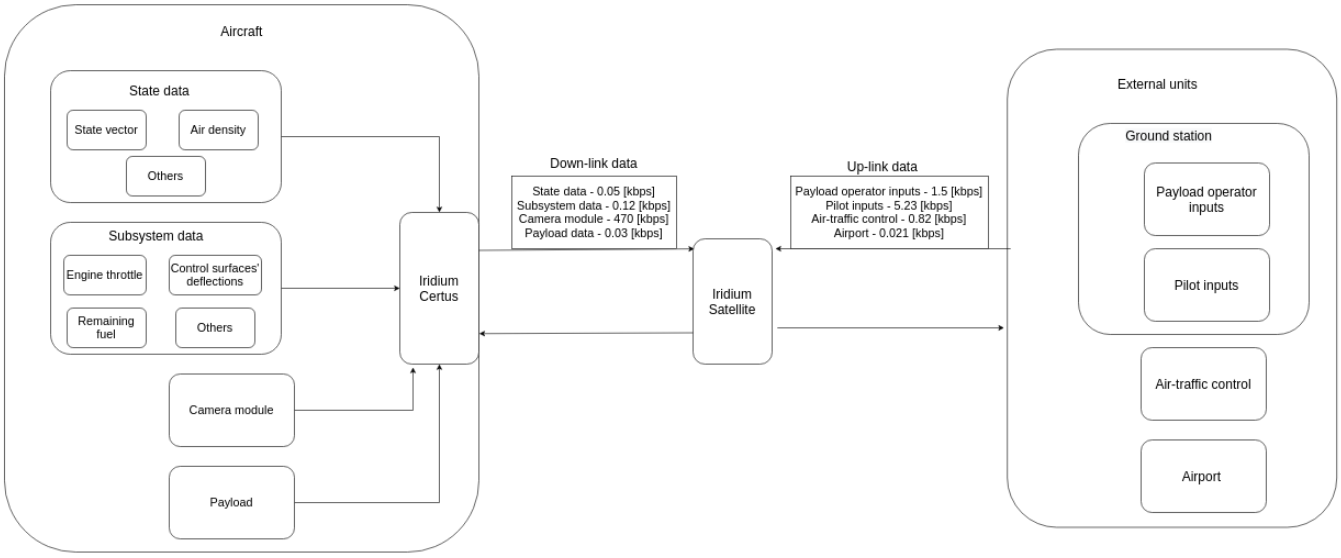

Figure 11.3: Communication flow between the aircraft and the external elements.

The aforementioned communication system of the aircraft is also tightly related to its internal computing and data handling systems. The computing system is responsible for running the on-board flight algorithms, issuing actuator commands and others. As a main computing unit was chosen the Nvidia Jetson AVG Xavier due to the following reasons. Firstly, due to its powerful graphics card, the Jetson is built for managing and processing great quantities of camera output, which this aircraft has and in the case the control system uses any kind of deep learning for the autonomous landing procedure. Moreover, it posses a great number of IO ports allowing for a myriad of sensors to be connected allowing for expansion of the avionics system. Finally, since the project focuses on availability and reliability, the Jetson stands as a prime candidate due to its proven history and low cost. As for the data handling system, it is responsible for managing the flow of data between the different communicating components both on-board and externally to the aircraft. A representation of the flow of data in the UAV can be seen in Figure 11.4.

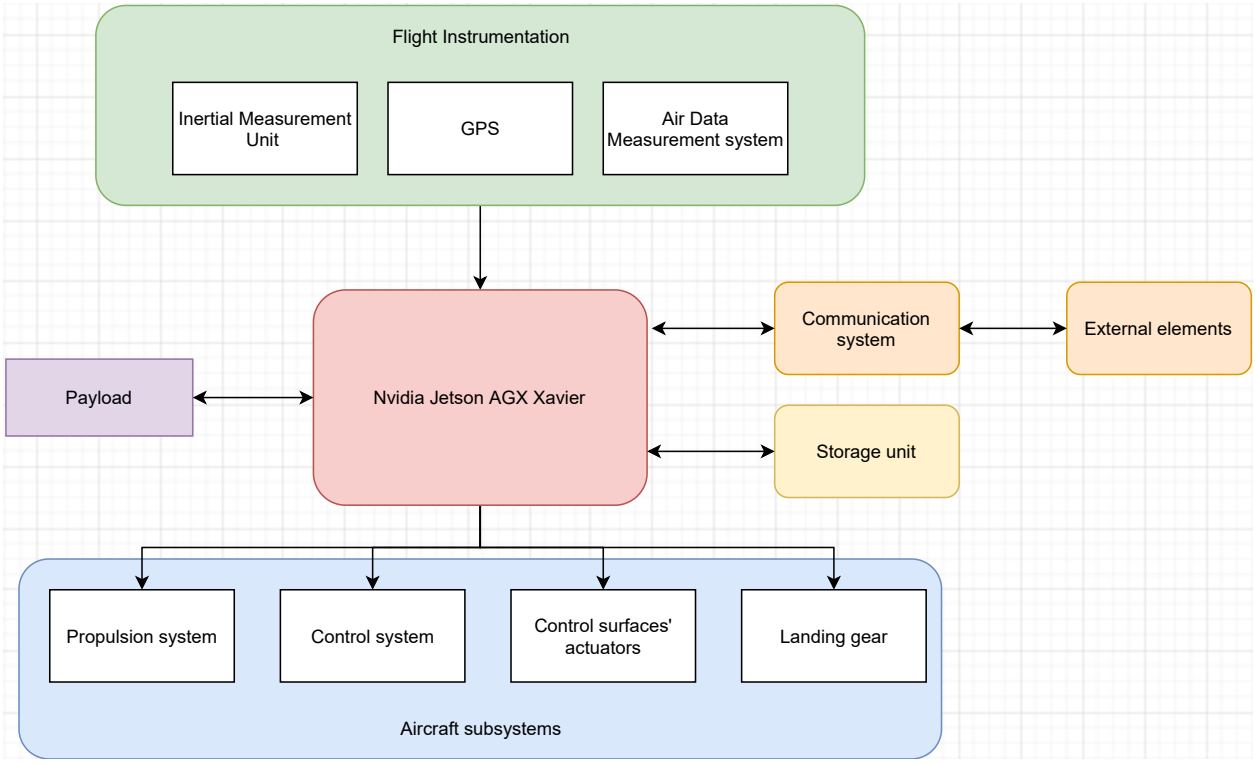

Figure 11.4: Internal data handling and command issuing of the aircraft.

11.3. Ground station facility

To facilitate the remote operation of the UAV, a ground station will need to be designed and constructed. Here a distinction has to be made between fixed and portable ground stations. For small UAV's such as drones, a portable ground station provides many pros such as reduced costs and higher availability, but because of this mission's requirements, this is not feasible. This is due to the fact that for a 20-hour-long mission, additional functionality is needed to support the pilot and give information about the state of the vehicle. Moreover, since a payload operator is needed to support the payload and its data, additional facilities will be needed for that. Therefore, it is decided that a dedicated ground station for the RePLASMA mission is the optimal decision. Some of operations carried out on the ground station are:

- Mission planning and waypoint setting.
- Telemetry processing and storing.
- Command aircraft.

Therefore, the following components must be present at the ground station facility. Firstly, to operate the aircraft during its mission, a trained pilot holding either a CPL or an ATPL is needed. To visually provide vital information about the state of the aircraft to the pilot, a video wall will be needed. Moreover, a flight control system tied to the aileron, ruddervator and engine of the aircraft must be provided to the pilot for control as well as additional buttons for landing gear deployment and such. To receive telemetry but also send commands to the aircraft, a communication system consisting of an antenna and a transceiver will be needed, meeting the data rates generated on-board the UAV. To navigate the aircraft, plan it mission and make sure it complies with the current air traffic, mission planning personnel and well as an air traffic officer will be required, who will be connected directly to the pilot. Finally, an independent payload operator will be there to interact with the payload on-board and analyze its data. A final representation of the ground station can be seen in Figure 11.5.

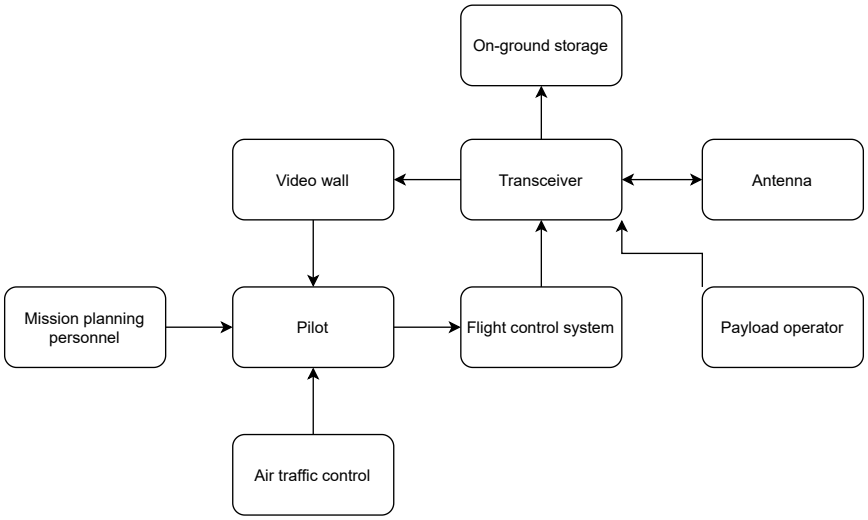

Figure 11.5: Ground static components and their relations.

11.4. Electrical subsystem design

To power the aircraft and its subsystems, it is vital that an electrical system is designed around it. It should be able to produce enough power to sustain the vehicle both on-ground and in-air. Moreover, the system should not have a single point of failure, meaning that even if a critical system fails, the aircraft shall not be left without power.

To do so, the different phases of a typical mission should be explored, starting off with the on-ground phase where the initial subsystem check if performed, the instrumentation is initialized, the engine is started up and taxiing begins. Initially, the aircraft is plugged into the on-ground electrical grid or the Ground Power Unit and therefore, no on-board energy generation is needed, only a power distribution system. After the engine is started and aircraft is disconnected, an alternator that converts the mechanical energy produced by the piston engine to electricity can utilized. This system can be used throughout the mission profile as the main source of power, but as mentioned early, a potential failure should not incapacitate the whole system and therefore, two additions are made, that is - a battery system and a ram-air turbine system.

The ram-air turbine (RAT) is a small turbine that converts the dynamic pressure generated by the air and the moving aircraft to electrical power. In case of main alternator failure during cruise flight, the RAT can be lowered from the fuselage and imposed into the free-stream air thus, generating electricity to power the UAV's vital system such as the avionics, the communication and the flight control systems. In the case that the free-stream dynamic pressure is not sufficient to generate enough power such as during take-off or landing, another source of energy will be needed. Therefore, a battery system will also be utilized. During normal operations, the batteries will only be charged and stay idle while if an emergency occurs as mentioned previously, their energy can be used in addition to the RAT to power the aircraft. The connections between the different components can be seen in Figure 11.6.

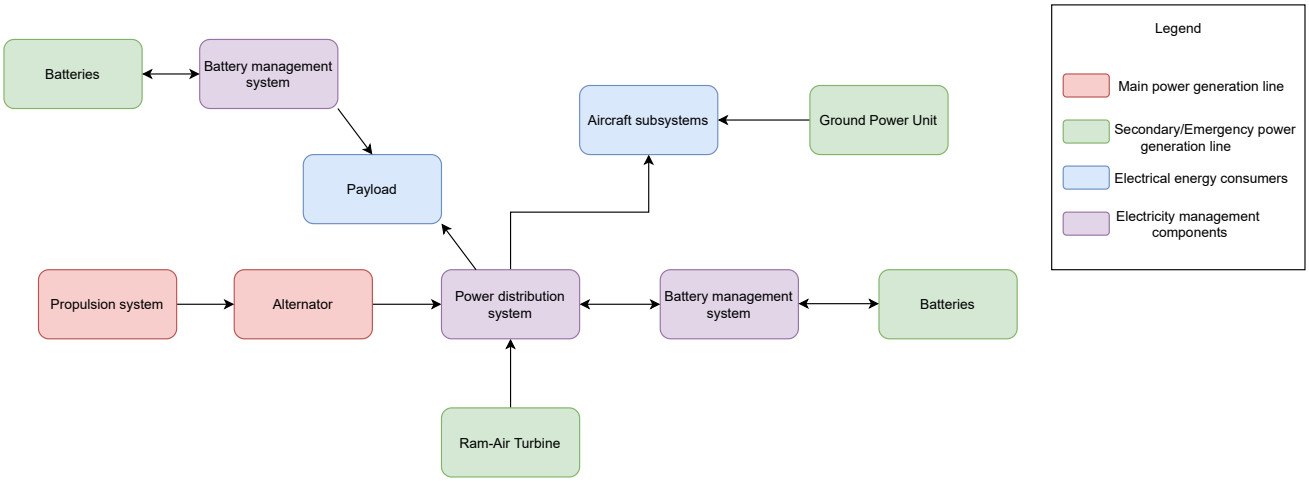

Figure 11.6: Electrical system of RePLASMA.

11.5. Software & hardware diagrams

Two very important aspects of the aircraft design are the software design and the interaction between the different hardware inside of the vehicle. In order to design the software efficiently, timely and bug-free, a clear overview of its task during the mission profile is needed. This specification should provide the logical flow of the software from the start-up of the vehicle until its landing. This flow can be observed in Figure 11.7.

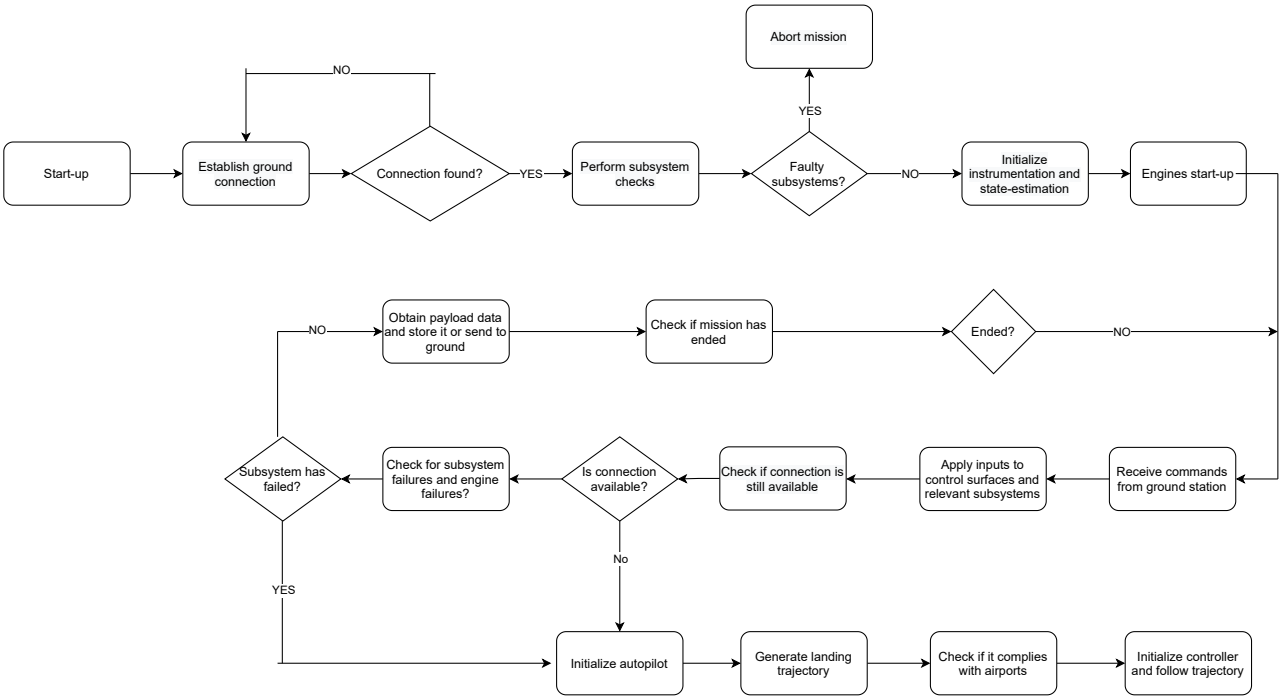

Figure 11.7: Software block diagram of RePLASMA.

Starting off, the first task of the software is to check whether a connection has been established with the on-ground station and whether all subsystems perform as expected and otherwise issue a mission abort command. If all subsystems function correctly, instrumentation can be switched on and the state estimation algorithms can start functioning to estimate the vehicle's pose, followed by engine start-up. From there a loop can be started where the software constantly receives and decodes the ground station commands, and applies them to the different subsystems and control surfaces. During this phase, in a case of a connection or a subsystem failure, the UAV's autopilot is engaged. A trajectory is generated using the algorithms explained in Section 10.6 and followed

using the defined controller. If no failures have occurred, payload data is obtained an sent via the down-link until the plane lands and the mission is complete.

Moreover, to achieve mission completion, a detailed interaction protocol between the hardware is needed. At the heart of it stands the computation & data handling module that dictates the operation of all other systems, be it actuation of control surfaces or setting the throttle level of the engine while to provide power to all systems on-board, the electrical system comes into play. A detailed diagram of all the interactions happening during the mission profile is given in Figure 11.8.

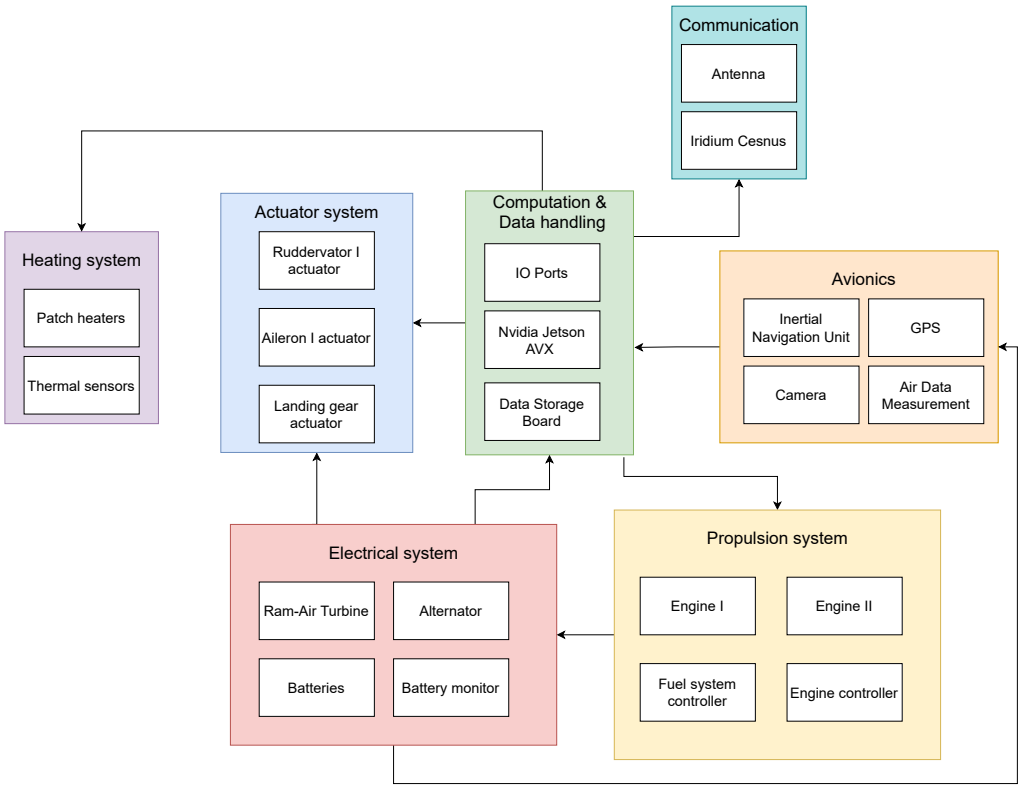

Figure 11.8: Hardware block diagram of RePLASMA.

12

Undercarriage

The undercarriage of the RePLASMA UAV is utilized at two critical phases of the mission profile, take off and landing. During these phases, it fulfills a number of key functions, such as but not limited to: absorbing take off, landing and taxiing loads, providing control for maneuverability as well as providing braking capacity [77]. This chapter aims to explain to the reader the design choices and driving parameters in the selection, sizing and positioning of the undercarriage subsystem of the RePLASMA UAV.

12.1. Undercarriage sizing & positioning process

The process of sizing and positioning the undercarriage on an aircraft is multi-stepped, with various junctions where requirements place constraints on design point selection. In order to illustrate this, Figure 12.1 provides an overview of the process.

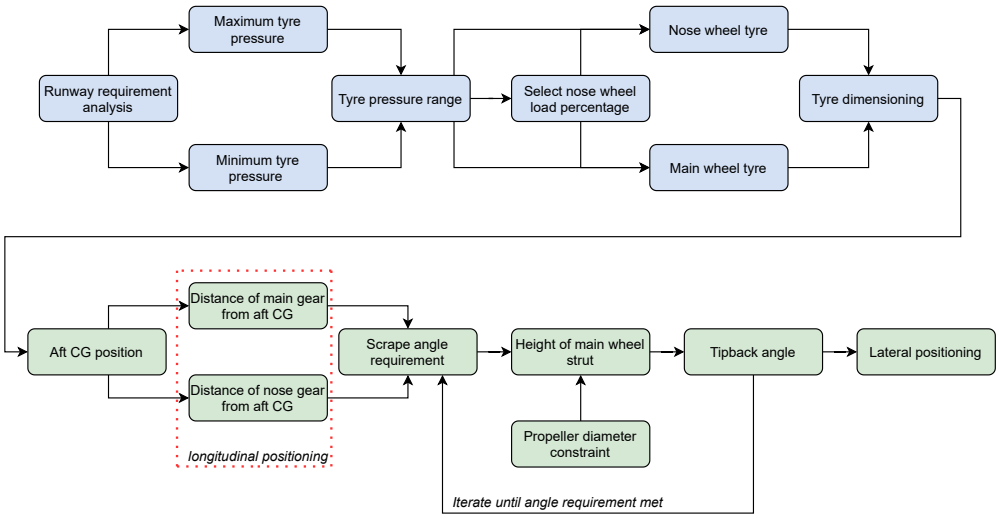

Figure 12.1: Overview of the landing gear design and positioning process.

12.2. Tyre sizing

12.2.1. Tyre pressure ranges

The reader may note that the start of the process is the analysis of runway requirements. This stems from the fact that the intended runway type dictates the tyre pressure required. This varies significantly between runways, with hard sand runways allowing 240 kPa of tyre pressure more than soft sand.

Runways across the world may be broadly classified into three types. Type one runways are unpre-

pared surfaces, including grass or gravel runways. Type two are flexible pavement runways, which includes surfaces such as asphalt or tarmac. Finally, type three runways are rigid, and typified by concrete surfaces. [15]. For type one runways, various semi empirical studies allow a range of required table pressures to be derived:

Table 12.1: Maximum allowable tyre pressure per surface for type one runways [15].

Surface	Maximum tyre pressure	Unit
Soft sand	170-240	kPa
Wet grass	210-310	kPa
Hard sand	280-410	kPa
Hard grass	310-410	kPa

In addition to this, types two and three runways are classified with a load classification number (LCN), which allows the calculation of required tyre pressure, by means of the following formula [15], for LCN values between 10 and 100:

$$p = 430 \cdot \ln(LCN) - 680 \tag{12.1}$$

Following this consideration, a maximum and minimum tyre pressure are chosen, based on desired mission profiles. The minimum tyre pressure was not considered the constraining factor for the system. The maximum tyre pressure was constraining, since lower tyre pressures could feasibly be achieved by de-pressurizing or adapting tyres.

12.2.2. Tyre load allocation

Following this, the nose wheel load must be decided. Typically, this value is approximately 8% of the maximum take off weight, to allow steer-ability. For an aircraft of the CS23 class, such as the RePLASMA UAV, the number of nose wheels is prescribed as 1, and main wheels prescribed as 2 in regulation. Following this, calculation of the loads on each tyre are done by:

$$P_{nw} = (0.08 \cdot MTOW) = 0.08 \cdot 4521 = 361.68 \text{ kg} \tag{12.2}$$

$$P_{mw} = \frac{(0.92 \cdot MTOW)}{2} = \frac{0.92 \cdot 4521}{2} = 2079.66 \text{ kg} \tag{12.3}$$

12.2.3. Tyre selection

Following the identification of the required tyre pressure and the load on each wheel, a variety of sources can be considered for tyre dimensions. For main wheel tyre selection, the following figures were used.

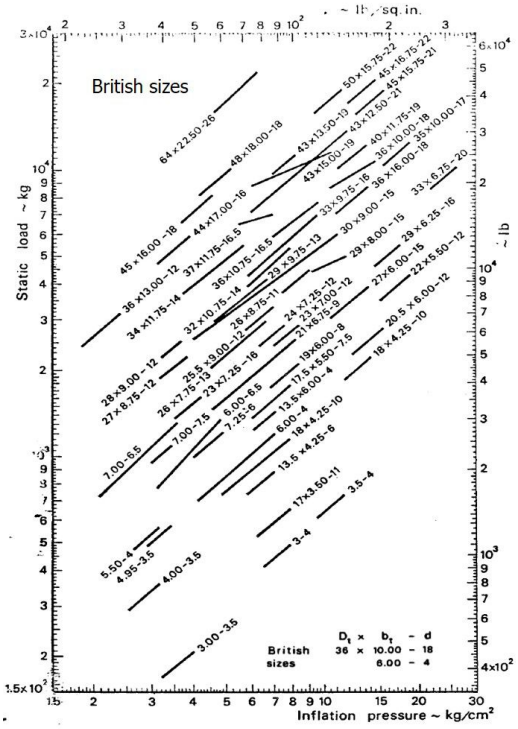

Figure 12.2: British tyre sizing chart [15]

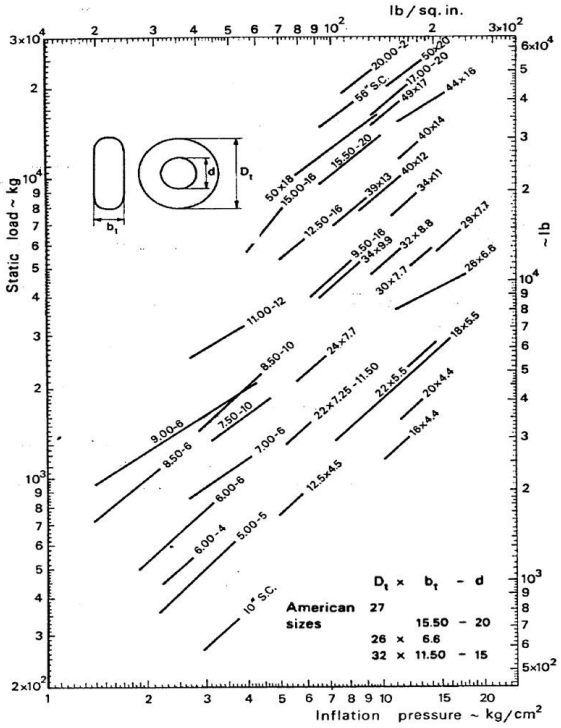

Figure 12.3: US tyre sizing chart. [15]

Both Figure 12.2 and Figure 12.3 provide tyre dimensions in inches, given an inflation pressure and a static load. The dimensions given are the outer diameter, the tyre width and the inner diameter. Both charts result in tyre dimensions that are different to the dimensions suggested by the other. In order to minimize mass, the aim is to minimize the overall tyre dimensions. The dimension selection of the tyres marks the end of the undercarriage sizing process, indicated in Figure 12.1 as blue filled boxes.

12.3. Undercarriage positioning

Following the selection of a tyre size, positioning the landing gear is the next task. The positioning process covers both the longitudinal and lateral positioning of the landing gear.

12.3.1. Longitudinal positioning

The next stage of the process is the positioning of the tyres. This has three key facets, longitudinally in the direction of the fuselage, the lateral positioning in the direction of the wings and the height of the tyres from the fuselage. In order to initiate this process, the aft most position of the center of gravity must be known.For this process, the aft most CG position was given by:

$$x_{CG_{aft}} = 0.465 \cdot l_f + 0.215 \cdot \text{MAC} = 4.12 \text{ m} \tag{12.4}$$

From this position of the CG, a moment equilibrium can be derived to balance the prescribed loads onto each element of the undercarriage, as well as their distance from the aft most center of gravity position (x_{cgaft}). If the distance from x_{cgaft} to the main wheels is l_m and the distance to the nose wheel is l_n, the moment equation becomes, with counterclockwise positive:

$$\Sigma M_{x_{CG_{aft}}} = (0.92 \cdot MTOW \cdot g) \cdot l_m - (0.08 \cdot MTOW \cdot g) \cdot l_n = 0 \tag{12.5}$$

Simplifying this:

$$\frac{l_m}{l_n} = \frac{0.08}{0.92} = 0.087 \tag{12.6}$$

Consequent to this, the scrape angle requirement must be considered. As per R. Vos [15], a first order approximation for the scrape angle requirement is the angle of attack that allows for 90% of the take off lift coefficient to be generated. From this constraint, another constraint is built in, due

to the propeller diameter. These constraints allow the initiation of the iterative process to estimate the parameters that allow the tip back angle to be calculated. The reader should note that the tip back angle must exceed the scrape angle. In order to derive this, the tipback angle is defined as follows:

$$\theta_{tip} = tan\left(\frac{\delta_{cgmw}}{0.5 \cdot D_{out} + H_{smw} + z_{cg} \cdot h_f}\right) \tag{12.7}$$

In this equation, the angle is defined as the ratio of the longitudinal distance between the aft CG and the main gear strut to the distance from the aft CG to the bottom of the main wheel. In this, δ_{cgmw} is the distance to the main wheel longitudinally. D_{out} indicates the outer diameter of the tyre, H_{smw} the height of the main wheel strut and h_f the height of the fuselage. z_{cg} is the percentage of the fuselage height at which the aft CG is positioned. In order to do this, an initial approximation is constructed by considering the wing and fuselage weights. For the fuselage, it's symmetrical nature allows a reasonable assumption that the center of gravity is located at half of the height. For the wing, the airfoil at the root has a thickness to chord of 15%. With a root chord of 2.5 m, this translates to a maximum height of 0.375 m. Taking the wing CG to lie at half of the height of the airfoil at root chord, 0.19 m from the top of the fuselage, or 0.81 m from the bottom of the fuselage. Hence, z_{cg} can be found:

$$z_{cg} = \frac{0.5 \cdot M_{fuselage} + 0.81 \cdot M_{wing}}{M_{fuselage} + M_{wing}} \tag{12.8}$$

For a fuselage mass of 719 kg and a wing mass of 962 kg:

$$z_{cg} = \frac{0.5 \cdot 719 + 0.81 \cdot 962}{962 + 719} = 0.677 \tag{12.9}$$

From the previous processes, the outer tyre diameter is fixed, and from earlier design stages the height of the fuselage is fixed. This leaves δ_{cgmw} and H_{smw} to be varied. However, Equation 12.6 indicates a ratio that constraints this. Since the aft CG is 4.12 m from the tip of the nose, placing a nose wheel forward of this point would increase the structural complexity of the strut unnecessarily. Hence, l_n may not exceed 4.12 m. Using a ratio of 0.087, the maximum value for l_m is:

$$l_{m_{max}} = 4.12 \cdot 0.087 = 0.358 \text{ [m]} \tag{12.10}$$

Hence, the range of values for δ_{cgmw} is from 0 to 0.358 m. Additionally, the constraints on H_{smw} are imposed by the presence of the propeller on the wing. As mentioned earlier, the middle of the wing, at the root chord is at 0.19 from the top of the fuselage, or 0.81 m from the bottom of the fuselage. It is assumed that this is the location of the spinner and thus origin of the propeller.The diameter of the propeller is given to be D_{prop}. Calculating the bottom most point of the aircraft less undercarriage, from the aft CG is:

$$z_{min} = 0.5 \cdot D_{prop} - (0.81 - z_{cg}) \tag{12.11}$$

Hence, for an estimated propeller diameter of 3 m, the lowest point of the aircraft less undercarriage is **1.367** m from the aft CG. This is 0.69 m from the bottom of the fuselage, requiring that:

$$0.5 \cdot D_{out} + H_{smw} > 0.69 \tag{12.12}$$

Leading to the constraint that:

$$H_{smw} > 0.69 - 0.5 \cdot D_{out} \tag{12.13}$$

Thus, the question of the landing gear design in longitudinal position can be boiled down to the selection of two design parameters: δ_{cgmw} and H_{smw}, with the following constraints.

1. $\theta_{tip} > \theta_{scrape}$
2. $0 < \delta_{cgmw} < 0.358$
3. $Hswm > 0.69 - 0.5 \cdot D_{out}$
4. $\theta_{scrape} = 10$

12.3.2. Lateral positioning

In addition to the longitudinal positioning of the undercarriage, the lateral positioning of the undercarriage is pertinent to the ability of the aircraft not tipping over. Given a set turnover angle, ϕ, the position of the undercarriage from the centre line in the spanwise direction is given by:

$$y_{mlg} \geq max \begin{cases} \dfrac{l_n + l_m}{\sqrt{\dfrac{l_n^2 \tan^2(\phi)}{z_{CG}^2} - 1}} & (12.14) \\ \dfrac{b}{2} - \dfrac{z_t}{\tan(\phi)} & (12.15) \\ y_p - \dfrac{z_n}{\tan(\phi)} & (12.16) \end{cases}$$

Additionally, two constraints exist. The second equation pertains to the required tip clearance, while the second ensures propeller clearance.

12.4. Final undercarriage

The following table presents the key parameters pertaining to the undercarriage.

	Nose gear	Main gear	Unit
Outer diameter	0.336	0.61	m
Tyre width	0.127	0.2	m
Inner diameter	0.102	0.25	m
Strut height	1.087	0.95	m
Distance to aft CG	4.025	0.35	m

13

Integrated Final Design

This chapter provides an overview of the final, integrated design. In Section 13.1, summaries of the important parameters describing the entire design are presented together with illustrations of the final rendered design. In Section 13.2 the requirement compliance is assessed by means of a compliance matrix.

13.1. Configuration & layout

After the design of every individual subsystem of the aircraft, the integration was done in CATIA resulting in the figures below. Figure 13.1 presents the different views of the UAV, namely the top, front and side view as well as an angled 3D view. Figure 13.2 illustrates the UAV in its full form, colored for reference.

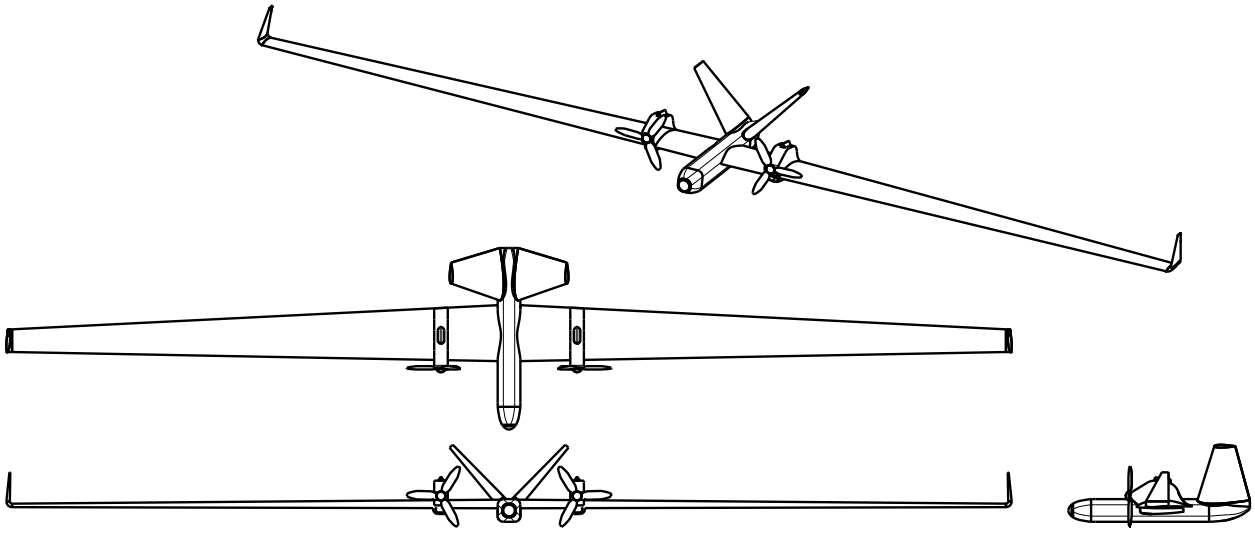

Figure 13.1: 3D, top, front and side view of the RePLASMA design, generated in CATIA.

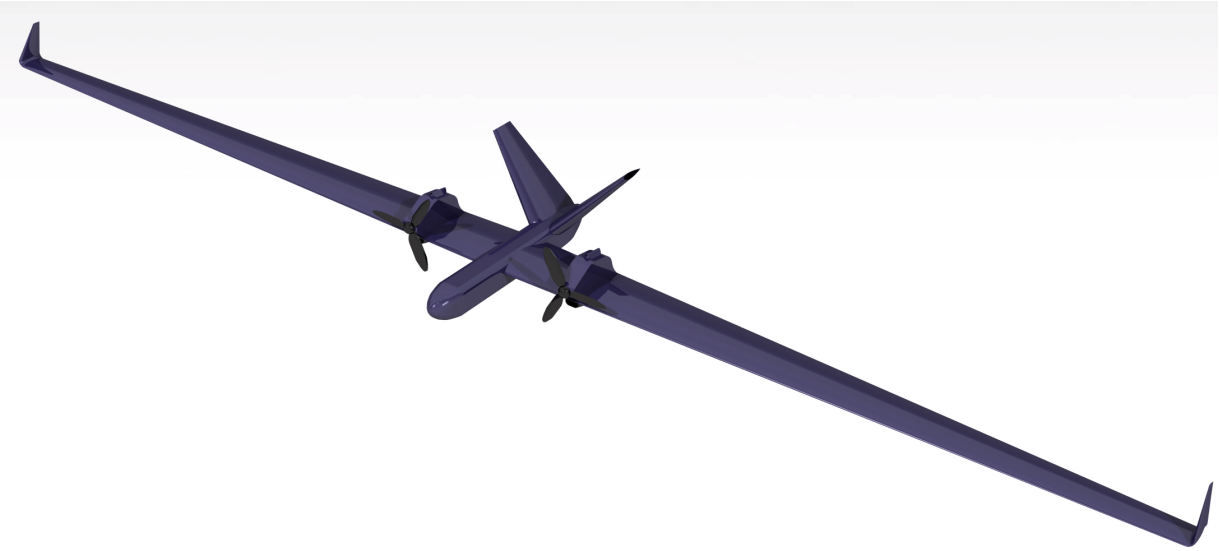

Figure 13.2: CAD render of the full aircraft generated in CATIA.

Furthermore, a summary of the main parameters contributing to the final design is given through four tables. Table 13.1 presents the relevant aerodynamic parameters calculated after the full aerodynamic analysis, as well as some parameters describing stability. General dimensions of the main components are given in Table 13.2, whereas Table 13.3 provides an overview of general parameters and choices made for the design. Finally, Table 13.4 presents the parameters and design choices made with regards to the propulsion system.

Table 13.1: Summary of the important aerodynamic and stability parameters after the detailed design.

Aerodynamic and Stability Parameters	**Numerical Value**
Aspect Ratio	25
$\alpha_{take-off}$	3.5°
α_{cruise}	4.5°
C_{D_0}	0.034
$C_{D_{cruise}}$	0.056
$C_{D_{take-off}}$	0.054
$C_{L_{cruise}}$	1.3
$C_{L_{take-off}}$	1.25
$\left(\frac{L}{D}\right)_{cruise}$	23.2
C_{m_α}	-0.41
C_{m_0}	0.15
C_{n_β}	0.15

Table 13.2: Summary of the dimensions of the basic design components.

Dimension Name	**Dimension Value**
Wing span	43.8 [m]
Wing area	77.6 [m^2]
Winglet height	1.5 [m]
Wing root chord	2.5 [m]
Wing tip chord	1 [m]
Fuselage length	8 [m]
Fuselage width	1 [m]
Fuselage height	1 [m]
V-tail halfspan	6.48 [m]
V-tail area	20.98 [m^2]
V-tail root chord	2.31 [m]
V-tail tip chord	0.93 [m]
Propeller diameter	3 [m]

Table 13.3: Summary of general parameters of importance after the detailed design.

General parameter	Value/Choice
Take-off mass	4521 [kg]
Payload mass	150 [kg]
Fuel mass	1536 [kg]
Wing mass	1019 [kg]
Fuselage mass	261 [kg]
Empennage mass	305 [kg]
Propulsion system mass	744 [kg]
Endurance	20 [h]
Cruise velocity	149 [m/s]
Wing airfoil	Custom optimized airfoil
Tail airfoil	NACA 0012
Wingbox material	Ti-6Al-4V
Fuselage material	Aluminum 7075
Empannage material	Aluminum 7075

Table 13.4: Summary of the main parameters and choices made on the propulsion system of the aircraft.

Propulsion characteristics	Value/Choice
Engine	GM 3.6L V6 LFX
Max power	300 [hp]
Engine mass	157 [kg]
Num. of engines	2
Max RPM	7200
Rated RPM	3800
Num. of pistons	6
Fuel type	E85
Num. of turbochargers	3
Num. of intercoolers	3

13.2. Compliance matrix

This section assesses whether all relevant, driving requirements were satisfied. Table 13.5 presents each driving requirement and the compliance status. Positive compliance implies compliance with the specific requirement after verification while negative compliance implies that the requirement is not met at the current point of design. Requirements with the <TBD> compliance status are not yet verified due to lack of detail of the verification method or simply due to lack of time. The verification of the <TBD> requirements is expected to be done in future stages until compliance is achieved with most of the requirements.

Table 13.5: Compliance matrix of driving requirements of the RePLASMA mission.

Requirement	Compliance Status
PLS-U-OPS-1:Mission shall facilitate sampling at an altitude above 25 km	Positive Compliance
PLS-U-OPS-2:Mission shall support in-situ processing of atmosphere samples	Positive Compliance
PLS-U-OPS-3:Mission shall meet its requirements at all latitudes all year	Positive Compliance
PLS-U-OPS-4:Mission shall not obey any take-off and landing distance requirements	Positive Compliance
PLS-U-OPS-5:Mission shall be operable from a remote base of operations	Positive Compliance
PLS-U-OPS-6:Mission shall be deployable from worldwide airfields without prejudice to **PLS-U-OPS-4**	Positive Compliance
PLS-U-OPS-7:Mission shall be operable by a ground crew by remote control	Positive Compliance
PLS-U-OPS-15:Aircraft shall be capable of autonomous landing	Positive Compliance
PLS-U-OPS-15.2:Aircraft shall be recoverable after landing due to engine failure	Positive compliace

Continued on next page

Table 13.5 – continued from previous page

Requirement	Compliance Status
PLS-U-OPS-15.3:Landing shall be performed without prejudice to **PLS-R-OPS-12** and **PLS-R-OPS-14**	Positive compliance
PLS-U-PERF-1:Mission shall have cruise endurance of 20 hours	Positive Compliance
PLS-U-PERF-2:Mission shall support a payload mass of 150 kg	Positive Compliance
PLS-U-PERF-3:Mission shall be remote controllable up to a distance of 1000 km	Positive Compliance
PLS-U-PERF-4:Mission shall operate in an airspeed range of 0.4 < M < 0.85	Positive Compliance
PLS-U-PERF-5:Mission shall remain operational in moderate turbulence	Positive Compliance
PLS-U-PERF-6:Mission shall remain operational up to -100°C	Positive Compliance
PLS-U-REL-1:Mission shall use commercially available technology	Positive Compliance
PLS-U-SUS-1:Mission shall use sustainable clean fuels	Positive Compliance
PLS-U-SUS-3:Mission shall be reusable or recyclable during decommissioning	Positive Compliance
PLS-U-COST-1:Mission shall establish no restrictions on budget	Positive Compliance
PLS-U-COST-2:Mission shall establish no restrictions on return of investment	Positive compliance
PLS-U-PROP-1:Mission shall use a reciprocating type of propulsion	Positive Compliance
PLS-R-PROP-06:Effects of cyclic temperature loading and environmental degradation shall not compromise structural integrity.	<TBD>
PLS-R-CS-03:Aircraft shall be stable such that loss of pilot input does not result in mission catastrophe.	Positive compliance
PLS-R-CS-04:Limits for center of gravity that provide for stable and controllable operation shall be documented.	Positive compliance
PLS-R-CS-05:Aircraft shall exhibit static longitudinal, lateral, and directional stability in normal operations.	Positive compliance
PLS-R-CS-06:Aircraft shall have dynamic short period and Dutch roll stability in normal operations.	<TBD>
PLS-R-CS-07:Aircraft shall not exhibit divergent longitudinal stability so as to increase the pilot's workload or endanger the aircraft.	Positive compliance
PLS-R-CS-08:Aircraft shall have controllable stall characteristics in straight and turning flight.	Positive compliance
PLS-R-STR-04:The structure must be free from any aero-elastic instability and excessive vibration.	<TBD>
PLS-U-AERO-05:The same airfoil shall be used in the span-wise direction	Positive compliance
PLS-U-PROP-13:The propulsion subsystem shall provide 431 [hp] of power	Positive compliance
PLS-U-OPS-15.1:The aircraft shall be able to detect engine failure.	Positive compliance
PLS-U-STR-19:The total structural mass should be minimized	Positive compliance
PLS-U-STR-20:The structural subsystem shall be able to protect all other subsystems from environmental and operational hazards	Positive compliance
PLS-U-STR-22:The structural subsystem shall be able to sustain all loads expected in its lifetime	Positive compliance

14

Operations & Cost

The aim of this chapter is to illustrate to the reader the concepts developed that are to be implemented during the operational lifetime of the RePLASMA mission. In order to do this, two key facets need to be analyzed. The first is the logistics and operations concept, the second is the analysis of the incurred costs. This includes costs for development, operations and decommissioning.

14.1. Operations & logistics concept

The conclusion of the design, manufacturing, testing and certification phases of design results in the initiation of the operational phase of the RePLASMA mission. It is in this phase that a myriad of regulations, dictate the procedures undertaken in the operational phase. In Figure 14.1 the operations and logistics diagram is shown.

- **Operations**: Regulations, pertaining to behavior both on the ground and in flight regimes define the procedures required of the aircraft in an operational phase. These procedures follow from requirements for the most part,but historical experience of UAV operations also provide useful insight into operational 'best practices'. EASA defines three concepts for UAV operations, based on the consequences a possible failure could have - Open, Specified and Certified - with RePLASMA classified as a certified UAV, resulting in operations similar to that of a regular airline.
- **In-air operations**: Since atmospheric data needs to be collected in different weather conditions, RePLASMA will operate in accordance with visual flight rules (VFR) and instrument flight rules (IFR). Thus, the pilot operating RePLASMA must be IFR certified. Additionally, the risk of a mid-air collision at cruise altitude is sufficiently low, [78] meaning no air traffic control assistance is required in cruise. For ascent and descent, air traffic control will be heeded. Finally, the capability to perform an autonomous landing in case of an engine failure of this UAV means that new algorithms are required to be developed.
- **Ground operations**: Firstly, since biofuel is a non-volatile fuel compared to hydrogen, no special operations will be needed with regards to fueling and a traditional approach as with kerosene could be used. Moreover, since the aircraft is operated by a pilot, taxiing in aerodromes would be no different to that of a conventional aircraft. A ground control station has to be provided in order to facilitate human control of the aircraft, which is related to extra costs. A potential problem, limiting the aerodromes that the UAV could operate in, is the span of the wing, reaching almost 47 m and placing the aircraft in an ICAO Code D category[1]. If that proves to be an operational problem, potentially in the next stages of the project, fixes such as using foldable wings could be applied.

[1] https://www.boeing.com/commercial/aeromagazine/articles/2010_q3/3/ [accessed 17/6/2021]

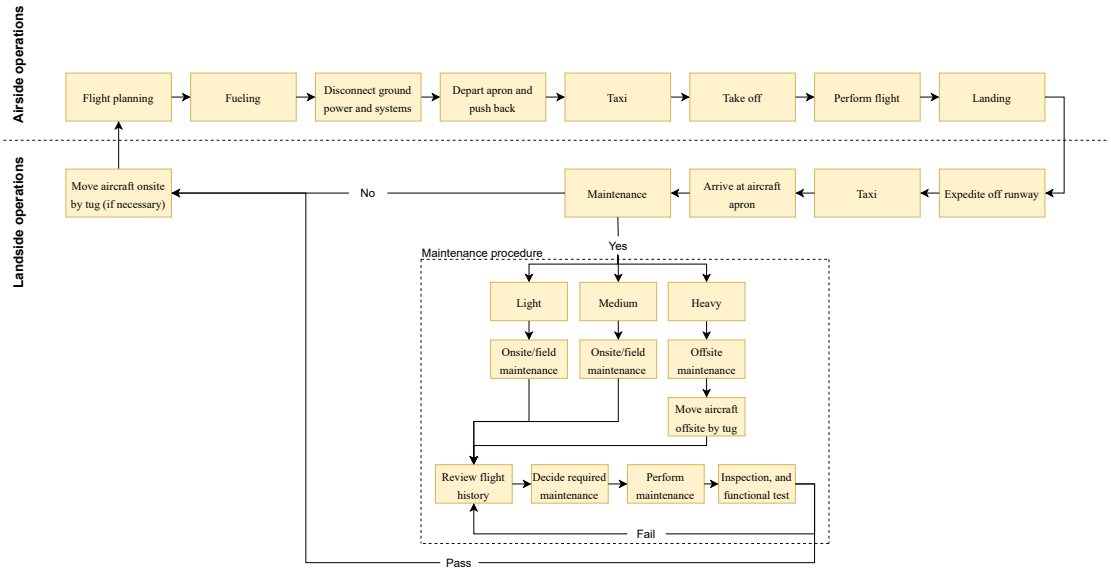

Figure 14.1: Operations and logistics diagram.

14.2. Cost & financial analysis

Beyond defining the operational flow of RePLASMA, the cost is a critical factor in understanding the value of a mission. The costs that are considered may be broadly demarcated as development and operational costs. Additionally the operational costs can be considered to be bifurcated into direct and indirect operational costs. In order to provide a more accurate view of the costs expected, Figure 14.2 depicts the cost breakdown structure. The first cost to consider is the development cost. Within design tools, reference is made to both software and hardware tools. This includes CATIA, ANSYS and manufacturing jigs. Certification refers to the costs incurred during the certification program. Furthermore, the employee costs pertain to the costs incurred in hiring, training and retaining a sufficient number of employees to carry through the mission. The exact time frame for this is described in Chapter 16. Finally, the material and component costs pertain to the costs of the materials and components required to build RePLASMA.

Development costs				
Item	**Unit price**	**Unit**	**Quantity**	**Total**
Labour	100	EUR/hr	80,000	8,000,000
Aluminium	6.8	EUR/kg	2000	13600
Titanium	17.64	EUR/kg	1000	17640
Components including propulsion	20,000	EUR	1	75,000
Certification	5,000,000	EUR	1	5,000,000
Testing	3,000,000	EUR	1	3,000,000

The costs for labor are assumed to be 100 euros per hour, since this reflects billing rates across most engineering firms. The duration of this cost is estimated to be 5 years, at 40 hours a week at 40 weeks per year. The cost of aluminium and titanium are derived in Chapter 9. The weight of the wing is allotted to titanium, while the rest of the air frame is composed of aluminium. Furthermore, the costs for certification and testing are estimates based on the costs of similar programs [2]. Additionally, one

[2]https://www.plm.automation.siemens.com/global/pl/our-story/customers/tlg-aerospace/51461/ [accessed

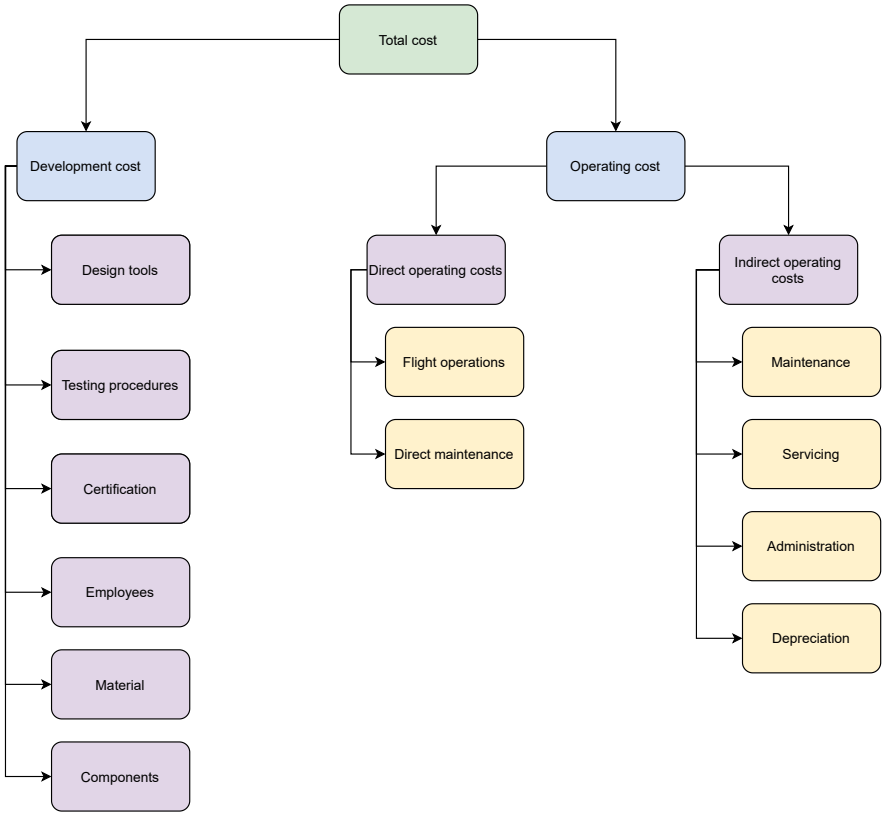

Figure 14.2: Cost breakdown structure for RePLASMA.

may consider the direct operating costs. The first direct operating cost is the cost of the fuel required. The amount of fuel required is approximately 1500 kg of E85 bioethanol.This is 1901 litres. At the time of writing, this fuel has a price of 1.35 euros per liter [3]. The next cost is that of the flight crew, paid for the duration of a flight, with a one hour buffer either side, for start up and shut down procedures. Additionally, the cost of airport handling fee's are derived from the average at airports within operational latitudes. For a night take off and a night landing, the handling fee is 6.02 and 5.08 euros per tonne of maximum take off weight, assuming a disconnected stand. The cost of the aircrew and maintenance crew are derived from the standard costs described by the Royal Dutch Airforce [4].

Direct operating costs				
Item	**Unit price**	**Unit**	**Quantity**	**Total**
Fuel	1.35	EUR/ltr	1901	2566.35
Flight crew	20	EUR/hr	24	480
Airport costs	11.10	EUR/tonnes	5	55.5
Inspection & maintenance	40	EUR/hr	2	80

At this stage of design, it is not feasible to estimate the costs with a higher level of fidelity, as the design remains very conceptual. None the less, the initial development costs total to just over 16.1 million euros. The operating costs per flight total to 3181.85 euros. This is similar to missions such as the Global hawk, with an initial unit price of 10 million USD in 1994. [5]

17/6/2021]
[3]https://www.businessinsider.nl/bio-ethanol-goedkoper-maar-waar-kun-je-tanken/ [accessed 17/6/2021]
[4]https://www.acom.nl/salarisschalen/ [accessed 17/6/2021]
[5]https://en.wikipedia.org/wiki/Northrop_Grumman_RQ-4_Global_Hawk [accessed 29/6/2021]

15

Manufacturing & Reliability

In this chapter, the production phase and operational characteristics of the aircraft will be outlined. In Section 15.1, the Manufacturing, Assembly and Integration plan will be presented. Lastly, the RAMS (Reliability, Availability, Maintainability, Safety) characteristics will be discussed in Section 15.2.

15.1. Manufacturing, assembly & integration plan

The Manufacturing, Assembly and Integration (MAI) plan describes the production phase of the aircraft and its components. The basis of the MAI-plan is a flow diagram containing the timeline of the three phases, which is given is Figure 15.1.

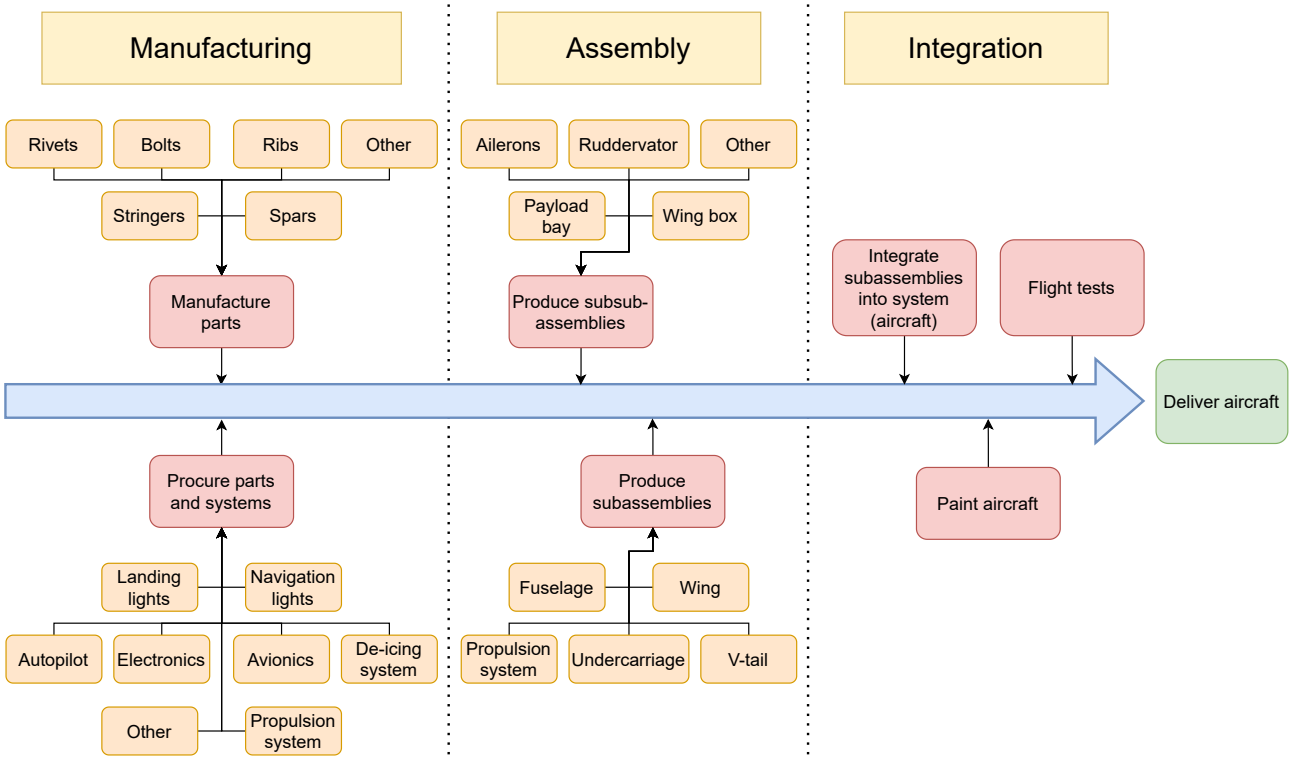

Figure 15.1: Production flow diagram.

The Manufacturing phase consists of two activities, namely the manufacturing of the single-piece parts and the procurement of several parts and systems that can not be manufactured as easy as the aforementioned single-piece parts. These two activities are run in parallel, speeding up the

process. One thing to note is that the propulsion system consists of three parts, namely the engine, intercooler and compressors, which also need to be procured separately. Furthermore, systems like communication and navigation fall under avionics. The Assembly stage is where the subsub-assemblies and sub-assemblies are produced. These activities can not be run in parallel, for example because the ailerons and wing box obviously need to be finished at an earlier stage. The Integration phase is the final phase, starting with integrating the sub-assemblies into one system, namely the aircraft. For example, the wing need to be integrated into the fuselage. Expensive parts such as the propulsion system and complex parts such as the tail and undercarriage will be integrated into the aircraft as late as possible, decreasing the production time and costs [79]. After the aircraft has been fully integrated, a layer of paint will be applied to the aircraft. And finally, the aircraft will need to pass several flight tests before being cleared for delivery.

15.2. RAMS characteristics

In this section, the RAMS characteristics of the RePLASMA UAV are evaluated, in order to determine the operational performance of the aircraft.

15.2.1. Reliability

The reliability of the aircraft plays an important role in the operational performance. For this reason, the different failure modes of the aircraft during the operational phase must be determined. A breakdown of these failure modes is presented in Figure 15.2. As can be seen in figure, most of the failure modes are dependent on the propulsion system and control surfaces. Another thing that can be done is to quantify the reliability of a system. Equation 15.1 gives this reliability. λ is the failure rate of a system and t is the time period over which the reliability is analyzed. Generally, aircraft are checked around every 400-600 hours. In the case of RePLASMA, this time period is taken as 600 because of the aircraft's specification.

$$R = e^{-\lambda t} \tag{15.1}$$

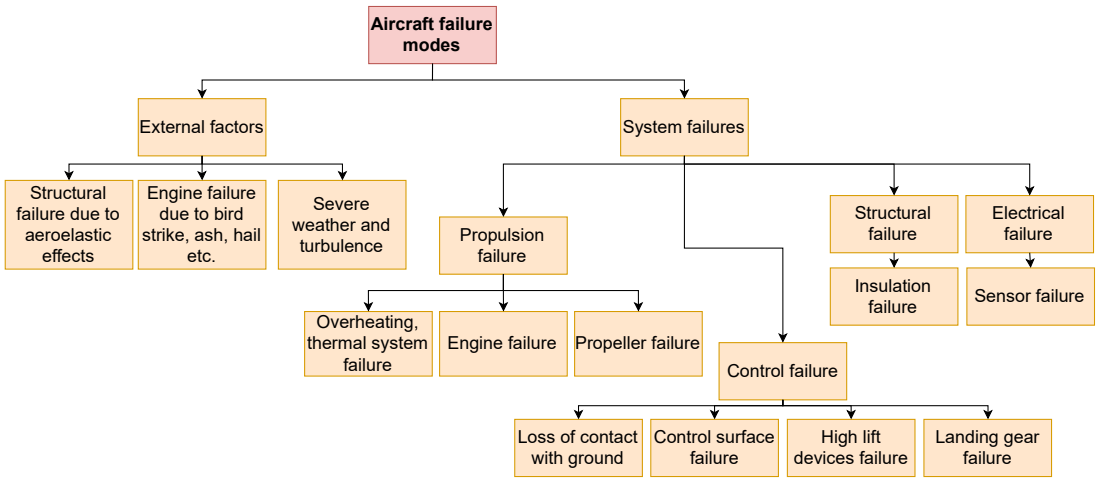

Figure 15.2: Possible failure modes during useful life period.

It is helpful to pick out the most critical systems failures can occur in and elaborate on them further.

- **Engine failure:** According to the Federal Aviation Administration, general aviation engines have a failure rate of about 1 every 10,000 flight hours. With RePLASMA having two engines, this results in a reliability of 0.9966 for the whole propulsion system. This is unfortunately the only system which reliability can be assessed quantitatively.
- **Flight controls and communications:** During the operational phase the reliability of the communications system is critical to the mission. From a system perspective, using off the

shelf and fail safe components will help reliability. On the other hand, many external factors such as unexpected harsh weather conditions, loss of contact, and cybercrime could affect the reliability on the system.

- **Electrical system:** Due to the extreme and varying temperature range the aircraft will experience, the wiring and electrical units will be more vulnerable to damage. Even though appropriate off-the-shelf technologies are available for these applications, this aspect has been considered during the design of the electrical system.

15.2.2. Availability

The availability of the aircraft is measured by the ability to execute the required functions during its lifetime[1], so it comes hand in hand with reliability. For example, the aircraft will not be available during refueling and maintenance activities such as engine check-ups and autopilot software maintenance. Furthermore, the ground personnel such as the pilots should also be available for the mission to be carried out. Availability also comes in another way: the aircraft should be available at the scheduled delivery date, namely in the year 2026. A more detailed analysis will be presented in Chapter 16, but it can already be said that the deadline will be made comfortably as because the estimate for entry into service is around mid 2026.

15.2.3. Maintainability

A list of systems that need maintenance must be set up in order to have a better overview of all maintenance activities, be it scheduled or unscheduled. The maintenance activities are divided in several categories, namely A, B and C. The A-category maintenance checks are performed every week, taking a approximately 4 hours of work by one mechanic. The B-category will be performed every 3 months, taking up a whole 8-hour working day by 2 mechanics. Lastly, the C-category maintenance checks will be performed twice a year, which will take 3 whole days by 4 mechanics. The list of maintenance checks along with their category can be found in Table 15.1.

Table 15.1: UAV maintenance activities along with their categories.

Maintenance activity	Category A	Category B	Category C
Engine check-ups	x		
Fuel tank inspection	x		
Control surface inspection	x		
Autopilot maintenance		x	
Onboard-system check-ups		x	
Wing structure inspection		x	
Landing gear maintenance			x
Thorough engine maintenance			x

15.2.4. Safety

It is essential to apply a redundancy philosophy to make sure that the aircraft stays controllable during failure modes. The first layer of built-in redundancy is the interplay between the autopilot and the pilot controlling the aircraft on the ground. For example, if the pilot is flying the aircraft remotely and the connection between the ground and the aircraft is lost, it is important that the autopilot then kicks in and takes over the control of the aircraft. If necessary, it must even be able to land itself in case the connection between the ground and aircraft cannot be restored. Furthermore, in case of an autopilot failure, the ground pilot must be ready to take over control in an instant.

Another redundancy philosophy is that both the autopilot and ground pilot should be able to safely land the aircraft in case of an engine failure, or bird strike. A bird strike at an altitude of 25 km is of course highly unlikely, but these things should definitely be taken into account. The aircraft obviously needs to climb to cruise altitude, during which bird strikes could happen.

[1] https://www.osti.gov/servlets/purl/1117172 [accessed 22/06/2021]

16

Future Outlook

The aim of this chapter is to provide the reader with an overview of the future of the RePLASMA project, following the conclusion of the design synthesis excercise. In order to do this, the chapter will present the project development logic, including a project gantt chart so as to place the design work conducted in the previous phases into a context relevant in the future. Furthermore, an example mission will be presented, so as to aid in visualizing the contexts in which the RePLASMA mission will operate.

16.1. Future project development

In order to define the current status of the RePLASMA mission, the reader may consider the following figure.

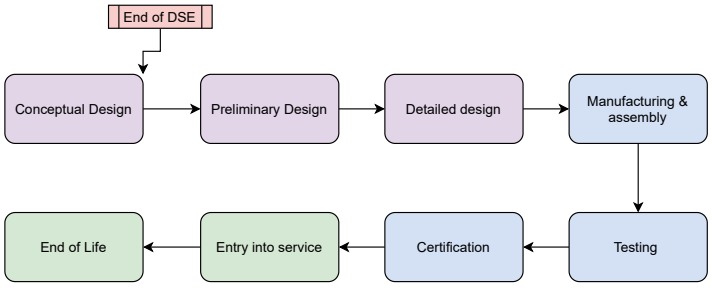

Figure 16.1: High level overview of project stages.

The design synthesis runs from the start of the conceptual design phase, and ends within this design phase, due to the limited time of the project. Following the conceptual design phase, where statistical and (semi-)empirical methods are used to design the aircraft, the preliminary and detailed design are conducted. These design phases focus on developing analyses specific to the RePLASMA mission. The level of fidelity increases throughout these stages, with the end of the detailed design typically marking the point in the process where the aircraft can be assembled, as all components are known and dimensioned. Following the manufacturing and assembly, various aspects of the RePLASMA system can be tested, eventually leading to certification in compliance with various regulations, such as but not limited to the CS23 specifications. This marks the entry into service of RePLASMA, which leads into the end of life phase after a sufficient operational lifetime. In order to elaborate upon the design phase, a more detailed overview of the preliminary and detailed design phases are provided in Figure 16.2 and Figure 16.3.

From Figure 16.2 it is clear that the preliminary design phase focuses on refining the ideas developed throughout the conceptual design phase. This includes a class 2.5 weight estimation, that is less reliant on statistical relationships. Furthermore, considering the integration of the air frame in a

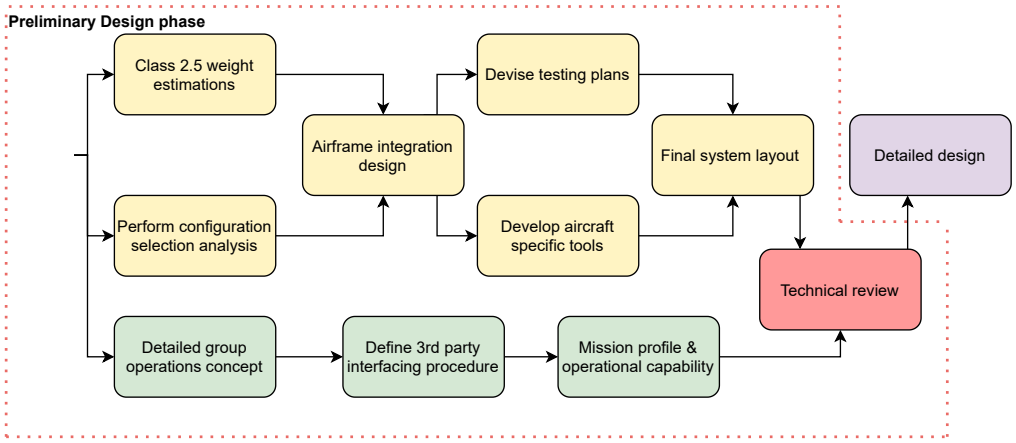

Figure 16.2: Preliminary design phase.

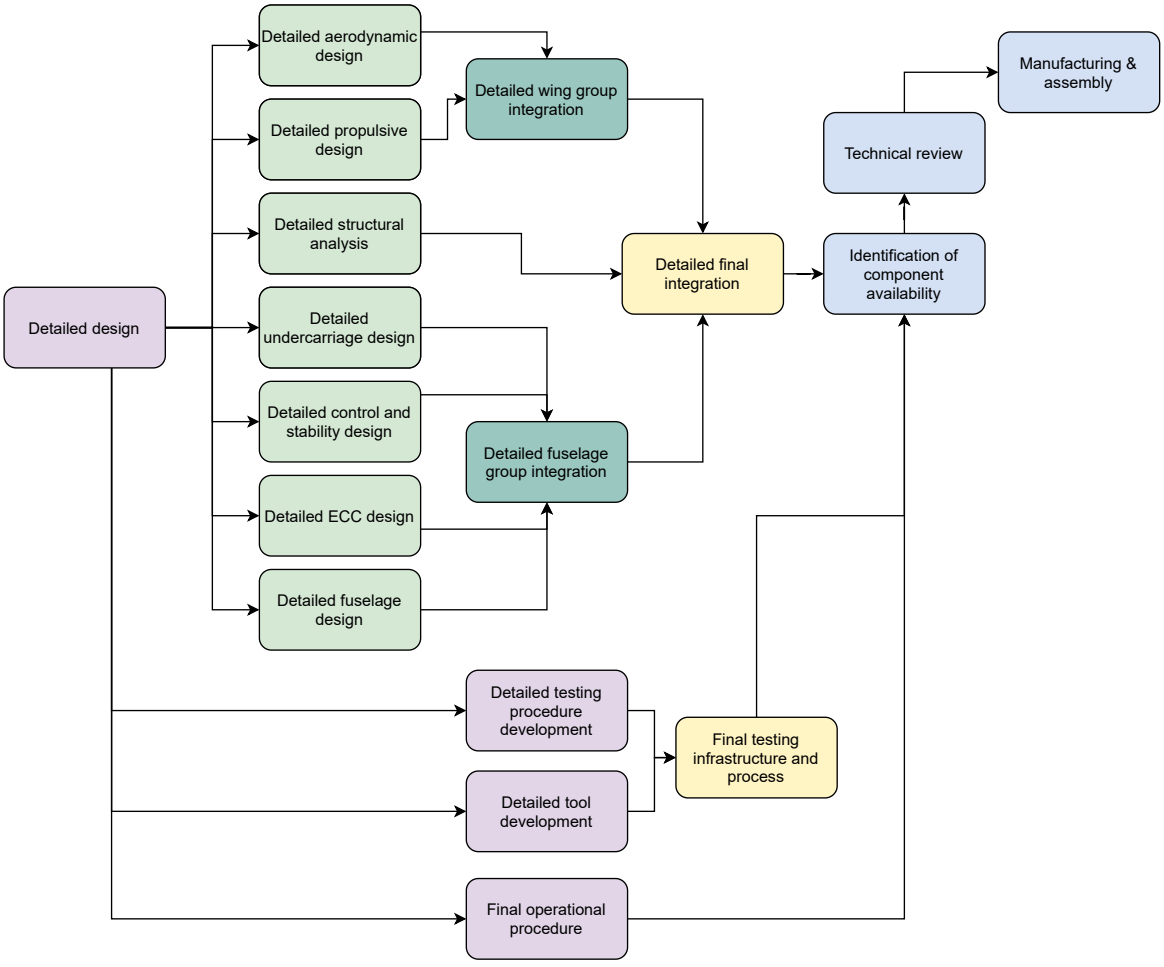

Figure 16.3: Detail design phase.

Phase	Start date	End date
Design synthesis exercise	04/2021	07/2021
Conceptual design	04/2021	10/2021
Preliminary design	11/2021	11/2022
Detail design	12/2022	12/2023
Manufacturing & assembly	01/2024	08/2024
Testing	09/2024	09/2025
Certification	06/2025	06/2026
Entry into service	07/2026	

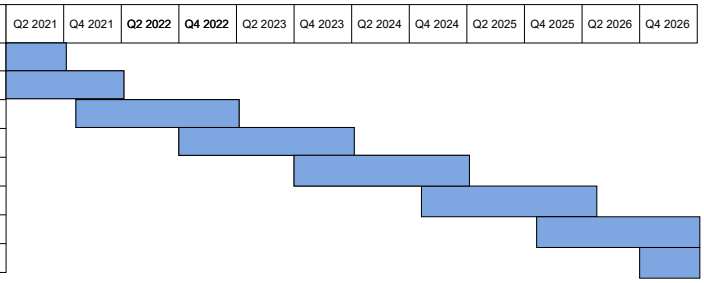

Figure 16.4: Project development gantt chart

more prudent manner is typical of the preliminary design phase. Additionally, the initial design of testing plans and aircraft specific design tools are required, so that a plan of implementation exists. In parallel, the operations on the ground must be considered in more detail, with a clear definition of procedures and demarcation of responsibilities with respect to third parties. Finally, the operational concept must be integrated with the technical system, so as to establish a detailed mission profile. This will allow the operational capability of the RePLASMA system to be defined, verified and presented to relevant stakeholders. The combination of the final system layout and the mission profile will be evaluated at a technical review, where a formal decision is made regarding proceeding with the detailed design phase. This decision is made on the basis of input from clients, as well as other facts such as risk mapping and operational feasibility.

Should the technical review yield a positive result, the detail design phase is initiated. In this phase, every technical subsystem is designed to a fidelity commensurate with that expected from detailed design. This includes aerodynamics, propulsion, structures, undercarriage, control and stability, electronics, control and command as well as the fuselage. Upon the completion of detailed design for these subsystems, the wing and fuselage group are integrated in parallel. These two groups meet and are integrated in the final integration, where the lowest level of design ensures no problems are found in subsystem interaction. In parallel to the subsystem design, testing procedures and tools need to be developed, and frameworks for implementation need to be devised, such that they may be implemented after the completion of the manufacturing and assembly phase. Another critical element of the detail design phase within the RePLASMA project is the identification of component availability, due to the requirement pertaining to the commercial availability of components. Finally, another technical review is held. This includes reviews of the subsystems, the operational plans as well as the manufacturing plan. Finally, the certification plan needs to be reviewed as well.

The Gantt chart below indicates an outline of the expected time markers associated with each of the design phases. The reader will notice that while the DSE and the conceptual design phase start at the same time, the conceptual design phase needs to extend for a further 3 months, to allow for time to finalize everything. Following this, both the preliminary and detail design phase have been assigned an approximate time line of 1 year each, on the assumption that a sufficient amount of resources are available to the mission. This is so, such that the time to entry of service is as fast as possible, in order to meet the pressing need for atmospheric science data. Following this, the manufacturing and assembly is slated to take 7 months, This is relatively short, however compliance with the requirement to have commercially available parts means the RePLASMA system should be possible to manufacture in less time that similar aircraft in its class. Finally, testing and certification could take upto 1.5 years, given the variety of subsystems that need to be tested and certified. On the basis of this, a feasible entry into service is the end of Q2 in 2026.

16.2. Example mission

As a form of proof-of-concept, this section will serve as a simulation of the design's performance under conditions of an exemplary mission. Figure 16.5 is a visual representation of the flight profile of a mission the design will likely conduct. Note that the axis are not to scale as Figure 16.5 serves to visualize a typical mission. The starting points of each segment from take-off to landing are denoted by numbers 0 through 7.

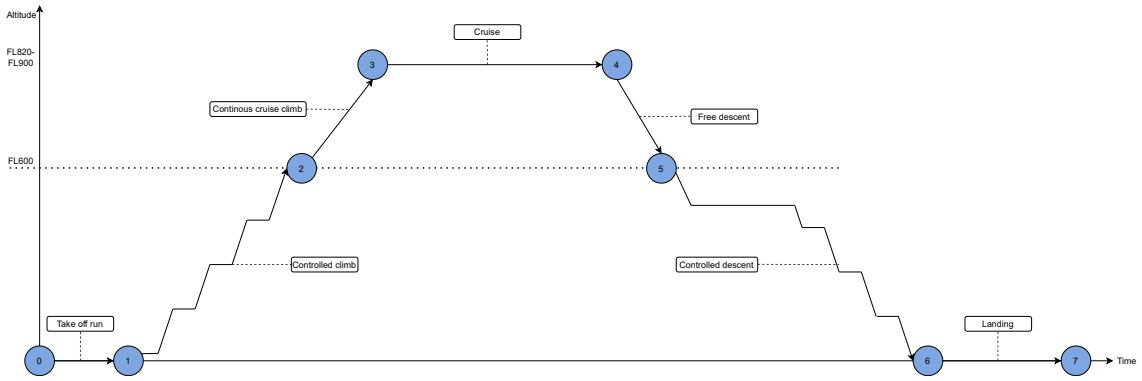

Figure 16.5: Flight profile of exemplary mission.

0-1: Take-Off Run This exemplary mission starts at sea level. At this point, the UAV would have started up and spooled to idle thrust. Once lined up on the runway, the throttle will engage such that the engines is running at 50% to provide a combined 1.88 kN of thrust, 259 Nm of torque at a speed of 2000 RPM. These are take-off specific values to avoid tip speeds above Mach 1. For the UAV at MTOW, the take-off speed required to generate sufficient lift equal to weight is approximately 27 m/s. At the point, the aircraft must rotate to an angle of attack5 ° by generating an angular acceleration of 15 [deg/s^2] as described in Section 7.3. To do so, maximum positive deflection is applied on the ruddervator in order to generate negative lift with the V-tail and pitch the aircraft.

1-2: Controlled Climb Once liftoff is achieved, the UAV will enter a controlled climb phase. The controlled ascent involves incremental steps in altitude at a climb rate of 5.8 m/s. This climb rate can only be sustained at the lower layers of the atmosphere due to the lower air density near cruise altitude. The controlled climb will be dictated up until flight level FL600 (60k ft) depending on air traffic control. FL600 and below is considered as controlled airspace, where the UAV and pilot at ground station must follow indications from the near ATC tower until reaching above FL600.

2-3: Free Climb Once FL600 is exceeded, the UAV can perform free climb without any restrictions from ATC. However, at this altitude, the UAV will have to reduce its climb rate to 5.0 m/s due to reduced air density and thus reduced lift generation.

3-4: Cruise Flight Once 25 km is reached, the UAV will enter its cruise phase where RePLASMA will perform the necessary measurements. The UAV must achieve 20+ hours of flight time during cruise phase. At that altitude, the propulsion system and compressor will be functioning near maximum performance. At this altitude, the engines will have to deliver 177 hp each running at 3400 RPM and 369 Nm of Torque in order match the power required. Based on this operating condition, the UAV can achieve a brake specific fuel consumption of approximately 200 g/kWh, which is below the limit established. In order to achieve the maximum endurance ratio of C_L^3/C_D^2, the flight computer will set the AoA respectively by trimming the ruddervator to the desired deflection angle.

4-5: Free Descent After cruise is completed, the craft will throttle down slightly and engage in a descent. The limit descent rate is yet to be defined but during this particular phases, there is in principle no restrictions imposed by ATC regarding descent rate. The main constraints will originate from the flight envelope defining the limit load factors and maximum dive speeds to avoid overspeeding and reducing structural stresses.

5-6: Controlled Descent After descending back down to FL600, contact with the ATC must be re-established with navigational instructions and descent vectors in order to re-engage in a controlled descent down to approach altitude.

6-7: Landing Due to the fact that no high-lift devices are utilized on-board the aircraft, during the landing phase, the vehicle will gradually reduce its speed without any lifting surfaces in order to reach its minimum speed, stall speed of 23 m/s, just above the landing runway. At touchdown, to slow the vehicle down, firstly, the breaking system will get engaged and the ruddervator will gradually be deflected to its maximum value in order to create maximum lift and thus, maximum induced drag. After 900 m the UAV will reach a standstill and post-mission operations can begin.

17

Conclusion & Recommendations

This report was produced with intention to present the design process and the results of these processes with regard to a high altitude long endurance UAV. In specific, this report focused on the detailed design of the sub-systems and the operations & logistics of the mission.

Within the subsystem design presented in Chapter 7 through Chapter 12, a number of conclusions and final design products were achieved. As a whole, the project duration culminated in an airframe, an aerodynamic system, an undercarriage, control system and communication system that fulfill all verifiable requirements derived from client expectations of the project along with relevant regulation derived requirement.

From the propulsion system in specific, the design ran slightly behind schedule due to the greatly augmented complexity due to the relatively unexplored altitude that RePLASMA is required to operate within, especially as a piston-powered aircraft. At this time of the publishing of this report, the propulsion system continues to be in development with positively verified simulated operation in altitudes in excess of 18 km. It is forecasted and planned that within three working days the propulsion system will be verified to operate at the altitude of 25 km prescribed by client requirements.

With regard to design processes, it was concluded that the sparseness of statistical data and design methodologies with regard to HALE UAVs greatly hampered the design pace of the project. On the converse, it was also concluded that design methodologies that use statistical regressions from other aircraft can be adapted sufficiently using sufficient engineering judgement for application to HALE UAVs. An example of this is the Class II weight estimation presented in Chapter 6.

Furthermore, recommendations for further design and the design of similar missions are divided by subsystem and presented below.

Aerodynamics

- The setup of a model to simulate engine intake flows and cooling flows would greatly increase the accuracy of the aerodynamic performance estimation.
- Calculation of the momentum drag of the cooling cowlings for a better drag approximation.
- Quantify the effect of winglets by means of testing or simulations
- Post the final design integration, higher fidelity models to optimize the contour and the interaction of different subsystems is strongly suggested.

Structures & Materials

- Make loading diagrams of the wing for torque and moment about z-axis. In this stage of the design, only the loading diagrams for the wing in the vertical direction have been taken into account.
- Perform shear and normal stress analysis of the wing box using FEM, because that was outside of the scope of the preliminary design.

- Perform structural analysis for the fuselage and tail using FEM, because that was also outside of the scope of the preliminary design.

Control & Stability

- The analysis of a design with a tailboom is strongly suggested as it might lead to a smaller tail and lower overall drag.

Undercarriage

- Analysis of landing gear integration in the wings could lead to greater lateral stability but the weight penalty in the slender wings would be a deciding factor.

Propulsion

- Establishing a more in-depth numerical model of the piston engine which accounts for the function of all major components would lead to a reduction in errors and assumptions when treating the system as a black-box.
- Conducting a reliability study on the GM 3.6L V6 LFX to determine how many cycles the engine can sustain before reaching potential failure cases wold provide more insight on the aircraft's life time.
- Establishing a thorough aircraft inspection procedure would contribute greatly into the longevity of the subsystem and the aircraft's lifetime due to the fact the systems in place are subject to extreme conditions.

18

Task Division

		Łabor, Jakub, 4876563	Prashar, Mayank, 4643526	Insinger, Guido, 4846419	van Spronsen, Mark, 4866959	Brachmi, Walid, 4554337	Korkmaz, Aytek, 4850459	Kandiyoor, Gopal, 4797795	Vretoudakis, Emmanouil, 4799216	Shokolarov, Aleksandar, 4836839	Deval, Prajwal, 4811526
	Executive Summary							x			
Chapter 1	Introduction						x				
Chapter 2	Project background		x		x				x	x	
Chapter 3	Requirements	x				x		x		x	
Chapter 4	Concept generation	x		x	x		x		x	x	x
Chapter 5	Design process flow							x		x	
Chapter 6	Sizing and weight estimation			x			x		x	x	x
Chapter 7	Aerodynamic design		x						x	x	x
Chapter 8	Propulsion	x	x	x		x					
Chapter 9	Structures and materials				x						
Chapter 10	Stability and control						x			x	
Chapter 11	Electronics, command and communications							x		x	
Chapter 12	Undercarriage							x			
Chapter 13	Integrated final design							x	x	x	
Chapter 14	Operations and cost			x				x		x	
Chapter 15	Manufacturing and reliability				x						
Chapter 16	Future outlook		x	x		x		x		x	
Chapter 17	Conclusion and recommendations					x			x		x
-	CAD Model							x			x

References

[1] Group 20. Replasma baseline report. Technical report, Technische Universiteit Delft, 2021.

[2] O. Naomi. The scientific consensus on climate change. *Science*, 306, 2004.

[3] D. Ehhalt and M. Prather. Atmospheric Chemistry and Greenhouse Gases. page 50.

[4] K. Sudo, M. Takahashi, J. Kurokawa, and H. Akimoto. Chaser: A global chemical model of the troposphere 1. model description. *Journal of Geophysical Research*, 107, sep 2002.

[5] I.C. Dedoussi. Implications of future atmospheric composition in decision-making for sustainable aviation, 2021.

[6] F.D. Quadros, M. Snellen, and I.C. Dedoussi. Regional sensitivities of air quality and human health impacts to aviation emissions. *Environmental Research Letters*, 15(10), 2020.

[7] M. Chanin. *The Role of the Stratosphere in Global Change*. Nato ASI Subseries I. Springer-Verlag Berlin Heidelberg, 1993.

[8] J.L. Dufresne, M.A. Foujols, and N. Vuichard. Climate change projections using the ipsl-cm5 earth system model: from cmip3 to cmip5. *Climate Dynamics*, 40, 2013.

[9] Group 20. Replasma midterm report. Technical report, Technische Universiteit Delft, 2021.

[10] P. O'Neil. Boeing High Altitude Long Endurance (HALE) UAS. page 19, 2012.

[11] D. Bents, T. Mockler, A. Maldonado, J. Hahn, J. Cyrus, P. Schmitz, J. Harp, and J. King. Propulsion selection for 85 kft remotely piloted atmospheric science aircraft. *NASA Technical Memorandum 107302*, 1996.

[12] R. Vos and J.A. Melkert. Fuselage design from tudelft ae1222-ii, 2017.

[13] R. Vos and J.A. Melkert. Wing and propulsion system design from tudelft ae1222-ii, 2017.

[14] J. Roskam. *Layout design of cockpit, fuselage, wing and empennage: cutaways and inboard profiles*. Darcorporation, 2002.

[15] R. Vos and J.A. Melkert. Empennage and gear design from tudelft ae1222-ii, 2017.

[16] H. Seung-Jae, K. Sang-Gon, K. Cheol-Won, and L. Yung-Gyo. Aerodynamic design of the solar-powered high altitude long endurance unmanned aerial vehicle. 2016.

[17] E. Torenbeek and H. Wittenberg. *Flight Physics*. Springer Netherlands, 2009.

[18] R. Mukesh, K. Lingadurai, and U. Selvakumar. Airfoil shape optimization using non-traditional optimization technique and its validation. *Journal of King Saud University - Engineering Sciences*, 26(2):191–197, 2014.

[19] V. Della, Pierluigi, E. Daniele, and E. D' Amato. An airfoil shape optimization technique coupling PARSEC parameterization and evolutionary algorithm. *Aerospace Science and Technology*, 32(1):103–110, January 2014.

[20] M. Drela. Xfoil: An analysis and design system for low reynolds number airfoils. volume 54, June 1989.

[21] D. Adrian, D. Sterian, M. Pricop, and I. Bunescu. Using genetic algorithms to optimize airfoils in incompressible regime. *INCAS BULLETIN*, 11:79–90, March 2019.

[22] T. Kenji, M. Wataru, A. Shigeru, and T. Yasuhiro. Effect of fuselage cross sections on aerodynamic characteristics of reusable launch vehicles in subsonic flow. *AIAA*, 55(641):288–292, 2007.

[23] S. Mahjoob, M. Mahmoud, and M. Taeibi-Rahni. Aerodynamic performance analysis of bodies with different cross-sections. *AIAA*, (1), June 2002.

[24] R.I. Aditya and A. Pant. A review on nose cone designs for different flight regimes. *International Research Journal of Engineering and Technology*, 07:3546–3554, August 2020.

[25] T. Oktay and M. Uzun. Aerodynamic tailcone shape optimization for autonomous navigation performance maximization of morphing aerial robot. May 2016.

[26] F. Götten, M. Havermann, C. Braun, M. Marino, and C. Bil. Improved form factor for drag estimation of fuselages with various cross sections. *Journal of Aircraft*, 58(3):549–561, 2021.

[27] S.A. Brandt, M. Post, D.W. Hall, F. Gilliam, T. Jung, and T.R. Yechout. The value of semi-empirical analysis models in aircraft design. *16th AIAA/ISSMO Multidisciplinary Analysis and Optimization Conference*, 2015.

[28] R. T. Whitcomb. A design approach and selected wind tunnel results at high subsonic speeds for wing-tip mounted winglets. July 1976.

[29] Aeronautical Research Council (Great Britain). *Theoretical Load Distribution on a Wing with Vertical Plates*. Reports & memoranda. H.M. Stationery Office, 1956.

[30] F. George. Understanding winglet technology.

[31] R.J. McGhee and W.D. Beasley. Low-speed aerodynamic characteristics of a 13-percent-thick medium-speed airfoil designed for general aviation application. August 1979.

[32] H. Schlichting. *Boundary-layer theory*. MacGraw-Hill, 1979.

[33] S.F. Hoerner. *Fluid-dynamic drag: theoretical, experimental and statistical information*. Hoerner Fluid Dynamics, 1992.

[34] M. Drela. Aerodynamics of heat exchangers for high-altitude aircraft. *Journal of Aircraft*, 33(1):176–184, 1996.

[35] J. Roskam. *Airplane design. Part III, Layout design of cockpit, fuselage, wing and empennage : cutaways and inboard profiles*. 1986.

[36] J.D. Naber and J.E. Johnson. In *Alternative Fuels and Advanced Vehicle Technologies for Improved Environmental Performance*, pages 197–224. Woodhead Publishing, 2014.

[37] Ethanol Producer Magazine. Will 100 LL fall to AGE85? June 2002.

[38] K. Thanikasalam, R. Mohsin, A. Fahmi, M. Zulkifli, N. Shawal, K. Ilanchelvi, M. Ananth, and E. Rajendaran. Ethanol content concerns in motor gasoline (mogas) in aviation in comparison to aviation gasoline (avgas). *IOP Conference Series: Materials Science and Engineering*, 370, May 2018.

[39] T.A. Snijders and J.A. Melkert. Using synthetic kerosene in civil jet aircraft. 2008.

[40] G.J.J. Ruijgrok. *Elements of airplane performance*. Vssd Pub, 2009.

[41] J.B. Heywood. *Internal Combustion Engine Fundamentals, 2nd Edition*. Mcgraw-Hill Education, 2018.

[42] Y.S. Kang, B.J. Lim, and B.J. Cha. Multi-stage turbocharger system analysis method for high altitude uav engine. *Journal of Mechanical Science and Technology*, 31:2803–2811, 2017.

[43] European Commission. Joint Research Centre. Institute for Environment and Sustainability. *Effect of fuel ethanol content on exhaust emissions of a flexible fuel vehicle*. Publications Office, 2009.

[44] D. Ipci and H. Karabulut. Thermodynamic and dynamic modelling of a single cylinder four stroke diesel engine. *Applied Mathematical Modelling*, 40, 11 2015.

[45] N. Kumma, K.G. Radha, T.R. Rao, K.M. Kumar, and S.R. Premkartikkumar. Experimental investigation on diesel engine fuelled with hythane gas. *International Journal of Mechanical Engineering and Technology*, 10:571–575, 02 2019.

[46] J. Kargul, M. Stuhldreher, D. Barba, C. Schenk, S. Bohac, J. McDonald, P. Dekraker, and J. Alden. Benchmarking a 2018 toyota camry 2.5-liter atkinson cycle engine with cooled-egr. volume 1, April 2019.

[47] B. Lee, D. Jung, D.N. Assanis, and Z. Filipi. Dual-stage turbocharger matching and boost control options. *Proceedings of the ASME Internal Combustion Engine Division 2008 Spring Technical Conference*, 2008.

[48] J.L. Loth, G.J. Morris, and P.B. Metlapalli. Staged turbocharging for high altitude ic engines. Technical report, American Institute of Aeronautics and Astronautics, Inc., 1997.

[49] S. Gordon and B. Mcbride. Computer program for calculation of complex chemical equilibrium compositions and applications. Part 1: Analysis. *NASA Reference Publication*, 1994.

[50] A. Bahadori and H.B. Vuthaluru. Estimation of air specific heat ratio at elevated pressures using simple predictive tool. *Energy Conversion and Management*, 52, 2011.

[51] N. Watson and M. S. Janota. *Turbocharging the internal combustion engine*. Palgrave, London, 1982.

[52] K. Kemal, S.G. Mustafa, H.A. Halil, C. Mücahit, and M.B. Tuna. Identification of flow phenomena over NACA 4412 wind turbine airfoil at low reynolds numbers and role of laminar separation bubble on flow evolution. *Energy*, 144:750–764, December 2017.

[53] R. MacNeill, D. Verstraete, and A. Gong. Optimisation of propellers for uav powertrains. *Propulsion and Power of Unmanned Aircraft Systems III*, 5090, July 2017.

[54] R. MacNeill and D. Verstraete. Blade element momentum theory extended to model low reynolds number propeller performance. *The aeronautical journal*, 121:835–857, May 2017.

[55] G.N. Barakos and A. Brocklehurst. A review of helicopter rotor blade tip shapes. *Progress in aerospace sciences*, 56, 2013.

[56] J. Mcbain. A simple electro-mechanical controllable pitch propeller. June 2019.

[57] M. Brown, A. Sánchez-Caja, J. Adalid, and S. Black. Improving propeller efficiency through tip loading. *Naval Hydrodynamics*, 30, 2014.

[58] S. Song, H. Zang, N. Duan, and J. Jiang. Experimental research and analysis on fatigue life of carbon fiber reinforced polymer (CFRP) tendons. *Materials*, 12(20):3383, October 2019.

[59] X. Gabrion, V. Placet, F. Trivaudey, and L. Boubakar. About the thermomechanical behaviour of a carbon fibre reinforced high-temperature thermoplastic composite. *Composites Part B: Engineering*, 95:386 – 394, 2016.

[60] T.H.G. Megson. *Introduction to Aircraft Structural Analysis*. Elsevier, 2018.

[61] M. Drela and S. Hall. Wing bending calculations, 2005.

[62] F. Oliviero. Systems engineering and aerospace design requirement analysis and design principles for a/c stability & control (part 2) from tudelft ae3211-i, 2021.

[63] F. Oliviero. Systems engineering and aerospace design: Design for lateral-directional aspects, design for ground operations from tudelft ae3211-i, 2021.

[64] E. Torenbeek. *Synthesis of Subsonic Airplane Design*. Delft University Press & Martinus Nijhoff Publishers, 1982.

[65] F. Nicolosi, D. Ciliberti, P. Della Vecchia, and S. Corcione. Aerodynamic design guidelines of an aircraft dorsal fin through numerical and experimental analyses. 2016.

[66] F. Nicolosi, D. Ciliberti, and L. De Luca. An improved preliminary design methodology for aircraft directional stability prediction and vertical tailplane sizing. 2016.

[67] A. Sanchez-Carmona and C. Cuerno-Rejado. Vee-tail conceptual design criteria for commercial transport aeroplanes. 2019.

[68] Á. Gómez-Rodríguez, A. Sanchez-Carmona, L. García-Hernández, and C. Cuerno-Rejado. Preliminary correlations for remotely piloted aircraft systems sizing. 2018.

[69] Z. Yi and W. Heping. A study of structure weight estimating for high altitude long endurance (hale) unmanned aerial vehicle (uav). 2006.

[70] M.H. Sadraey. *Aircraft Design: A Systems Engineering Approach*. Aerospace Series. Wiley, 2012.

[71] D. Raymer. *Aircraft Design: A Conceptual Approach, Sixth Edition*. American Institute of Aeronautics and Astronautics, Inc., Washington, DC, 2018.

[72] J.C. Naftel. Nasa global hawk: Project overview and future plans. Technical report, NASA Dryden Flight Research Center, 2013.

[73] L. Wang, Z. Zhang, and P. Sun. Quaternion-based kalman filter for ahrs using an adaptive-step gradient descent algorithm. *International Journal of Advanced Robotic Systems*, 12(9):131, 2015.

[74] A. Fakharian, T. Gustafsson, and M. Mehrfam. Adaptive kalman filtering based navigation: An imu/gps integration approach. In *2011 International Conference on Networking, Sensing and Control*, pages 181–185, 2011.

[75] A. Fallast and B. Messnarz. Automated trajectory generation and airport selection for an emergency landing procedure of a CS23 aircraft. *CEAS Aeronautical Journal*, 8(3):481–492, September 2017.

[76] B. Albaker and N. Abd Rahim. Flight path pid controller for propeller-driven fixed- wing unmanned aerial vehicles. *International Journal of Physical Sciences*, 6, 04 2011.

[77] N.C. Heerens. Landing gear design in an automated design environment. Technical report, Delft University of Technology, 2014.

[78] R.E. Weibel and R.J. Hansman. Safety considerations for operation of unmanned aerial vehicles in the national airspace system. page 107, November 2006.

[79] Sinke J. Production of aerospace systems: Joining & assembly, introduction – mechanical fastener, 2021.